

Optic-flow processing in the pretectum of larval zebrafish
as revealed by the FuGIMA method

Dissertation

der Fakultät für Biologie

der Ludwig-Maximilians-Universität

München

Vorgelegt von

Anna Sophia Elisabeth Kramer

16. Mai 2019



Erstgutachter (Betreuer):

Prof. Herwig Baier

Zweitgutachterin:

Prof. Laura Busse

Abgabe der Arbeit:

16. Mai 2019

Mündliche Prüfung:

21. Oktober 2019

Im Gedenken an meinen Opa („*Wie geht es den Fischen?*“)

Summary

Detection of whole-field motion (optic flow) is important for animals. A fish drifting in a river, for example, experiences translational optic flow, to which it reacts with swimming movements. The basis for the detection of optic flow is the detection of movement, which occurs in the retina. In larval zebrafish, a model organism used in neurobiology, retinal ganglion cells (RGCs) specific for motion detection in each direction, send their axons to the pretectum in the diencephalon, amongst other targets. In the pretectum, neurons responding to different combinations of monocular and binocular motion are intermingled. To investigate if there is a spatial relationship among neurons encoding different motion cues needed for optic flow detection, I applied the optogenetic method FuGIMA (function-guided inducible morphological analysis). FuGIMA makes it possible to analyze the morphology of a neuron, which was previously functionally characterized. Specifically, we investigated neurons of the monocular direction-selective (DS, “simple”) and translation-selective (“complex”) response classes. Indeed, neurons of the two classes were found to vary in their morphology: neurites of some monocular, DS neurons innervate the pretectal arborization field 5 (AF) of RGCs, no neurites of translation-selective neurons extend there. Furthermore, direction-selective RGCs terminate in AF5 and to a lesser degree in AF6. Therefore, AF5 is the area, where RGCs can pass on DS information to pretectal monocular neurons. Both classes of investigated pretectal neurons, however, innervate the area at the dorsal border of AF6. Therefore, this region positions itself as the relay site between the monocular direction-selective and translation-selective response classes. As neurons analyzed with FuGIMA (FuGIMA neurons) were rather short and did not project to pre-motor brain areas, I searched in a single-neuron atlas for equivalents to FuGIMA neurons. Most of the 38 pretectal projection neurons (PPNs), whose somata lie in the same region as these of FuGIMA neurons, project to one of two described premotor centers: the cerebellum or the reticular formation (ventral hindbrain).

On the basis of these findings, we postulate that motion information underlying the sensation of optic flow is processed in the following way to drive swimming behavior: relevant motion cues are detected by DS RGCs, which synapse with dendrites of monocular DS pretectal neurons in AF5. Pretectal neurons extending into AF5 in turn further process these motion cues in concert with neighboring translation-selective neurons in the pretectum before this information is transmitted to pre-motor centers, namely the cerebellum and the reticular formation, which drive behavioral output. Only the new method FuGIMA in combination with other data sets allowed this investigation from different perspectives.

Zusammenfassung

Eine großräumige Bewegung im Blickfeld, den sog. optischen Fluss, wahrzunehmen, stellt für Tiere eine wichtige Fähigkeit dar. Beispielsweise erfährt ein abdriftender Fisch translationalen optischen Fluss, worauf er mit Schwimmbewegungen reagiert. Grundlage des Erkennens von optischen Fluss ist die Detektion von Bewegung, welche in der Retina erfolgt. In der Zebrafischlarve, einem Modelltier der Neurobiologie, senden retinale Ganglionzellen (*retinal ganglion cells*, RGCs), die spezifisch auf Bewegung in einer Richtung reagieren, ihre Axone u. a. in das Prätektum im Zwischenhirn. Im Prätektum liegen Neurone, welche auf unterschiedliche Kombinationen von monokularer- und binokularer Bewegung reagieren, gemischt nebeneinander. Um herauszufinden, welche Stellung benachbarte Neurone mit unterschiedlichen Antwortmustern im neuronalen Schaltkreis zur Erkennung von optischem Fluss haben, wandte ich in der hier beschriebenen Arbeit die optogenetische Methode FuGIMA (*Function-guided Inducible Morphological Analysis* – an der Funktion ausgerichtete morphologische Analyse) an. Mittels FuGIMA kann die Morphologie einer Zelle, welche zuvor funktionell charakterisiert wurde, untersucht werden. Tatsächlich unterscheiden sich zwei Klassen von prätektalen bewegungssensitiven Neuronen: Während Neuriten von manchen monokularen, richtungsselektiven Neuronen das Verästelungsfeld 5 der RGCs (*arborization field*, AF) innervieren, erstrecken sich keine Neuriten von translationsselektiven Neuronen dorthin. In AF5 wiederum, und zu einem geringeren Anteil in AF6, enden richtungsselektive RGCs. Dort kann also richtungsselektive Information an prätektale monokulare Neurone weitergegeben werden. Beide Klassen der untersuchten Neuronen innervieren die Region an der dorsalen Grenze von AF6. Dadurch bietet sich diese Region zum Informationsaustausch zwischen den untersuchten Klassen an. Da die mit FuGIMA markierten Neuriten eher kurz waren und nicht zu bekannten prämotorischen Gehirnzentren projizierten, suchte ich in einer Sammlung von einzelnen Neuronen (*single-neuron atlas*) nach Äquivalenten zu FuGIMA-Neuronen. Fast alle 38 prätektalen Projektionsneurone, deren Somata in derselben Region liegen wie die der FuGIMA-Neurone, projizieren zu einem von zwei beschriebenen prämotorischen Zentren: dem Kleinhirn (Cerebellum) oder der retikularen Formation (ventrales Stammhirn).

Zusammengefasst postulieren wir, dass dem optischen Fluss zugrundeliegende Bewegungsinformationen über folgende Zentren in Schwimmbewegung umgesetzt werden: ausgehend von richtungsselektiven RGCs, dann über AF5 zu monokularen richtungsselektiven prätektalen Neuronen, weiter zu benachbarten translationsselektiven Neuronen und von dort zu zwei prämotorischen Zentren, dem Cerebellum und der retikularen Formation. Dabei ermöglichte erst die neue Methode FuGIMA sowie die Kombination verschiedener Datensätze diese Betrachtung aus unterschiedlichen Blickwinkeln.

Publications and author contributions

The research and methods development described in this thesis build on and/or incorporate work by my colleagues, as indicated.

Dominique Förster, **Anna Kramer**, Herwig Baier, Fumi Kubo. 2018. Optogenetic precision toolkit to reveal form, function and connectivity of single neurons. *Methods*, 150: 42-48. DOI: [10.1016/j.ymeth.2018.08.012](https://doi.org/10.1016/j.ymeth.2018.08.012).

Author contribution: DF, HB, and FK conceived the project. DF established the optobow suite. **AK** established FuGIMA in the pretectum, DF in the optic tectum. DF, **AK**, HB, and FK wrote the manuscript.

Michael Kunst, Eva Laurell, Nouwar Mokayes, **Anna Kramer**, Fumi Kubo, Antonio M. Fernandes, Dominique Förster, Marco Dal Maschio, Herwig Baier. 2019. A cellular-resolution atlas of the larval zebrafish brain. *Neuron*, 103: 21-38. DOI (Sneak Peek version): [10.2139/ssrn.3257346](https://doi.org/10.2139/ssrn.3257346).

Author contribution: MK and HB conceived the experiments and wrote the paper. EL performed the experiments. MK performed analysis. NM wrote the code for the online platform and analysis tools for the single neuron database. **AK**, FK, AMF, DF, and MDM helped verify the successful alignment of single-neuron tracings.

Anna Kramer, Yunmin Wu, Herwig Baier, Fumi Kubo. 2019. Neuronal architecture of a visual center that processes optic flow. *Neuron*, 103: 118-132. DOI: [10.1016/j.neuron.2019.04.018](https://doi.org/10.1016/j.neuron.2019.04.018).

Author contribution: HB and FK conceived the project. **AK** performed FuGIMA experiments, generated the *UAS:FuGIMA* and *UAS:FuGIMA-C3PA* transgenic lines and performed anatomical registrations and complementation analyses. YW performed the imaging on RGC terminal responses and analyzed the direction-selective responses in RGCs. FK generated the *UAS:syGCaMP6s* transgenic line. **AK**, YW, and FK annotated arborization fields. **AK**, YW, HB, and FK wrote the manuscript.

Acknowledgements

“No man is an island” (*J. Donne*) – likewise, I did not write this thesis, or pursue the underlying work, in isolation. Rather, many people supported me during the six years of PhD time at the Max Planck Institute of Neurobiology, Martinsried, and the preparation of this work.

First, I want to thank Herwig for giving me this opportunity to join the lab already as a master’s student and letting me work on several projects focused on methods development. His supervision allowed me to develop my critical thinking and independence. I am deeply grateful for Fumi’s hands-on support and supervision, especially in the later PhD years and leading up to the publications.

Reinhard Köster and Leanne Godinho helped shaping this work as external members of my thesis advisory committee (TAC) and I am grateful for their realistic evaluations and friendly motivation.

Koichi Kawakami, Fumi and the Japan Society for the Promotion of Science (JSPS) made a dream come true – my stay at the National Institute of Genetics (NIG) in Mishima, Japan. I not only had the unique chance to work on the FuGIGEx method, but also got to know this fascinating and beautiful country.

All the members of the Baier lab, past and present, made this lab feel like a small village. I very much enjoyed the critical questions during lab meetings, pushing us forward, and the cooperative atmosphere. Thanks for all the support and fun, especially to my “neighbors” in the small lab. In particular, I would like to thank Dominique for the initial support in molecular biology, sharing his excitement for complex optogenetic techniques and initiation of the FuGIMA method. Furthermore, thanks to Yunmin for the close and motivating collaboration on the RGC mapping. Irene took on many challenging requests of mine for molecular work and I am grateful for her help. In addition, I want to thank Alison for valuable comments on this thesis and especially her excellent introduction to zebrafish work, from which I benefit to this day.

The work with zebrafish larvae would not be possible without good care for adult fish. Therefore, I want to thank Karin, Krasimir, and Stephanie together with all animal caretakers for outstanding fish care.

Life has its ups and downs, but pursuing a PhD was at times an emotional rollercoaster ride for me. Therefore, I thank my friends both at the institute and outside for their support and motivation. Finally, I whole-heartedly thank my family and Mathieu for their love and unshakeable belief in me.

Contents

Summary	iv
Zusammenfassung.....	v
Publications and author contributions.....	vi
Acknowledgements.....	vii
List of abbreviations.....	xi
1 Introduction.....	1
1.1 Early processing of visual information.....	1
1.1.1 The retina – the first stage of visual processing	1
1.1.2 Retinal targets in the brain.....	1
1.2 The motion-sensitive “visual channel”	3
1.3 Central motion processing in larval zebrafish.....	4
1.3.1 Motion processing in the optic tectum	4
1.3.2 Responses to whole-field motion.....	5
1.4 Pretectum and accessory optic system (AOS).....	6
1.4.1 Composition.....	6
1.4.2 Function.....	8
1.4.3 Connectivity	10
1.4.4 Downstream of the pretectum/AOS: Cerebellum and inferior olive	11
1.5 Tools to study the brain	12
1.5.1 The larval zebrafish as a model for neuroscience research	12
1.5.2 Establishment of transgenic zebrafish lines	13
1.5.3 Fluorescent proteins.....	14
1.5.4 Optogenetics – perfectly complementing zebrafish advantages	15
1.5.5 Two-photon microscopy	16
1.5.6 Image registration with ANTs	17
1.5.7 Combining functional and morphological analysis in pretectal neurons	18
1.5.7.1 Electrophysiology	18
1.5.7.2 Photoactivatable GFP	18
1.5.7.3 Function-guided inducible morphological analysis (FuGIMA)	19
1.6 Aims of this thesis.....	21
2 Manuscripts.....	22
2.1 Manuscript 1	22
2.2 Manuscript 2	30
2.3 Manuscript 3	92

3	<i>Discussion</i>	151
3.1	Broader implications of the described findings	151
3.2	Pretectal organization	152
3.2.1	Specific pretectal areas described in larval zebrafish	152
3.2.2	Characterization by responses to visual stimuli	153
3.2.3	Characterization by circuit manipulation	154
3.2.4	Characterization by transgenic expression patterns	156
3.2.5	Correspondences between larval and adult zebrafish pretectum	157
3.3	Potential improvements of FuGIMA	159
3.3.1	Increasing the signal-to-noise ratio of paGFP	159
3.3.2	Automated targeting of cells	160
3.3.3	Automated tracing	161
3.4	Further technical considerations	161
3.4.1	Perspective on identified pretectal projection neurons	161
3.4.2	New transgenic lines to investigate pretectal processing	163
4	<i>Outlook</i>	164
4.1	Functional imaging combined with electron microscopy (EM)	164
4.2	What is next? Function-guided inducible gene expression (FuGIGEx)	165
	<i>References</i>	<i>I</i>
	<i>Eidesstattliche Erklärung (Affidavit)</i>	<i>XIII</i>

List of figures

Figure 1: Retinal ganglion cell (RGC) axons terminate in several areas of the brain.....	2
Figure 2: Retinofugal projections of three types of DS-RGCs in mammals.	4
Figure 3. Zebrafish larvae respond to whole-field motion with stereotyped behaviors.....	6
Figure 4: The adult zebrafish pretectum contains many afferent and efferent connections....	8
Figure 5: Pretectal neurons respond differentially to monocular and binocular optic flow. ..	10
Figure 6: Establishment of transgenic zebrafish lines using the Tol2 transposase system.	14
Figure 7: Functional imaging - ideal for neuroscience in larval zebrafish.	16
Figure 8: FuGIMA - anatomical and morphological characterization of single neurons.	20
Figure 9: Localization of motion-sensitive neurons in the pretectum.....	155
Figure 10: Brain-wide activity changes after ablation of functionally defined clusters.	156
Figure 11: Neuronal clusters overlapping with/in close proximity to the FuGIMA-VOI.....	158
Figure 12: A better FuGIMA? Function-guided inducible gene expression (FuGIGEx).....	166

List of abbreviations

Abbreviation	Full term
2p	Two-photon
AF	Arborization field
AMC	Anterior medial cluster
ANTs	Advanced normalization tools
AOS	Accessory optic system
APN	Accessory pretectal nucleus
dLGN/vLGN	Dorsal/ventral lateral geniculate nucleus
DNA	Deoxyribonucleic acid
dpf	Days post fertilization
DS	Direction-selective
DTN	Dorsal terminal nucleus
EM	Electron microscopy
FP	Fluorescent protein
FuGIMA	Function-guided inducible morphological analysis
GECI	Genetically encoded calcium indicator
GFP	Green fluorescent protein
hpf	Hours post fertilization
Hz	Hertz
IO	Inferior olive
IPL	Inner plexiform layer
LTN	Lateral terminal nucleus
MTN	Medial terminal nucleus
NOT	Nucleus of the optic tract
OFF	Response to light decrements
OKR	Optokinetic response/reflex
OMR	Optomotor response
ON	Response to light increments
paGFP	Photoactivatable GFP
PCe	Central pretectal nucleus
PCo	Paracommissural pretectal nucleus
Pi	Intercalated pretectal nucleus
PPn	Periventricular pretectal nucleus
PPN	Pretectal projection neuron
PSm/PO	Magnocellular superficial plus posterior pretectal nucleus

Abbreviation	Full term
PSp	Parvocellular superficial pretectal nucleus
RGC	Retinal ganglion cell
ROI	Region of interest
SyN	Symmetric normalization
UAS	Upstream activating sequence
VTRZ	Ventral tegmental relay zone
z-stack	Series of single focal plane images delineating a volume

1 Introduction

Many animals, including humans, rely heavily on visual information to navigate in their environment, escape from predators, and find food and conspecifics. Understanding how the central nervous system generates the sense of vision and appropriate behavioral responses is not only highly interesting in itself, but also serves as a blueprint to investigate neuronal processing in general. Our understanding of the brain relies heavily on the immense technological leaps made in the last 50 years, enabling many scientific breakthroughs. Thus, the following introduction will summarize both the biological and technological foundations of the work presented in this thesis.

1.1 Early processing of visual information

1.1.1 The retina – the first stage of visual processing

The eye is not merely a sensor, but rather the first visual processing center. In larval zebrafish (the model organism used in this work, see section 1.5.1, page 12), eyes are the most prominent sensory organs, observable as early as 24 hours post fertilization (hpf), when retinal pigmentation commences (Kimmel, et al., 1995). Development of the retina and the optic tract rapidly progresses and beginning from 3 days post fertilization (dpf) visually driven behaviors develop (Easter and Nicola, 1996). At 7-8 dpf, half of the neurons of a larva's brain are in its retinae (Zimmermann, et al., 2018).

The zebrafish retina is typical for vertebrates, comprising of five neuronal classes (photoreceptors – i.e. rods and cones, bipolar cells, amacrine cells, horizontal cells, and retinal ganglion cells (RGCs)). The neurons are located in three cell body layers interspersed with two neuropil/synaptic layers (outer nuclear layer, outer plexiform layer, inner nuclear layer, inner plexiform layer - IPL, ganglion cell layer). Photoreceptors react to changes in light level by modulating the release of the neurotransmitter glutamate, to which bipolar cells respond depending on their molecular makeup (reviewed in Dhande, et al. (2015)). Axons of different bipolar and amacrine cell types terminate in distinct layers of the IPL and RGCs in turn receive inputs from bipolar and amacrine cells depending on their dendritic stratifications in the IPL. RGCs, the sole output neuron type of the retina, then relay distinct tuning to various features of the visual image to the brain.

1.1.2 Retinal targets in the brain

In adult mice, over 30 functional RGC types are described (Baden, et al., 2016). They project to ~49 retinofugal targets in the brain in different combinations (Martersteck, et al., 2017, Morin and

Studholme, 2014), with the dorsal lateral geniculate nucleus (dLGN) and the superior colliculus being the major targets (the latter is innervated by >90% of RGCs; **Figure 1C**, page 2). In larval zebrafish, the core features of retinofugal projections are preserved, however with lower complexity. Here, RGC axons fully cross the midline and innervate the brain in ten distinct arborization fields (AFs; **Figure 1A**)(Burrill and Easter, 1994, Robles, et al., 2014). AFs 1 to 9 are mostly devoid of somata and surrounded by the preoptic region, the thalamus, the hypothalamus, the accessory optic system and the pretectum, whereas AF 10 is located in the neuropil of the optic tectum, the homolog of the mammalian superior colliculus (Wullmann, et al., 1996). Combining dendritic stratifications with axonal targeting, more than 50 morphological types of RGCs have been described in zebrafish (Robles, et al., 2014)(see **Figure 1B** for axonal types).

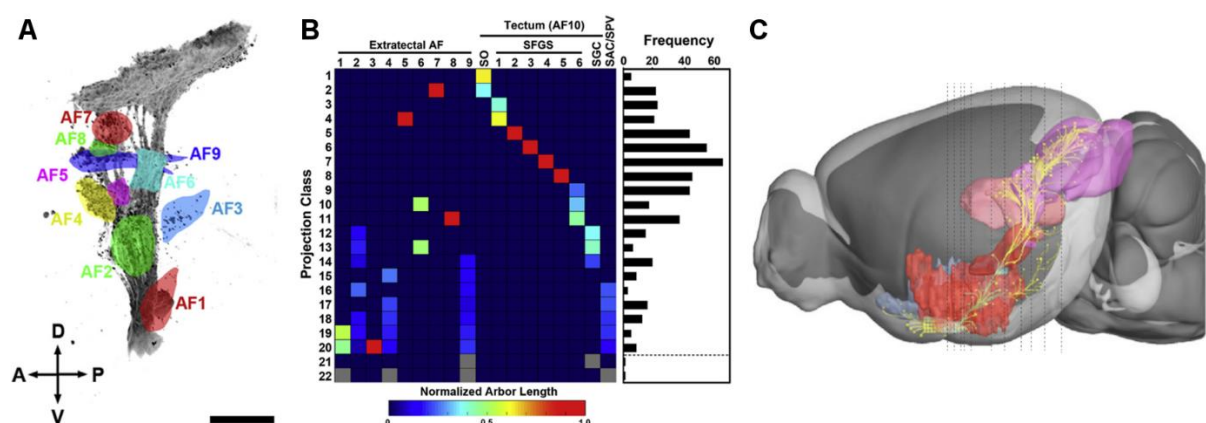


Figure 1: Retinal ganglion cell (RGC) axons terminate in several areas of the brain. **A:** In larval zebrafish, RGC axons project to the contralateral hemisphere, where they terminate in ten distinct arborization fields (AFs, numbered from ventral to dorsal), with AF 10 located in the optic tectum. **B:** RGC axons innervate AFs in different, specific combinations, giving rise to 20 projection classes. **C:** RGC axons of adult mice target ~ 59 brain areas. Lateral view of a mouse brain (3D rendering) shows RGCs (yellow) and innervated brain regions (red: hypothalamus; blue: amygdala/pallidum; pink: thalamus; purple: midbrain). Images shown in A and B modified from Robles, et al. (2014)(with permission); the image shown in C is modified from Martersteck, et al. (2017)(license: CC BY NC ND).

It has been proposed that functionally distinct RGC types terminate in different AFs, thereby separating parallel visual channels, i.e. circuits dedicated to the processing of certain image features. This spatial separation of relay areas optimizes separate processing for distinct visual features (Dhande and Huberman, 2014). Furthermore, it provides an entry point to investigate feature-selective circuits. Examples for such spatial separation of functional representations in AFs of larval zebrafish are sensitivity of AF4 to increasing or decreasing levels of ambient light, responses of AFs 6, 8 and deeper SFGS layers to looming stimuli, and responses of AF7 to prey-like objects (Semmelhack, et al., 2014, Temizer, et al., 2015, Zhang, et al., 2017).

1.2 The motion-sensitive “visual channel”

The retina extracts information about motion from the visual scene, thereby establishing the motion-sensitive visual channel. Direction-selective (DS) neurons respond differently to motion in opposing directions, i.e. activation by visual stimuli moving in the preferred direction and no response or suppression during movement in the opposite direction (null direction)(Barlow and Hill, 1963). Photoreceptors, however, are direction unselective and solely respond to changes of light level, as elicited by objects moving through the photoreceptor’s receptive field. To infer direction and velocity of motion, retinal processing compares signals across photoreceptors. How DS responses are established was intensely studied theoretically and experimentally in vertebrates and invertebrates over the last decades (reviewed in (Borst and Euler, 2011, Dhande, et al., 2015)). Different retinal subtypes involved in motion processing are currently best studied in mammals. Here, ON or OFF bipolar cells, responding to light increments or decrements, respectively, project their axons into different layers of the IPL. As a result, the IPL is subdivided into ON (bordering the ganglion cell layer) and OFF layers (bordering the inner nuclear layer). RGCs extend their dendrites into one or more IPL layers, thereby inheriting the respective tuning. Starburst amacrine cells are responsible for establishing DS tuning of DS-RGCs by suppressing activity during motion in the null-direction (Briggman, et al., 2011). Tuning of DS-RGCs varies with their topological distribution over the retina, giving them a predisposition to detect translational and rotational optic flow (Sabbah, et al., 2017). DS-RGCs, which comprise ON-OFF DS-RGCs, ON DS-RGCs and OFF DS-RGCs, project to a variety of brain areas, and provide the foundation with which to subserve different processing functions (**Figure 2**, page 4). A subgroup of DS-RGCs, which are tuned to slow motion (about $1 - 3^\circ/s$), projects to the accessory optic system (AOS)(reviewed in Schiller (2010)). Although historically these had been classified as ON DS-RGCs, at least in mice this population contains, aside from three monostratified ON DS-RGCs, one forward- and one downward-sensitive ON-OFF DS-RGC subtype (reviewed in Dhande, et al. (2015)). In mammals, ON DS-RGCs project to the AOS nuclei, namely the nucleus of the optic tract (NOT), and the dorsal, lateral and medial terminal nuclei (DTN, LTN and MTN, respectively).

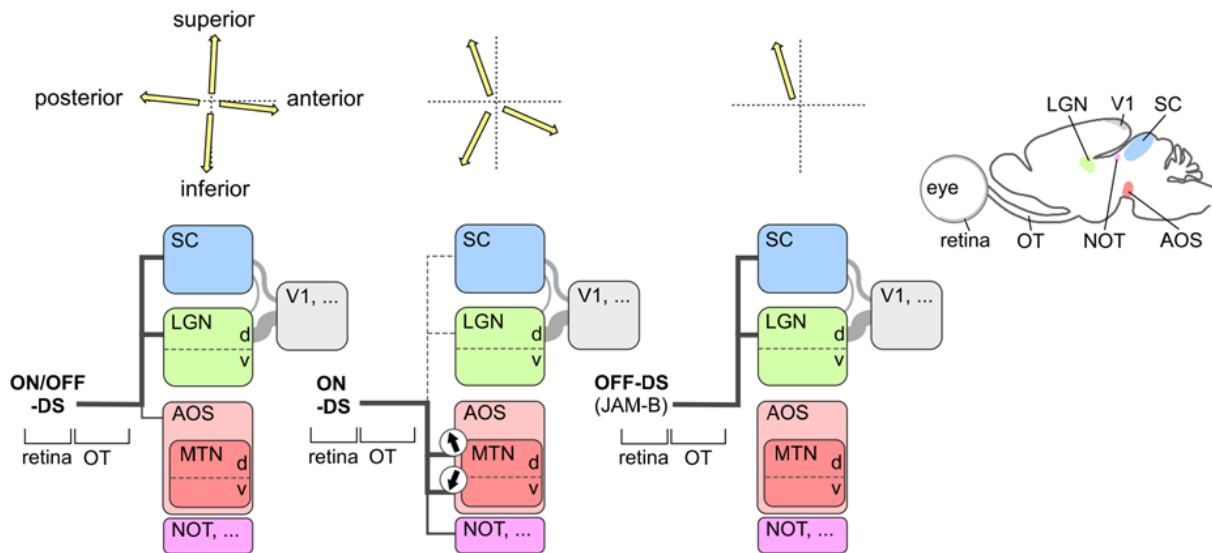


Figure 2: Retinofugal projections of three types of DS-RGCs in mammals. **Top left:** population tuning of DS-RGC types. **Bottom left:** Schematic of projection patterns of DS-RGC types from the retina to retinorecipient/visual brain centers. Line width corresponds to relative contribution of interconnections, colors as in the brain schematic (right). OT: optic tract, SC: superior colliculus, LGN: lateral geniculate nucleus, d: dorsal, v: ventral, V1: primary visual cortex, AOS: accessory optic system, MTN: medial terminal nucleus, NOT: nucleus of the optic tract. **Right:** Schematic of sagittal brain section with retinorecipient/visual brain centers highlighted (modified from Borst and Euler (2011)(with permission)).

1.3 Central motion processing in larval zebrafish

While zebrafish follow the general vertebrate *Bauplan*, important differences compared to mammals make highlighting their anatomy and the status of research regarding motion processing in zebrafish larvae worthwhile.

1.3.1 Motion processing in the optic tectum

The optic tectum, the homologue of the mammalian superior colliculus, is the largest visual center in lower vertebrates. Moreover, it receives multisensory input, despite its dominance in visual processing and the intense research thereof. In larval zebrafish, the optic tectum is important for at least two essential behaviors driven by motion vision, namely prey capture and predator avoidance (Barker and Baier, 2015, Gahtan, et al., 2005). DS information reaches the tectum via DS-RGCs that project to the superficial layer of the *stratum fibrosum et griseum superficiale* (SFGS1) in the neuropil of the optic tectum/AF10 (Nikolaou, et al., 2012). These DS-RGCs respond to motion in three equally spaced directions. The two main cell types of the optic tectum, the periventricular neurons (PVNs) and the superficial interneurons (SINs) both contain a DS subpopulation. Of the SINs, which are characteristic due to their soma location in the superficial layer and a widely branching arbor, most visually responsive neurons are DS, with one of three preferred directions (Abbas, et al., 2017).

Furthermore, SINS are mainly tuned to motion of large stimuli (~ 50 degrees)(Barker, et al., 2017, Del Bene, et al., 2010, Preuss, et al., 2014, Yin, et al., 2019). The PVNs, however, respond to smaller stimuli (~ 20 degrees) and the four preferred directions observed in the PVN population align with the cardinal axes (Abbas, et al., 2017, Yin, et al., 2019). Inhibitory inputs to PVNs shape their response to the null direction (Gabriel, et al., 2012, Grama and Engert, 2012). While the optic tectum is essential for behaviors driven by local motion, e.g. prey capture, its ablation does not abolish behaviors evoked by whole-field motion (Roeser and Baier, 2003). Therefore, at least two visual channels of motion processing exist in the larval zebrafish.

1.3.2 Responses to whole-field motion

While local motion, such as a small moving dot, gives an animal information about other agents in the environment, global or whole-field motion is an indication of self-motion. Images drifting across large portions of the retina generate the sensation of optic flow (Gibson, 1954)(**Figure 3A**, page 6). Binocular integration of optic flow experienced by the two eyes allows for the distinction between two main patterns: The sensation of translation results from both eyes viewing motion of the same direction, i.e. forward and backward, while the sense of rotation results from motion in opposite directions in two eyes, i.e. clock-wise or counter-clock-wise. In larval zebrafish, two hard-wired behaviors in response to rotating and translating optic flow are the optokinetic response/reflex (OKR) and the optomotor response/reflex (OMR), respectively. In OKR, fish slowly follow the perceived motion with their eyes, which prevents retinal slip and sustains visual acuity. These slow phases are interspersed by rapid and short resets of the eye position, called saccades. In OMR, fish swim in the same direction of the perceived translational motion, to stabilize themselves e.g. as they would in a stream, thereby compensating for self-motion (**Figure 3B, C**). While larvae as young as 4-5 dpf reliably perform OKR, OMR is stably performed in 6-7 dpf larvae (Neuhauss, et al., 1999, Orger, et al., 2004, Orger, et al., 2008, Orger, et al., 2000, Portugues and Engert, 2009, Rinner, et al., 2005). Both OKR and OMR are conserved across other teleost fish and vertebrates (reviewed in Masseck and Hoffmann (2009a)). Due to the early onset and stable performance of OKR and OMR in zebrafish larvae, mutagenesis screens used these behaviors to elucidate genetic components of the underlying visual pathways (Brockerhoff, et al., 1995, Neuhauss, et al., 1999).

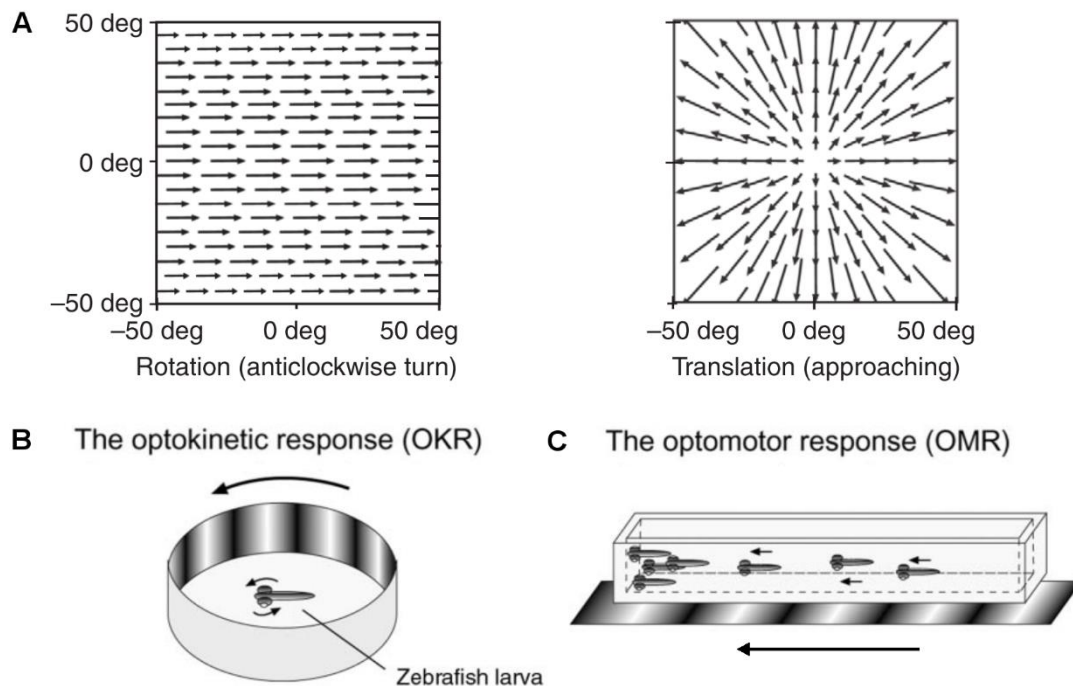


Figure 3. Zebrafish larvae respond to whole-field motion with stereotyped behaviors. **A:** Flow-fields of rotational and translational optic flow, with arrows depicting the velocity vectors of motion at each location of the visual field. **B:** Rotational optic flow elicits the optokinetic response (OKR), characterized by eye movements following the perceived motion, interspersed by fast resets, the saccades. **C:** Translational optic flow to the front elicits the optomotor response (OMR), where larvae swim with the perceived motion. Image A modified from Horseman, et al. (2011), images B and C modified from Roeser and Baier (2003)(both with permission).

1.4 Pretectum and accessory optic system (AOS)

The neural substrates of horizontal OKR in mammals are the pretectal nucleus of the optic tract (NOT) and the dorsal terminal nucleus (DTN) of the accessory optic system (AOS; reviewed in Giolli, et al. (2005) and (Huang and Neuhauss, 2008)). The following section is meant to describe the respective nuclei concerning anatomy and function in mammals and fish. However, in the case of literature on the fish pretectum, terminology and homology has not yet reached a consensus, thus warranting further research (reviewed in Anadón (2017)).

1.4.1 Composition

Based on the prosomeric model of forebrain organization, the pretectum is located in the caudal diencephalon, rostrally delineated by the thalamus and caudally by the midbrain (Lauter, et al., 2013, Rubenstein, et al., 1994). The term pretectum describes nuclei in a “poorly defined anatomical region” surrounding the posterior commissure (mostly ventrally), which are collectively termed pretectum due to their relative position anterior to the optic tectum (Anadón, 2017). The pretectum is comprised of several retinorecipient and non-retinorecipient nuclei of distinct connectivity. The

non-mammalian homologue of the NOT is the pretectal nucleus lentiformis mesencephali (Mckenna and Wallman, 1981).

The term AOS focuses on the retinal origin of subsumed parts. Thus, the AOS comprises retinofugal tracts targeting a series of terminal nuclei, namely the DTN, MTN, and LTN, which line the posterior superior fasciculus of the optic tract (reviewed in Giolli, et al. (2005)). While the mammalian NOT and AOS nuclei are similar with respect to connectivity, neuropharmacology, and function, they differ in terms of cytoarchitecture and gene expression (specifically expression of calcitonin gene related peptide). Resulting from technical limitations to separate them, they are commonly referred to in junction, as NOT/DTN (Giolli, et al., 2005). The non-mammalian homologue of the AOS is the nucleus of the basic optic root. In fish, exemplary in goldfish, the identity of the AOS homologue is controversial: while it was structurally described to comprise the basal optic root and the two terminal nuclei P1 and P2, a functional investigation identified only one pretectal nucleus, termed pretectal area (APT, see below)(Finger and Karten, 1978) (Massey and Hoffmann, 2009b). In larval zebrafish, the pretectum is located directly ventral to the optic tectum, laterally extending from the midline to the optic tract.

Subdivisions in nuclear areas of the pretectum of larval zebrafish are difficult to draw due to the lack of apparent cluster boundaries. In contrast, sub-branches of the optic tract and its associated AFs are highly structured; therefore, correspondence between AFs and adult pretectal nuclei were suggested (Burrill and Easter, 1994). For adult zebrafish, a recent study by Yáñez, et al. (2018) described several pretectal nuclei. Here, the conclusions of this study are discussed in detail as it is the most recent and comprehensive study concerning the question of pretectal organization in zebrafish, and thus most applicable to the work presented in this thesis. Using dye tracing, the authors identified the following regions and nuclei in the pretectum: 1) the superficial pretectum with the parvocellular (Psp) and magnocellular superficial plus posterior pretectal (PSm/PO) nuclei; 2) the central pretectum with the accessory pretectal nucleus (APN), the intercalated pretectal nucleus (Pi) and central pretectal nucleus (PCe); 3) the periventricular pretectum with the periventricular pretectal nucleus (PPn, subdivided into ventral – PPv – and dorsal – PPd) and the pretectal paracommissural nucleus (PCo); as well as 4) the dorsal accessory optic nucleus (Yáñez, et al., 2018)(**Figure 4**, page 8).

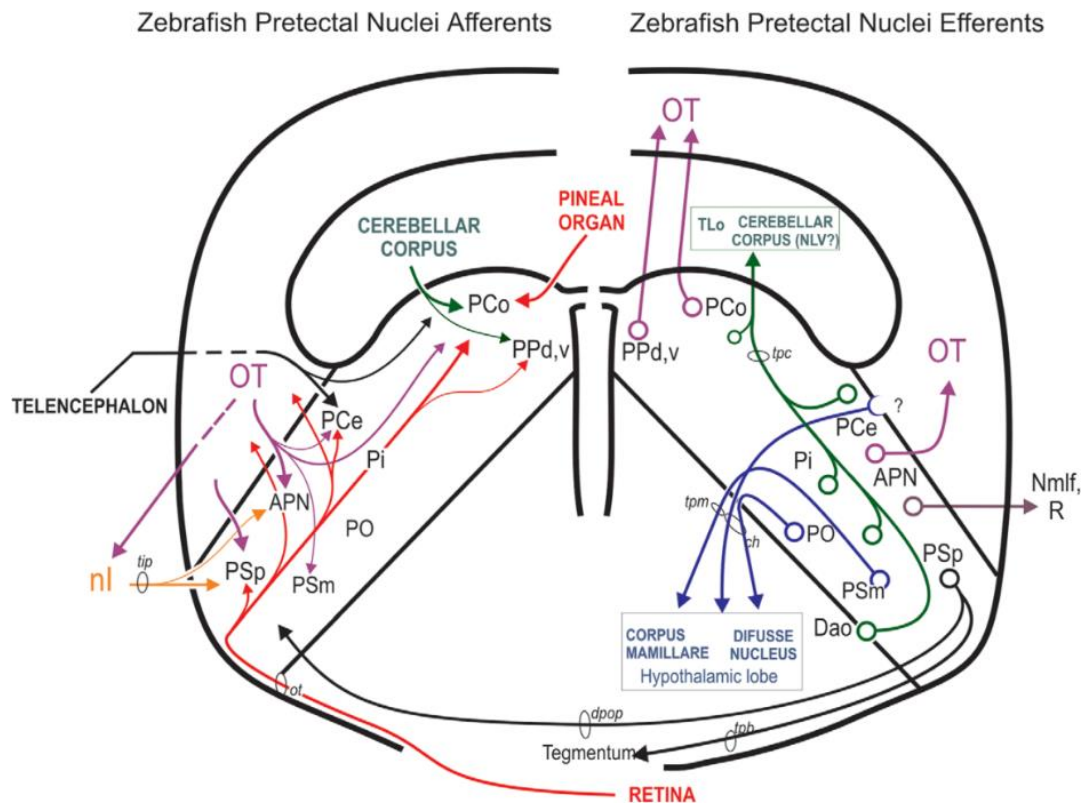


Figure 4: The adult zebrafish pretectum contains many afferent and efferent connections. Schematic transverse view depicting afferents (left) and efferents (right) of pretectal nuclei. APN, accessory pretectal nucleus; ch, horizontal commissure; Dao, dorsal accessory optic nucleus; dpop, dorsal postoptic commissure; nl, nucleus isthmi; NLV, lateral valvular nucleus; Nmlf, nucleus of the medial longitudinal fascicle; OT, optic tectum; ot, optic tract; PCe, central pretectal nucleus; PCo, paracommissural pretectal nucleus; Pi, intercalated pretectal nucleus; PO, posterior pretectal nucleus; PPD, dorsal periventricular pretectal nucleus; PPv, ventral periventricular pretectal nucleus; PSm, magnocellular superficial pretectal nucleus; PSp, parvocellular superficial pretectal nucleus; R, superior raphe; tip, isthmo-pretectal tract; TLo, torus longitudinalis; tpb, pretectobulbar tract; tpc, pretectocerebellar tract; tpm, pretecto-mammillary tract (Yáñez, et al., 2018)(with permission).

1.4.2 Function

Functionally, neurons of AOS nuclei in mammals have very large receptive fields and are tuned to motion at slow speeds ($\sim 1^\circ/\text{s}$; reviewed in Giolli, et al. (2005)). AOS nuclei show different responses to optic flow: While the preferred direction of MTN and LTN neurons is approximately up- or downward, DTN neurons respond best to horizontal motion in the temporo-nasal direction. The pretectal NOT shows the same preference as DTN. In fish, the pretectum was previously implicated in responses to optic flow (Easter, et al., 1978, Klar and Hoffmann, 2002). In larval zebrafish, about 40 % of pretectal neurons are DS, comprising of four populations approximately tuned to the cardinal directions (up, down, naso-temporal, temporo-nasal) and spatially intermingled (Wang, et al., 2019). In adult rainbow trout, neurons with vertical and horizontal preferred directions of motion are intermingled in the AOS and pretectal nuclei (Klar and Hoffmann, 2002). Similarly, the APT of

adult goldfish contains DS neurons tuned to rotation around the different axes of the semicircular canals (Masseck and Hoffmann, 2009b). Activation of the pretectum in mammals as well as larval zebrafish is sufficient to elicit OKR, while pretectal inactivation or lesions extinguish this behavior (Cazin, et al., 1980, Kubo, et al., 2014, Schiff, et al., 1988).

A recent study by Kubo, et al. (2014) characterized responses of pretectal neurons in zebrafish larvae to optic flow. Specifically, the authors sought to distinguish responses to monocular and binocular optic flow, evoked by moving gratings in a LED arena (**Figure 5 B, C**, page 10). With functional imaging, the study found that pretectal neurons possessed a variety of response patterns (**Figure 5 A, D**). These response patterns fall into three main classes: 1) neurons responding to monocular visual stimulation or binocular summing thereof, so-called “simple” response types (example cell 6, **Figure 5 D**), and 2) so-called “complex” response types, whose response profile is best explained by an inhibition from neurons tuned to motion seen by the other eye (example cell 5, **Figure 5 D**), and 3) other unclassified response types (Kubo, et al., 2014). A few response types stand out, as they frequently occur in each fish. Within the simple response types, the four most frequent types are monocular direction-selective neurons, tuned to motion in one eye, moving nasalward or temporalward (monocular tuned to nasalward left presentation of motion – MoNL; similarly: temporalward left - MoTL, temporalward right - MoTR, nasalward right - MoNR). Within the complex response types, the most frequent groups are translation- and rotation-selective (Kubo, et al., 2014).

Based on this detailed description of pretectal response patterns, hypotheses about the underlying neuronal circuit can be generated. As monocular DS neurons mimic responses of contralateral DS-RGCs, they might function as interneurons, locally relaying DS tuning. In contrast, complex response type neurons, which possess a more refined tuning better correlated with OKR/OMR, might project to pre-motor centers to drive those behaviors. Conflicting circuit hypotheses regarding the establishment of complex response types driving OKR and OMR exist in the literature. Namely, while Kubo, et al. (2014) suggested that monocular DS information converges in the pretectum, thereby giving rise to complex response types sufficient to drive these behaviors, Naumann, et al. (2016) posited the center of relevant integration lies in the hindbrain. Thus, this discrepancy warrants experimental clarification of the anatomical basis of pretectal processing and binocular integration underlying the OKR and OMR.

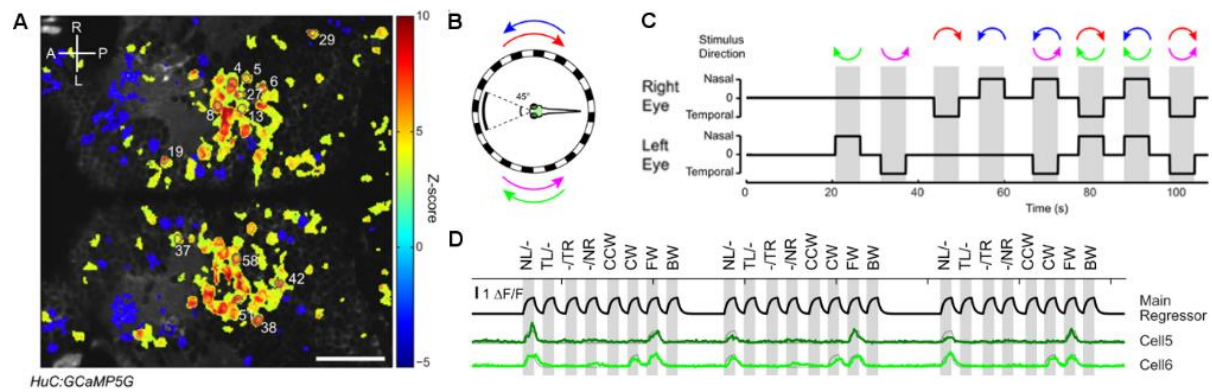


Figure 5: Pretectal neurons respond differentially to monocular and binocular optic flow.

A: Functional imaging in the pretectum during whole-field motion stimulation. **B:** Schematic of whole-field motion stimulation using a LED arena, with gratings moving nasal- and temporalward and independently to both hemispheres (green arrow: nasalward left/NL, magenta arrow: temporalward left/TL, red arrow: temporalward right/TR, blue arrow: nasalward right/NR). **C:** Schematic of the optic flow stimulus consisting of eight motion phases, four monocular ones (see B) and four binocular ones, composed of the monocular stimuli (CCW: counter-clock-wise, CW: clock-wise, FW: forward, BW: backward). **D:** Fluorescence traces of two example neurons (cells 5 and 6) responding to some phases of the eight-phasic motion stimulus. Of note is the similar, but not identical response pattern of cells no. 5 and 6, and their neighboring anatomical location (see A). Due to the simple tuning to the NL motion component, cell no. 6 is an example of a “simple” response type neuron. The response type of cell 5 was classified as “complex” due to the suppression resulting from the TR motion component during CW stimulation (modified from Kubo, et al. (2014)(with permission)).

1.4.3 Connectivity

Dye tracing studies in several animals elucidated the connectivity of the AOS/pretectum, thus some of these connections are the prime candidates for forming the anatomical basis of OKR/OMR downstream of the AOS/pretectum. In mammals, afferents to the AOS stem mainly from the contralateral retina, however with a species-dependent variance in the degree of ipsilateral projections. Interestingly, retinal terminals are located mainly on distal, but not proximal, dendrites of AOS neurons (Lenn, 1972). In NOT, varying portions of binocular neurons were observed (e.g. 50 % in the lower mammal opossum (Volchan, et al., 1989) and 80 % in cats (Hoffmann and Distler, 1989a)). At the same time, these animals show different sources of binocularity: an inhibitory connection between the NOTs via a commissural route was described in opossums (Pereira, et al., 2000), but this is absent in cats and rats (Schmidt, et al., 1995). In turn, the neural substrate for symmetry of OKR (equally strong responses to e.g. temporo-nasal and naso-temporal motion during monocular stimulation), and binocularity of the NOT in higher mammals (eutherians; including cats and rodents) are caused by ipsilateral projections from visual cortex to the NOT, which form later in development (reviewed in (Ibbotson, et al., 2002), Masseck and Hoffmann (2009a)).

Efferent connections of the AOS mainly target the brainstem and other oculomotor areas. Pre-oculomotor targets of the AOS were described in birds, but not in mammals. There, multisynaptic connections to oculomotor neurons may be present to complement connections to vestibular nuclei in coordinating eye movements. Furthermore, less defined projections to the reticular system via the ventral tegmental relay zone (VTRZ; a loosely defined area in the ventral midbrain tegmentum) and vestibular nuclei exist. A pronounced projection targets the inferior olive (IO) via a direct and an indirect pathway. Direct projections of the NOT/DTN run ipsilaterally in the medial longitudinal fasciculus, crossing only at the level of the IO and targeting the caudal dorsal cap of the IO. The indirect pathway runs contralaterally via the VTRZ, which in turn projects to the IO. It was suggested that the bilateral projections could be beneficial for the symmetry of the OKR (Blanks et al., 1995; Blanks et al., 2000). Lastly, a pre-cerebellar pathway, likely via the VTRZ, is controversial in mammals, however, a direct connection targeting the cerebellar cortex was described in fish, turtles and birds (reviewed in Masseck and Hoffmann (2009a)). Furthermore, neurons of the NOT target the ventral lateral geniculate nucleus (vLGN) (reviewed in Giolli, et al. (2005)).

In adult zebrafish, pretectal afferents originate from the retina, the telencephalon, the optic tectum, the cerebellum and the nucleus isthmi (Yáñez, et al., 2018). Specifically, PSp, APN, PCe, Pi, PCo and PPd,v receive retinal inputs (Yáñez, et al., 2018)(**Figure 4**, page 8). While DS-RGC terminals in the optic tectum of zebrafish larvae are well described (section 1.3.1, page 4), the identity of motion representations in the pretectum had not yet been clarified. Although functional evidence is lacking, morphological analysis of the RGC projectome suggests that DS-RGCs form collaterals in the RGC arborization field 5, thereby providing motion information to the pretectum (Robles, et al., 2014). Pretectal efferents of adult zebrafish project to the optic tectum, the torus longitudinalis, the cerebellar corpus, the lateral hypothalamus, as well as tegmental regions (Yáñez, et al., 2018)(**Figure 4**, page 8). Furthermore, pretectal nuclei are likely highly interconnected, although it is unknown to what extent.

1.4.4 Downstream of the pretectum/AOS: Cerebellum and inferior olive

The cerebellum, a major brain region controlling motor output conserved between mammals and teleosts, receives input via two pathways. Firstly, climbing fibers originate in the contralateral inferior olive in the posterior hindbrain, a nucleus implicated in motor timing and motor learning. Secondly, teleost mossy fibers originate from precerebellar nuclei including the pretectum and dorsal tegmental nuclei. The principal cerebellar neurons, Purkinje cells, receive excitatory input via these two streams and integrate visual and motor signals of different spike features (Knogler et al.

2019). Cerebellar processing is increasingly being investigated in larval zebrafish, where cerebellar layers are detectable from 5 dpf on (Bae, et al., 2009).

Functionally, responses of the cerebellum to whole-field motion are spatially segregated. Caudal Purkinje cells are active during optic-flow evoked saccadic eye movements/OKR and their inhibition impairs saccades, while rostro-medial Purkinje cells are active during optic-flow induced swimming, and their inhibition impairs swimming movements (Matsui, et al., 2014). A third population, interspersed between the motion-sensitive regions, responds to luminance changes (Knogler, et al., 2019). The functional segregation of the cerebellum is attributed to segregated functional pathways via the IO (Knogler, et al., 2019). Indeed, neurons of the MTN tuned to vertical motion (not the DTN), innervate the rostral part of the dorsal cap of the IO, whereas pretectal neurons tuned to horizontal motion innervate the caudal part of the dorsal cap of the IO. This segregation was also functionally characterized (reviewed in Giolli, et al. (2005)).

1.5 Tools to study the brain

While biological questions drive research, technology enables experiments leading to larger advances in our understanding. Therefore, I will introduce the model system, larval zebrafish, and tools underlying the work presented in this thesis in the following sections.

1.5.1 The larval zebrafish as a model for neuroscience research

To answer challenging biological questions, researchers often use a model system with reduced complexity. Aside from mammalian model organisms, small non-mammalian animals such as the fruit fly, *Drosophila melanogaster*, and the zebrafish, *Danio rerio*, are increasingly popular to investigate the visual systems. George Streisinger, Charles Kimmel, and colleagues at the University of Oregon established the zebrafish as a model organism in the 1980's (Stahl, 1995). Zebrafish are teleost fish and belong to the large family of cyprinids, just as e.g. the goldfish (*Carassius auratus*), whose neurobiology is also well investigated (Wullimann, et al., 1996). Endemic to small rivers, rice fields and wetlands in India and the Himalayan region, zebrafish prefer shallow water with low water flow and overhanging vegetation (Arunachalam, et al., 2013, Engeszer, et al., 2007, Spence, et al., 2008). This small vertebrate (typically < 40 mm) permits easy husbandry in the laboratory, including year-around breeding, a large clutch size (several hundred eggs), and a short generation time of about 3 months (reviewed in Meyers (2018)). Zebrafish are furthermore advantageous for biological research due to their external fertilization, fast embryonic development, and amenability to genetic manipulation. When trunk pigmentation is absent (i.e., chemically suppressed or in mutants lacking melanophores), larvae are transparent (Antinucci and Hindges, 2016, Lister, et al., 1999). Pairing this

“window into the body” with transgenic expression of fluorescent proteins plays to the full strength of these animals. Furthermore, larval zebrafish exhibit a limited behavioral repertoire, which has been exploited as an entry point to study underlying genes and brain circuits (reviewed in Friedrich, et al. (2010)). In terms of neuroscience research, zebrafish are advantageous, as their nervous system is similar in brain structure to those of other vertebrates, but with typically lower complexity, as the number of neurons per type is reduced (reviewed in Kalueff, et al. (2014)).

1.5.2 Establishment of transgenic zebrafish lines

To establish a transgenic line (**Figure 6**, page 14), the Tol2 transposon system is routinely used in zebrafish (Kawakami, et al., 2000). Initially, a solution containing the plasmid DNA (the gene of interest flanked by Tol2 recombination sites), Tol2 mRNA and a dye (for visual control of the injection) is pressure-injected into a fertilized egg at the one cell stage. For transient and sparse expression, the concentration of DNA and RNA is decreased and the mix is injected later, e.g. at the four-cell stage. To establish a stable transgenic line, injected larvae are screened for expression of the transgene and, if applicable, a transgenesis marker (e.g. “bleeding heart”, expression of mCherry under the heart-specific *cmlc2* promoter). We raised fluorescent fish (“expressors”) to adulthood, then outcrossed them to wild-type fish, and likewise screened their progeny for expression.

Today, large collections of transgenic zebrafish lines are available from different laboratories, or centrally from the Zebrafish International Resource Center (ZIRC) at the University of Oregon. Lines allowing exogenous expression of e.g. fluorescent proteins typically rely on either direct promoter fusions (mimicking the endogenous promoter expression) or binary systems, such as the Gal4/UAS-system (**Figure 6B**). The Gal4/UAS system is based on two transgenes, namely 1) the transcription factor Gal4, which is expressed under the control of e.g. a tissue-specific promoter and 2) the gene of interest, which is expressed when the Gal4 protein binds to the Upstream Activation Sequence (UAS). The Gal4/UAS system was adapted from *Drosophila* and allows straightforward combinations of driver and expressor lines (Scheer and Campos-Ortega, 1999). Hundreds of Gal4 lines were established in gene- and enhancer trap screens, such as the line Gal4s1101t used in this work (Asakawa, et al., 2008, Bergeron, et al., 2012, Davison, et al., 2007, Scott and Baier, 2009, Scott, et al., 2007). Due to the random insertion of the trapping cassette into the host genome, the resulting lines show very diverse expression patterns of frequently unmapped genomic loci. Transgenic lines are indispensable for zebrafish neuroscience research, as they allow fluorescent labeling of neurons and/or addition of functionality by expressing e.g. optogenetic tools (see below). As of today, other means of exogenous expression of transgenes, especially viral delivery, are not yet well established.

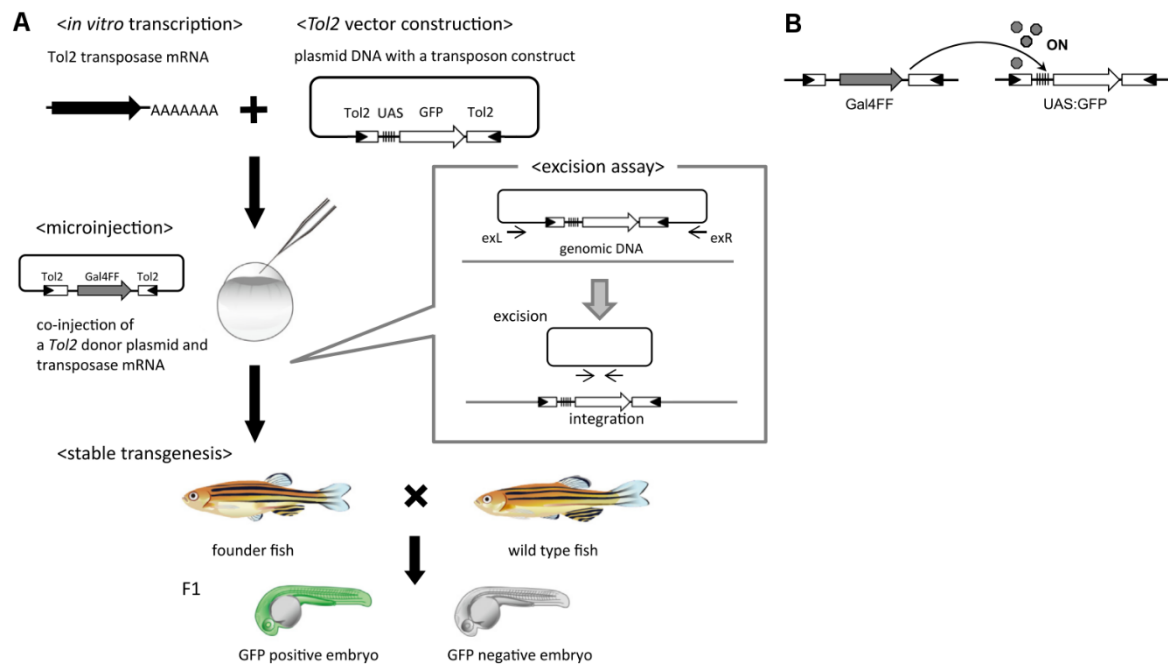


Figure 6: Establishment of transgenic zebrafish lines using the Tol2 transposase system. A, top: The injection mix contains Tol2 transposase mRNA and plasmid DNA with the genetic construct flanked by Tol2 recognition sites. **A, middle:** Upon injection of the mix into the one-cell stage of the embryo/zygote, Tol2 transposase enables random integration of the genetic construct into genomic DNA. When the injected fish expresses Gal4, already the F0 generation may express the reporter construct and show e.g. fluorescence. **A, bottom:** A fish is a so-called founder, when outcrossing it to a wild type fish yields fluorescent progeny. **B:** GFP is expressed, when the Gal4 transcription factor protein, expressed from its respective gene, and the UAS:GFP construct are present in the same cell (schematic modified from Kawakami, et al. (2016)(with permission)).

1.5.3 Fluorescent proteins

The use of fluorescent proteins (FPs), which are excited by and subsequently emit light, has revolutionized research in the life sciences. This was underscored by the Nobel Prize in chemistry awarded to Osamu Shimomura, Martin Chalfie and Roger Y. Tsien “for the discovery and development of the green fluorescent protein, GFP” in 2008 (NobelPrize.org). FPs are oftentimes fused to a label, which specifies the destination of the fusion protein. Depending on the destination of the label, FPs can highlight molecules, but also cell compartments or entire cells. For *in vivo* applications in zebrafish, the DNA of FPs is conveniently delivered into cells by standard methods (see section 1.5.2, page 13), then FPs are transgenically expressed, e.g. fused to a protein-of-interest. GFP is the quintessential FP and was initially isolated from the jellyfish *Aequorea victoria*. It is comprised of 238 amino acids, which overall form a rigid β -barrel structure, rendering GFP very compact and stable. Furthermore, GFP fluorescence does not require cofactors or other molecular partners. These advantages make GFP ideally suited to label cells *in vivo* and extensively applied in

neuroscience research. Even more so, numerous variants of GFP and other FPs are now available, which are superior due to e.g. improved brightness, photostability and spectral features.

1.5.4 Optogenetics – perfectly complementing zebrafish advantages

Optogenetics is a recent and elegant technique to probe interactions between cells, and is especially widely used in neuroscience. The term optogenetics emerged in the year 2006. It refers to genetically encoded elements, which are functionally modulated by light beyond the mere generation of fluorescence. Both directions of information flow are possible: transforming optical signals into physiological responses with actuators and *vice versa*, monitoring cellular states with sensors (Miesenböck, 2009). The use of light to modulate molecular function is advantageous, due to the non-invasive nature and superior spatial and temporal resolution of such interactions (single-cell targeting and millisecond precision). A restricted definition of optogenetics often refers exclusively to the control of neuronal activity with light, mostly realized via the ectopic expression of photoreceptors from e.g. photosynthetic organisms. The inverse, deducing neuronal activity with photogenic sensors, is commonly termed “functional imaging” or “optical recording” and is now a well-established technique in neuroscience research. Genetically encoded calcium sensors (GECIs) are FPs that change their fluorescence state upon binding with calcium ions (Ca^{2+}). As Ca^{2+} rushes into the cytoplasm during neuronal activation, GECIs can be used to visualize neuronal activity *in vivo*. One can thereby deduce neuronal activity by time-series imaging under a fluorescence microscope (**Figure 7**, page 16). GECIs have in part replaced electrophysiology, which is traditionally used to record neuronal activity, due to e.g. the ease of application and parallel sampling from many neurons. The most frequently used GECI representatives currently stem from the GCaMP family, with GCaMP6s achieving a several-fold increase of fluorescence over the baseline during neuronal activation (Chen, et al., 2013, Nakai, et al., 2001).

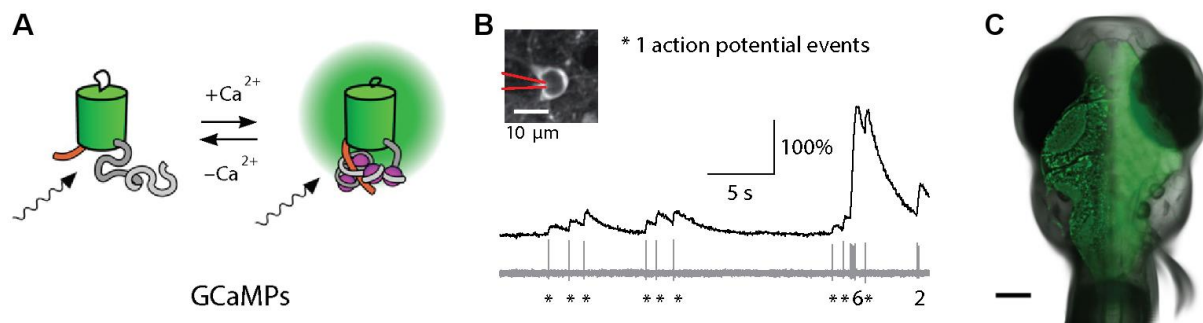


Figure 7: Functional imaging - ideal for neuroscience in larval zebrafish. **A:** Upon the binding of calcium ions (Ca^{2+}), which are released into the cytoplasm during neuronal activation, the genetically encoded Ca^{2+} sensor GCaMP undergoes a conformational change, resulting in fluorescence (modified from Perez Koldenkova and Nagai (2013)(with permission)). **B:** The GCaMP6s signal is a very good readout for neuronal activity as shown by simultaneous optical and electrophysiological recordings (top trace: GCaMP fluorescence, bottom trace: spikes). Inset: image of a neuron expressing GCaMP6s with overlaid schematic of the electrode tip used for electrophysiological recordings (modified from Chen, et al. (2013)(with permission)). **C:** Composite image of a zebrafish larva's head without skin pigmentation, including the pigmented eyes (black) and the GCaMP expressing brain (shown in green). An image slice acquired using a laser-scanning microscope is overlaid on an anatomical image (left hemisphere), showing individual cells labeled with GCaMP. Scale bar: 100 μm (modified from Fetcho (2012)(with permission)).

1.5.5 Two-photon microscopy

Typically, FPs are illuminated with light of a wavelength that maximally excites the fluorophore, such as 488 nm for GFP. To restrict the area of activation and thus improve the image, several strategies are employed including focused illumination with a laser-scanning microscope. However, light scattering in tissue leads to a broadening of the focal point and impaired image resolution with increasing imaging depth. This is especially the case with blue light, as light scattering is wavelength-dependent.

Two-photon laser scanning microscopy (2p microscopy), as developed about 30 years ago (Denk, et al., 1990), fills this gap. The principle behind this revolutionary approach is that a fluorophore can be excited when it absorbs two longer-wavelength photons simultaneously, thereby combining their energy (e.g. 920 nm for GFP (Blab, et al., 2001)). Technically, the probability of such an event which is normally very rare, is increased by using a strongly focused beam of infrared light from a laser pulsed in femtosecond range intervals. As a result, the focal point is highly restricted, making 2p microscopy advantageous due to 1) superior spatial resolution, especially with higher imaging depth, and 2) a higher signal-to-background ratio. Furthermore, it is beneficial for *in vivo* or long-term imaging, as red light causes less photo-damage and photo-bleaching than UV/blue light (reviewed in Svoboda and Yasuda (2006)). As infrared light is typically invisible to the experimental animal, it does not interfere with visual stimulation, an important consideration in visual

neuroscience. Due to its compelling advantages, 2p microscopy is now state-of-the-art for functional imaging and single-cell optogenetics, for larval zebrafish (reviewed in Renninger and Orger (2013)), but also in larger animals such as mice.

1.5.6 Image registration with ANTs

Comparisons between different samples, e.g. individual fish, are sometimes imprecise. Image registration can bridge this gap by determining an optimal geometric mapping between two or more images, thereby transforming individual images into a common coordinate space, where they can be directly compared (Avants and Johnson, 2014). Image registration is common in fields such as geography, computer vision, and biomedical imaging, including neuroscience. The recent generation of brain atlases demonstrates the power of image registration. It is the key technique underlying the larval zebrafish whole-brain atlases Z-Brain (Randlett, et al., 2015), the Zebrafish Brain Browser (ZBB)(Marquart, et al., 2015), the Virtual Brain Explorer for Zebrafish (ViBE-Z)(Ronneberger, et al., 2012), and the single-neuron atlas (**Manuscript 2**, page 23). The basis of these atlases is a standard brain/template, an average of multiple image z-stacks. In addition, multiple image z-stacks containing further information, e.g. expression patterns, functional annotations, or immunohistochemical patterns, are registered to this standard brain. After registration of a new image to such an atlas, it can be compared to all annotations available in the standard brain coordinate system.

The state-of-the-art image registration and segmentation software package is Applied Normalization Tools (ANTs) (Avants, et al., 2008, Avants, et al., 2011, Avants, et al., 2010). This command-line application became popular in the MRI field and beyond after many successes in image registration competitions. Typically, image registration with ANTs, which works on 2D, 3D and 4D data, is performed in three steps: first a rigid transformation (linear), then an affine transformation (linear), and finally a diffeomorphic transformation (non-linear). In ANTs, the particularly powerful algorithm symmetric normalization (SyN) is used for non-linear transformation, which can preserve maps, accommodate small and large deformation problems and is invertible (Avants, et al., 2008, Klein, et al., 2009). The ANTs registration result is a composite of these three steps, and comprises the transformed image as well as deformation information files (containing information about pixel displacements between the original image and the registered image). By applying the deformation information to derivatives of the original image, e.g. other channels, time-series or tracings, in a so-called co-registration, these derivatives are transferred to the template coordinate space as well.

Among the various additional functionalities contained in ANTs, the template-building feature is worth mentioning. It creates averaged templates, well suited as templates for subsequent registration. While ANTs is even capable of overcoming specimen deformations due to permeabilization and fixation of sample tissue, its application can be limited due to a very large demand for memory and computing time (Marquart, et al., 2017). Furthermore, expert inspection of the registration process is necessary, as “image registration is an art as well as science” (Avants and Johnson, 2014).

1.5.7 Combining functional and morphological analysis in pretectal neurons

While assessing neuronal activity has been essential to investigate processing in the brain, several additional features, including connectivity and gene expression pattern, determine neuronal identity. To understand neuronal circuits better, it would therefore be advantageous to combine analyses of different perspectives, e.g. characterization of single neurons in terms of biochemical properties, function and connectivity. Technological advances increasingly allow combinations of techniques that, mostly due to technical reasons, previously seemed incompatible. One example is functional and morphological characterization of single cells.

1.5.7.1 Electrophysiology

The classic technique to record neuronal activity is electrophysiology, where an electrode is inserted into the tissue to measure changes in electrical properties, e.g. of single cells. The experimenter can further inject a dye into the recorded neuron at the end of the recording, thus rendering its morphology visible. However, the invasive nature and low throughput of this technique can be limiting. Furthermore, electrophysiology is more readily applicable to superficial tissues, such as the optic tectum of zebrafish larvae (Gabriel et al., 2012), while application to deeper brain tissues remains challenging.

1.5.7.2 Photoactivatable GFP

Based on GFP, two remarkable classes of so-called photochromic FPs have emerged: 1) photoactivatable FPs, which can permanently switch either from a non-fluorescent to a highly fluorescent state or between different fluorescent states, and 2) photoswitchable FPs where switching is reversible, typically by illumination with different wavelengths or spontaneously/over time (reviewed in Shcherbakova, et al. (2014)). Photoactivatable GFP (paGFP), the most prominent example, is dark in its native conformation and is rapidly activated to a highly fluorescent state (bright green, excitation with 488 nm light) upon illumination with UV light (~ 400 nm)(Patterson

and Lippincott-Schwartz, 2002). Specifically, resulting from a single amino acid substitution (T203H), the amino acid Glu222 located in close proximity to the chromophore undergoes an irreversible decarboxylation, which then permits fluorescence of the chromophore (Henderson, et al., 2009). Due to the irreversibility and strong fluorescence change, paGFP is ideally suited to highlight e.g. a subset of tagged structures during an experiment. PaGFP has been applied to investigate translation and transcription, axonal transport, and cell fate amongst other cellular processes (Datta and Patterson, 2012). However, as the site of photoactivation lies inside the protein, no antibody is currently able to distinguish between the dark and fluorescent states. This prevents the use of paGFP in combination with immunohistochemistry.

PaGFP was used to highlight groups of neurons in *Drosophila* (Datta, et al., 2008, Frank, et al., 2015, Ruta, et al., 2010) and zebrafish (Ahrens, et al., 2012, Bianco, et al., 2012). Similarly, several reports used the green-to-red photo convertible FPs Dendra and Kaede in zebrafish (Mohr, et al., 2016, Schuster and Ghysen, 2013, Scott, et al., 2007). Furthermore, paGFP was used in combination with nuclear localized GCaMP, to guide photoactivation (Dunn, 2015). This analysis allowed neurons located in a functionally determined area to be traced. However, as neurons in larval zebrafish are tightly packed and often not segregated into discrete nuclei, neurons of undetermined identity might be included in the highlighted population. We therefore sought to further refine photoactivation and apply paGFP tracing to individual, functionally characterized neurons, thus improving specificity.

1.5.7.3 Function-guided inducible morphological analysis (FuGIMA)

To achieve morphological analysis of single, functionally characterized neurons, we combined the FPs nuclear localized GCaMP6s (nls-GCaMP6s) and paGFP. We termed this new technique “Function-guided inducible morphological analysis” (FuGIMA)(**Figure 8**, page 20). Specifically, the nuclear localization of nls-GCaMP6s allows its distinction from cytosolic photoactivated paGFP, as both FPs emit green light.

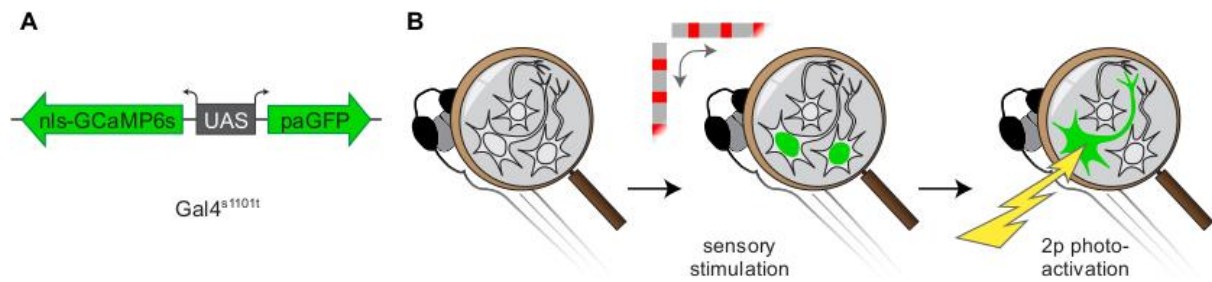


Figure 8: FuGIMA - anatomical and morphological characterization of single neurons. **A:** Schematic of *UAS:FuGIMA*. Nuclear localized GCaMP6s (nls-GCaMP6s) and photoactivatable green fluorescent protein (paGFP) are co-expressed from the bidirectional UAS (Janus-UAS; (Distel, et al., 2010, Paquet, et al., 2009) under the control of a Gal4 driver (here *Gal4^{51101t}*). **B:** Schematic of the FuGIMA principle. In the inactive state, both fluorescent proteins (paGFP and nls-GCaMP6s) are non- or weakly fluorescent. During sensory stimulation, here with moving gratings, neuronal activity is recorded. Following the detection of a cell-of-interest (COI) based on its response type, focused two-photon illumination (750 nm) in the soma of the COI photo-activates paGFP, rendering the cell brightly labeled. Due to diffusion of bright paGFP, the COI's morphology becomes visible (Image from manuscript 3).

Two FuGIMA projects were simultaneously initiated: the application of FuGIMA in the optic tectum, as undertaken by Dominique Förster and Linda Jordan, and in the pretectum, as described in this thesis. Thus far, we published two papers, the first with a description of the method (together with the optobow suite in Förster, et al. (2018), **manuscript 1**, page 22), followed by the second paper with the application of FuGIMA in the pretectum (**manuscript 3**, page 30).

1.6 Aims of this thesis

To fill a gap in the understanding of whole-field motion processing in the pretectum, namely how different response types of pretectal motion-sensitive neurons are established and where DS information is processed in the local circuit, I aimed to address the following points with the work presented in this dissertation:

- Establish the novel method FuGIMA to combine functional and morphological analysis in single cells (**manuscript 1**, page 22)
- Apply FuGIMA to optic-flow responsive neurons in the pretectum of larval zebrafish to investigate potential morphological differences between functionally distinct neurons (**manuscript 3**, page 92)
- Complement neuron types found with FuGIMA with single-neuron tracings from a single-neuron atlas (**manuscript 2**, page 30) to find potential output neurons of the optic flow processing circuit and thereby test predictions regarding pretectal connectivity (**manuscript 3**, page 92)

Moreover, with the work of my colleagues also contained in the jointly published papers, we combined various datasets to answer questions not addressable with only one technique. We successfully outlined a visual pathway that underlies behavior in larval zebrafish, focusing on processing steps from the retina to pre-motor centers.

2 *Manuscripts*

2.1 Manuscript 1

Dominique Förster, **Anna Kramer**, Herwig Baier, Fumi Kubo. 2018. Optogenetic precision toolkit to reveal form, function and connectivity of single neurons. *Methods*, 150: 42-48. DOI: [10.1016/j.ymeth.2018.08.012](https://doi.org/10.1016/j.ymeth.2018.08.012)

All-optical methods enable the control and monitoring of neuronal activity with minimal perturbation of the system. Although imaging and optogenetic manipulations can be performed at cellular resolution, the morphology of single cells in a dense neuronal population has often remained unresolvable. Here we describe in detail two recently established optogenetic protocols for systematic description of function and morphology of single neurons in zebrafish. First, the Optobow toolbox allows unbiased mapping of excitatory functional connectivity. Second, the FuGIMA technique enables selective labeling and anatomical tracing of neurons that are responsive to a given sensory stimulus or correlated with a specific behavior. Both strategies can be genetically targeted to a neuronal population of choice using the Gal4/UAS system. As these in vivo approaches are non-invasive, we envision useful applications for the study of neuronal structure, function and connectivity during development and behavior.



Optogenetic precision toolkit to reveal form, function and connectivity of single neurons



Dominique Förster^a, Anna Kramer^a, Herwig Baier^{a,✉}, Fumi Kubo^{b,✉}

^a Max Planck Institute of Neurobiology, Department Genes – Circuits – Behavior, Am Klopferspitz 18, 82152 Martinsried, Germany

^b National Institute of Genetics, Center for Frontier Research, 1111 Yata, Mishima, Shizuoka 411-8540, Japan

ARTICLE INFO

Keywords:

Zebrafish
Optogenetics
Two-photon microscopy
Optobow
FuGIMA
Photoactivatable GFP (paGFP, PA-GFP)

ABSTRACT

All-optical methods enable the control and monitoring of neuronal activity with minimal perturbation of the system. Although imaging and optogenetic manipulations can be performed at cellular resolution, the morphology of single cells in a dense neuronal population has often remained unresolvable. Here we describe in detail two recently established optogenetic protocols for systematic description of function and morphology of single neurons in zebrafish. First, the Optobow toolbox allows unbiased mapping of excitatory functional connectivity. Second, the FuGIMA technique enables selective labeling and anatomical tracing of neurons that are responsive to a given sensory stimulus or correlated with a specific behavior. Both strategies can be genetically targeted to a neuronal population of choice using the Gal4/UAS system. As these *in vivo* approaches are non-invasive, we envision useful applications for the study of neuronal structure, function and connectivity during development and behavior.

1. Introduction

The function of a neural circuit arises from the wiring among its constituent cells. The wiring, in turn, is the result of processes that pattern the shape of axons and dendrites and control the formation of specific synaptic contacts. Due to the dense cell clustering in most brain regions and the superposition of parallel circuits within these regions, systematic attempts to determine a functional connectivity map of morphologically different cell types with high resolution have been time-consuming and low-throughput [1]. We recently developed two optogenetic strategies, Optobow and FuGIMA, to map functional and morphological connectivity patterns of neurons. These non-invasive, optical techniques exploit the power of zebrafish as an *in vivo* model for whole-brain imaging and optogenetics [2,3] and are routinely combined with the Gal4/UAS system for straightforward genetic targeting of defined neuronal populations. Excitation of neurons is achieved by an optogenetic actuator, while neuronal activity is simultaneously recorded by a genetically encoded calcium indicator, e. g. GCaMP6f or GCaMP6s. These toolkits are versatile and, in their advanced versions, implement photoactivatable GFP (paGFP, also known as PA-GFP [4]) for selective labeling of individual neurons following their functional identification. Our photoactivation protocol builds on previous efforts to highlight cells of interest, including applications of paGFP or photoconvertible proteins such as Kaede and Dendra [5–10]. This article

presents detailed protocols for Optobow and FuGIMA and should serve as a guide for choice, application and troubleshooting of these all-optical tools.

2. Optobow

2.1. Description of the method

The Optobow toolbox comprises a set of genetic constructs, which allow mapping of functional excitatory connections *in vivo* [7]. The general principle is that an optogenetic actuator (ChrimsonR) and a genetically encoded calcium sensor (GCaMP6) are linked on a single transgene, but separated by a set of incompatible pairs of loxP sites (Fig. 1). Upon Cre recombination, this configuration leads to random and mutually exclusive expression of either the actuator or the sensor in various cell types of one neuronal population, dependent on the expression of the Gal4 transcription factor. In response to optogenetic ChrimsonR stimulation, functionally connected cells are identified by GCaMP6 activity. Neurons expressing the actuator or indicator are, at the same time, genetically endowed with spectral variants of fluorescent proteins (FPs; Fig. 1 B and C). This facilitates the description of cell morphologies and projection patterns of participating neurons. In the absence of Cre recombinase, cells express the blue-fluorescent membrane marker mCerulean, which serves as a background label of

[✉] Corresponding authors.

E-mail addresses: hbaier@neuro.mpg.de (H. Baier), fumikubo@nig.ac.jp (F. Kubo).

<https://doi.org/10.1016/j.ymeth.2018.08.012>

Received 26 April 2018; Received in revised form 24 August 2018; Accepted 31 August 2018
Available online 05 September 2018

1046-2023/© 2018 Elsevier Inc. All rights reserved.

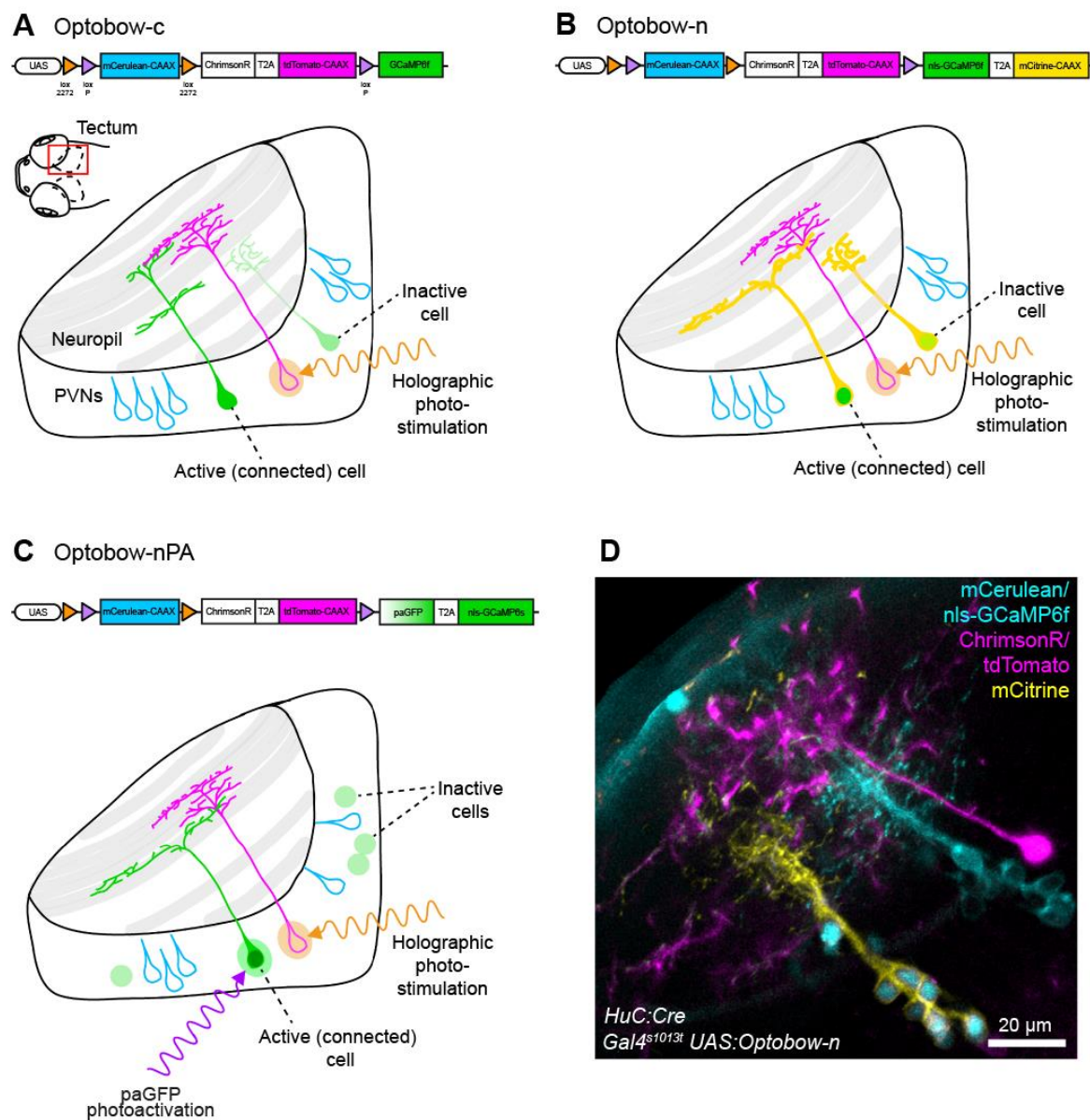


Fig. 1. Optobow allows all-optical identification of functionally connected cells. Different Optobow versions and schematics for expression in tectal periventricular neurons (PVNs) are illustrated. (A) With Optobow-c, Cre recombination leads to expression of either ChrimsonR/tdTomato (magenta) or cytoplasmic GCaMP6f (green). Cells without Cre activity, expressing mCerulean, are indicated by blue outlines. The CAAX motif targets fluorescent proteins to cell membranes. Computer-generated holography (orange) allows photostimulation of single 'ChrimsonR' cells. Functionally connected cells are identified by increased GCaMP6 fluorescence (dark green). (B) Optobow-n replaces cytoplasmic GCaMP6f with nuclear localization signal (nls)-tagged GCaMP6f. Membranes of the nls-GCaMP6f cells are fluorescently labeled by co-expression of mCitrine. (C) In Optobow-nPA, all 'nls-GCaMP6f' cells co-express photoactivatable GFP (paGFP). Functionally connected single cells can be targeted for paGFP photoactivation, to visualize their morphology. (D) Tectal expression of Optobow-n in a living 5 dpf larva. Dense clonal cell clusters expressing mCitrine (yellow) or mCerulean (cyan) are visible (see 2.3). (For interpretation of the references to colour in this figure legend, the reader is referred to the web version of this article.)

the cell population of interest.

Different versions of Optobow have been developed, modifying the cassettes of the reporter construct. In Optobow-c, the use of cytoplasmic GCaMP6f allows to monitor calcium activity in cell body and neuropil regions upon ChrimsonR stimulation in the presynaptic cell (Fig. 1A). In Optobow-n, GCaMP6f localization is restricted to the nucleus by means of a nuclear localization signal (nls), and the bright FP mCitrine is co-

expressed, targeted to the cell membrane (Fig. 1B and D). This configuration on the one hand facilitates segmentation of single-cell GCaMP6f activity, and on the other hand allows tracing of single-cell morphologies of responding cells. In situations in which connectivity and morphology of densely packed neurons are investigated, Optobow-nPA is the construct of choice (Fig. 1C). Here, the permanent membrane marker mCitrine of Optobow-n is replaced by expression of paGFP.

After a responsive cell has been identified by nuclear GCaMP6s activity, paGFP can be activated exclusively in this single cell to reveal its morphology (see 3.2 and Appendix A1 for a detailed protocol of paGFP photoactivation).

2.2. Application

Depending on the desired experiment, three choices need to be made for the optimal Optobow configuration: (1) the appropriate Gal4 driver (among the many hundreds that are now available) [5,11–18], (2) the appropriate Cre line (a pan-neuronal, transient/mosaic driver is often sufficient) and (3) the most suitable Optobow version (see 2.3 for details).

The following protocol describes the use of Optobow-n to interrogate circuitry in the tectum of 5–7 dpf (days post fertilization) zebrafish larvae. For this experiment, we crossed transgenic fish carrying Gal4s1013t and UAS:Optobow-n to wild-type fish. The HuC:Cre (elavl3:Cre) plasmid containing Tol2 arms is injected, together with Tol2 transposase RNA, both at a concentration of 25 ng/μl, into embryos at the one-cell stage. At 24 hpf (hours post fertilization), larvae are screened for sparse expression of red and green/yellow fluorophores (tdTomato and nls-GCaMP6f/mCitrine) at a fluorescent sorting scope. We had discovered in preliminary studies that in our favorite tectum-specific Gal4 line, Gal4s1013t, notochord expression at 24 hpf nicely predicts later tectal expression. One may therefore use sparse expression in the notochord as an easily screenable proxy for successful mosaic expression in the tectum. After sorting, carriers were transferred to 1-phenyl-2-thiourea (PTU)-containing Danieau's solution to prevent melanin pigment formation. At 5 dpf, larvae were embedded in 2% low-melting point agarose and transferred to the confocal microscope for further screening and initial imaging.

Preferred laser lines are 405 nm (for mCerulean and nls-GCaMP6f excitation), 515 nm (for mCitrine excitation), and 561 nm (for tdTomato excitation). A sequential scan using this configuration allows for separation of nls-GCaMP6f and mCitrine, as only GCaMP6f will be excited by UV light. When working with Optobow-nPA, it is not recommended to use the 405 nm line for initial imaging, as this will lead to unintentional paGFP photoactivation in cells within the field of view. At the confocal, larvae need to be screened again for sparse and preferably strong Optobow expression. We found that a ratio of 1–3 ChrimsonR/tdTomato-expressing cells and 1–20 GCaMP6-expressing cells per tectum is ideal for this type of experiment. A high-resolution stack should be acquired before transferring selected larvae to the two-photon (2P) microscope.

For mapping functional connectivity, any 2P microscope setup that allows independent imaging and photostimulation at different wavelengths can be used. Further, any cellular-resolution photostimulation technique can be applied to excite ChrimsonR either at 760 nm or at 1020 nm. In our hands, two-photon computer-generated holography [6] turned out to be ideal, as it most efficiently integrates light-evoked currents in single cells and has unmatched cellular or even subcellular resolution in 3D [19–21]. For photostimulation, different laser intensities (max. 1 mW μm⁻²) and pulse durations (100–700 ms) need to be tested, depending on the various conditions (actuator expression levels, tissue depth, etc.). An issue, which is often neglected during 2P optogenetic stimulations, is non-specific sample heating, induced by linear and non-linear light absorption by the tissue. As this strongly depends on the experimental conditions, we suggest to fine-tune the parameters according to a model for local temperature rise, which was recently provided by Picot et al. (2018) [22]. To monitor nls-GCaMP6f activity in more than 10 cells simultaneously, simple line scans, rather than area scans, across the labeled nuclei should be performed to achieve faster GCaMP6 signal acquisition. Although scanning at 900–920 nm will lead to weak excitation of mCitrine, changes in nuclear GCaMP6 fluorescence intensity can clearly be differentiated.

Activity sampling with high-frequency line scans (250–350 Hz)

allowed us to correlate the response onset delays with physical distance between pre- and postsynaptic neurite arbors [7]. On average, cell pairs, whose neurite arbors did not overlap, showed longer response latencies than all other identified neurons, suggesting polysynaptic transmission.

For the analysis of GCaMP6 signals, standard algorithms for registration and noise subtraction can be used, e.g. the toolbox for Calcium Imaging Analysis (CalmAn; Giovannucci et al., unpublished). Upon identification of a cell, which shows calcium responses that are tightly locked to the photostimulation pulses, neuronal morphologies can be traced semi-automatically or manually using different software packages, including Imaris (Bitplane), neuTube [23], or ImageJ (Simple Neurite Tracer plugin [24]).

We recommend to validate the results and especially the photostimulation method by different control experiments. First, to ensure spatial specificity of the photostimulation method, off-target stimulations using the same power density should be performed. Second, to exclude photodamage evoked by photostimulation, GCaMP6 cells not expressing ChrimsonR could be targeted by various stimulation protocols (different pulse lengths and intensities). Any change in GCaMP6 baseline fluorescence will report undesirable photobleaching or cell damage. In addition, the user could still apply the same experimental parameters to cells that co-express ChrimsonR and GCaMP6, to be able to judge the effectiveness of optogenetic stimulation in the specific neural tissue of choice. Co-expression can be achieved by co-injections of UAS:Optobow and HuC:Cre plasmids, as described in the Troubleshooting Section 2.3.

2.3. Troubleshooting and shortcuts

A critical initial step for all Optobow experiments is to prepare larvae with strong, but sparse expression patterns. Sparse labeling of both pre- and postsynaptic populations will be required to unambiguously identify and trace cellular morphologies of functionally connected cells. Further, dense expression of the ChrimsonR actuator increases the risk for inadvertent photostimulation of neurons, closely neighboring the targeted cell. We therefore have generated different transgenic fish lines with the Optobow constructs stably integrated into the genome, all varying in the extent of genetic variegation [7]. Besides, both UAS:Optobow and Cre plasmids can be co-injected, together with Tol2 RNA (all at a concentration of 25 ng/μl), again modifying the range of sparse expression. This also facilitates interrogation of circuits in mutant fish, without the need for prior crossing to transgenic Optobow lines. In that case, larvae additionally need to be screened for the absence of FP co-expression in the same cell, since the injection of the Optobow plasmid can lead to multiple copies of plasmids per cell and the mutually exclusive expression of the actuator and sensor may not be achieved anymore. In some cases, cells expressing the same genetic marker appear to form clonal clusters, indicating that the cells divided after Cre recombination took place (Fig. 1 D). If the cell clusters are too dense, temporal control over Cre expression by a heat-shock promoter is recommended [25]. Heat-shock conditions will depend on the Gal4 driver at hand and have been tested from 12 hpf up to 3 dpf, with durations from 5 to 30 min. As the promoter itself is somewhat leaky, even the absence of heat shocks might lead to the desired sparseness of expression.

Bleaching of FPs might occur throughout Optobow experiments, due to the intensive confocal and 2P imaging protocol. This especially happens to tdTomato in the presynaptic cell during repeated photostimulation events. It is therefore recommended to acquire a high-resolution stack at the confocal microscope, prior to 2P imaging, to obtain the morphology of the presynaptic cell. Another possibility is to visualize photobleached tdTomato by anti-RFP immunohistochemistry staining, following *in vivo* experiments [7].

Spontaneous muscle contractions are a common source for movement artefacts during *in vivo* calcium imaging in 6 dpf, or older, larvae.

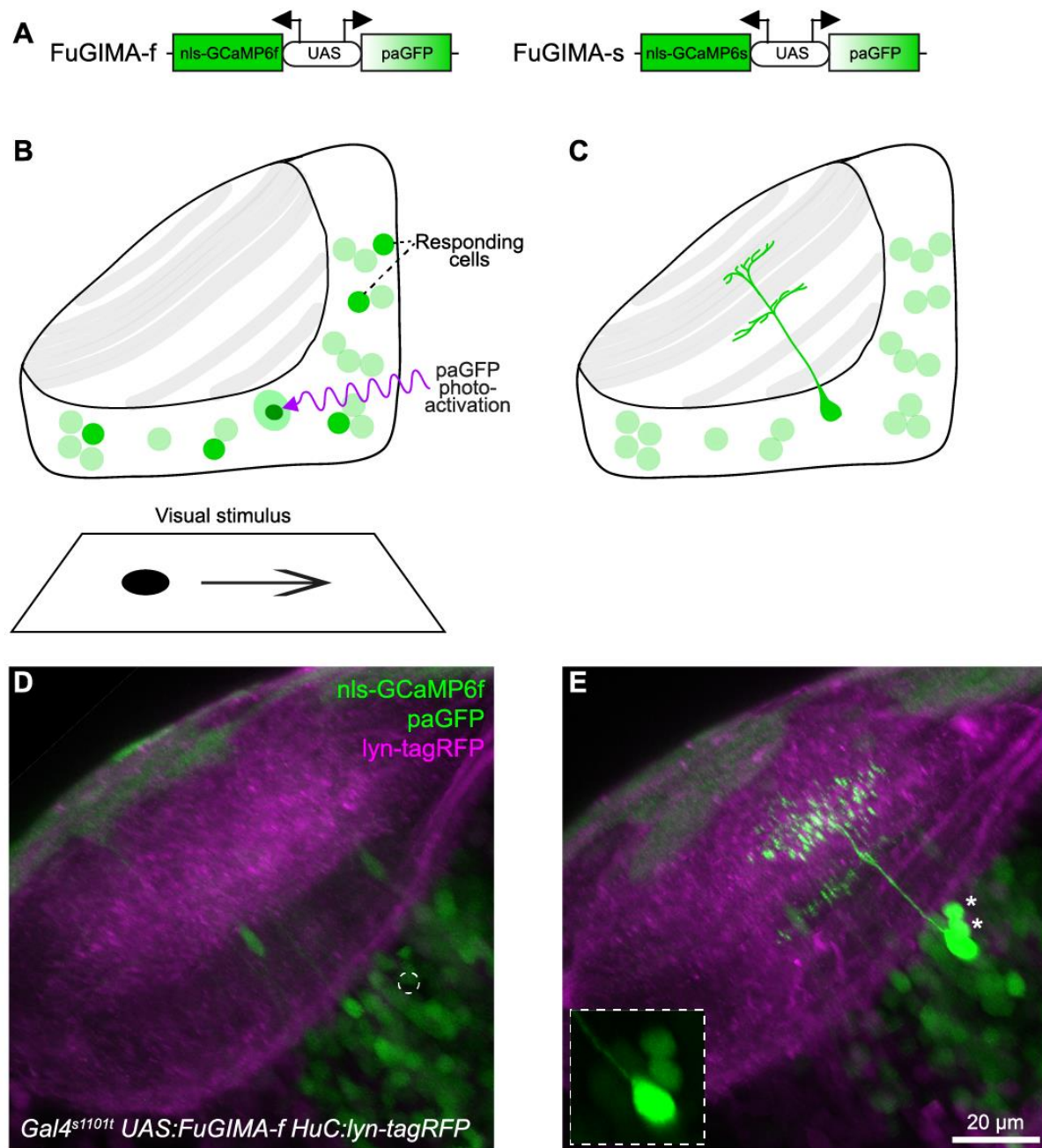


Fig. 2. The FuGIMA method reveals single-cell morphologies of functionally identified cells. (A) A bidirectional UAS is used for co-expression of either nuclear-localized (nls-)GCaMP6f in FuGIMA-f, or nls-GCaMP6s in FuGIMA-s, and paGFP. (B) Illustration depicts FuGIMA expression in a larva that is visually stimulated during microscopic imaging. Responding cells are highlighted by increased nls-GCaMP6f fluorescence (dark green). A single cell can be selected for paGFP photoactivation. (C) Diffusion of photoactivated, cytoplasmic paGFP will label the axonal and dendritic morphology of the cell of interest (COI). (D) In vivo expression of FuGIMA-f (green) in tectal cells of a 5 dp larva. Co-expression of a neuronal membrane marker (HuC:lyn-tagRFP, magenta) serves as a reference label. A circular region for photoactivation is indicated. (E) 30 min after photoactivation, a single cell is highlighted. Unintentional and weak photoactivation in adjacent neurons (asterisks) does not interfere with unambiguous morphological tracing of the COI. A less saturated image of the cell body region is shown in the lower left. (For interpretation of the references to colour in this figure legend, the reader is referred to the web version of this article.)

Anesthesia while performing Optobow experiments, using tricaine methanesulfonate (MS-222) is not recommended, as it might interfere with calcium imaging and neuronal excitability [26–28]. Instead,

injections or bath applications of larvae in α -bungarotoxin (see 3.2) or embedding in higher concentrations of agarose (> 2%) will diminish movement artefacts.

3. FuGIMA

3.1. Description of the method

FuGIMA (function-guided inducible morphological analysis) allows to observe the morphology of a neuron identified based on its neuronal activity, e.g. responding to a presented sensory stimulus. To this end, the nuclear-localized calcium indicator nls-GCaMP6f or nls-GCaMP6s [7], and the photoactivatable cytoplasmic protein paGFP [4] are co-expressed in a neuronal population of interest (Fig. 2). Specifically, in our UAS:FuGIMA plasmids, the genes for both proteins are located on either side of a bidirectional UAS cassette allowing their stoichiometric expression (Fig. 2A; Janus-UAS, reviewed in [29]). Under a 2P microscope, larvae are presented with various visual stimuli, and calcium responses are monitored simultaneously (Fig. 2B and D). Upon identification of a cell of interest (COI), paGFP photoactivation is performed directly at the 2P microscope, by restricting the focus of illumination to the smallest possible volume, ensuring that only the COI will be highlighted (Fig. 2C and E). The use of a nuclear-localized GCaMP6 variant not only facilitates segmentation of individual neurons in time series analysis, but also allows spatial separation from cytosolic paGFP. Furthermore, using only green FPs in FuGIMA leaves other wavelengths available for other purposes, e.g. a red FP to label anatomical landmarks, which may be used as a reference for image registration to a standard brain. For a detailed description of registration to a standard fish brain, we refer to Marquart et al. (2017) [30].

3.2. Application

In preparation of the experiment, transgenic fish expressing FuGIMA under control of the pan-neuronal driver *Gal4s1101t* need to be crossed to fish expressing the reference marker *HuC:lyn-tagRFP* [6]. All larvae should be selected for the homozygous *mitfa*^{-/-} (nacre) mutation, in which the lack of melanocytes is beneficial for imaging at the 2P microscope. About two days prior to the experiment, embryos are screened for red and strong green fluorescence. This pre-selection is advisable, since we observed that, depending on the choice of the *Gal4* driver, green fluorescence, i.e. nls-GCaMP6f or nls-GCaMP6s signal, and hence the paGFP expression can be too weak (see 3.3 Troubleshooting). Optionally, fish can be screened for native, unconverted paGFP, using a UV filter and restricting the exposure to a minimum to prevent photoactivation [4]. On the day of the experiment (typically at 5–7 dpf), the brightest 10% of the pre-sorted larvae are selected for embedding in 2% agarose. As the presentation of visual stimuli can evoke strong movements, e.g. struggles or startle responses, we paralyze the fish to prevent movement artefacts during functional imaging. To this end, mounted fish are anesthetized with tricaine and intraperitoneally injected with an α -bungarotoxin mix (2 mg/ml α -bungarotoxin, 0.1% phenol red, freshly prepared on ice). Sufficient paralysis is achieved by the injection of a bolus barely visible under the dissecting microscope, while neuronal responses were decreased in fish injected with α -bungarotoxin filled up into the brain ventricle. To remove the tricaine anesthetic (which would otherwise compromise neural activity), embedded fish need to be washed with Danieau's solution at least three times before the experiment.

For visual stimulation, functional imaging and photoactivation, the fish is placed under the microscope of choice. In sparsely expressing and superficial tissues, a confocal microscope can be used; however, we recommend to photoactivate paGFP in two-photon mode. This is particularly important for densely labeled tissues in order to avoid unintended photoactivation of neighboring cells (see 3.3 Troubleshooting). The microscope needs to be equipped with a laser tunable to 750, 920 and 1020 nm, to photoactivate paGFP, excite GFP/GCaMP6 and excite tagRFP/GFP/GCaMP6, respectively.

At the beginning of the imaging session, an overview image of a large field of view is acquired for later orientation. Subsequently,

functional imaging is performed in a region of interest (ROI) while presenting the visual stimulus, both according to standard protocols. Specifically, since the visual stimulation light could interfere with the detection of GCaMP6, we present the visual stimulus using red spectrum light, either by a red LED arena or a projector with a filter that blocks green spectrum light. To determine which cell should be photoactivated (COI), imaged time series can be analyzed online (microscope software) or exported and analyzed offline using a custom-written script or ImageJ. Depending on the research question, extracting the $\Delta F/F_0$ time series of individual nuclei and comparing it to the stimulus pattern might be sufficient. Once the COI is determined, it needs to be relocalized using the initial overview image to zoom in on the COI for photoactivation. Photoactivation of paGFP is performed as described in detail in the Appendix (see also 3.3).

Finally, after allowing paGFP to diffuse into the neurites of the photoactivated cell, we acquire an overview z-stack with a large field of view, ideally spanning the whole brain but minimally including all the highlighted neurites of the COI. Furthermore, the image resolution should be high enough to allow for later neurite tracing. Simultaneously, the lyn-tagRFP reference channel can be acquired to allow for image registration into a reference brain.

In general, it is possible to highlight more than one neuron per fish, if their dendritic and axonal arbors remain physically and visually separated from each other. In order to avoid labeling two overlapping neurons, we recommend photoactivating only one cell per brain hemisphere, i.e. max. two cells per fish.

For tracing and registration, the different channels of the acquired large volume z-stacks should be separated. While there are many automated tracing algorithms available, in our experience, a low signal-to-noise ratio of paGFP often necessitates manual reconstruction. We use either the Simple Neurite Tracer plugin for ImageJ or the software neuTube to obtain .swc tracing files (see also 2.2).

Finally, to compare all traced neurons from different fish in the context of one brain, the lyn-tagRFP reference channel can be used for registrations into a standard brain. The resulting registration information can be applied to .swc files to transfer the tracing into the coordinate space of the standard brain.

3.3. Troubleshooting

The most delicate step of this protocol is the photoactivation of paGFP. In a tissue in which FuGIMA is expressed in densely packed cells (e.g. tectum), cell bodies neighboring the COI and bypassing neurites are equally susceptible to photoactivation. However, crossing neurites of different neurons typically cannot be disentangled during tracing. Therefore, greatest care needs to be taken to center the paROI (region of interest for photoactivation) onto the COI in three dimensions as well as to avoid drift or other movements of the specimen during photoactivation. In case of incomplete paralysis after α -bungarotoxin injection, functional imaging might still be performed and complemented with post-hoc movement correction of the time series (e.g. Template Matching and Stack Alignment plugin for ImageJ [31]). In this case we recommend adding tricaine after functional imaging, but before photoactivation.

Traceability of a neuron critically depends on the amount of photoactivated paGFP molecules and their diffusion into neurites. Our photoactivation protocol consists of 15 cycles of illumination, allowing paGFP molecules activated in the first cycle of the protocol to diffuse already during the remaining photoactivation session. In addition we suggest waiting 30–60 min before acquiring the final z-stack to extend the diffusion time. We found that, in the spinal cord, axons over 200 μ m in length can be labeled following photoactivation of paGFP in the soma, similar to paGFP labeling of groups of neurons in other brain regions of zebrafish [8–10]. However, this diffusion distance will vary depending on neurite caliber and initial concentration of photoactivated molecules. Similarly, the time required for paGFP

fluorescence to reach maximal intensity after the photoactivation is also dependent on such parameters. Therefore, we suggest that the diffusion length as well as the time to maximal paGFP fluorescence should be empirically determined for each experiment. As expression varies between neurons, the brightness of nls-GCaMP6f expression can be used as a proxy for the expression levels of co-expressed paGFP. The presented protocol was tested in local tectal and pretectal neurons in 5–6 dpf old zebrafish larvae and paGFP and GCaMP6 were expressed using strong Gal4 driver lines. We suggest to initially determine a protocol for the neuron type under investigation by co-labeling neurons with another FP. This can be achieved e.g. by transient and sparse expression of a membrane targeted red FP and photoactivation until a complete overlap is achieved. Alternatively, claims based on FuGIMA tracings should consider the possibility of an incomplete filling, especially of small diameter axons.

As reported previously for the Gal4/UAS system in general [32,33], we have observed that the UAS:FuGIMA transgene expression is susceptible to stochastic silencing, i.e. the expression becomes variegated and potentially weaker over generations. This silencing effect, on the one hand, brings advantages for sparse expression of FuGIMA, leaving less possibility of unintentional photoactivation of adjacent cells. On the other hand, the silencing effect works negatively when the neuron types of interest comprise a minor part of the whole population, since the expression of FuGIMA might be absent in this group of cells. Therefore, use of suitable lines should be considered depending on the purpose of the experiments.

4. Conclusions

Here we described optical methods, Optobow and FuGIMA, for interrogating neural circuit functions by linking physiological responses,

Appendix

A1. Detailed protocol for paGFP photoactivation at the 2P microscope (also see Fig. A1).



Zooming in on the COI, the focal plane is moved to the center of the nuclear GCaMP6 signal in z-dimension. While placing the paROI onto the nucleus, adjust the frame size to a minimum, e.g. $0.8 \times 0.8 \mu\text{m}^2$.

It is advantageous to briefly double-check the unchanged location of the COI, by acquiring a small-scale overview scan (OS) before

morphology and functional connectivity of a neuronal population. The Optobow tool has been used successfully in the tectum, a brain area, which is known to integrate multiple sensory modalities [7,34]. In addition, the nucleus of the medial longitudinal fascicle (nMLF), a visuomotor brain area located ventrally to the tectum, has been successfully investigated with all-optical circuit tools [6]. As these cells show good excitability by ChrimsonR stimulation [7], Optobow analysis should therefore be useful for the identification of nMLF circuitry. The FuGIMA tool has been successfully applied in both tectal and pretectal circuits (D. F., A. K., H. B. and F. K., unpublished observations). Future studies are likely to reveal wider applications of the tools in other brain regions and/or for other sensory modalities. FuGIMA should be applicable to the fruitfly *Drosophila* as well, due to previous uses of paGFP and nls-GCaMP [35,36]. Furthermore, these tools can be used in genetic mutants or disease models to uncover how circuit properties are altered under these conditions. Due to the non-invasive, in vivo conditions in which the experiments are performed, these tools are also compatible with observing development, maturation and plasticity of a neuronal circuit.

Acknowledgements

We thank Marco Dal Maschio and all members of the Baier lab for helpful discussions throughout the project. Support was provided by the Max Planck Society (all authors), the DFG Priority Programme in Next-Generation Optogenetics (SPP 1926; H. B.), the DFG Priority Programme in Computational Connectomics (SPP 2041; F. K.), the Excellence Centre for Integrated Protein Science Munich (CIPSM; H. B.), the European Molecular Biology Organization (EMBO ALTF 104-2013; D. F.) and the Japan Society for the Promotion of Science (international research fellow, short-term postdoctoral fellowship, A. K.).

	Excitation wavelength	Pulsing sequence	Scanning area	Detection channel
① Overview image	1020 nm		Whole brain/ large field of view	green + red
② Functional imaging	920 nm		Small region of interest	green
③ Photo-activation “test rounds”	920 nm		overview scan	green
	750 nm	1 x 200 ms	paROI	-
	920 nm		overview scan	green
	750 nm	3 x 200 ms, 1 Hz	paROI	-
	920 nm		overview scan	green
				
Full protocol	750 nm	40 x 200 ms, 1 Hz	paROI	-
	920 nm		overview scan	green
				
④ Overview z-stack	1020 nm		Whole brain/ large field of view	green + red

15 x,
5 min interval

Fig. A1. Detailed protocol of the photoactivation procedure for FuGIMA at the 2P microscope. (1) An initial overview image of a large field of view is acquired at 1020 nm, detecting green and red emission. (2) Functional imaging of a smaller region of interest is performed at 920 nm, detecting green GCaMP6 emission. (3) Phases of photoactivation in the paROI window at 750 nm without detection are alternated with brief overview scans (OS) at 920 nm, detecting green emission. Two ‘test-rounds’ with 1 x and 3 x 200 ms, 1 Hz scanning periods precede the full protocol consisting of 40 x 200 ms, 1 Hz scanning periods, repeated 15 times with 5 min intervals. Schematic drawings depict the stepwise photoactivation of cytosolic paGFP. (4) Finally, a large field of view, high-resolution z-stack is acquired including the highlighted neuron at 1020 nm, detecting green and red emission.

photoactivation. To test whether the COI responds to photoactivation and to assure the centered position of the paROI, we start with two 'test rounds'. For this, tune the laser to 750 nm, turn off the detection PMTs (photomultiplier tubes) and scan for 200 ms using the paROI with a laser intensity of 3–4 mW. To observe the amount of photoactivation, tune the laser to 920 nm, turn on the PMTs and take a snapshot with an OS. One should be able to observe a slight increase in fluorescence compared to the pre-activation image. If the paROI location remained in focus, we tune the laser again to 750 nm, turn off the PMTs and scan for 3×200 ms, at 1 Hz frequency, using the paROI. Then tune the laser back to 920 nm, turn on the PMTs and again take a snapshot by an OS. Now, a clear increase in fluorescence in the whole cell compared to the pre-activation image should be visible.

The full protocol consists of 15 cycles in total with 5 min intervals. For one such cycle, the photoactivation step is repeated, this time with 40×200 ms, at 1 Hz. After tuning the laser back to 920 nm etc., the COI should now be bright green, in clear contrast to all neighboring neurons. Subsequent cycles do not lead to a visible change of fluorescence in the soma but serve to increase the pool of activated paGFP. To allow bright paGFP to diffuse, we wait 30–60 min before acquisition of the final z-stack. This diffusion time was empirically determined and depends on the characteristics of the neuron type under investigation.

References

- [1] L. Petreanu, D. Huber, A. Sobczyk, K. Svoboda, Channelrhodopsin-2-assisted circuit mapping of long-range callosal projections, *Nat. Neurosci.* 10 (2007) 663–668, <https://doi.org/10.1038/nn1891>.
- [2] R. Portugues, K.E. Severi, C. Wyart, M.B. Ahrens, Optogenetics in a transparent animal: circuit function in the larval zebrafish, *Curr. Opin. Neurobiol.* 23 (2012) 119–126, <https://doi.org/10.1016/j.conb.2012.11.001>.
- [3] F. Del Bene, C. Wyart, Optogenetics: a new enlightenment age for zebrafish neurobiology, *Dev. Neurobiol.* 72 (2012) 404–414, <https://doi.org/10.1002/dneu.20914>.
- [4] G.H. Patterson, J. Lippincott-Schwartz, A photoactivatable GFP for selective photolabeling of proteins and cells, *Science* 297 (2002) 1873–1877, <https://doi.org/10.1126/science.1074952>.
- [5] E.K. Scott, L. Mason, A.B. Arrenberg, L. Ziv, N.J. Gosse, T. Xiao, et al., Targeting neural circuitry in zebrafish using GAL4 enhancer trapping, *Nat. Meth.* 4 (2007) 323–326, <https://doi.org/10.1038/nmeth1033>.
- [6] M. Dal Maschio, J.C. Donovan, T.O. Helmbrecht, H. Baier, Linking neurons to network function and behavior by two-photon holographic optogenetics and volumetric imaging, *Neuron* 94 (2017) 774–789.e5, <https://doi.org/10.1016/j.neuron.2017.04.034>.
- [7] D. Förster, M. Dal Maschio, E. Laurell, H. Baier, An optogenetic toolbox for unbiased discovery of functionally connected cells in neural circuits, *Nat. Commun.* 8 (2017) 116, <https://doi.org/10.1038/s41467-017-00160-z>.
- [8] T.W. Dunn, Y. Mu, S. Narayan, O. Randlett, E.A. Naumann, C.-T. Yang, et al., Brain-wide mapping of neural activity controlling zebrafish exploratory locomotion, *eLife* 5 (2016) e12741, <https://doi.org/10.7554/eLife.12741>.
- [9] I.H. Blanco, L.-H. Ma, D. Schoppik, D.N. Robson, M.B. Orger, J.C. Beck, et al., The tangential nucleus controls a gravito-inertial vestibulo-ocular reflex, *Curr. Biol.* 22 (2012) 1285–1295, <https://doi.org/10.1016/j.cub.2012.05.026>.
- [10] M.B. Ahrens, J.M. Li, M.B. Orger, D.N. Robson, A.F. Schier, F. Engert, et al., Brain-wide neuronal dynamics during motor adaptation in zebrafish, *Nature* 485 (2012) 471–477, <https://doi.org/10.1038/nature11057>.
- [11] H. Baier, E.K. Scott, Genetic and optical targeting of neural circuits and behavior—zebrafish in the spotlight, *Curr. Opin. Neurobiol.* 19 (2009) 553–560, <https://doi.org/10.1016/j.conb.2009.08.001>.
- [12] D. Förster, I. Arnold-Ammer, E. Laurell, A.J. Barker, A.M. Fernandes, K. Finger-Baier, et al., Genetic targeting and anatomical registration of neuronal populations in the zebrafish brain with a new set of BAC transgenic tools, *Sci. Rep.* 7 (2017) 5230, <https://doi.org/10.1038/s41598-017-04657-x>.
- [13] K. Kawakami, K. Asakawa, A. Muto, H. Wada, Tol2-mediated transgenesis, gene trapping, enhancer trapping, and Gal4-UAS system, *Methods Cell Biol.* 135 (2016) 19–37, <https://doi.org/10.1016/bs.mcb.2016.01.011>.
- [14] G.D. Marquart, K.M. Tabor, M. Brown, J.L. Strykowski, G.K. Varshney, M.C. LaFave, et al., A 3D searchable database of transgenic zebrafish Gal4 and Cre lines for functional neuroanatomy studies, *Front. Neural Circuits* 9 (2015) 78, <https://doi.org/10.3389/fncl.2015.00078>.
- [15] H. Otsuna, D.A. Hutcheson, R.N. Duncan, A.D. McPherson, A.N. Scoresby, B.F. Gaynes, et al., High-resolution analysis of central nervous system expression patterns in zebrafish Gal4 enhancer-trap lines, *Dev. Dyn.* 244 (2015) 785–796, <https://doi.org/10.1002/dvdy.24260>.
- [16] C. Satou, Y. Kimura, H. Hirata, M.L. Suster, K. Kawakami, S.-I. Higashijima, Transgenic tools to characterize neuronal properties of discrete populations of zebrafish neurons, *Development* 140 (2013) 3927–3931, <https://doi.org/10.1242/dev.09531>.
- [17] K. Asakawa, M.L. Suster, K. Mizusawa, S. Nagayoshi, T. Kotani, A. Urasaki, et al., Genetic dissection of neural circuits by Tol2 transposon-mediated Gal4 gene and enhancer trapping in zebrafish, *Proc. Natl. Acad. Sci.* 105 (2008) 1255–1260, <https://doi.org/10.1073/pnas.0704963105>.
- [18] J.M. Davison, C.M. Akitake, M.G. Goll, J.M. Rhee, N. Gosse, H. Baier, et al., Transactivation from Gal4-VP16 transgenic insertions for tissue-specific cell labeling and ablation in zebrafish, *Dev. Biol.* 304 (2007) 811–824, <https://doi.org/10.1016/j.ydbio.2007.01.033>.
- [19] J.P. Rickgauer, K. Delisseroth, D.W. Tank, Simultaneous cellular-resolution optical perturbation and imaging of place cell firing fields, *Nat. Neurosci.* 17 (2014) 1816–1824, <https://doi.org/10.1038/nn.3866>.
- [20] A.M. Packer, L.E. Russell, H.W.P. Dalgleish, M. Häusser, Simultaneous all-optical manipulation and recording of neural circuit activity with cellular resolution in vivo, *Nat. Meth.* 12 (2015) 140–146, <https://doi.org/10.1038/nmeth.3217>.
- [21] O.A. Shemesh, D. Tanese, V. Zampini, C. Linghu, K. Platkevich, E. Ronzitti, et al., Temporally precise single-cell-resolution optogenetics, *Nat. Neurosci.* (2017) 1–16, <https://doi.org/10.1038/s41593-017-0018-8>.
- [22] A. Picot, S. Dominguez, C. Liu, I.-W. Chen, D. Tanese, E. Ronzitti, et al., Temperature rise under two-photon optogenetic brain stimulation, *Cell Reports* 24 (2018) 1243–1253.e5, <https://doi.org/10.1016/j.celrep.2018.06.119>.
- [23] L. Feng, T. Zhao, J. Kim, neuTube 1.0: A new design for efficient neuron reconstruction software based on the SWC format, *eNeuro* 2 (2015) ENEURO.0049–14.2014, <https://doi.org/10.1523/ENEURO.0049-14.2014>.
- [24] M.H. Longair, D.A. Baker, J.D. Armstrong, Simple Neurite Tracer: open source software for reconstruction, visualization and analysis of neuronal processes, *Bioinformatics* 27 (2011) 2453–2454, <https://doi.org/10.1093/bioinformatics/btr390>.
- [25] X. Le, D.M. Langenau, M.D. Keefe, J.L. Kutok, D.S. Neuberg, L.I. Zon, Heat shock-inducible Cre/Lox approaches to induce diverse types of tumors and hyperplasia in transgenic zebrafish, *Proc. Natl. Acad. Sci. USA* 104 (2007) 9410–9415, <https://doi.org/10.1073/pnas.0611302104>.
- [26] B.F. Fosque, Y. Sun, H. Dana, C.T. Yang, T. Ohyama, M.R. Tadross, et al., Labeling of active neural circuits in vivo with designed calcium integrators, *Science* 347 (2015) 755–760, <https://doi.org/10.1126/science.1260922>.
- [27] D.T. Frazier, T. Narahashi, Tricaine (MS-222): effects on ionic conductances of squid axon membranes, *Eur. J. Pharmacol.* 33 (1975) 313–317, [https://doi.org/10.1016/0014-2999\(75\)90175-2](https://doi.org/10.1016/0014-2999(75)90175-2).
- [28] S. Attili, S.M. Hughes, Anaesthetic tricaine acts preferentially on neural voltage-gated sodium channels and fails to block directly evoked muscle contraction, *PLoS ONE* 9 (2014) e103751, <https://doi.org/10.1371/journal.pone.0103751>.
- [29] T. Weber, R. Köster, Genetic tools for multicolor imaging in zebrafish larvae, *Methods* 62 (2013) 279–291, <https://doi.org/10.1016/j.ymeth.2013.07.028>.
- [30] G.D. Marquart, K.M. Tabor, E.J. Horstick, M. Brown, A.K. Geoca, N.F. Polys, et al., High-precision registration between zebrafish brain atlases using symmetric diffeomorphic normalization, *GigaScience* 6 (2017) 1–15, <https://doi.org/10.1093/gigascience/glx056>.
- [31] Q. Tseng, I. Wang, E. Duchemin-Pelletier, A. Azioune, N. Carpi, J. Gao, et al., A new micropatterning method of soft substrates reveals that different tumorigenic signals can promote or reduce cell contraction levels, *Lab Chip* 11 (2011) 2231–2240, <https://doi.org/10.1039/c0lc00641f>.
- [32] M.G. Goll, R. Anderson, D.Y.R. Stainier, A.C. Spradling, M.E. Halpern, Transcriptional silencing and reactivation in transgenic zebrafish, *Genetics* 182 (2009) 747–755, <https://doi.org/10.1534/genetics.109.102079>.
- [33] C.M. Akitake, M. Macurak, M.E. Halpern, M.G. Goll, Transgenerational analysis of transcriptional silencing in zebrafish, *Dev. Biol.* 352 (2011) 191–201, <https://doi.org/10.1016/j.ydbio.2011.01.002>.
- [34] A.W. Thompson, G.C. Vanvallegheem, L.A. Heap, E.K. Scott, Functional profiles of visual-, auditory-, and water flow-responsive neurons in the zebrafish tectum, *Curr. Biol.* (2016) 743–754, <https://doi.org/10.1016/j.cub.2016.01.041>.
- [35] V. Ruta, S.R. Datta, M.L. Vasconcelos, J. Freeland, L.L. Looger, R. Axel, A dimorphic pheromone circuit in *Drosophila* from sensory input to descending output, *Nature* 468 (2010) 686–690, <https://doi.org/10.1038/nature09554>.
- [36] J.-M. Weislogel, C.P. Bengtson, M.K. Müller, J.N. Hörtzsch, M. Bujard, C.M. Schuster, et al., Requirement for nuclear calcium signaling in *Drosophila* long-term memory, *Sci. Signal.* 6 (2013), <https://doi.org/10.1126/scisignal.2003598>.

2.2 Manuscript 2

Michael Kunst, Eva Laurell, Nouwar Mokayes, **Anna Kramer**, Fumi Kubo, António M. Fernandes, Dominique Förster, Marco Dal Maschio, Herwig Baier. 2019. A cellular-resolution atlas of the larval zebrafish brain. *Neuron*, 103: 21-38. DOI (Sneak Peek version): [10.2139/ssrn.3257346](https://doi.org/10.2139/ssrn.3257346).

Understanding brain-wide neuronal dynamics requires a detailed map of the underlying circuit architecture. We built an interactive cellular-resolution atlas of the zebrafish brain at six days post-fertilization (6 dpf) based on the reconstructions of over 2,000 individually GFP-labeled neurons. We clustered our dataset in 'morphotypes', establishing a unique database of quantitatively described neuronal morphologies together with their spatial coordinates in vivo. Over one hundred transgene expression patterns (mainly Gal4 lines) were imaged separately and co-registered with the single-neuron atlas. By annotating 72 non-overlapping brain regions, we generated from our dataset an inter-areal wiring diagram of the larval brain, which serves as ground truth for synapse-scale, electron microscopic reconstructions. Interrogating our atlas by 'virtual tract tracing' has already revealed previously unknown wiring principles in the tectum and the cerebellum. In conclusion, we present here an evolving computational resource and visualization tool, which will be essential to map function to structure in a vertebrate brain.

A cellular-resolution atlas of the larval zebrafish brain

Michael Kunst¹, Eva Laurell¹, Nouwar Mokayes¹, Anna Kramer¹, Fumi Kubo^{1,2},
António M. Fernandes¹, Dominique Förster¹, Marco Dal Maschio^{1,3}, Herwig Baier^{1,4}

¹ Department Genes – Circuits – Behavior, Max Planck Institute of Neurobiology, 82152 Martinsried, Germany

² Present address: National Institute of Genetics, Center for Frontier Research, 1111 Yata, Mishima, Shizuoka, 411-8540, Japan

³ Present address: Department of Biomedical Sciences, Padua Neuroscience Center, University of Padua, 35158 Padua, Italy

⁴ Lead Contact

*Correspondence: hbaier@neuro.mpg.de

Summary

Understanding brain-wide neuronal dynamics requires a detailed map of the underlying circuit architecture. We built an interactive cellular-resolution atlas of the zebrafish brain at six days post-fertilization (6 dpf) based on the reconstructions of over 2,000 individually GFP-labeled neurons. We clustered our dataset in 'morphotypes', establishing a unique database of quantitatively described neuronal morphologies together with their spatial coordinates in vivo. Over one hundred transgene expression patterns were imaged separately and co-registered with the single-neuron atlas. By annotating 72 non-overlapping brain regions, we generated from our dataset an inter-areal wiring diagram of the larval brain, which serves as ground truth for synapse-scale, electron microscopic reconstructions. Interrogating our atlas by 'virtual tract tracing' has already revealed previously unknown wiring principles in the tectum and the cerebellum. In conclusion, we present here an evolving computational resource and visualization tool, which will be essential to map function to structure in a vertebrate brain.

Introduction

The brain's ability to perceive sensory information and coordinate movement is based on the dynamic interactions of interconnected nerve cells, which are often distributed over several brain regions. Due to the complexity of neuronal networks, it is challenging to pinpoint the role of individual cells, or cell types, in these processes. Progress should come from efforts that successfully link patterns of neural activity to their anatomical substrate (Alivisatos et al., 2012; Bauer et al., 2018; Panzeri et al., 2017; Sporns et al., 2005). For functional neuroanatomy to be informative, connectivities among neurons have to be determined in a systematic, unbiased fashion and visualized in an atlas format. Resolving the entire wiring diagram of a brain requires dense electron-microscopic reconstructions of nervous tissue volumes, preferably at the scale of individual synapses (Denk and Horstmann, 2004; Hildebrand et al., 2017; Ohyama et al., 2015; Varshney et al., 2011; Zheng et al., 2018). To understand basic organizational features of the brain, however, synapse-scale resolution may often not be necessary. Rather, mesoscopic descriptions of brain connectivity using light-microscopy (LM) provide a sufficient framework for the generation of testable hypotheses (Bohland et al., 2009; Mitra, 2014). Furthermore, building EM connectomes relies on the tracing of fibers over hundreds or thousands of sections. A catalog of reproducible cell shapes and inter-areal projection patterns will serve as "ground truth" to weed out continuation and merging errors and thus speed up ongoing EM efforts.

A brain-wide wiring diagram based on single-neuron reconstructions has been generated for *Drosophila melanogaster* (Chiang et al., 2011), revealing the general network structure and predicting whole-brain information flow (Shih et al., 2015). A similar approach has recently been performed in mice (Oh et al., 2014). However, due to the large size and complexity of the mouse brain, it was not feasible to perform this approach at the level of individual cells; instead, a grid-based approach to map anatomical connections between brain regions was used. This has the disadvantage that multiple cell types are labeled and information about individual collateral branching patterns is lost (Mitra, 2014). Also, there are currently no methods available to measure whole-brain activity with cellular resolution in mice.

Larval zebrafish (*Danio rerio*) offer several advantages for a comprehensive brain atlas project. Their translucency and small brain size, combined with an extensive arsenal of genetic tools (Baier and Scott, 2009; Friedrich et al., 2013) as well as quantitative behavioral assays (Orger and de Polavieja, 2017), make it possible to monitor and manipulate brain-wide neural activity, while the animal is responding to sensory stimuli and displaying movements of the eyes and tail (Ahrens et al., 2013; Portugues et al., 2014; Dal Maschio et al., 2017). Here we have expanded the larval zebrafish toolkit

by creating a digital neuroanatomy platform, which includes an unbiased catalog of cell morphologies, together with their spatial coordinates and long-range projections.

Our approach employed the stochastic and unbiased labeling of individual neurons in different, but age-matched, brains, which are then morphed into a common coordinate system ("standard brain") (see Hawrylycz et al., 2011). We show here that this format is expandable, as it can easily incorporate other reconstructed neurons. Importantly, transgene expression patterns (e.g., from the growing collection of zebrafish Gal4, Cre and Q lines) can be straightforwardly superimposed, instantly returning information about circuit composition and sharpening hypotheses about potential connectivity. To illustrate the power of this evolving resource, we have extracted new topographic principles in the tectum and cerebellum. Extending this approach to the whole brain, a first version of the connectome of the larval zebrafish brain has emerged. Computational models of circuit function are currently based solely on imaging with slow optical indicators and are therefore largely unconstrained by anatomical realities (Naumann et al., 2016). The open and interactive platform architecture of our new resource makes it possible to integrate optical recordings with cell-resolved anatomy of the activated brain regions. This application of our atlas resource has already been realized in the accompanying article by Kramer et al. (this issue).

Results

A new digital resource allows co-registration of independent neuron tracings to a standard brain

To digitally catalog the morphologies and positions of neurons and compare them among individual fish, we developed a workflow to label, scan, and digitize single neurons and subsequently align them to a common coordinate framework (Figure 1A). To reveal the morphology of neurons we made use of a fluorescent reporter transgene, *BGUG*, which encodes a highly variegated, membrane-targeted GFP driven from the upstream activating sequence (UAS) of the yeast transcription factor Gal4 (Xiao and Baier, 2007). When crossed to Gal4-VP16 driver lines, this approach leads to extremely sparse GFP expression in one, or very few, random neurons that are part of the overall Gal4 pattern. We used pan-neuronally expressing Gal4 lines (*elavl3:Gal4* and *Gal4s1101t*) to sample neurons from all brain regions in an unbiased manner. We focused our attention on neurons that can be traced in their entirety, excluding reticulospinal projection neurons. To generate high signal-to-noise ratio, we adapted the passive CLARITY method (PACT) (Treweek et al., 2015) to larval zebrafish. As the clearing method quenches the GFP fluorescence, we visualized labeled neurons via antibody staining directed against GFP epitopes. Each brain was also stained with an antibody to Synapsin (SYP), which outlines the neuropil areas and yields a highly stereotyped pattern across individuals.

In order to co-register individual *BGUG*-labeled neurons, we first generated a standard brain by averaging the SYP patterns from twelve larval zebrafish at 6 dpf (Figure 1B and C). To account for deformations introduced by our labeling protocol, we used the iterative symmetric group-wise normalization (SyGN) approach provided by the ANTs toolkit (Avants et al., 2010). This iterative process does not favor any one individual, but rather represents an unbiased average of the population (Figure 1C and S1). Individual fish brains containing *BGUG*-labeled cells were then aligned to this template using the SYP reference channel, and the transformation was applied computationally to the traced neurons (Figure 1D). Using this workflow, we generated an atlas of 1709 stochastically chosen neurons that cover the entire brain.

To demonstrate that our labeling technique samples from the entire brain in an unbiased fashion we analyzed the distribution of the somas of traced neurons in 36 brain regions (see below) and compared it to a mask of cell bodies (Figure S2A). When we compared the relative distribution, we could find that both soma location and cell body mask correlated well, i.e. regions with a relatively large cell body area also contained a higher number of somas from traced neurons ($R=0.48$, Figure S2B and C). In addition, since our single-cell labeling is based on the Gal4/UAS-expression system, we are also able to target certain cell-types using more restrictive driver lines. To demonstrate this,

more than two hundred tracings, obtained using more specific drivers (*vglut2a:Gal4*, *Gal4s1171t*, *lhx9:Gal4*, *Gal4s1013t*), were added (Figure 1E, Video S1). When we analyzed this dataset for labeling bias, we found that the correlation increased with the added neurons ($R=0.59$, Figure S2D). This improved correlation was most notable in the case of the tectum (arrow in Figure S2E). Taken together, our workflow labels neurons throughout the brain in an apparently unbiased fashion, reflecting the expression pattern of the Gal4 driver used.

Single neuron morphologies can be aligned to transgene expression patterns and other data

modalities

To provide flexibility for efforts using reference channels other than SYP, we generated shape-based averages for commonly used immunohistochemical labels and transgenic reporters (Figure 2A). These include ERK1/2 and HuC/D antibodies, as well as the *elavl3:lynTagRFP*, *bAct2B:GFP*, *vGlut2a:DsRed*, *elavl3:GCaMP5G*, *elavl3:nlsGCaMP6S* and *elavl3:H2BGCaMP6S* transgenic reporter lines. With the aid of these bridging registrations, we crosslinked our database to existing anatomical resources, including Z-Brain (Randlett et al., 2015) and the Zebrafish Brain Browser (Marquart et al., 2015). Importantly, we could also incorporate the expression patterns of Gal4 lines generated by various laboratories into our platform (Asakawa et al., 2008; Förster et al., 2017; Scott et al., 2007) (Figure 2B).

Rather than imaging the entire brain, researchers often prefer a more targeted approach, focusing on a specific brain region (e. g., Kubo et al., 2014). To accommodate such datasets in our resource, we developed a computational pipeline that enables us to register subvolumes to the standard brain. As a proof of principle, we aligned a set of 55 mitral cell tracings from a previous publication (Miyasaka et al., 2014). Mitral cells are projection neurons that carry information from the olfactory bulbs to several forebrain regions. In this case, only the brain subvolume containing the forebrain and habenula had been acquired using the presynaptic marker SV2 as the reference channel. Reasoning that SV2 should have a similar labeling pattern to SYP, we cropped our SYP reference stain to match the region imaged by Miyasaka et al. and used this as the template to successfully align their mitral cell tracings to our standard brain (Figure 2C). Finally, we integrated a large-scale dataset of tectal projection-neuron tracings ($n = 133$) recently generated by our lab (Helmbrecht et al., 2018, Fig. 2B₆). Together the success of these efforts shows that our resource is backwards compatible with previous single-cell tracing efforts, provided a bridging registration to one of the available reference markers can be established.

Registration accuracy has subcellular resolution across individual brains

To measure the accuracy of the registration, we then identified five landmarks within the SYP pattern (fiber landmarks) and 20 from compact cell clusters in various co-registered Gal4 patterns (nuclei landmarks), which were easily recognizable across individual brains (Figure 3A; Figure S3A), and measured the Euclidean distances to their counterparts in the standard brain (see STAR Methods). The distance varied between 0.22 μm and 14.13 μm with most data point between 2 and 7 μm and a median of 4.38 μm (Figure S3B and C), comparable to what has been described in *Drosophila* (Jefferis et al., 2007). It is unknown to what extent this positional variability is biological in nature or caused by registration errors. In any case, this value corresponds to a fraction of the typical cell body diameter in larval brains (3-7 μm) and confirms the large degree of stereotypy in brain architecture, which appears to extend to the positioning of individual nuclei and axon tracts. These values are derived from samples that have been inspected manually for successful alignment. For each neuron we manually inspected the alignment of the underlying image stack (see STAR Methods).

As a test case for registration accuracy, we asked if we could detect the well-known laminar organization of retinal ganglion cell (RGC) axon terminals in the neuropil of the optic tectum (Robles et al., 2014). Individual laminae are about 4-10 μm in thickness. When the 42 RGC traces from our database were displayed together, individual retinotectal laminae could be discerned (Figure 3B, C, D). The vast majority of RGCs in our dataset terminate in the SFGS layers of the tectal neuropil (36/42), most of them exclusively so (26/42). Fewer RGCs project to other layers of the tectum (4/42), and a small subset project to visual areas outside of the tectum (2/42). This distribution is similar to what has been reported in a sample of 450 RGCs traced in a previous study (Robles et al., 2014). We were also able to detect some of the more infrequent RGC types including those that have collaterals in both arborization field AF7 and the tectal SO layer (Semmelhack et al., 2014), as well as a multi-collateral RGC type that projects to the tectal SAC/SPV layer and multiple AFs in the thalamus and the pretectum (Robles et al., 2014).

To test if our registration procedure retained the well-known retinotopy of RGC terminations in the tectum, we subdivided our RGC dataset into those that originated in the nasal, temporal, dorsal, and ventral quadrants of the retina and inspected their projection sites in the tectum. We found, reassuringly, that their axons primarily terminate in the posterior, anterior, ventral and dorsal quadrants of the tectal neuropil, respectively (Figure 3E, F), in agreement with earlier studies (Baier et al., 1996; Robles et al., 2014; Springer and Mednick, 1985; Stuermer, 1988). In conclusion, digital

co-registration of 42 separately sampled RGCs in our standard brain faithfully reveals the architecture of the retinotectal projection along its retinotopic and laminar axes.

An interactive web-interface enables browsing and searching for neurons in predefined subvolumes

To make the atlas easily accessible to the community we generated a repository (http://fishatlas.neuro.mpg.de/zebrafishatlas/main_page#), and programmed a user interface with the following major functionalities:

1) *Visualization*: Neurons are initially visualized in a 3D interactive browser (in this case we choose RGCs as an example set of neurons) (Figure S4A, Video S2). The user has multiple options to change the appearance of the neurons (e.g. color, soma size, and neurite thickness) as well as the option to mirror neurons to either hemisphere of the brain for display purposes (Figure S4B₁). For each neuron, a link to the metadata is provided, e.g. lab of origin, Gal4-driver, cell type (if available), as well as original publication in which the neuron was described (Figure S4C₁). In addition, it is possible to display the brain regions innervated by a particular neuron, with the option to limit the search to only specific parts of the neuron (Figure S4C₂). Once the user has found an interesting neuron, morphologically similar neurons can be identified using NBLAST (Costa et al., 2016) (Figure S4C₃). The current 3D view can be exported as an image by taking a screen shot (Figure S4D), or alternatively by downloading the tracings and using external visualization software (Figure S4B₂).

2) *Location-based search*: To search our database for neurons in specific brain regions, we generated a basic segmentation of the larval zebrafish brain that consists of 79 brain regions covering 81% of the entire brain volume. In our example case, we selected the retina and the tectal neuropil to search for RGCs (Figure S4E, Video S3). Once the user selected one or more brain regions it is possible to perform searches on the individual regions, i.e. looking for projection neurons by searching for neurons that have their somata in the region but also terminate outside of it (Figure S4F). For more complex search function involving two or more brain regions, an advanced search function is available (Figure S4G). The user can perform logical AND/OR searches and can specify which part of the neurons is in which brain region. In our example we searched for neurons that have their somata in the retina and fiber terminals in the tectal neuropil to find all RGCs in our dataset.

3) *Expression pattern-based search*: Currently there is no consensus annotation of all the different brain regions in the larval zebrafish. One reason for that is the difficulty of defining regional boundaries due to the lack of clear anatomical demarcations. Brain regions or parts thereof can often be labeled by gene expression pattern. In order to guide the selection of specific brain regions, we

aligned the unique expression patterns of 221 Gal4 lines and other markers to our standard brain (see above). This collection currently encompasses the Gal4 patterns from the Zebrafish brain browser database (ZBB; <https://science.nichd.nih.gov/confluence/display/burgess/Brain+Browser>), as well as 96 new lines. In our specific example, we used a recently created BAC transgenic line that expresses GFP in cholinergic neurons (Förster et al., 2017). Based on the GFP expression, we selectively marked the oculomotor nucleus and searched for neurons in this region (Figure S4H, Video S4). Often, brain regions are not defined by the expression of one marker but by the combination of multiple. To accommodate this feature, we added the possibility to visualize multiple channels simultaneously (Figure S4I).

“Virtual tract tracing” reveals the spatial organization of multimodal inputs to the tectum

We next asked if we could employ the brain atlas to discover novel wiring principles in the tectum. To this end, we focused on the proposed segregation of visual and non-visual innervations (Basso and May, 2017; Filosa et al., 2016; Li et al., 2018; Meek, 1983; Pérez-Pérez et al., 2003). Prior work in adult teleosts had demonstrated that the non-retinal inputs tend to target different layers in the tectal neuropil than RGCs (Meek, 1983), but such laminar separation has not been investigated in the much smaller brains of zebrafish larvae. We visualized the well-described retinorecipient layers (Robles et al., 2013; Roeser and Baier, 2003; Xiao and Baier, 2007; Xiao et al., 2005) side by side with those innervated by other afferents from our dataset (Figure 4A and 4B). We visualized RGCs that target the tectal neuropil (40/42) and mirrored them to each hemisphere for comparison of ipsi- and contralateral tectal innervation (green and orange, Figure 4A and 4B). Non-retinal cells ($n = 36$) projecting to the tectum with soma in the left hemisphere were mirrored to the right hemisphere (purple, Figure 4A and 4B). The majority of these afferents (22/36) originated from cells on the same side of the brain, but we also detected neurons that innervated both (9/36) or the contralateral (5/35) tectal hemisphere. Overlaying retinal and non-retinal axons revealed that both populations are highly segregated within the tectal neuropil: While RGC axons are innervating the superficial layers, mainly SFGS, as reported before, non-retinal inputs primarily target deeper layers, such as SAC, in which RGC axons are absent (Figure 4C).

We analyzed this dataset at the individual neuron level to determine the origin of non-retinal input. We manually subdivided the 36 non-retinal afferents in 18 classes, based on soma location and projection pattern (Figure 5D), and generated a wiring diagram of non-retinal tectal input (Figure S5). Most classes contain only one neuron, but others have up to 9 (Class 6; Figure 4D). The majority of cells originate in the thalamus (10/37), and a recent manuscript described these as sensitive to looming and luminance decrease (Heap et al., 2018). In addition to the thalamus, other prominent

input arises from the nucleus isthmi (NI, 8/37, Class 2, 17, and 18) as well as the medial octavolateralis nucleus (MON, 4/37, Class 1). The latter area receives inputs from lateral line neuromasts and is sensitive to water currents (Thompson et al., 2016). In total, we identified 15 distinct regions that innervate the tectum (Figure S5), including some that process sensory information (e.g., MON and thalamus) or the internal state (e.g. intermediate hypothalamus and reticular formation). Taken together, anatomical data extracted from our brain atlas corroborate a function of the tectum in multimodal integration of sensory information and internal state.

The brain atlas reveals a topographic organization of cerebellar projections

The cerebellum of vertebrates is involved in coordinated smooth movements and motor learning. One of the organizing principles proposed for the cerebellum is functional regionalization (Manni and Petrosini, 2004). In zebrafish, two similar visual stimuli that trigger distinct motor outputs (optokinetic and optomotor responses) have been shown to evoke region-specific activity of Purkinje cells (Matsui et al., 2014). In addition, a topographical map for processing of different sensory modalities was found in granule cells (Knogler et al., 2017). To find evidence for a topographic organization of the output pathways, we investigated the neurons that projected out of the cerebellum. There are two cell types that provide output for the cerebellum, Purkinje cells (PCs) and eurydendroid cells (ECs). PCs exclusively send their projection to the MON while ECs provide a more diverse output of the cerebellum (Bae et al., 2009).

We found 121 cerebellar output cells, whose cell bodies reside along the medio-to-lateral and rostral-to-caudal extent of the cerebellar corpus. The majority of those are ECs (91/121) and the rest are PCs (30/121). Their projections extend to a variety of brain regions, including the thalamus, the hypothalamus, the tegmentum, the nucleus of medial longitudinal fascicle, the oculomotor and trochlear nucleus as well as the reticular formation and the medulla oblongata (Figure S5A). The NBLAST algorithm (Costa et al., 2016) was used to hierarchically cluster the individual cells based on their morphological similarity (Figure 5A). Of the eight major clusters, one (cluster 7) consisted exclusively of all PCs, with the remaining ECs distributed over the other seven clusters. Color coding these clusters (Figure 5B and C) revealed that the dendrites of the individual EC clusters tile the granule cell layer, suggesting segregation of inputs. Interestingly, the different clusters projected to distinct target regions (Figure S6A). Dendrites of clusters 1, 2 and 3 are arrayed topographically along the medial-to-lateral axis at the same rostro-caudal level; this order is preserved, albeit flipped, for their axon projections in the tegmentum (Figure S6B). We observed a different pattern for EC connections to the thalamus. Here, dendrites of clusters 1, 3, and 5 show almost perfect tiling in the granule layer, yet their axons intermingle within the thalamus (Figure S6C). Cluster 4 ECs are distinct

from other clusters in that they provide the sole input to the ipsilateral intermediate hypothalamus (Hi), as well as the majority of inputs to the ipsilateral tegmentum. Such topographic relationships provide entry points into studies of the cerebellum's functional specializations, as they may guide experimental interventions to particular sites in the brain.

Neurons are classifiable based on their locations and morphologies using NBLAST

We classified all 2,141 neurons (including mitral cells and tectal projection neurons) by morphology and innervation pattern using NBLAST. Similarity scores were calculated to perform hierarchical clustering (Figure 6A, B; Video S5). Looking at the dendrogram, it becomes apparent that separable clusters of neurons exist. When we cut the resulting dendrogram at a height of 8 we end up with 22 distinct clusters. At this cutoff, we can already see clusters identical to known cell classes (Figure 6C). Examples are cluster 13 (oculomotor neurons) and cluster 14 (RGCs). However, at this cutoff, many clusters are still heterogeneous. For example, cluster 12 consists of multiple neuron types located in the forebrain. When we lowered the cutoff to 3, cluster 12 contained at least 6 distinguishable morphological types ('morphotypes'; Figure 6D). Three of those are part of the olfactory pathway. Sub-cluster 12-2 consists of olfactory receptor neurons (ORNs) that convey information from the olfactory epithelium to the olfactory bulb (OB) and sub-cluster 12-4 consists of mitral cells (see Figure 2C for comparison). Sub-cluster 12-1 is composed of local interneurons of the olfactory bulb that modulate information transfer between the ORNs and the mitral cells. In addition, we could also find three clusters of pallial/subpallial neurons (sub-cluster 12-3, 12-5, and 12-6) that show strong overlap with the projections of the mitral cells and could potentially be downstream targets.

The clustering approach successfully isolates well-known cell types and discovers apparently new ones. Three examples of known types are neurons that provide input from the ventral entopeduncular nucleus to the habenula (Turner et al., 2016) (vENT-Hb; Figure S7A₁), habenular output neurons that project to the interpeduncular nucleus (Nln) and the superior raphe (Amo et al., 2010) (Hb_PN; Figure S7A₂), as well as tangential neurons that provide input from the tangential nucleus to the oculomotor nucleus and the nMLF (Bianco et al., 2012) (Figure S7A₃). Among the novel types are tegmental neurons that project to the hypothalamus and pallium (T-Hi/P, Figure S7B₁), neurons of the nucleus isthmi that innervate the thalamus, torus semicircularis, and the reticular formation (NI-RF/TS/Th; Figure S7B₂), as well thalamic neurons that project to the hypothalamus and the medial part of the reticular formation (Th-Hr/mRF; Figure S7B₂).

Lowering the threshold also leads to a splitting up of distinct cell types into further sub-clusters that appear not to reflect bona fide cell types. For instance, RGCs can be further subdivided based on their dendritic morphology and axonal projection pattern (Robles et al., 2014), and, when we

lowered the height at which the dendrogram was cut, RGCs were split up in separate clusters (Figure S7C). However, the difference between individual clusters primarily reflected the position of the cell bodies and dendrites within the retina and the respective retinotopic mapping of the axons in the tectal neuropil, rather than collateral patterns or laminar stratification. In summary, our catalog of cell morphologies can be automatically organized using NBLAST leading to the classification of cell classes. However, such first-pass results have to be carefully interpreted, as NBLAST tends to weight cell-body location and neurite orientation more heavily than morphological parameters.

Combing single-cell tracings with annotation of brain regions generates a mesoscale connectome

To generate a brain-wide undirected connectivity matrix, we divided the brain into 36 non-overlapping regions at approximately similar ontological level (Figure 7). These regions cover ~82% of the brain volume. Since the regions are bilaterally symmetric we divided them into a left hemispheric region and a right one, for a total of 72 brain regions. While this annotation is not exhaustive, we can use it to generate a mesoscale connectome, which will evolve with further knowledge of anatomical boundaries and the addition of more cells. We chose an undirected connectivity matrix since the distinction of dendritic and axonal arbors is not always as obvious as in the previous examples shown in Figs. 4, 5, S5, and S6.

Connection strengths between individual brain regions were calculated from the total sum of neurite lengths in each of the possible combination of two brain regions from all neurons that connect them (see STAR Methods). To prevent biases in connection strength arising from different sizes, we normalized connection strength by the total volume of the two brain region pairs. This approach revealed connection strengths that span a range greater than 10^5 -fold across the brain. The observed connection strength follows a lognormal distribution (Figure 8A) and decays exponentially as a function of distance (Figure 8B; $R=0.39$) in accordance with previous results from other animals (Betz et al., 2018; Ercsey-Ravasz et al., 2013; Oh et al., 2014) and consonant with an economic network organization, which minimizes wiring lengths (Bullmore and Sporns, 2012).

The resulting connectivity matrix allowed us to perform hierarchical clustering of brain regions by similarity of input and outputs (Figure 8C). For each brain region, the 3D center of masses was plotted in our standard brain (Figure 8D; Video S6), with the colors reflecting the clusters of Figure 8C. We also plotted the connectivity matrix as a 3D wiring diagram, with the size of the nodes representing the node degree (number of neurons which connect to or from that brain region) and the thickness of the connections representing the normalized connection strength (Figure 8E; Video S7). Various levels of organization become immediately apparent indicating a non-random

organization. Closer inspection reveals two main clusters. One (cluster 1, red) consists of nodes that show a high degree of connectivity that strongly participate in the overall network structure. This cluster consists mainly of the subdivisions of the reticular formation and the raphe nucleus. The other clusters (white rectangle) are more heterogeneous. For example, cluster 2 (green) consists mostly of peripherally located ganglia that convey sensory information to specific central brain regions or motor information to the muscles but has fewer and weaker connections to the rest of the network (e.g. olfactory epithelium or vagal motor neurons). In addition, we also find strongly reciprocally connected brain regions. For example, the two main regions of the telencephalon (pallium and subpallium) form strong connections with each other and their respective counterpart on the contralateral hemisphere as well as the preoptic region of the hypothalamus and the posterior tuberculum (cluster 3, cyan).

Discussion

The larval zebrafish is increasingly being used to address fundamental questions of nervous-system organization and circuit function at the whole-brain level (Vanwalleghem et al., 2018), yet its neuro-anatomy is still relatively uncharted. Here we introduce a novel resource, which will be beneficial to approaches that attempt to tie neuronal function to the structure of the underlying circuitry. We generated a dataset of 1,955 single neurons tracings, which we aligned to an average standard brain. We verified, using a set of stereotyped anatomical landmarks, that registration accuracy is at subcellular resolution ($\sim 4\ \mu\text{m}$) and faithfully recapitulates known wiring principles such as retinotopic organization and layer-specific innervation of RGC axonal arborizations. To ensure cross-platform compatibility and to enable submission of external data into our platform, we registered additional reference stains to the standard brain, including commonly used antibody stains and calcium indicator transgene expression patterns. Single-cell data from subvolume imaging experiments can be incorporated with little effort, as demonstrated by the successful addition of 55 olfactory bulb mitral cells previously reconstructed by a different lab (Miyasaka et al., 2014), as well as additional 133 single neuron tracing previously published (Helmbrecht et al., 2018). We enriched our dataset with a collection of Gal4 and GFP transgenic expression patterns (Förster et al., 2017; Marquart et al., 2015; Randlett et al., 2015; Scott et al., 2007). Earlier work used EM-tracings of neurons with myelinated axons (Hildebrand et al., 2017). This dataset was largely limited to peripheral and spinal projection neurons and therefore complements this resource.

Our constantly growing dataset can be viewed online (http://fishatlas.neuro.mpg.de/zebrafishatlas/main_page#). This web-portal allows to interactively search for neurons and visualize them in relation to other neurons, commonly used marker stains, and transgene expression patterns. The complete toolbox of searching, browsing and viewing features is available to the community and will be expanded to accommodate other data modalities. For instance, the here presented resource will be useful for researchers who wish to search for anatomical connections between functionally correlated regions in whole-brain imaging studies (Ahrens et al., 2013; Portugues et al., 2014). Our database has been used successfully by an accompanying study (Kramer et al., this issue) to complement GCaMP6 imaging studies investigating neuronal circuits processing optic flow. The authors could find long-range projection neurons that connect the pretectal area to the cerebellum and the reticular formation, providing a sensorimotor pathway suggested to drive behavioral responses to optic flow.

To facilitate data mining and discovery of novel neuronal cell types, we analyzed our dataset using the NBLAST algorithm, which was developed for a large single-neuron dataset of fruit flies (Costa et

al., 2016). An all-by-all comparison of the entire dataset provided us with a morphological similarity matrix on which we performed hierarchical clustering. By adjusting the height at which to cut the resulting dendrogram, we were able to identify multiple already known cell classes, confirming the robustness of NBLAST. We also discovered several novel types by inspection. However, such first-pass results have to be carefully interpreted, as NBLAST tends to weight cell-body and neurite location more strongly than intrinsic morphological parameters. Moving forward, we envision this database to become an open-access repository similar to NeuroMorpho.org (Akram et al., 2018; Ascoli et al., 2007). While a comprehensive cell type census is more likely to come from genetic expression profiling, such single-cell RNA sequencing (McKenna et al., 2016; Pandey et al., 2018; Raj et al., 2018), a morphological classification of zebrafish neurons, ideally with their transcriptional profiles and developmental lineages, will be tremendously useful for experimental and computational neuroscientists alike.

To gain insight into the general architecture of the larval zebrafish brain, we constructed a cellular-resolution mesoscale connectome. For this, we divided the brain into 72 non-overlapping brain regions and determined their pairwise connection strengths to generate an undirected graph that we subjected to further analysis. Already at the current stage of our database with only about 2% of the entire neuronal complement covered, several organizational principles become evident. The interareal connection strengths exhibit a lognormal distribution and are decaying exponentially with distance. This is consistent with the theory of economic brain network organization, which states that brains are dominated by short range connections to minimize wiring costs (Bullmore and Sporns, 2012). We found that the larval zebrafish brain displays a core/periphery organization with brain regions mainly related to sensory or motor function falling into one module and more central regions involved in higher-order integration falling into other modules. For example, we found that the forebrain together with the preoptic region and the posterior tuberculum comprises a distinct module anatomically separated from the mid- and hindbrain which seem to be much more strongly interconnected. This agrees with a whole-brain imaging experiment that reported stronger correlation of spontaneous activity between mid- and hindbrain compared to the forebrain (Ahrens et al., 2013). We do caution in overinterpreting our results since a large number of morphotypes still needs to be described. However, given the simplicity of our workflow and the ease with which data from other labs can be incorporated into our standard brain (as illustrated by the mitral cells), a complete census will be accomplished in the next few years. In addition, with a growing dataset it may become possible to apply machine learning algorithms to differentiate between axons and dendrites (Lee et al., 2014).

To demonstrate the immediate utility of our dataset, we performed virtual tract tracing of the afferent fibers innervating the tectum. First, we investigated the laminar organization of modality-specific inputs and showed that RGC and non-retinal axons are segregated, with RGCs targeting medial to superficial layers and non-retinal fibers primarily targeting deeper layers. This is in accordance with the situation in adult goldfish (Meek, 1983). When we further investigated the individual cells that provide non-retinal inputs we identified 18 different cell classes. The most prominent non-retinal input to the tectum arises from the thalamus. Such thalamo-tectal neurons have recently been reported to respond to dimming of the visual field (Heap et al., 2018). Another prominent input arises from the contralateral MON, which receives sensory input from the lateral line and the inner ear (Liao and Haehnel, 2012; McCormick, 1989). Consistent with this anatomical arrangement, functional imaging detected responses to contralaterally applied water flow and auditory stimuli in the deeper layers of the tectum (Thompson et al., 2016). We further showed that the majority of these axons also branched in the torus semicircularis (Fame, 2006), a feature that was not known from previous work. The tectum is from a network perspective ideally located to connect sensory areas directly with motor areas. Yet it is also well enough integrated with the rest of the brain so that information from other brain regions can exert influence over sensorimotor transformations taking place in the tectum. This principle of extrinsically modulated “labeled lines” was demonstrated for the decision to approach or avoid a visual object based on its size. Larval zebrafish chase after small, prey-like dots and escape from large ones (Barker and Baier, 2015). The tectal output channels that steer the animal’s movements toward or away from the object are anatomically segregated (Helmbrecht et al., 2018). The decision between approach and avoidance is mediated by the tectum, and hunger stimuli from the serotonergic system can shift the animal’s behavioral tendency to approach larger stimuli that would normally evoke escapes (Filosa et al., 2016). Our dataset revealed additional inputs from central brain regions (PO, PT, T), which may modulate this decision-making process.

Our dataset allowed us to describe, for the first time, the topographic organization of the cerebellar projection neurons. Teleosts lack the deep cerebellar nuclei of mammals; instead, they have a specialized cell class, the eurydendroid cells (ECs), that receive direct input from Purkinje cells and project widely to other brain regions (Bae et al., 2009). The collection of 91 ECs from our database innervate a large proportion of the mid- and hindbrain. Using NBLAST (Costa et al., 2016), we divided the ECs into seven different classes. Closer inspection of their projection patterns revealed a topographical organization. Their dendrites tile anatomically compact regions of the granule cell layer, and their axons project to distinct, yet partially overlapping, brain regions. This topographical output provides an anatomical substrate for how regionalized Purkinje cell activity gets converted

into distinct motor patterns as was demonstrated for the optomotor and optokinetic reflexes (Matsui et al., 2014). Taken together, the high-fidelity co-registration feature of our resource makes it possible to carry out virtual tract tracing studies to test hypotheses *in silico* and discover new wiring principles.

Another area of investigation that will benefit greatly from this new resource are dense electron-microscopic (EM) reconstructions of circuit structure (Denk and Horstmann, 2004; Hildebrand et al., 2017; Ohyama et al., 2015; Varshney et al., 2011; Zheng et al., 2018). The tracing of fibers over hundreds or thousands of ultrathin sections requires high spatial resolution and image contrast and is notoriously prone to continuation and merging errors, especially for long-range projections. Such errors will be spotted more reliably if EM-derived wiring diagrams can be compared to a catalog of realistic cell shapes and projection patterns. Our cell-resolved atlas thus provides an anatomical "ground truth", which will be necessary to assemble the complete synapse-scale connectome of the larval zebrafish brain and will contribute to our understanding of brain-wide neuronal dynamics.

Acknowledgements

We thank J. Donovan and M. Al-Kasar for help with the design and implementation of the interactive web portal, C. Bühler for help with tracings, R. Kasper and the MPIN imaging facility for technical support imaging the Gal4 lines, K. Slanchev and S. Steinhäuser for help with fish maintenance and husbandry, M. Wüllmann and O. Randlett for feedback on brain annotation and all members of the Baier for helpful discussions. We are grateful to H. Burgess, G. Marquart, Y. Yoshihara, N. Miyasaka and K. Kawakami for sharing data and fish lines. This study utilized the high-performance computational capabilities of the Linux cluster at the Max Planck Computing and Data Facility (MPCDF, <https://www.mpcdf.mpg.de/>). Funding was provided by the Max Planck Society and the DFG (SFB 870, Assembly and Function of Neuronal Circuits).

Author Contributions

M.K and H.B conceived the experiments and wrote the paper. E.L performed the experiments. M.K. performed analysis. N.M wrote the code for the online platform and analysis tools for the single neuron database. D.F, M.A.F, M. D. M., F. K., and A.K helped verify the successful alignment of single-neuron tracings.

Declaration of Interest

None.

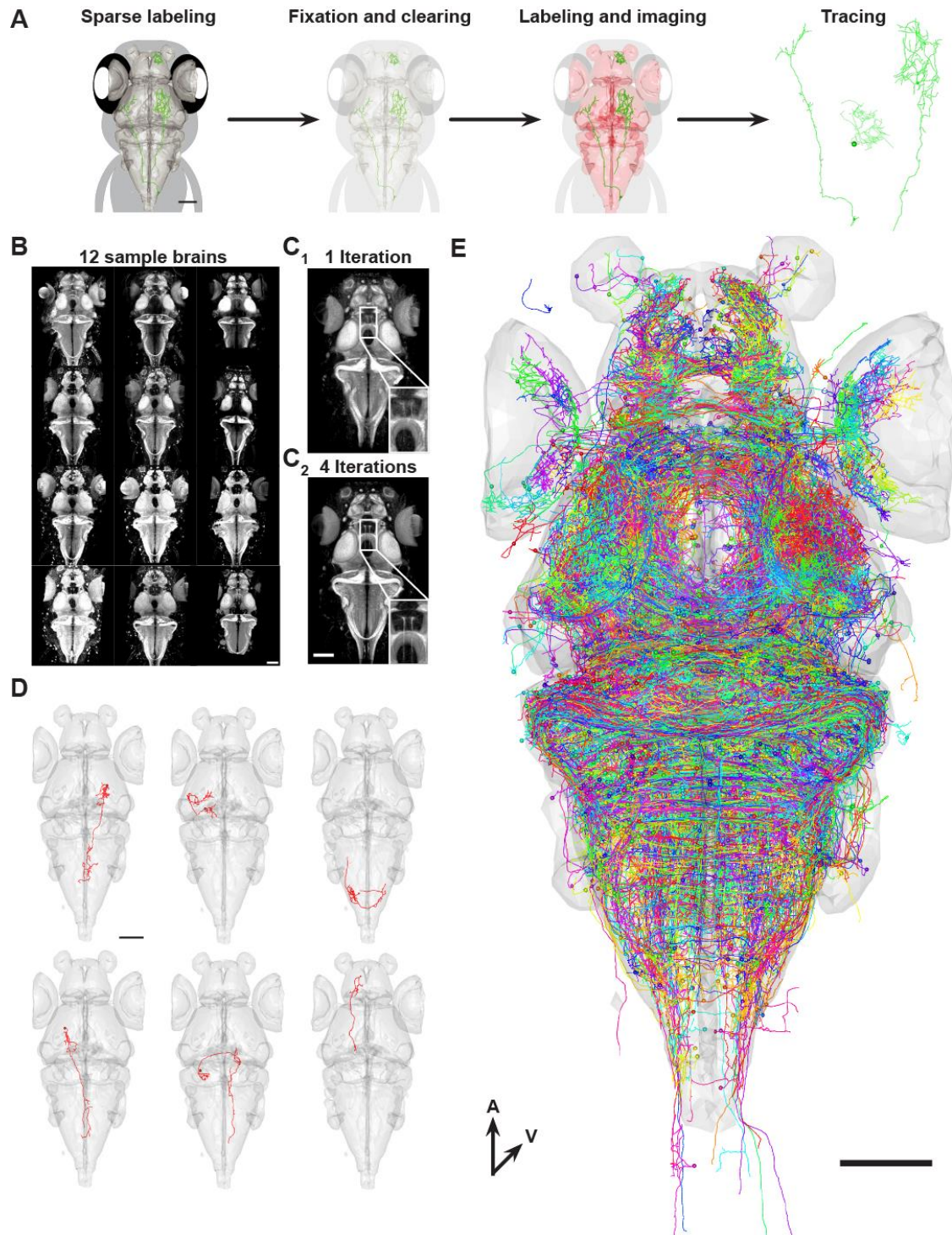
Figures

Figure 1: Construction of a single-neuron atlas. (A) Workflow for generating single-neurons tracings. (B) Images of 12 representative brains used to generate a shape-based average template. Brains were labeled with an antibody against the presynaptic protein synapsin. (C) Shape-based average template brain after 1 iteration (C₁) and 4 iterations (C₂). Inset shows higher magnification of the torus longitudinalis neuropil. (D) Examples of individually traced neurons from different brains aligned to our template brain (grey surface). (E) Overlay of all neurons (n=1955) generated by our workflow. Colors of neurons are assigned randomly.

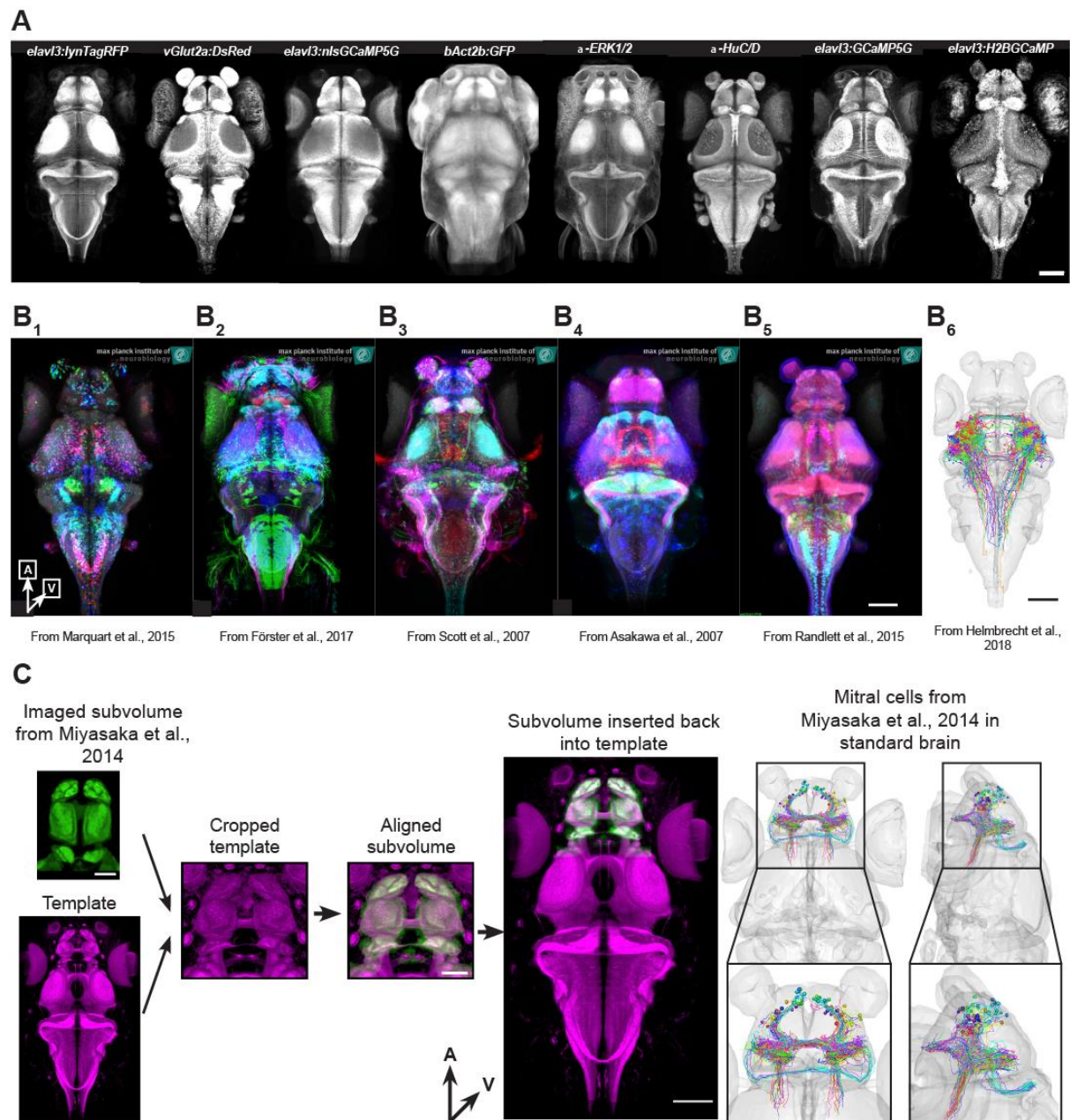


Figure 2: Integration of external data. (A) 8 examples of additional reference stains that can be used to align data to our resource. A, anterior; V, ventral. Scale bar represent 100 μ m. (B) Examples of Gal4-line expression patterns and single neuron tracings from different projects aligned to our common coordinate system. (B₁) Enhancer-trap (ET) lines expressing *UAS-Kaede* from (Marquart et al., 2015). (B₂) BAC-trangenetic lines expressing *UAS-Dendra* from (Forster et al., 2017). (B₃) ET-lines expressing *UAS-Dendra* from (Scott et al., 2007). (B₄) Enhancer-trap (ET) lines expressing *UAS-GFP* from (Asakawa et al., 2008). (B₅) Various expression pattern from (Randlett et al., 2015). (B₆) Tectal projection neurons from (Helmbrecht et al., 2018). All scale bars represent 100 μ m. (C) Integration of mitral cell tracing from (Miyasaka et al., 2014). Our reference brain was cropped to match the template of the original data. After successful alignment, the cropped volume was reinserted into the full-site reference brain. The various transformation steps were also applied to the mitral cell tracings. A, anterior; V, ventral. Scale bars in subvolume represent 50 μ m all other scale bars represent 100 μ m.

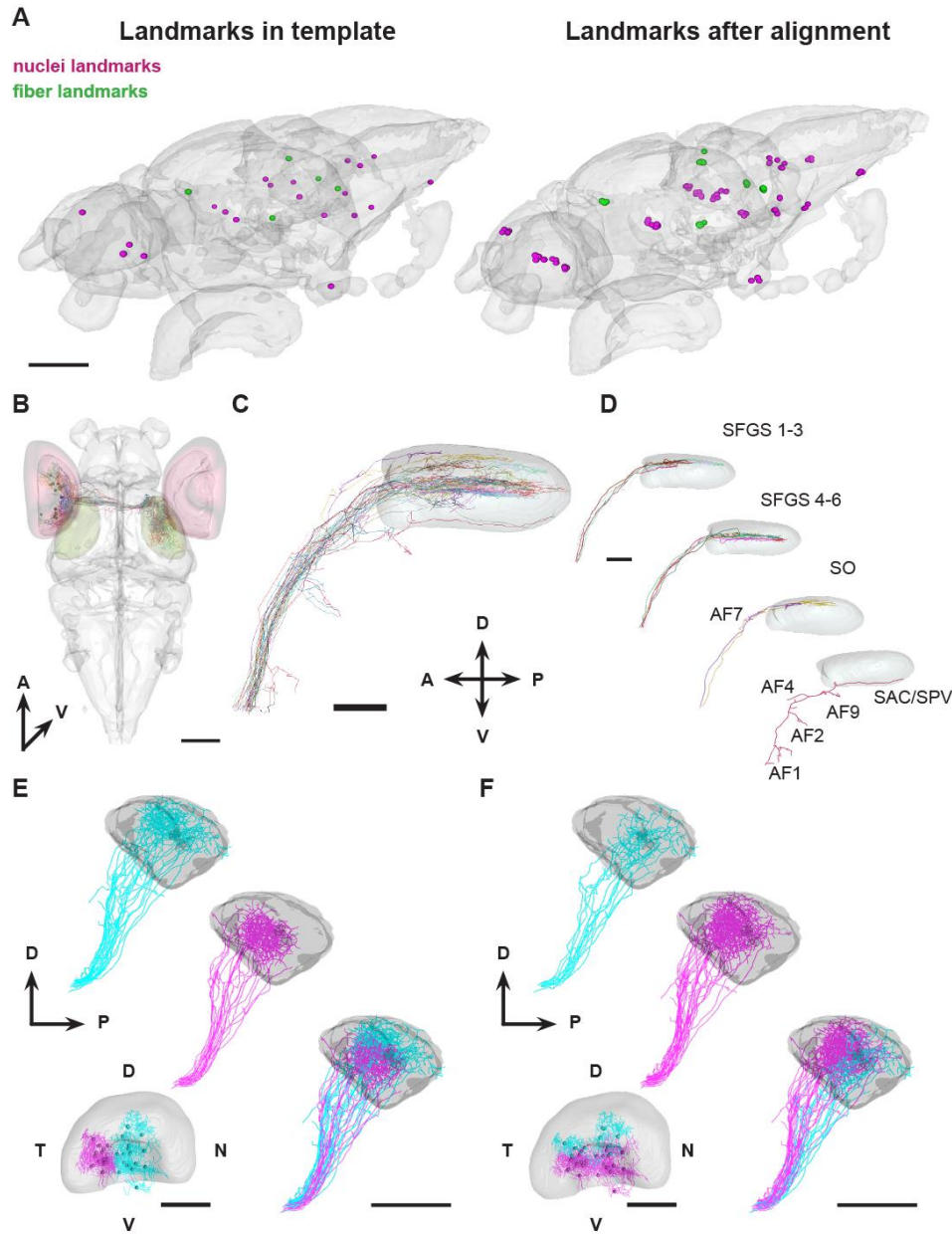


Figure 3: Verification of registration accuracy. (A) Left: Location of fiducial points overlaid in outline of standard brain (grey). Right: Location of the same fiducial points identified in original images after alignment to standard brain. Scale bar represents 100 μ m. (B) RGCs extracted from our database overlaid in outline of standard brain (grey). Surfaces of the retina (red) and tectal neuropil (green) are also shown. Scale bar represents 100 μ m. (C) Lateral view of the tectal neuropil highlighting the layered innervation of RGC. Scale bar represents 20 μ m. (D) Examples of RGCs identified by layer specific innervation of tectal layers and arborization fields (AFs). Scale bar represents 20 μ m. (E) Overlay of temporal (magenta) and nasal (cyan) RGCs in the retina (bottom left) and tectal neuropil (top left to bottom right). All scale bars represents 100 μ m. (F) Overlay of ventral (magenta) and dorsal (cyan) RGCs in the retina (bottom left) and tectal neuropil (top left to bottom right). All scale bars represents 100 μ m. A, anterior; AF1, arborization field 1; AF2, arborization field 2; AF4, arborization field 4; AF7, arborization field 7; AF9, arborization field 9; D, dorsal; P, posterior; SAC/SPV, boundary between the stratum album centrale and the stratum periventriculare; SFGS 1-3, stratum fibrosum et griseum superficiale 1-3; SFGS 4-6, stratum fibrosum et griseum superficiale 4-6; SO, stratum opticum; V, ventral.

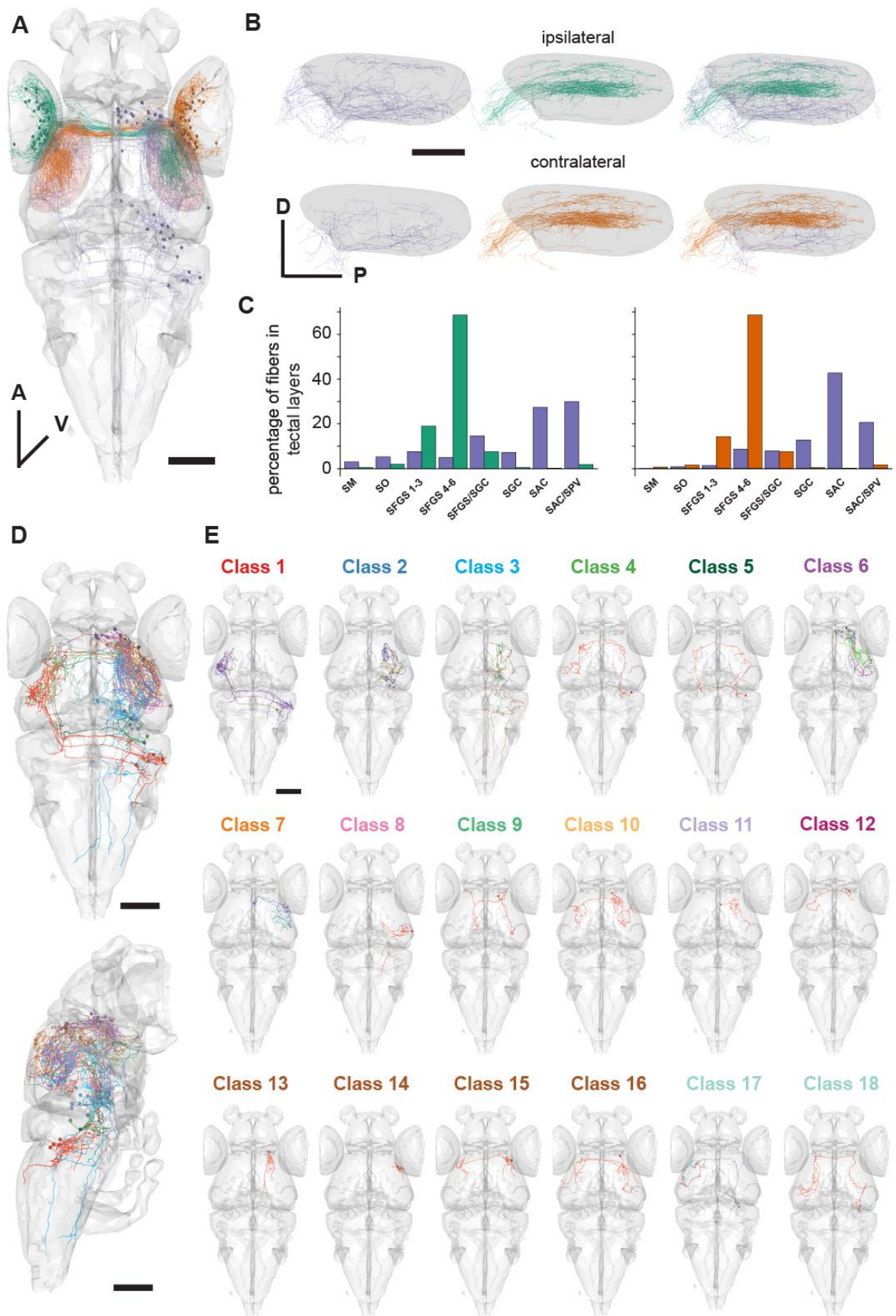


Figure 4: Analysis of non-retinal tectal afferents. **(A)** Overlay of all RGCs mirrored to the right (orange) and left (green) hemisphere and all non-retinal afferents (purple) mirrored to the right hemisphere in outline of standard brain (grey). **(B)** Lateral view of the tectal neuropil highlighting the anatomical segregation of retinal and non-retinal input to the ipsi- and contralateral tectum. Scale bar represents 50 μm . **(C)** Bar plots displaying the percentage of overall fiber length in the different layers of the ipsi- and contralateral tectum for retinal (green and orange) and non-retinal afferents (purple). **(D)** Overlay of all non-retinal afferents mirrored to the right hemisphere in outline of standard brain (grey). Different colors represent the different classes. All scale bars represent 100 μm . **(E)** Individual classes of non-retinal afferents displayed side-by-side in outline of standard brain (grey). Scale bar represents 100 μm . A, anterior; AF1, arborization field 1; AF2, arborization field 2; AF4, arborization field 4; AF7, arborization field 7; AF9, arborization field 9; D, dorsal; P, posterior; SAC, stratum album centrale; SAC/SPV, boundary between the stratum album centrale and the stratum periventriculare; SFGS, stratum fibrosum et griseum superficiale; SFGS/SGC, boundary between the stratum fibrosum et griseum superficiale and the stratum griseum centrale; SM, stratum marginal; SO, stratum opticum; V, ventral.

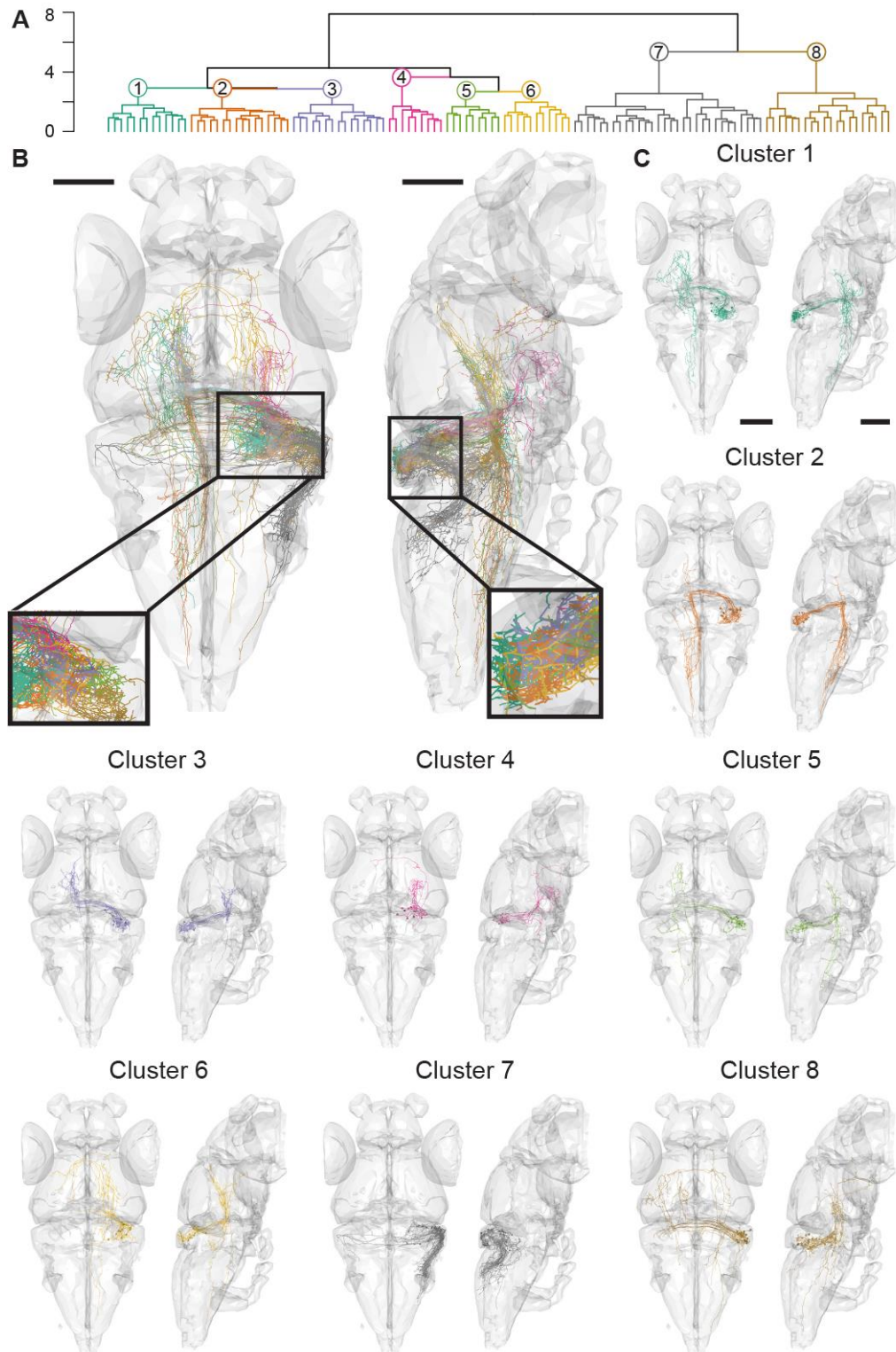


Figure 5: Topographic organization of cerebellar output. (A) Hierarchical clustering (HC) of cerebellar efferents based on NBLAST similarity scores. Colors indicate the different clusters. (B) Overlay of all cerebellar efferents mirrored to the right hemisphere in outline of standard brain (grey). Different colors represent the different clusters from (A). Black rectangles represent regions zoomed in. Purkinje cells (cluster 7) were omitted for clarity. (C) Individual classes of cerebellar efferents displayed side-by-side in outline of standard brain (grey). All scale bars represent 100 μ m. A, anterior; P, posterior; V, ventral.

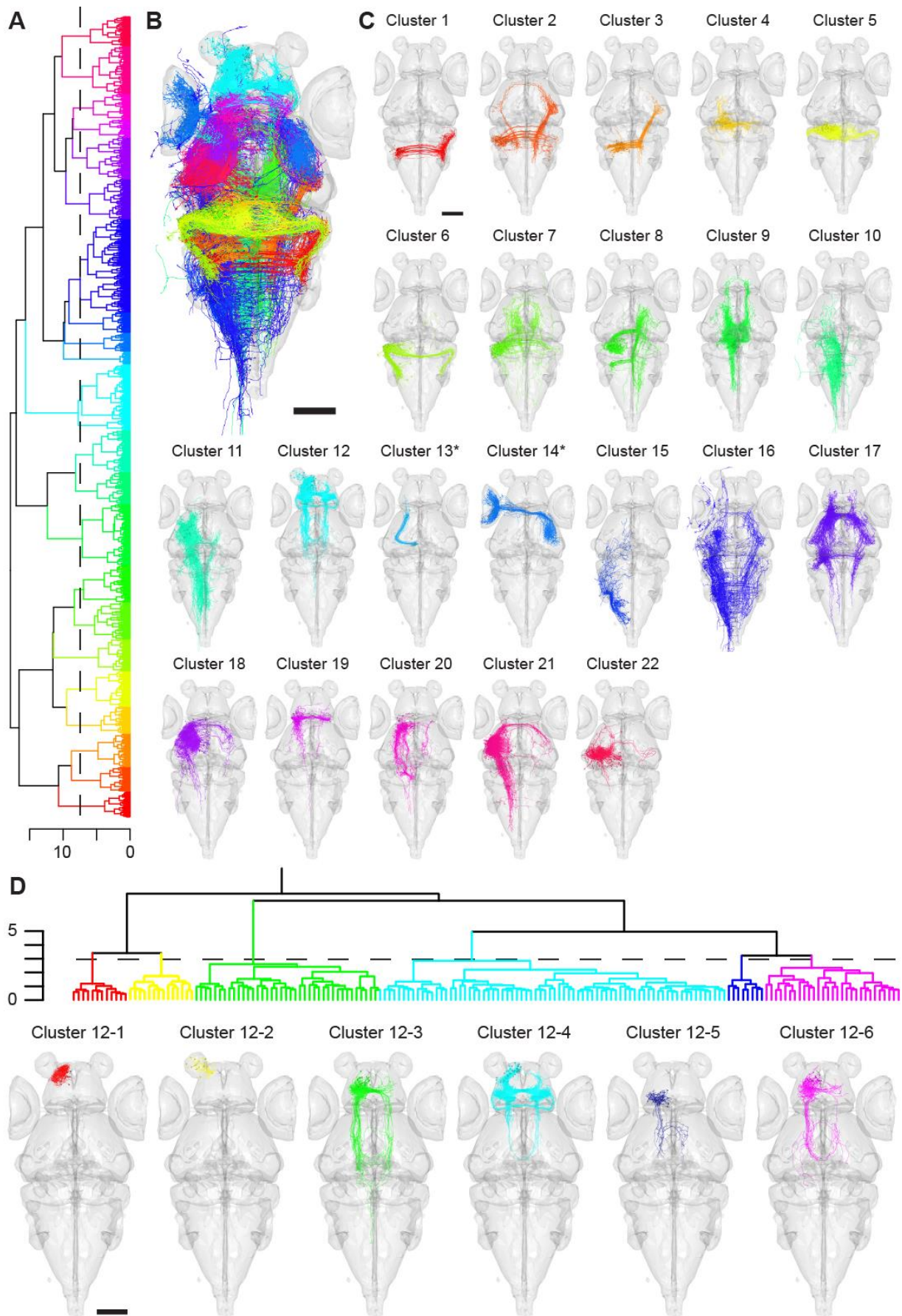


Figure 6: Organization and classification of neurons using NBLAST. (A) HC of all neurons based on NBLAST similarity scores. Colors indicate the different clusters. Dashed line indicates the height at which the dendrogram, was cut. **(B)** Overlay of all neurons mirrored to the right hemisphere in outline of the standard brain (grey). Different colors represent the different clusters from (A). **(C)** Individual clusters of neurons displayed side-by-side in outline of the standard brain (grey). Asterisks denote cluster of known cell types. **(D)** HC of neurons from cluster 12 in (C). Colors indicate the different clusters. Dashed line indicates the height at which the dendrogram was cut. All scale bar represent 100 μm . A, anterior; V, ventral.

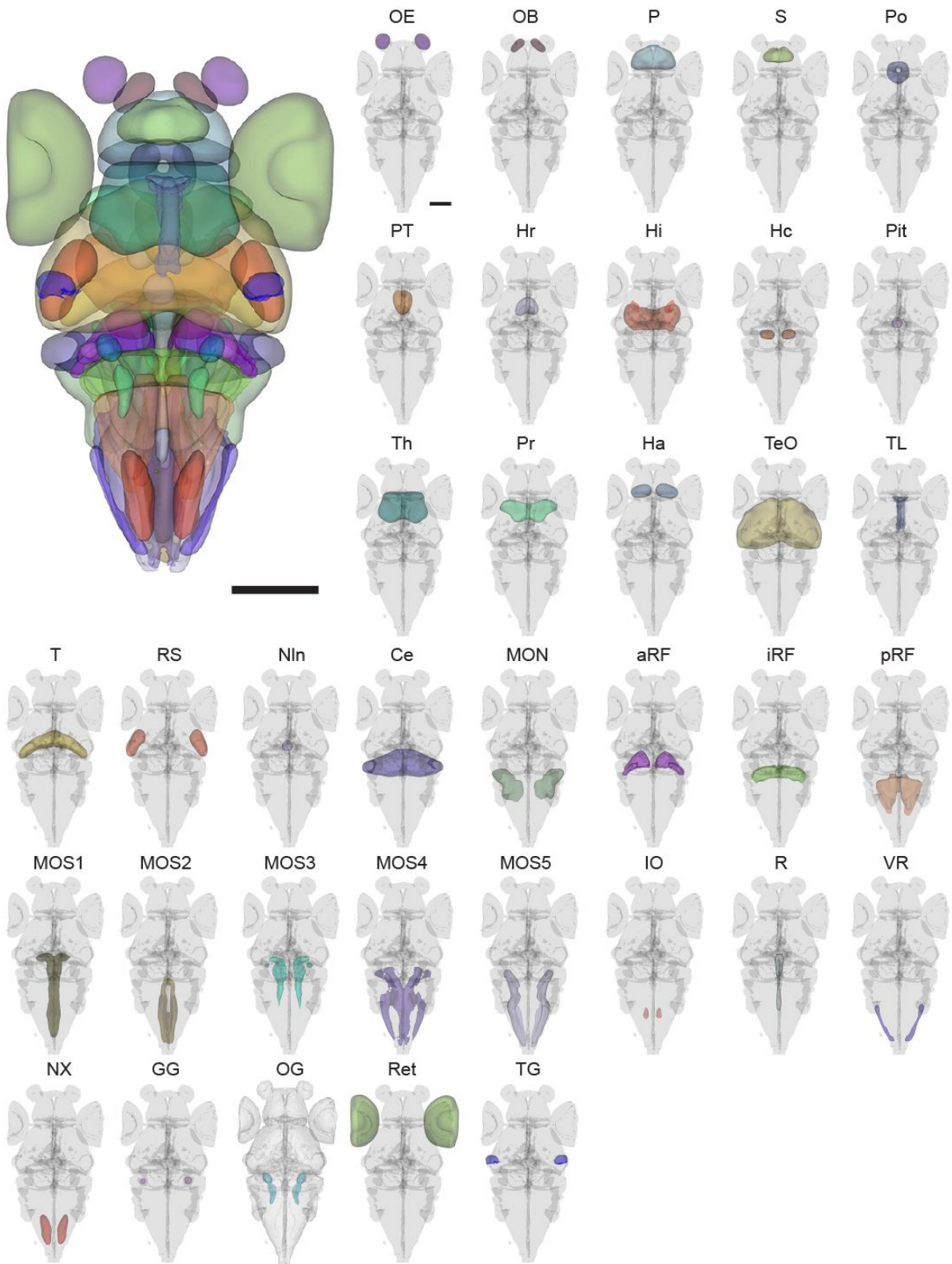


Figure 7: Brain annotation for graph theoretical analysis. 36 brain regions were manually defined. Different colors for the brain regions are selected randomly. For explanation of brain region abbreviations see Table S1. All scale bars represent 100 μ m.

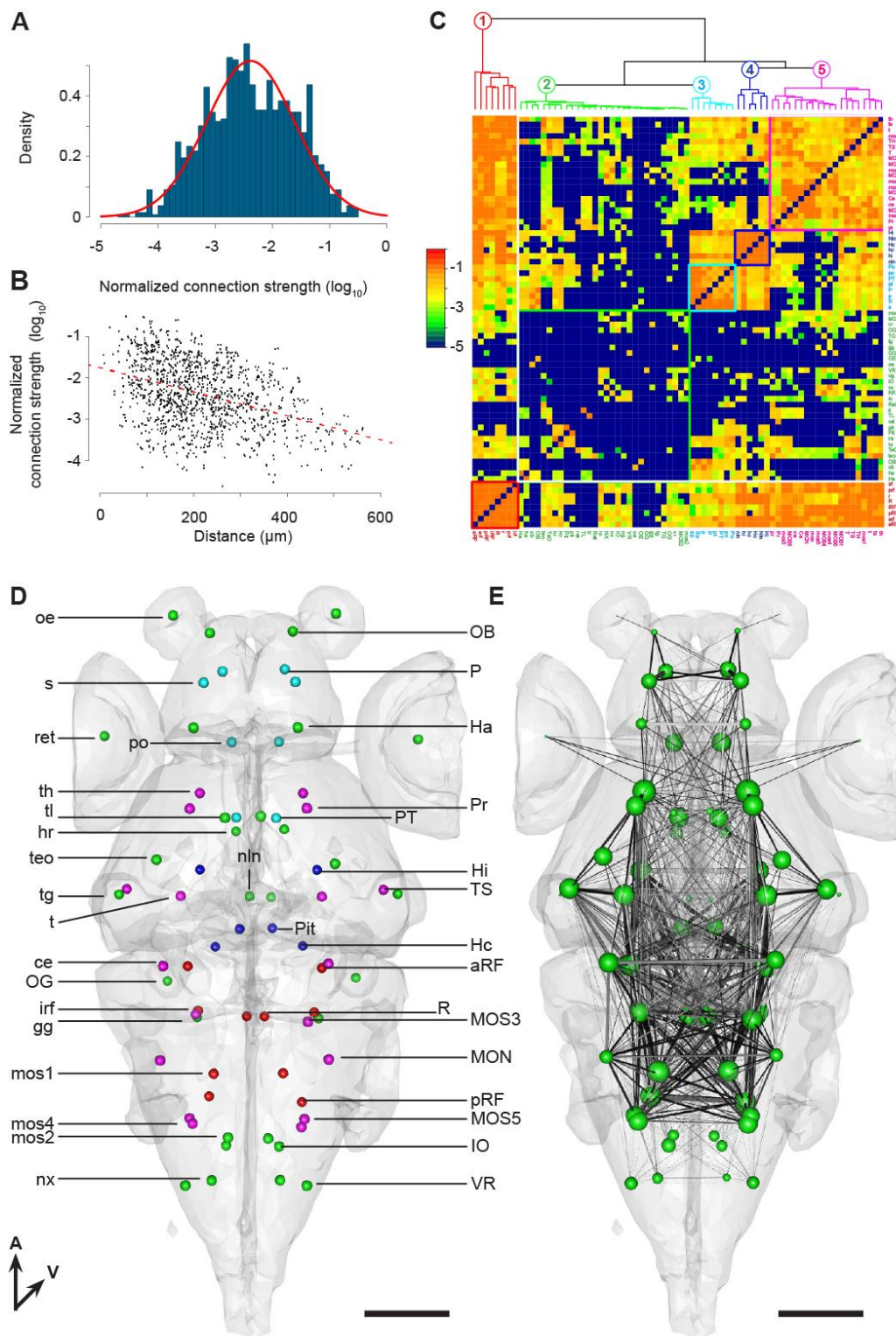


Figure 8: A brain-wide wiring diagram of the larval zebrafish brain. **(A)** Distribution of normalized connection strengths between brain regions. **(B)** Correlation between internodal distance and normalized connection strength. **(C)** Inter-region connectivity matrix of the larval zebrafish brain, derived from normalized connection strengths between brain regions. Brain regions in lowercase are located in the left hemisphere and brain regions in uppercase on the right. Brain regions with similar connection profile are clustered together. For explanation of brain region abbreviations see Table S1. **(D)** Brain regions displayed as center of masses in outline of standard brain (grey). Colors represent cluster from (C). For explanation of brain region abbreviations see Table S1. **(E)** Brain-wide wiring diagram of the larval zebrafish brain. Location of brain regions is the same as in (D). Size of nodes reflects the node degree and thickness of edges the normalized connection strengths. All scale bar represents 100 μm . A, anterior; V, ventral.

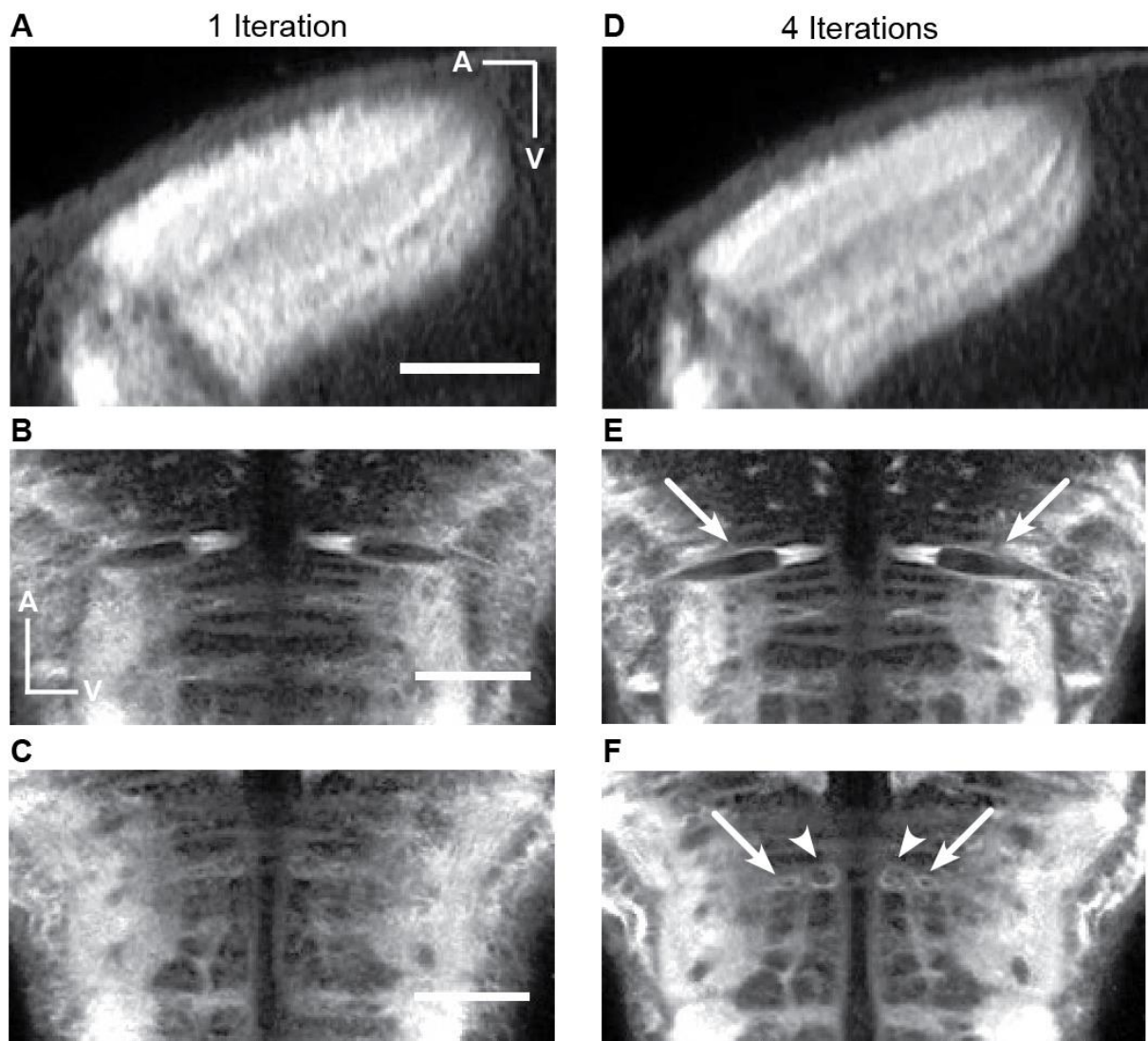
Supplementary Information

Figure S1. Related to Figure 1: Improvement of granularity of the shape-based average brain after multiple iterations. (A-C) Single optical slices through the tectum (A) and the hindbrain (B and C) after one iteration. All scale bars represent 50 μm . (D-E) Single optical slices through the tectum (A) and the hindbrain (B and C) after four iterations. In the case of the tectum, individual tectal layers become more obvious and clearer after 4 iterations compared to one. Arrows in (B) highlight the Mauthner cells. Arrows and arrowheads in (C) highlight additional identifiable reticulospinal neurons. In both cases the neurons become either more sharply defined (B), or in the case of (C), only are recognizable after multiple iterations.

Figure S2 - related to Figure 1

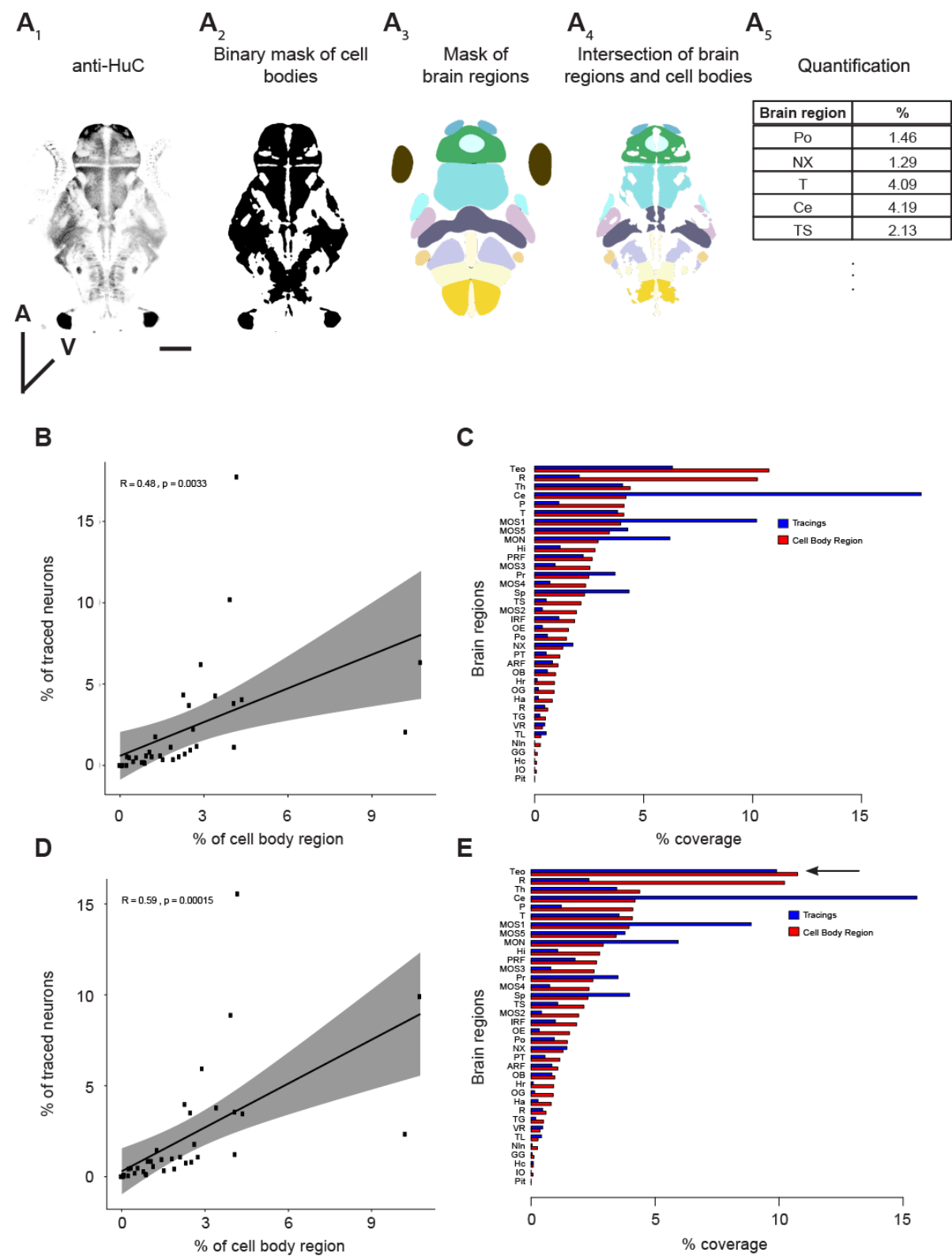


Figure S2. Related to Figure 1: Analysis of labeling bias. (A) Workflow to calculate the expected relative contribution of each brain region to the single-neuron database. Neuronal cell bodies were labeled using an antibody directed against the post-mitotic marker HuC/D (A_1). The staining was converted into a binary mask (A_2) and this mask was intersected with a mask of 36 brain regions (A_3). The result of this intersection is a mask that contains only the cellular portions of each brain region (A_4). Based on this, we calculated the volume of each brain region in relation to the total volume (A_5). Scale bar represents 100 μm . **(B and C)** Scatterplot (B) and barplot (C) showing correlation between the cell body region and the soma of traced neurons for individual brain regions for the pan-neuronal dataset. **(D and E)** Same as in B and C but for the complemented dataset.

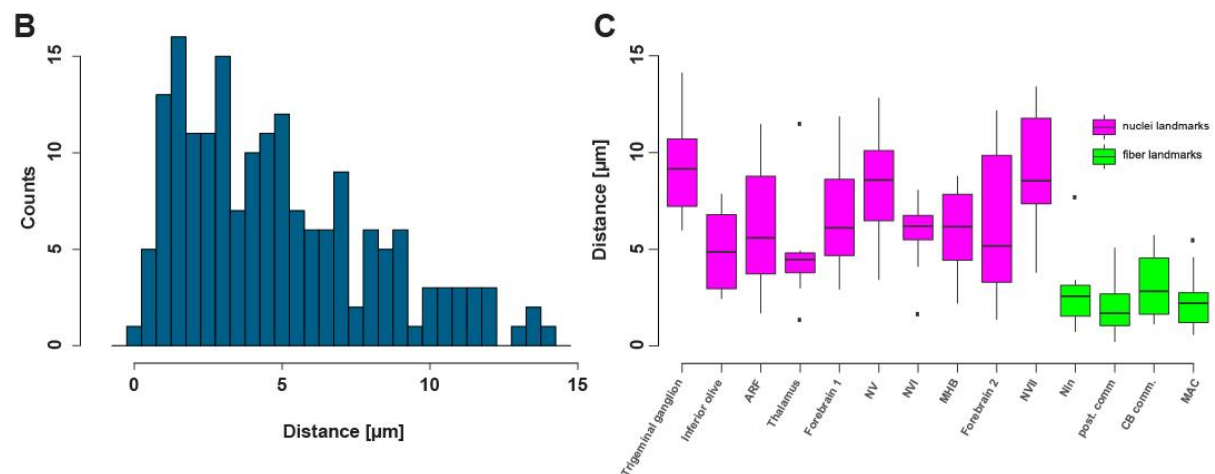
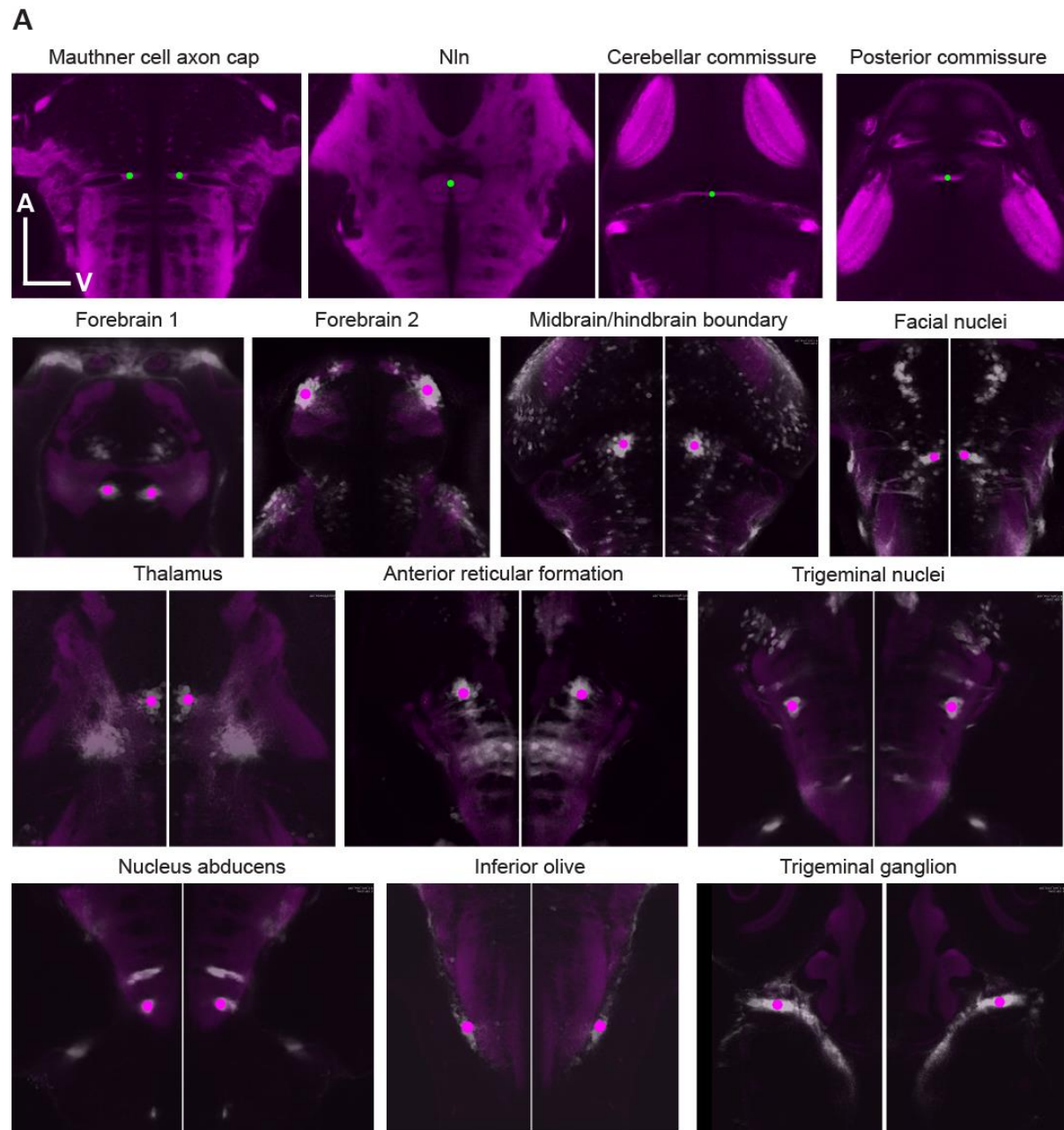


Figure S3. Related to Figure 3: Location of fiducial points used for measurement of registration accuracy. (A) Single optical planes throughout the SYP-standard brain as well as through multiple different average Gal4-pattern indicating the location of the fiducial points (fiber landmarks are in green and nuclei landmarks are in magenta). (B) Histogram of all distances measured between fiducial points aligned to the standard brain and their respective counterpart in the standard brain. (C) Boxplot indicating the alignment accuracy for the individual fiducial points. Magenta refers to nuclei (Gal4-pattern) based landmarks and green to fiber (SYP-pattern) based landmarks.

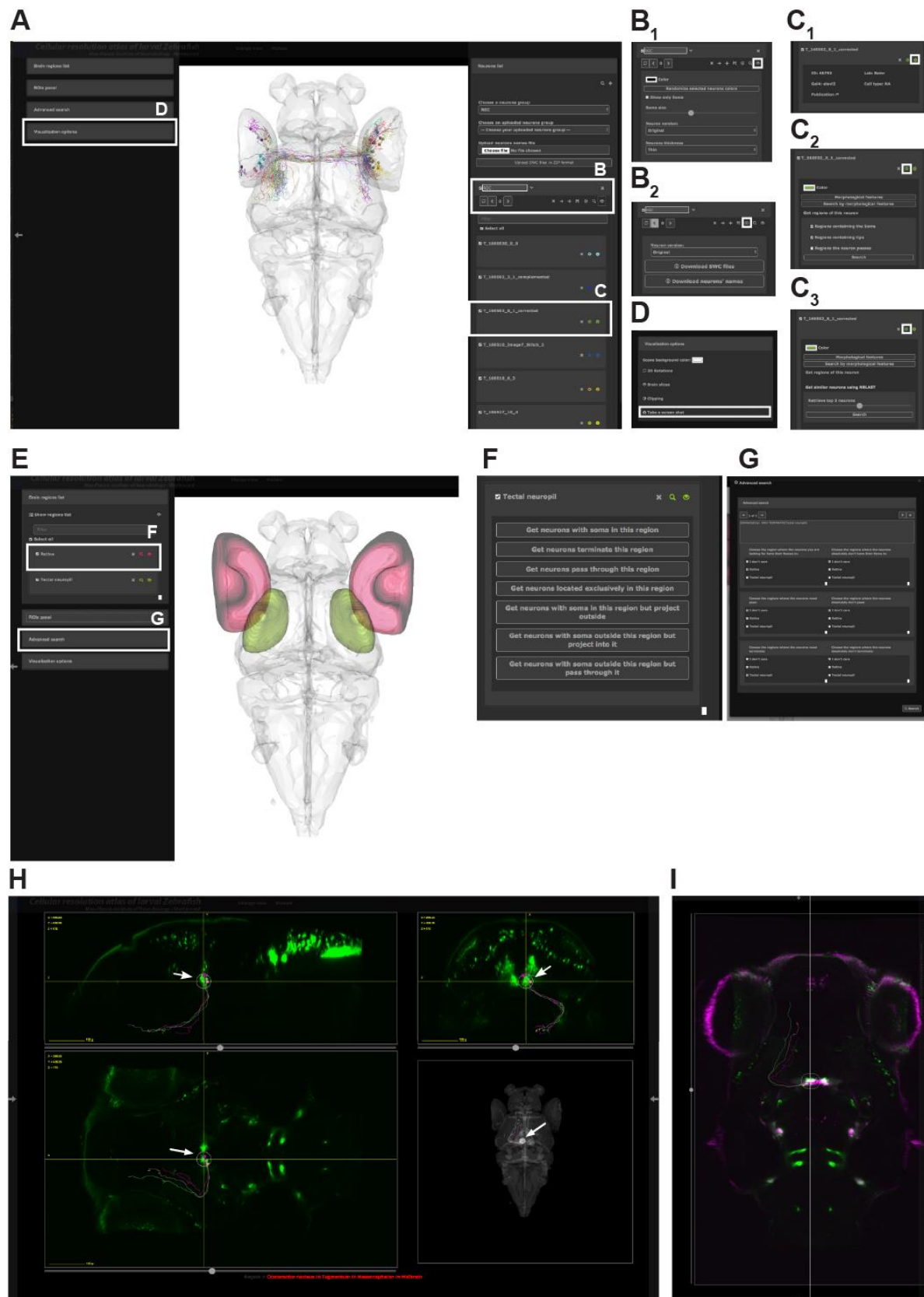


Figure S4. Related to Figure 3: An interactive web-portal to explore single neuron data. (A)

Interactive 3D viewer showing individual RGCs. White boxes indicate specific submenus to manipulate neurons and letters refer to figure panels with further explanation. **(B-D)** Specific submenus highlighted in (A). White box indicates icon that needs to be clicked to expand the menu and show option. **(B)** Manipulation of entire neuron groups. **(B₁)** Visualization options for all selected neurons in a group. Users can change the color, show only the soma and also change the size of the displayed soma, flip the entire group to one hemisphere and adjust the thickness level of neurites. **(B₂)** All selected neurons can be either downloaded as .swc files or their names can be downloaded into a text file that can be later uploaded to our website to only display those neurons. When downloading the tracings as a .swc file, the user can choose to download them in their original state or flipped to one of the two hemispheres. **(C)** Manipulation of single neuron tracings. **(C₁)** Each neuron has metadata attached to it including a unique ID, the lab of origin, the Gal4-line that drove expression in that neuron, the cell-type (if already known), as well as the publication (in the form of a hyperlink), in which the tracing was originally described. **(C₂)** For each individual neuron it is possible to display the brain regions innervated by it. Users can limit their search to specific parts of the neuron. **(C₂)** Once a neuron of interest was found users, can look for neurons with a similar morphology using NBLAST. **(D)** Users can export the current 3D view by taking a screenshot and saving the image to their hard drive. **(E-G)** Atlas based search functions. **(E)** Interactive 3D viewer showing selected brain regions. In this case we chose the retina (red) and tectal neuropil (green). White boxes indicate specific submenus to manipulate search function and letters refer to figure panels with further explanation. **(F)** Options to search for neurons in a single brain region. **(G)** Advanced search options for multiple brain regions. Users can perform simple AND/OR search functions and can specify to only for search for specific parts of the neuron in each brain region. **(H)** User-defined ROI search function guided by a specific expression pattern. In this case we used *Chat:Gal4* to visualize cranial nuclei in green. Arrows indicate the position of the ROI in the oculomotor nuclei with the accompanying oculomotor neurons resulting from a search for neurons with their soma within that ROI. **(I)** Overlay of *Chat:Gal4* and *isl1:GFP*.

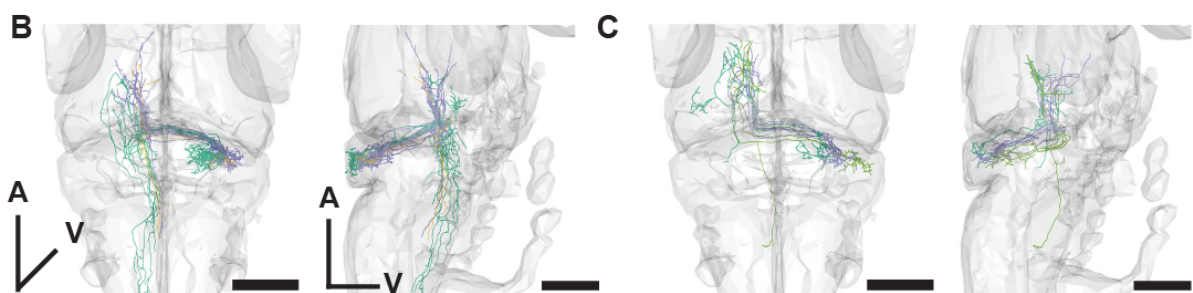
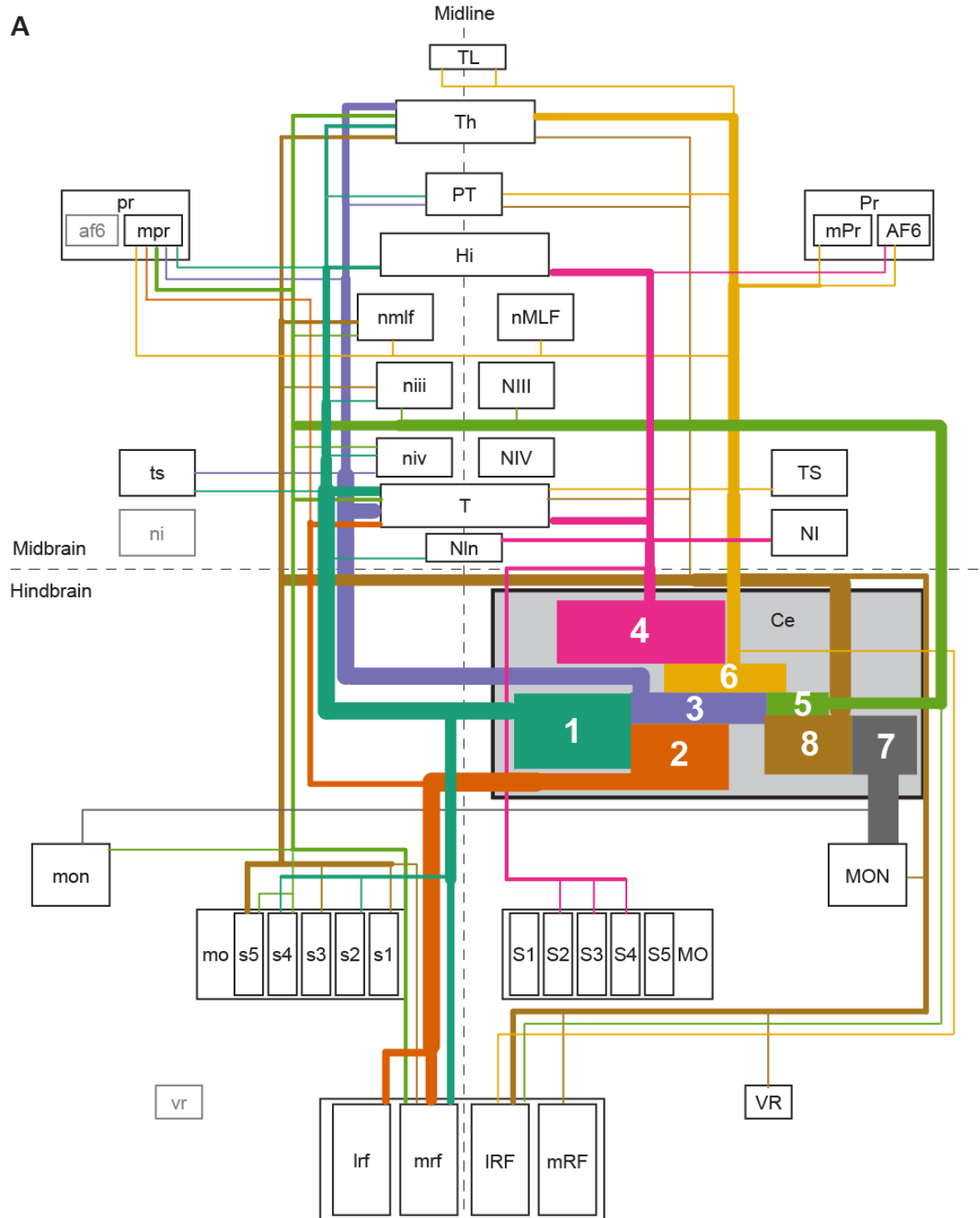


Figure S6. Related to Figure 5: Wiring diagram for cerebellar efferents. (A) The coloring scheme reflects the different classes and is the same as in Fig. 5. Line thickness is proportional to the number of neurons per class. Light grey regions receive only ipsilateral input. AF6, arborization field 6; Ce, cerebellum; Hi, intermediate hypothalamus; IO, inferior olive; IRF, lateral reticular formation; M3, migrated area of eminentia thalami; MO, medulla oblongata; MON, medial octavolateralis nucleus; mPR, medial pretectum; mRF, medial reticular formation; NI, nucleus isthmi; NIII, oculomotor nucleus; NIV, trochlear nucleus; NIn, interpeduncular nucleus; MLF, nucleus of the medial longitudinal fascicle; PO, preoptic area; PT, posterior tuberculum; RF, reticular formation; S1, stripe 1 of MO; S2, stripe 2 of MO; S3, stripe 3 of MO; S4, stripe 4 of MO; S5, stripe 5 of MO; T, tegmentum; Th, thalamus; TL, torus longitudinalis; TS, torus semicircularis; VR, vagal region. **(B)** Example of topographical mapping between the cerebellum and the tegmentum. All scale bars represent 100 μm . **(C)** Example of convergence of inputs from multiple clusters in the thalamus. All scale bars represent 100 μm .

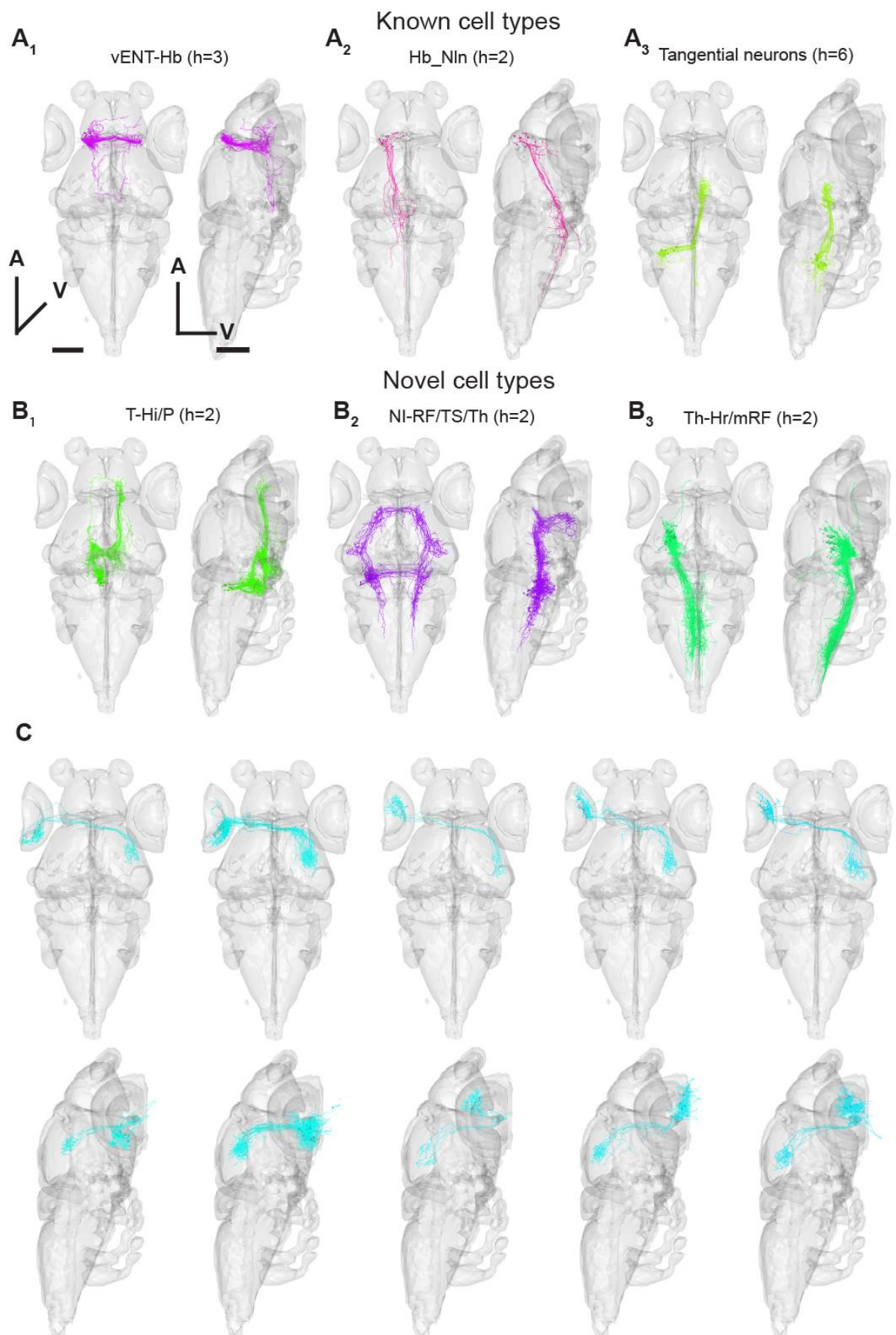


Figure S7. Related to Figure 6: Application of NBLAST to organize neurons. (A) Examples of previously described neurons that could be discovered by hierarchical clustering of NBLAST similarity score. The value in the brackets indicates at which dendrogram height the described cluster first appears. All scale bars represent 100 μm . **(B)** Examples of previously undescribed types of neurons. The names indicate the soma location as well as the innervation patterns of the fibers. The value in the brackets indicates at which dendrogram height the described cluster first appears. **(C)** Further subdividing the RGC cluster (Cluster 14 in Fig. 6B) leads to artificial types that are mainly characterized based on their retinotopic organization and not on their specific innervation of AFs and tectal layers.

Table S1. Related to Figure 8: Summary of brain regions.

Brain region	Origin	X	Y	Z	Abbr.	Vol
L_Cerebellum	Wullmann and Mueller (2005)	187	504	260	ce	1087593
R_Cerebellum	Wullmann and Mueller (2005)	383	507	260	Ce	1139670
L_Glossopharyngeal ganglion	Wullmann and Mueller (2005)	164	566	40	gg	23784
R_Glossopharyngeal ganglion	Wullmann and Mueller (2005)	409	570	40	GG	9314
L_Habenula	Wullmann and Mueller (2005)	222	229	233	ha	239132
R_Habenula	Wullmann and Mueller (2005)	342	228	233	Ha	198323
L_Medulla Oblongata strip 1	Kinkhabwala et al., 2011	243	640	245	mos1	601111
R_Medulla Oblongata strip 1	Kinkhabwala et al., 2011	327	641	245	MOS1	691010
L_Medulla Oblongata strip 2	Kinkhabwala et al., 2011	260	710	279	mos2	273669
R_Medulla Oblongata strip 2	Kinkhabwala et al., 2011	308	710	279	MOS2	294387
L_Medulla Oblongata strip 3	Kinkhabwala et al., 2011	216	585	209	mos3	359462
R_Medulla Oblongata strip 3	Kinkhabwala et al., 2011	352	577	209	MOS3	341466
L_Medulla Oblongata strip 4	Kinkhabwala et al., 2011	216	686	281	mos4	453697
R_Medulla Oblongata strip 4	Kinkhabwala et al., 2011	353	686	281	MOS4	529316
L_Medulla Oblongata strip 5	Kinkhabwala et al., 2011	220	694	286	mos5	559564
R_Medulla Oblongata strip 5	Kinkhabwala et al., 2011	349	691	286	MOS5	567318
L_Medial octavolateral nucleus	Liao and Haehnel (2012)	187	611	292	mon	457585
R_Medial octavolateral nucleus	Liao and Haehnel (2012)	384	612	292	MON	461773
L_Octaval ganglion	Wullmann and Mueller (2005)	196	556	100	og	64702
R_Octaval ganglion	Wullmann and Mueller (2005)	374	554	100	OG	59294
L_Olfactory bulb	Wullmann and Mueller (2005)	233	121	150	ob	163004
R_Olfactory bulb	Wullmann and Mueller (2005)	333	122	150	OB	165214
L_Olfactory epithelium	Wullmann and Mueller (2005)	183	101	118	oe	256155
R_Olfactory epithelium	Wullmann and Mueller (2005)	381	101	118	OE	236153
L_Pallidum	Wullmann and Mueller (2005)	228	180	177	p	736075
R_Pallidum	Wullmann and Mueller (2005)	338	180	177	P	728949
L_Pituitary	Wullmann and Mueller (2005)	270	458	55	pit	29676
R_Pituitary	Wullmann and Mueller (2005)	299	457	55	Pit	39978
L_Posterior tuberculum	Wullmann and Mueller (2005)	258	348	108	pt	241444
R_Posterior tuberculum	Wullmann and Mueller (2005)	307	347	108	PT	220375
L_Raphe nucleus	Wullmann and Mueller (2005)	271	587	169	r	141165
R_Raphe nucleus	Wullmann and Mueller (2005)	294	588	169	R	150970
L_Retina	Wullmann and Mueller (2005)	84	255	93	ret	4658432
R_Retina	Wullmann and Mueller (2005)	474	248	93	Ret	3805342
L_Tegmentum	Wullmann and Mueller (2005)	199	436	188	t	683361
R_Tegmentum	Wullmann and Mueller (2005)	370	435	188	T	676192
L_Thalamus	Wullmann and Mueller (2005)	220	312	179	th	984842
R_Thalamus	Wullmann and Mueller (2005)	345	311	179	Th	946196
L_Torus longitudinalis	Wullmann and Mueller (2005)	262	326	294	tl	58442
R_Torus longitudinalis	Wullmann and Mueller (2005)	303	328	294	TL	46938
L_Torus semicircularis	Wullmann and Mueller (2005)	126	433	157	ts	450263
R_Torus semicircularis	Wullmann and Mueller (2005)	440	431	157	TS	455121
L_Trigeminal ganglion	Wullmann and Mueller (2005)	109	446	101	tg	81547
R_Trigeminal ganglion	Wullmann and Mueller (2005)	458	445	101	TG	65532
L_Vagal region	Wullmann and Mueller (2005)	214	762	297	vr	76777
R_Vagal region	Wullmann and Mueller (2005)	357	763	297	VR	49632
L_Anterior reticular formation	This study	201	528	165	arf	468685
R_Anterior reticular formation	This study	366	526	165	ARF	462227
L_Caudal hypothalamus	Wullmann and Mueller (2005)	229	515	90	hc	124595
R_Caudal hypothalamus	Wullmann and Mueller (2005)	340	516	90	Hc	128417
L_Inferior olive	Wullmann and Mueller (2005)	254	745	199	io	10891
R_Inferior olive	Wullmann and Mueller (2005)	319	744	199	IO	12492
L_Intermediate hypothalamus	Wullmann and Mueller (2005)	209	417	96	hi	1072225
R_Intermediate hypothalamus	Wullmann and Mueller (2005)	357	416	96	HI	1032515
L_Intermediate reticular formation	This study	210	583	168	irf	511321
R_Intermediate reticular formation	This study	354	581	168	IRF	519884
L_Interpeduncular nucleus	Wullmann and Mueller (2005)	304	484	140	nln	94181
R_Interpeduncular nucleus	Wullmann and Mueller (2005)	263	483	140	Nln	94691
L_Posterior reticular formation	This study	225	693	183	prf	657919
R_Posterior reticular formation	This study	341	686	183	PRF	650094
L_Preoptic region	Wullmann and Mueller (2005)	254	256	106	po	270516
R_Preoptic region	Wullmann and Mueller (2005)	313	256	106	PO	263312
L_Pretectum	Wullmann and Mueller (2005)	214	325	221	pr	439624
R_Pretectum	Wullmann and Mueller (2005)	352	325	221	Pr	422166
L_Rostral hypothalamus	Wullmann and Mueller (2005)	253	370	63	hr	195773
R_Rostral hypothalamus	Wullmann and Mueller (2005)	314	372	63	Hr	188048
L_Subpallidum	Wullmann and Mueller (2005)	245	167	113	s	413101
R_Subpallidum	Wullmann and Mueller (2005)	322	169	113	S	434308
L_Tectum	Wullmann and Mueller (2005)	179	386	257	teo	3235995
R_Tectum	Wullmann and Mueller (2005)	388	381	257	TeO	3170917
L_Vagus motor neurons	Wullmann and Mueller (2005)	245	756	298	nx	170538
R_Vagus motor neurons	Wullmann and Mueller (2005)	326	757	298	NX	188491

Video S1. Related to Figure 1: 3D rotation of all neurons generated by our workflow which are aligned to our standard brain.*

Video S2. Related to Figure 3: Tutorial video demonstrating how to visualize and manipulate neurons using our interactive web-browser.*

Video S3. Related to Figure 3: Tutorial video demonstrating how to search for neurons using our pre-defined brain annotation.*

Video S4. Related to Figure 3: Tutorial video demonstrating how to interactively search for neurons using custom ROI and expression pattern.*

Video S5. Related to Figure 6: 3D rotation of all neurons color coded according to cluster identity from Figure 6.*

Video S6. Related to Figure 8: 3D rotation showing the centroids of brain regions used for generating the brain-wide wiring diagram. Centroids are color coded according to cluster identity from Figure 8C.*

Video S7. Related to Figure 8: 3D rotation of brain-wide wiring diagram shown in Figure 8E.*

*For videos, please refer to the online version of the manuscript, once published.

STAR Methods

CONTACT FOR REAGENT AND RESOURCE SHARING

Further information and requests for resources and reagents should be directed to and will be fulfilled by the Lead Contact, Herwig Baier (hbaier@neuro.mpg.de).

EXPERIMENTAL MODEL AND SUBJECT DETAILS

For all experiments in this study we used 5-7 days post fertilization (d.p.f.) larvae. At this stage, the sex of the larvae is not defined. All animal procedures conformed to the institutional guidelines set by the Max Planck Society and were carried out in accordance with an animal protocol approved by the regional government (Regierung von Oberbayern).

Zebrafish procedures and lines

Fish were raised at 28°C on a 14h light/10h dark cycle in Danieau's solution (17 mM NaCl, 2 mM KCl, 0.12 mM MgSO₄, 1.8 mM Ca(NO₃)₂, 1.5 mM HEPES). Pigmented larvae destined to be imaged were kept in Danieau's solution containing 0.003% 1-phenyl-2-thiourea from the age of 24 hpf (hours post-fertilization) to inhibit melanogenesis. For single neuron labeling, the transgenic fish line: *Tg(brn3c:GAL4, UAS:gap43-GFP)s318t* (BGUG) was crossed to either transgenic fishline *Tg(elavl3:Gal4)zf349* or *Tg(Et(e1b:GAL4)s1101t*. These larvae were subsequently PACT cleared, immunostained and imaged as fixed samples (see below). To establish a segmented brain atlas as well as to align the expression patterns of various transgenic fish lines to our standard brain, *Tg(elavl3:lyn-tagRFP)mpn404* and *Tg(actb2:loxP-eGFP-loxP-lynTagRFPT)y272* were crossed to transgenic Gal4 lines from <https://fishatlas.neuro.mpg.de/zebrafishatlas/> and the following transgenic fish lines: *Tg(elavl3:nlsGCaMP6s)mpn400*, *Tg(elavl3:Hsa.H2B-GCaMP6s)* and *Tg(elavl3:GCaMP5G)a4598*. These larvae were imaged live (see below).

METHOD DETAILS

PACT tissue clearing

At 6 dpf, larvae were anesthetized in a lethal dose of tricaine for 5 minutes and thereafter transferred into 10 ml ice-cold PACT hydrogel monomer solution A₄P₄ (4% acrylamide and 4% paraformaldehyde in PBS) supplemented with 0.25% VA-044, and kept at 4°C over night. For degassing, samples were placed with an open lid in a desiccation chamber filled with dry ice. Oxygen was removed via a vacuum pump and the desiccation chamber was thereafter transferred to a 55-60°C water bath so the dry ice would melt and fill the chamber with CO₂. After all oxygen was

replaced by CO₂, the tube lid was closed, avoiding any exposure to oxygen, and the tubes were removed from the desiccation chamber and placed on a shaker at 37°C for two hours to facilitate the polymerization of the hydrogel. Samples were transferred from the hydrogel solution and put into 50 ml canonical tubes containing clearing solution (4% SDS and 200 mM boric acid in dH₂O) and kept at 37°C for 5-6 days under gentle shaking. During the clearing step, the solution was changed every other day. Once clearing was complete, samples were washed 3 times for 10 minutes in PBT and thereafter kept in PBT at 4°C over night or longer.

Immunocytochemistry

Samples were incubated in 150 mM Tris-HCl, pH 9, for 5 min at room temperature followed by 15 min at 63 °C for antigen retrieval. Larvae were washed again in PBT prior to a 45 min digest with Trypsin EDTA (1x Trypsin-EDTA Solution, Sigma, diluted 1:20) on ice. PBT-washed larvae were blocked in 5% goat serum, 1% BSA, and 1% DMSO in PBT. Primary antibodies were added in blocking solution for 5 days. Secondary antibodies were Alexa-conjugates (Invitrogen) and added 1:300 in PBT for 3-4 days at 4 °C. Washed samples were postfixed for 45 min in 4% paraformaldehyde at room temperature, rinsed, and thereafter transferred to 87% glycerol.

Imaging and tracing

For live imaging, 6–7 dpf larvae were anesthetized in 0.016% tricaine and embedded in 2% low-melting-point agarose. Imaging was performed on a Zeiss LSM-780, a LSM-700, or a Leica SP8 confocal microscope, using a 20×/1.0 NA water-dipping objective. For imaging fixed samples, larvae were embedded in 87% glycerol, and imaging was performed at a Zeiss LSM-780 using a 25×/0.8 NA multi-immersion objective. In both cases, whole-brain images were acquired by tiling the brain into two individual image stacks along the anterior posterior axis and subsequently stitched, using either ZEN software (black edition, v8.0; Zeiss) or LAS X on the SP8. Images were corrected for fluorescence attenuation in the z-dimension using the brightness correction function in the respective software. Samples used for single neuron tracing were scanned at a resolution of 0.3×0.3×0.3µm (xyz), while Gal4 expression pattern were scanned with isotropic voxel size of 1µm.

Individual neurons were semi-automatically traced using the freeware NeuTube (Feng et al., 2015) and saved as individual swc files (Cannon et al., 1998). In total, we scanned 1278 fish for a total of 1955 tracings (1.53 tracings per fish).

Template generation and image registration

For the original template we generated an unbiased shape-based average template by using `antsMultivariateTemplateConstruction2.sh` (Avants et al., 2010), a shell script in the Advanced Normalization Tools (ANTs) software. We chose 12 representative brains stained for the presynaptic marker Synapsin (SYP). This process is iterative and leads to an improvement in template quality with each iteration. A template after a single iteration (Figure 1C₁; Figure S1A-C) already displays marked improvements compared to each of the individual fish that were used to generate the average brain by cancelling out/removing the deformations introduced by our PACT protocol. However, despite these advantages, the template appears to be blurry and it is hard to discern finer anatomical details. For example, it is very difficult to recognize the neuropil of the torus longitudinalis (TLn; Figure 1C₁, inset) or the individual layers of the optic tectum (Figure S1A) as well as individual identifiable cells of the reticulospinal system (e.g. Mauthner cells; Figure S1B, C). After four iterations (Figure 1C₂; Figure S1D-F) the general appearance of the template was markedly improved, as evidenced by the clear emergence of the TLn (Figure 1C₂, inset) as well as the individual tectal layers (Figure S1D) and reticulospinal neurons. (Figure S1E, F). Additional reference stains were imaged with a second channel containing a marker already present in our common coordinate framework and this marker was used as a bridge to our template space. Brain with single-neuron labeling were aligned to our standard brain using either SYP, HuC/D, or ERK1/2 or a combination thereof using the parameters for fixed samples described in (Marquart et al., 2017) using the `antsRegistration` function in ANTs. Single neuron tracings were aligned using the `antsApplyTransformToPoints` function. The quality of alignment is strongly dependent on the original image quality. Furthermore, the image quality can be vastly different between brain regions in an individual fish. To ensure that alignment quality of neurons is high, aligned brains were manually scored by expert analysts and only neurons that innervated regions that were deemed as successfully aligned were used for further analysis.

For alignment of GAL4 pattern imaged live we generated a shape based average templates of the transgenic lines *Tg(elavl3:lyn-tagRFP)mpn404* and *Tg(actb2:loxP-eGFP-loxP-lynTagRFPT)y272* using the procedure described above. Gal4 lines were crossed to one of those references and to either *Tg(UAS:Dendra-kras)s1998t*, *Tg(5xUAS:EGFP)* or, *Tg(UAS-E1b:NFSB-mCherry)* to visualize Gal4 expression patterns. For each line we imaged 3-6 larvae and generated a shape-based average brain. We aligned both the types of images of the individual brains as well as the shape-based averages to our live template brain. We again used the optimal parameters for alignment of live-images as described previously (Marquart et al., 2017). To compare Gal4-expression obtained through live imaging with single-neuron data from fixed samples we generated a bridging registration between

live and fixed. We chose four lines (*TgBAC(vglut2a[slc17a6b]:loxP-DsRed-loxP-GFP)nns9*, *Tg(tph2:nfsB-mCherry)y226*, *Tg(elavl3:lyn-tagRFP)mpn404*, *Tg(isl1:GFP)*) that displayed similar expression when imaged live or after fixation, clearing, and staining. We used a similar approach to integrate our Gal4 database with the Z-Brain and zebrafish brain browser (ZBB). We chose four lines present in the ZBB database (*Tg(elavl3:nlsmCardinal)*, *TgBAC(gad1b:GFP)*, *Tg(isl1:GFP)*, *TgBAC(vglut2a[slc17a6b]:loxP-DsRed-loxP-GFP)nns9*) and aligned them to the respective lines in our database (*Tg(elavl3:nlsGCaMP6s)mpn400*, *TgBAC(gad1b:GFP)*, *Tg(isl1:GFP)*, *TgBAC(vglut2a[slc17a6b]:loxP-DsRed-loxP-GFP)nns9*). For incorporation of Z-Brain we made use of the fact that their database has been already incorporated into ZBB and we just applied the transformations to the data present in ZBB.

Registration accuracy

To measure the registration accuracy, we first identified the various fiducial points in the original unidentified image stacks using the Slicer software and saved their x, y, and z coordinates in a text file. Next, we registered those stacks using a reference channel to our standard brain and applied the transformations to coordinates of the fiducial points.

Quantification of tectal innervation

To measure the relative innervation of individual tectal layers by retinal and non-retinal afferents we measured the total length of all fibers within the tectal neuropil on each side of the brain. Since RGCs all project to the contralateral tectum, we mirrored all RGCs to both hemispheres. Ipsi- and contralateral labels in Figure 5B relates to the soma location of non-retinal afferents. Next, we measured the fibers length in each tectal layer and divided it by the total length per tectum to calculate the relative contribution of each cell group for the individual layers.

Neuron clustering using NBLAST

To flip all neurons to one hemisphere of the brain we followed the procedure described in (Manton et al., 2014). Briefly, to create a mirroring registration we chose four representative stacks (*TgBAC(gad1b:GFP)*, *TgBAC(vglut2a[slc17a6b]:loxP-DsRed-loxP-GFP)nns9*, α -HuC/D, and α -SYP), flipped those images along the horizontal axis and registered the original versions of the stacks to the flipped version using ANTs as described previously. We manually determined the midline of the brain and categorized neurons as left or right hemispheric based on soma location. Neurons were flipped to the opposite side of the brain and the mirroring registration was applied using the `antsApplyTransformToPoints` function. Pairwise NBLAST scores were computed either for all cerebellar efferents or for the entire dataset (the `nblast_allbyall` function in the `nat.nblast` package

at <https://github.com/jefferislab/nat.nblast> was used). We used unsupervised hierarchical clustering with Ward's method based on the NBLAST scores (the `nhclust` function in the `nat` package at <https://github.com/jefferis/nat> was used). Visualisation was performed using the `plot.neuron` and `plot-surfaces` function of the `nat` package.

Brain segmentation

To provide a framework for graph theoretical analysis we manually segmented the brain into 36 brain regions using the open source software 3D slicer (<https://www.slicer.org/>). Neuroanatomical annotation was based primarily on (Mueller and Wullimann, 2005) with the main exception of the individual stripes in the medulla oblongata which was based on (Kinkhabwala et al., 2011). Specific information about the brain regions can be found in Table S1. To aid in determining brain region boundaries which are notoriously hard to determine in larval zebrafish we made use of the large collection of Gal4 lines and expression patterns present in our database. If possible, we determined a brain region based on a single expression pattern (e.g. *Is/1* to label cranial nuclei) but more often we used a combination of multiple expression pattern.

Generation of a mesoscale connectome

For generating an interareal connectivity matrix we split the 36 brain regions into left and right hemisphere, leaving us with 72 brain regions. To determine the connectivity between brain regions we measured which brain regions a neuron innervated. We only considered a brain region to be innervated by a neuron if a neuron had either tips or a soma in it. This was done to prevent false positive assignment of neurons whose fibers only pass through a region. Since our dataset only comprises about 2% of the total number of brain cells and almost all neurons in the brain are bilaterally symmetric, we decided to double our dataset and mirror all neurons to the contralateral hemisphere. Furthermore, we only considered neurons whose fiber length in a brain region exceeds 10 μm to excluded false positive results from neurons that are located at the border of brain regions that gets falsely assigned to a brain region due to alignment inaccuracies. We removed all local interneurons by excluding neurons that can only be assigned to one brain region. We converted this dataset into an adjacency matrix by summing the lengths for all neurons that connect a pair of brain regions the following way:

$Data[R \times N]$ is a matrix that contains the lengths of all the neurons in each brain region where (R) is the number of brain regions, and (N) is the number of neurons.

$$Data = \begin{bmatrix} n_{00} & n_{01} & n_{02} & \dots & n_{0N} \\ n_{10} & n_{11} & n_{12} & \dots & n_{1N} \\ n_{20} & n_{21} & n_{22} & \dots & n_{2N} \\ \dots & \dots & \dots & \dots & \dots \\ n_{R0} & n_{R1} & n_{R2} & \dots & n_{RN} \end{bmatrix}$$

where $Data[i, j] = n_{ij}$: neuron's (j) length inside region (i).

$CM[R \times R]$ is the connectivity matrix.

$$CM = [cm_{ij}], \text{ where } cm_{ij} = \sum_{k=1}^N (Data[i, k] + Data[j, k]) * \omega$$

Where:

$$\omega = \begin{cases} 1, & i \neq j \wedge Data[i, k] \geq ml \wedge Data[j, k] \geq ml \\ 0, & \text{Otherwise} \end{cases}$$

$$i, j \in [0, R]$$

ml : is the minimum accepted length of a neuron inside a brain region ($ml = 10\mu$)

$$CM = \begin{bmatrix} 0 & cm_{01} & cm_{02} & \dots & cm_{0R} \\ cm_{10} & 0 & cm_{12} & \dots & cm_{1R} \\ cm_{20} & cm_{21} & 0 & \dots & cm_{2R} \\ \dots & \dots & \dots & \dots & \dots \\ cm_{R0} & cm_{R1} & cm_{R2} & \dots & 0 \end{bmatrix}$$

Since our annotation contains brain regions of various sizes and to remove any bias in connection strengths arising from this we normalized connection strengths by dividing it by the volume of the pair of brain regions connected.

QUANTIFICATION AND STATISTICAL ANALYSIS

To measure the distance between the aligned fiducial points and the same point identified in the standard brain (Figure 3A) we measured the Euclidean distance using the `dist` function of the R base package. For determining the distribution of normalized connection strength (Figure 8A), we used the `fitdistrplus` package provided by R (<https://cran.r->

project.org/web/packages/fitdistrplus/index.html). Distances between brain regions (Figure 8B) were calculated as the Euclidean distance between the center of mass for each pair of brain regions and the correlation between the connection strength was calculated using the `cor` function in R. To order brain region based on similar connectivity profiles (Figure 8C) we performed unsupervised hierarchical clustering using Ward's method.

DATA AND SOFTWARE AVAILABILITY

All custom software will be made available upon request. Neuron tracings, brain region segmentations, and transformation files are available for download on a special section on our web-portal (<https://fishatlas.neuro.mpg.de/neurons/downloads>).

KEY RESOURCES TABLE

REAGENT or RESOURCE	SOURCE	IDENTIFIER
Deposited Data		
Single-neuron tracings	This paper	http://fishatlas.neuro.mpg.de/neurons/main_page
Gal4-expression pattern	This paper	http://fishatlas.neuro.mpg.de/neurons/main_page
Antibodies		
Chicken anti-GFP	Invitrogen	A10262, RRID: AB_2534023
Rabbit anti-ERK1/2	Cell Signaling Technology	9102, RRID: AB_330744
Mouse anti-HuC/D	Invitrogen	A21271, RRID:AB_221448
Rabbit anti-Synapsin 1/2	Synaptic Systems	106002, RRID:AB_887804
Chemicals, Peptides, and Recombinant Proteins		
Photoinitiator	Wako Chemicals	VA-044
Experimental Models: Organisms/Strains		
Zebrafish <i>Tg(brn3c:GAL4, UAS:gap43-GFP)s318t (BGUG)</i>	Xiao and Baier, 2007	ZFIN ID: ZDB-ALT-070423-6
Zebrafish <i>Tg(Et(e1b:GAL4)s1101t)</i>	Scott et al., 2007	ZFIN ID: ZDB-ALT-070716-2
Zebrafish <i>Tg(elavl3:Gal4)zf349</i>	Akerboom et al., 2012	ZFIN ID: ZDB-ALT-121024-4
Zebrafish <i>Tg(14xUAS:mCherry)s1984t, TgBAC(slc17a6b:Gal4FF) zK145P24</i>	Heap et al., 2013; Satou et al., 2013	ZFIN ID: ZDB-ALT-130702-1; ZFIN ID: ZDB-ALT-131127-1
Zebrafish <i>TgBAC(vglut2a[slc17a6b]:loxP-DsRed-loxP-GFP)nns14</i>	Satou et al., 2013	ZFIN ID: ZDB-ALT-110413-5
Zebrafish <i>Tg(UAS-E1b:NfsB-mCherry)c264</i>	Otsuna et al., 2015	ZFIN ID: ZDB-ALT-070316-1
Zebrafish <i>Tg(elavl3:lyn-tagRFP)mpn404</i>	Dal Maschio et al., 2017	ZFIN ID: ZDB-ALT-170731-38
Zebrafish <i>Tg(elavl3:nlsGCaMP6s)mpn400</i>	Dal Maschio et al., 2017	ZFIN ID: ZDB-ALT-170731-37
Zebrafish <i>Tg(actb2:loxP-eGFP-loxP-lynTagRFPT)y272</i>	Horstick et al., 2015	ZFIN ID: ZDB-ALT-150721-8

Zebrafish <i>Tg(elavl3:Hsa.H2B-GCaMP6s)jf5</i>	Freeman et al., 2014	ZFIN ID: ZDB-ALT-141023-2
Zebrafish <i>Tg(elavl3:GCaMP5G)a4598</i>	Ahrens et al., 2013	ZFIN ID: ZDB-ALT-130924-1
Zebrafish <i>Tg(sst3:Gal4-VP16)mpn219</i>	Förster et al., 2017a	ZFIN ID: ZDB-ALT-170908-20
Zebrafish <i>Tg(galn:Gal4-VP16)mpn213</i>	Förster et al., 2017a	ZFIN ID: ZDB-ALT-170908-13
Zebrafish <i>Tg(gad1b/GAD67:Gal4-VP16)mpn155</i>	Förster et al., 2017a	ZFIN ID: ZDB-ALT-160726-5
Zebrafish <i>Tg(chata:Gal4-VP16)mpn202</i>	Förster et al., 2017a	ZFIN ID: ZDB-ALT-170908-4
Zebrafish <i>Tg(drd2a:Gal4-VP16)mpn211</i>	Förster et al., 2017a	ZFIN ID: ZDB-ALT-170908-9
Zebrafish <i>Tg(Et(-1.5hsp70l:Gal4-VP16)s1013t)</i>	Scott et al., 2007	ZFIN ID: ZDB-ALT-070420-14
Zebrafish <i>Tg(Et(-0.6hsp70l:Gal4-VP16)s1020t)</i>	Scott et al., 2007	ZFIN ID: ZDB-ALT-070420-21
Zebrafish <i>Tg(Et(fos:Gal4-VP16)s1168t)</i>	Scott et al., 2007	ZFIN ID: ZDB-ALT-080327-136
Zebrafish <i>Tg(Et(-0.6hsp70l:Gal4-VP16)s1171t)</i>	Scott et al., 2007	ZFIN ID: ZDB-ALT-080327-139
Zebrafish <i>Tg(Et(fos:Gal4-VP16)s1113t)</i>	Scott et al., 2007	ZFIN ID: ZDB-ALT-080327-86
Software and Algorithms		
Advanced Normalization Tools (ANTs)	Avants et al., 2008	http://stnava.github.io/ANTs/
NeuTube	Feng et al., 2015	https://www.neutracing.com/
Fiji	Schindelin et al., 2012	https://fiji.sc/
FluoRender	Wan et al., 2012	http://www.sci.utah.edu/software/fluorender.html
3DSlicer	Fedorov et al., 2012	https://www.slicer.org/
Python 2.7	Python.org	https://www.python.org/
R	The R project	https://cran.r-project.org/
R nat package	Jefferis et al., 2007	https://cran.r-project.org/web/packages/nat/index.html
R nat.nblast package	Costa et al., 2016	https://cran.r-project.org/web/packages/nat.nblast/index.html
R fitdistrplus package	Delignette-Muller and Dutang, 2015	https://cran.r-project.org/web/packages/fitdistrplus/index.html
R iGraph package	Csárdi and Nepusz	http://igraph.org/
R rgl package		https://cran.r-project.org/web/packages/rgl/index.html
R qgraph package	Epskamp et al., 2012	https://cran.r-project.org/web/packages/qgraph/
R brainigraph package		https://cran.r-project.org/web/packages/qgraph/

References

- Ahrens, M.B., Orger, M.B., Robson, D.N., Li, J.M., and Keller, P.J. (2013). Whole-brain functional imaging at cellular resolution using light-sheet microscopy. *Nat Methods* 10, 413–420.
- Akram, M.A., Nanda, S., Maraver, P., Armañanzas, R., and Ascoli, G.A. (2018). An open repository for single-cell reconstructions of the brain forest. *Sci. Data* 5, 180006.
- Alivisatos, A.P., Chun, M., Church, G.M., Greenspan, R.J., Roukes, M.L., and Yuste, R. (2012). The brain activity map project and the challenge of functional connectomics. *Neuron* 74, 970–974.
- Amo, R., Aizawa, H., Takahoko, M., Kobayashi, M., Takahashi, R., Aoki, T., and Okamoto, H. (2010). Identification of the Zebrafish Ventral Habenula As a Homolog of the Mammalian Lateral Habenula. *J. Neurosci.* 30, 1566–1574.
- Asakawa, K., Suster, M.L., Mizusawa, K., Nagayoshi, S., Kotani, T., Urasaki, A., Kishimoto, Y., Hibi, M., and Kawakami, K. (2008). Genetic dissection of neural circuits by Tol2 transposon-mediated Gal4 gene and enhancer trapping in zebrafish. *Proc. Natl. Acad. Sci.* 105, 1255–1260.
- Ascoli, G.A., Donohue, D.E., and Halavi, M. (2007). NeuroMorpho.Org: A Central Resource for Neuronal Morphologies. *J. Neurosci.* 27, 9247–9251.
- Avants, B.B., Yushkevich, P., Pluta, J., Minkoff, D., Korczykowski, M., Detre, J., and Gee, J.C. (2010). The optimal template effect in hippocampus studies of diseased populations. *Neuroimage* 49, 2457–2466.
- Bae, Y.-K., Kani, S., Shimizu, T., Tanabe, K., Nojima, H., Kimura, Y., Higashijima, S., and Hibi, M. (2009). Anatomy of zebrafish cerebellum and screen for mutations affecting its development. *Dev. Biol.* 330, 406–426.
- Baier, H., and Scott, E.K. (2009). Genetic and optical targeting of neural circuits and behavior — zebrafish in the spotlight. *Curr. Opin. Neurobiol.* 19, 553–560.
- Baier, H., Klostermann, S., Trowe, T., Karlstrom, R.O., Nusslein-Volhard, C., and Bonhoeffer, F. (1996). Genetic dissection of the retinotectal projection. *Development* 123.
- Barker, A.J., and Baier, H. (2015). Sensorimotor Decision Making in the Zebrafish Tectum. *Curr. Biol.* 25, 2804–2814.

Basso, M.A., and May, P.J. (2017). Circuits for Action and Cognition: A View from the Superior Colliculus. *Annu. Rev. Vis. Sci.* 3, 197–226.

Bauer, A.Q., Kraft, A.W., Baxter, G.A., Wright, P.W., Reisman, M.D., Bice, A.R., Park, J.J., Bruchas, M.R., Snyder, A.Z., Lee, J.M., et al. (2018). Effective Connectivity Measured Using Optogenetically Evoked Hemodynamic Signals Exhibits Topography Distinct from Resting State Functional Connectivity in the Mouse. *Cereb Cortex* 28, 370–386.

Betz, R.F., and Bassett, D.S. (2018). Specificity and robustness of long-distance connections in weighted, interareal connectomes. *Proc. Natl. Acad. Sci. U. S. A.* 115, E4880–E4889.

Bianco, I.H., Ma, L.-H., Schoppik, D., Robson, D.N., Orger, M.B., Beck, J.C., Li, J.M., Schier, A.F., Engert, F., and Baker, R. (2012). The Tangential Nucleus Controls a Gravitoinertial Vestibulo-ocular Reflex. *Curr. Biol.* 22, 1285–1295.

Bohland, J.W., Wu, C., Barbas, H., Bokil, H., Bota, M., Breiter, H.C., Cline, H.T., Doyle, J.C., Freed, P.J., Greenspan, R.J., et al. (2009). A proposal for a coordinated effort for the determination of brainwide neuroanatomical connectivity in model organisms at a mesoscopic scale. *PLoS Comput Biol* 5, e1000334.

Bullmore, E., and Sporns, O. (2012). The economy of brain network organization. *Nat. Rev. Neurosci.* 13, 336–349.

Cannon, R.C., Turner, D.A., Pyapali, G.K., and Wheal, H. V (1998). An on-line archive of reconstructed hippocampal neurons. *J Neurosci Methods* 84, 49–54.

Chiang, A.S., Lin, C.Y., Chuang, C.C., Chang, H.M., Hsieh, C.H., Yeh, C.W., Shih, C.T., Wu, J.J., Wang, G.T., Chen, Y.C., et al. (2011). Three-dimensional reconstruction of brain-wide wiring networks in *Drosophila* at single-cell resolution. *Curr Biol* 21, 1–11.

Costa, M., Manton, J.D., Ostrovsky, A.D., Prohaska, S., and Jefferis, G.S.X.E. (2016). NBLAST: Rapid, Sensitive Comparison of Neuronal Structure and Construction of Neuron Family Databases. *Neuron* 91, 293–311.

Dal Maschio, M., Donovan, J.C., Helmbrecht, T.O., and Baier, H. (2017). Linking Neurons to Network Function and Behavior by Two-Photon Holographic Optogenetics and Volumetric Imaging. *Neuron* 94, 774–789 e5.

Denk, W., and Horstmann, H. (2004). Serial Block-Face Scanning Electron Microscopy to Reconstruct Three-Dimensional Tissue Nanostructure. *PLoS Biol.* 2, e329.

Ercsey-Ravasz, M., Markov, N.T., Lamy, C., Van Essen, D.C., Knoblauch, K., Toroczkai, Z., and Kennedy, H. (2013). A Predictive Network Model of Cerebral Cortical Connectivity Based on a Distance Rule. *Neuron* 80, 184–197.

Fame, R.M. (2006). Second-order projection from the posterior lateral line in the early zebrafish brain. *Neural Dev.* 28.

Feng, L., Zhao, T., and Kim, J. (2015). neuTube 1.0: A New Design for Efficient Neuron Reconstruction Software Based on the SWC Format. *ENeuro* 2.

Filosa, A., Barker, A.J., Dal Maschio, M., and Baier, H. (2016). Feeding State Modulates Behavioral Choice and Processing of Prey Stimuli in the Zebrafish Tectum. *Neuron* 90, 596–608.

Forster, D., Arnold-Ammer, I., Laurell, E., Barker, A.J., Fernandes, A.M., Finger-Baier, K., Filosa, A., Helmbrecht, T.O., Kolsch, Y., Kuhn, E., et al. (2017). Genetic targeting and anatomical registration of neuronal populations in the zebrafish brain with a new set of BAC transgenic tools. *Sci Rep* 7, 5230.

Friedrich, R.W., Genoud, C., and Wanner, A.A. (2013). Analyzing the structure and function of neuronal circuits in zebrafish. *Front Neural Circuits* 7, 71.

Hawrylycz, M., Baldock, R.A., Burger, A., Hashikawa, T., Johnson, G.A., Martone, M., Ng, L., Lau, C., Larsen, S.D., Nissanov, J., et al. (2011). Digital Atlasing and Standardization in the Mouse Brain. *PLOS Comput. Biol.* 7, e1001065.

Heap, L.A.L., Vanwalleghe, G., Thompson, A.W., Favre-Bulle, I.A., and Scott, E.K. (2018). Luminance Changes Drive Directional Startle through a Thalamic Pathway. *Neuron* 99, 293–301.e4.

Helmbrecht, T.O., dal Maschio, M., Donovan, J.C., Koutsouli, S., and Baier, H. (2018). Topography of a Visuomotor Transformation. *Neuron* 100, 1429–1445.e4.

Hildebrand, D.G.C., Cicconet, M., Torres, R.M., Choi, W., Quan, T.M., Moon, J., Wetzel, A.W., Champion, A.S., Graham, B.J., Randlett, O., et al. (2017). Whole-brain serial-section electron microscopy in larval zebrafish. *Nature* 545, 345–349.

- Jefferis, G.S.X.E., Potter, C.J., Chan, A.M., Marin, E.C., Rohlfsing, T., Maurer, C.R., and Luo, L. (2007). Comprehensive maps of *Drosophila* higher olfactory centers: spatially segregated fruit and pheromone representation. *Cell* 128, 1187–1203.
- Kinkhabwala, A., Riley, M., Koyama, M., Monen, J., Satou, C., Kimura, Y., Higashijima, S.-I., and Fetcho, J. (2011). A structural and functional ground plan for neurons in the hindbrain of zebrafish. *Proc. Natl. Acad. Sci. U. S. A.* 108, 1164–1169.
- Knogler, L.D., Markov, D.A., Dragomir, E.I., Štíh, V., and Portugues, R. (2017). Sensorimotor Representations in Cerebellar Granule Cells in Larval Zebrafish Are Dense, Spatially Organized, and Non-temporally Patterned. *Curr. Biol.* 27, 1288–1302.
- Kramer, A, Wu, Y., Baier, H., Kubo, F. (2019). Neuronal architecture of a visual center that processes optic flow. *Neuron, this issue*
- Kubo, F., Hablitzel, B., Dal Maschio, M., Driever, W., Baier, H., and Arrenberg, A.B. (2014). Functional Architecture of an Optic Flow-Responsive Area that Drives Horizontal Eye Movements in Zebrafish. *Neuron* 81, 1344–1359.
- Lee, Y.-H., Lin, Y.-N., Chuang, C.-C., and Lo, C.-C. (2014). SPIN: A Method of Skeleton-Based Polarity Identification for Neurons. *Neuroinformatics* 12, 487–507.
- Li, L., Feng, X., Zhou, Z., Zhang, H., Shi, Q., Lei, Z., Shen, P., Yang, Q., Zhao, B., Chen, S., et al. (2018). Stress Accelerates Defensive Responses to Looming in Mice and Involves a Locus Coeruleus-Superior Colliculus Projection. *Curr. Biol.* 28, 859–871.e5.
- Liao, J.C., and Haehnel, M. (2012). Physiology of afferent neurons in larval zebrafish provides a functional framework for lateral line somatotopy. *J. Neurophysiol.* 107, 2615–2623.
- Manni, E., and Petrosini, L. (2004). A century of cerebellar somatotopy: a debated representation. *Nat. Rev. Neurosci.* 5, 241–249.
- Manton, J.D., Ostrovsky, A.D., Goetz, L., Costa, M., Rohlfsing, T., and Jefferis, G.S.X.E. (2014). Combining genome-scale *Drosophila* 3D neuroanatomical data by bridging template brains. *BioRxiv* 006353.
- Marquart, G.D., Tabor, K.M., Brown, M., Strykowski, J.L., Varshney, G.K., LaFave, M.C., Mueller, T., Burgess, S.M., Higashijima, S., and Burgess, H.A. (2015). A 3D Searchable Database of Transgenic Zebrafish Gal4 and Cre Lines for Functional Neuroanatomy Studies. *Front Neural Circuits* 9, 78.

Marquart, G.D., Tabor, K.M., Horstick, E.J., Brown, M., Geoca, A.K., Polys, N.F., Nogare, D.D., and Burgess, H.A. (2017). High-precision registration between zebrafish brain atlases using symmetric diffeomorphic normalization. *Gigascience* 6, 1–15.

Matsui, H., Namikawa, K., Babaryka, A., and Köster, R.W. (2014). Functional regionalization of the teleost cerebellum analyzed in vivo. *Proc. Natl. Acad. Sci.* 111, 11846–11851.

McCormick, C.A. (1989). Central Lateral Line Mechanosensory Pathways in Bony Fish. In *The Mechanosensory Lateral Line*, (Springer, New York, NY), pp. 341–364.

McKenna, A., Findlay, G.M., Gagnon, J.A., Horwitz, M.S., Schier, A.F., and Shendure, J. (2016). Whole-organism lineage tracing by combinatorial and cumulative genome editing. *Science* 353, aaf7907.

Meek, J. (1983). Functional anatomy of the tectum mesencephali of the goldfish. An explorative analysis of the functional implications of the laminar structural organization of the tectum. *Brain Res.* 287, 247–297.

Mitra, P.P. (2014). The circuit architecture of whole brains at the mesoscopic scale. *Neuron* 83, 1273–1283.

Miyasaka, N., Arganda-Carreras, I., Wakisaka, N., Masuda, M., Sumbul, U., Seung, H.S., and Yoshihara, Y. (2014). Olfactory projectome in the zebrafish forebrain revealed by genetic single-neuron labelling. *Nat Commun* 5, 3639.

Mueller, T., and Wullimann, M. (2005). *Atlas of Early Zebrafish Brain Development*, 2nd Edition | Dr. Thomas Mueller, Mario Wullimann | ISBN 9780124186699.

Naumann, E.A., Fitzgerald, J.E., Dunn, T.W., Rihel, J., Sompolsky, H., and Engert, F. (2016). From Whole-Brain Data to Functional Circuit Models: The Zebrafish Optomotor Response. *Cell* 167, 947–960 e20.

Oh, S.W., Harris, J.A., Ng, L., Winslow, B., Cain, N., Mihalas, S., Wang, Q., Lau, C., Kuan, L., Henry, A.M., et al. (2014). A mesoscale connectome of the mouse brain. *Nature* 508, 207–214.

Ohyama, T., Schneider-Mizell, C.M., Fetter, R.D., Aleman, J.V., Franconville, R., Rivera-Alba, M., Mensh, B.D., Branson, K.M., Simpson, J.H., Truman, J.W., et al. (2015). A multilevel multimodal circuit enhances action selection in *Drosophila*. *Nature* 520, 633–639.

- Orger, M.B., and de Polavieja, G.G. (2017). Zebrafish Behavior: Opportunities and Challenges. *Annu Rev Neurosci* 40, 125–147.
- Pandey, S., Shekhar, K., Regev, A., and Schier, A.F. (2018). Comprehensive Identification and Spatial Mapping of Habenular Neuronal Types Using Single-Cell RNA-Seq. *Curr. Biol.* 28, 1052–1065.e7.
- Panzeri, S., Harvey, C.D., Piasini, E., Latham, P.E., and Fellin, T. (2017). Cracking the Neural Code for Sensory Perception by Combining Statistics, Intervention, and Behavior. *Neuron* 93, 491–507.
- Pérez-Pérez, M.P., Luque, M.A., Herrero, L., Núñez-Abades, P.A., and Torres, B. (2003). Afferent connectivity to different functional zones of the optic tectum in goldfish. *Vis. Neurosci.* 20, 397–410.
- Portugues, R., Feierstein, C.E., Engert, F., and Orger, M.B. (2014). Whole-brain activity maps reveal stereotyped, distributed networks for visuomotor behavior. *Neuron* 81, 1328–1343.
- Raj, B., Wagner, D.E., McKenna, A., Pandey, S., Klein, A.M., Shendure, J., Gagnon, J.A., and Schier, A.F. (2018). Simultaneous single-cell profiling of lineages and cell types in the vertebrate brain. *Nat. Biotechnol.* 36, 442–450.
- Randlett, O., Wee, C.L., Naumann, E.A., Nnaemeka, O., Schoppik, D., Fitzgerald, J.E., Portugues, R., Lacoste, A.M., Riegler, C., Engert, F., et al. (2015). Whole-brain activity mapping onto a zebrafish brain atlas. *Nat Methods* 12, 1039–1046.
- Robles, E., Filosa, A., and Baier, H. (2013). Precise lamination of retinal axons generates multiple parallel input pathways in the tectum. *J. Neurosci.* 33, 5027–5039.
- Robles, E., Laurell, E., and Baier, H. (2014). The Retinal Projectome Reveals Brain-Area-Specific Visual Representations Generated by Ganglion Cell Diversity. *Curr. Biol.* 24, 2085–2096.
- Roeser, T., and Baier, H. (2003). Visuomotor behaviors in larval zebrafish after GFP-guided laser ablation of the optic tectum. *J. Neurosci.* 23, 3726–3734.
- Scott, E.K., Mason, L., Arrenberg, A.B., Ziv, L., Gosse, N.J., Xiao, T., Chi, N.C., Asakawa, K., Kawakami, K., and Baier, H. (2007). Targeting neural circuitry in zebrafish using GAL4 enhancer trapping. *Nat. Methods* 4, 323–326.
- Semmelhack, J.L., Donovan, J.C., Thiele, T.R., Kuehn, E., Laurell, E., and Baier, H. (2014). A dedicated visual pathway for prey detection in larval zebrafish. *Elife* 3, 4878.

Shih, C.T., Sporns, O., Yuan, S.L., Su, T.S., Lin, Y.J., Chuang, C.C., Wang, T.Y., Lo, C.C., Greenspan, R.J., and Chiang, A.S. (2015). Connectomics-based analysis of information flow in the *Drosophila* brain. *Curr Biol* 25, 1249–1258.

Sporns, O., Tononi, G., and Kötter, R. (2005). The Human Connectome: A Structural Description of the Human Brain. *PLOS Comput. Biol.* 1, e42.

Springer, A.D., and Mednick, A.S. (1985). A quantitative study of the relative contribution of different retinal sectors to the innervation of various thalamic and pretectal nuclei in goldfish. *J. Comp. Neurol.* 242, 369–380.

Stuermer, C.A. (1988). Retinotopic organization of the developing retinotectal projection in the zebrafish embryo. *J. Neurosci.* 8, 4513–4530.

Thompson, A.W., Vanvalleghem, G.C., Heap, L.A., and Scott, E.K. (2016). Functional Profiles of Visual-, Auditory-, and Water Flow-Responsive Neurons in the Zebrafish Tectum. *Curr. Biol.* 26, 743–754.

Treweek, J.B., Chan, K.Y., Flytzanis, N.C., Yang, B., Deverman, B.E., Greenbaum, A., Lignell, A., Xiao, C., Cai, L., Ladinsky, M.S., et al. (2015). Whole-body tissue stabilization and selective extractions via tissue-hydrogel hybrids for high-resolution intact circuit mapping and phenotyping. *Nat Protoc* 10, 1860–1896.

Turner, K.J., Hawkins, T.A., Yáñez, J., Anadón, R., Wilson, S.W., and Folgueira, M. (2016). Afferent Connectivity of the Zebrafish Habenulae. *Front. Neural Circuits* 10.

Vanvalleghem, G.C., Ahrens, M.B., and Scott, E.K. (2018). Integrative whole-brain neuroscience in larval zebrafish. *Curr. Opin. Neurobiol.* 50, 136–145.

Varshney, L.R., Chen, B.L., Paniagua, E., Hall, D.H., and Chklovskii, D.B. (2011). Structural Properties of the *Caenorhabditis elegans* Neuronal Network. *PLoS Comput. Biol.* 7, e1001066.

Xiao, T., and Baier, H. (2007). Lamina-specific axonal projections in the zebrafish tectum require the type IV collagen Dragnet. *Nat Neurosci* 10, 1529–1537.

Xiao, T., Roeser, T., Staub, W., Baier, H., Nüsslein-Volhard, C., and Bonhoeffer, F. (2005). A GFP-based genetic screen reveals mutations that disrupt the architecture of the zebrafish retinotectal projection. *Development* 132, 2955–2967.

Zheng, Z., Lauritzen, J.S., Perlman, E., Robinson, C.G., Nichols, M., Milkie, D., Torrens, O., Price, J., Fisher, C.B., Sharifi, N., et al. (2018). A Complete Electron Microscopy Volume of the Brain of Adult *Drosophila melanogaster*. *Cell* 174, 730–743.e22.

2.3 Manuscript 3

Anna Kramer, Yunmin Wu, Herwig Baier, Fumi Kubo. 2019. Neuronal architecture of a visual center that processes optic flow. *Neuron*, 103: 118-132. DOI: [10.1016/j.neuron.2019.04.018](https://doi.org/10.1016/j.neuron.2019.04.018).

Animals use global image motion cues to actively stabilize their position by compensatory movements. Neurons in the zebrafish pretectum distinguish different optic flow patterns, e.g. rotation and translation, to drive appropriate behaviors. Combining functional imaging and morphological reconstruction of single cells, we revealed critical neuroanatomical features of this sensorimotor transformation. Terminals of direction-selective retinal ganglion cells (DS-RGCs) are located within the pretectal retinal arborization field 5 (AF5), where they meet dendrites of pretectal neurons with simple tuning to monocular optic flow. Translation-selective neurons, which respond selectively to optic flow in the same direction for both eyes, are intermingled with these simple cells, but do not receive inputs from DS-RGCs. Mutually exclusive populations of pretectal projection neurons innervate either the reticular formation or the cerebellum, which in turn control motor responses. We posit that local computations in a defined pretectal circuit transform optic flow signals into neural commands driving optomotor behavior.

Neuronal architecture of a visual center that processes optic flow

Anna Kramer¹, Yunmin Wu¹, Herwig Baier¹, Fumi Kubo^{1,2*}

¹ Max Planck Institute of Neurobiology, Department Genes – Circuits – Behavior, Am Klopferspitz 18, 82152 Martinsried, Germany

² National Institute of Genetics, Center for Frontier Research, 1111 Yata, Mishima, Shizuoka, 411-8540, Japan

*Lead Contact: F.K. (fumikubo@nig.ac.jp)

Summary

Animals use global image motion cues to actively stabilize their position by compensatory movements. Neurons in the zebrafish pretectum distinguish different optic flow patterns, e.g. rotation and translation, to drive appropriate behaviors. Combining functional imaging and morphological reconstruction of single cells, we revealed critical neuroanatomical features of this sensorimotor transformation. Terminals of direction-selective retinal ganglion cells (DS-RGCs) are located within the pretectal retinal arborization field 5 (AF5), where they meet dendrites of pretectal neurons with simple tuning to monocular optic flow. Translation-selective neurons, which respond selectively to optic flow in the same direction for both eyes, are intermingled with these simple cells, but do not receive inputs from DS-RGCs. Mutually exclusive populations of pretectal projection neurons innervate either the reticular formation or the cerebellum, which in turn control motor responses. We posit that local computations in a defined pretectal circuit transform optic flow signals into neural commands driving optomotor behavior.

Introduction

When animals actively move, or are passively carried through the environment, their visual systems experience continuous movement of stationary features in the visual scene. Neuronal circuits use the drifting retinal images to compute global image motion (optic flow) in order to adjust the animal's body posture and position and stabilize the direction of gaze. In teleost fish and other vertebrates, the optokinetic response (OKR) and the optomotor response (OMR) are typical optic flow-driven behaviors that compensate for self-motion (Masseck and Hoffmann, 2009a). Eye movements accompanying the OKR consist of slow following phases, which minimize retinal slip, interspersed by quick reset phases. The OMR is characterized by locomotion in the direction of the perceived motion. This ensures that the animal does not drift away from its location, for instance in a flowing water stream. Zebrafish larvae older than 5 days post-fertilization (>5 dpf) exhibit both robust OKR and OMR (Neuhauss et al., 1999; Orger et al., 2004; Orger et al., 2008; Orger et al., 2000; Portugues and Engert, 2009; Rinner et al., 2005).

Retinal ganglion cells (RGCs) are the sole output neuron class of the retina. In zebrafish larvae, all RGC axons cross the midline and terminate in nine arborization fields (AFs, numbered AF1 to AF9) in the preoptic area/hypothalamus, the thalamus and the pretectum, in addition to the optic tectum, which is AF10 (Burrill and Easter, 1994; Robles et al., 2014). Each AF and each of the ten layers of the tectum receive input from of a distinct combination of morphologically and functionally identifiable RGC types, which form parallel processing channels for specific visual features, such as prey-like objects, looming stimuli and decreasing or increasing ambient light levels (Robles et al., 2014; Semmelhack et al., 2014; Temizer et al., 2015; Zhang et al., 2017). A unifying hypothesis posits that behaviorally relevant information is packaged in spatially segregated information channels (Dhande and Huberman, 2014), which in turn evoke distinct adaptive behaviors (Baier, 2000; Helmbrecht et al., 2018). Therefore, knowledge of AF tuning provides a productive entry point to decipher the "division of labor" among the different visual and visuomotor processing streams.

Broad activation of the pretectum (accessory optic system) is sufficient to evoke OKR in mammals and zebrafish, while lesions or experimental inactivation suppresses this behavior (Cazin et al., 1980; Kubo et al., 2014; Schiff et al., 1988). This observation led to the prediction that the subset of RGCs that encodes the direction of movement, namely the DS-RGCs (Barlow and Hill, 1963; Dhande and Huberman, 2014), carry information about image motion to the pretectal area. Previous anatomical work in zebrafish had shown that the RGCs that project to the direction-selective (DS) sublayer of the optic tectum, the SFGS1 (Gabriel et al., 2012; Gebhardt et al., 2013; Nikolaou et al., 2012), also form collateral branches in AF5 (Robles et al., 2014). This observation made AF5 a prime candidate

for the pretectal neuropil region that receives DS-RGC inputs. Until now, however, DS-RGC responses had not been detected in AF5. Rather, a recent study annotated the neighboring area AF6 as the DS-RGC recipient area (Naumann et al., 2016). One goal of the current study was to precisely map DS-RGC inputs within the pretectum to resolve this discrepancy.

In lateral-eyed animals such as zebrafish, each eye samples roughly one hemisphere of the visual world. Therefore, integrating visual inputs from both eyes is an obvious strategy for discriminating translational vs. rotational optic flow (i.e., movement in the same or in the opposite directions for left and right eye) (Masseck and Hoffmann, 2009a, b; Sabbah et al., 2017; Wang et al., 2019; Wylie et al., 1998). Functional imaging had shown that most pretectal neurons in zebrafish fall into one of two broad categories: 1) “simple” optic flow-responsive cells, which are driven by DS inputs from one eye, and 2) “complex” cells that respond to translational optic flow and are suppressed by rotational optic flow (Kubo et al., 2014). In a parsimonious wiring diagram, “simple”, monocular pretectal cells might combine their DS tuning across hemispheres to generate the responses of “complex” translation-selective neurons (Kubo et al., 2014). The latter cells might then convey the processed information to premotor centers in the hindbrain, which in turn initiate the OMR.

To test the anatomical predictions of this wiring diagram, we set out to determine the cellular composition of the pretectal optic-flow processing circuit and test predictions of its input and output pathways. We found that the majority of DS-RGCs terminate in AF5, consistent with earlier anatomical findings (Robles et al., 2014). Morphological reconstructions of optic-flow responsive pretectal cells showed that the putative dendrites of simple monocular cells overlap with DS-RGC presynaptic terminals in AF5. Complex translation-selective cells have different morphologies and project neurites into a neuropil region abutting, and overlapping with, AF6. Long-range projections connect the optic-flow sensitive pretectal area to the cerebellum, the reticular formation and other motor-related centers. Together, our work, integrating diverse functional and anatomical datasets, traces a universally important visual pathway with cellular resolution from the retina to the hindbrain.

Results

FuGIMA approach allows reconstruction and visualization of functionally identified pretectal neurons

We asked how optic flow information is represented by cell types of the pretectum. The pretectum is an anatomically complex region comprised of retinorecipient and non-retinorecipient cells (Yáñez et al., 2018). Pretectal cells with different functional properties are intermingled (Kubo et al., 2014; Naumann et al., 2016). To reveal the morphologies of optic-flow responsive pretectal neurons, we employed the all-optical method FuGIMA (function-guided inducible morphological analysis) (Förster et al., 2018). FuGIMA is based on the co-expression of nuclear localized GCaMP6s (nls-GCaMP6s) and cytoplasmic photoactivatable GFP (paGFP) under the control of a bidirectional UAS (Janus-UAS; Distel et al., 2010; Paquet et al., 2009) (Figure 1A). Although both nls-GCaMP6s and photoactivated paGFP emit green fluorescence, signals from the two proteins are separated by way of their nuclear vs. cytoplasmic localization, thus allowing their combination in the same cell.

We used zebrafish larvae expressing the FuGIMA components in all neurons by crossing the pan-neuronal driver *Gal4s1101t* with *UAS:FuGIMA* (see STAR Methods). Neuronal activity in the pretectum was recorded by imaging of nls-GCaMP6s signals upon stimulation with whole-field motion (Figure 1B). The visual stimulus protocol consisted of monocular and binocular optic flow patterns (horizontally moving gratings) in a sequence of eight phases: four monocular phases with gratings shown to the left or right side of the fish, moving either nasally or temporally, and four binocular phases, namely backward, forward, clockwise and counter-clockwise motions (Figure S2A). Responses to each of the eight phases were used to assign to each cell a barcode, which represents the stimulus combination to which the cell is tuned (Kubo et al., 2014) (Figure 1C). A cell of interest was then chosen for photoactivation, based on its response to optic flow, and labeled by focusing 750 nm laser light in 2p mode onto the soma (Figures 1D-F). Photoactivated paGFP diffuses into the neurites and, after several hours, reveals the morphology of the cell (Förster et al., 2018) (Figure 1G). The maximum distance over which neurites can be traced is dependent on the diffusion properties of paGFP and was empirically determined to be around 200 μm (Figures S1A, B; see STAR Methods).

Pretectal neurons with optic flow tuning differ in their morphologies from non-motion-sensitive neurons

Out of the 256 (2^8) theoretically possible barcodes, we focused on the following three response classes (Kubo et al., 2014): simple monocular DS (comprising four response types), complex

translation-selective (eight response types), and non-motion-sensitive as controls (activity not locked to any motion phase; Figure 1C). We used a regressor-based analysis to semi-automatically identify response types of interest in a near-online fashion (see three exemplary GCaMP6s fluorescent traces in Figure 1D). Among these cells, we selected one cell of interest for photoactivation (correlation map of regressor 1; Figures 1E, F). After allowing for diffusion of GFP fluorescence, cells of interest were manually traced (Figure 1G) and registered to a standard brain for interindividual comparisons, via a reference marker (*HuC:lyn-tagRFP*) (Figures 1H, I; Figures S1D, E; see STAR Methods).

We reconstructed the morphologies of 58 pretectal neurons from 46 fish (30 monocular DS neurons, 19 translation-selective neurons, and 9 non-motion-sensitive neurons; for individual calcium traces, see Figures S2B, C). The respective frequencies of response types detected in our FuGIMA dataset was overall similar to Kubo et al. (2014); however, monocular DS neurons responding to nasalward motion (i.e., MoNR and MoNL) located in the brain ipsilateral to the visually stimulated eye were not identified in this limited dataset (Figures S2D, E).

Motion-sensitive neurons in our FuGIMA dataset showed overall similar morphologies; their stem neurite pointed in a lateral-anterior-ventral direction (Figure 2A). The neurites of non-motion-sensitive neurons, on the other hand, typically branched and extended in the anterior and posterior directions, suggesting that the morphologies of optic-flow sensitive cells differ fundamentally from those of the non-motion-sensitive control neurons (Figure 2A). Cell bodies of monocular DS neurons were widely distributed in an anterior-lateral domain, whereas the translation-selective neurons were located in a more confined, posterior-medial domain (Figure S4B).

Neurons with monocular DS vs. binocular translational optic flow tuning differ in their AF projection patterns

To examine which FuGIMA neurons are potentially retinorecipient, we registered RGC axon projections (Figure 2B) to the standard brain (Figures S3A, B; see STAR Methods). Guided by known anatomical features (Burrill and Easter, 1994; Robles et al., 2014), the volumes of AFs 4-10 could be reliably annotated (see STAR Methods; Movie S2). We found that the majority of optic-flow responsive cells (35 of 49; 71 %) overlapped with one or more of the AFs. We noticed that monocular DS cells (6 of 30; 20 %) extended neurites into AF5, regardless of their preferred direction (Figures 2D left, E left, F; individual tracings in Figure S4A), while translation-selective neurons did not receive inputs from the AF5 region. On the other hand, both monocular DS and translation-selective classes densely branch in a region that is abutting, and overlapping with, the dorsal part of AF6. In fact, all

translation-selective cells project ventrally in the direction of AF6, regardless of whether they are responsive to forward or backward motion (Figures 2D middle, 2E right).

The analysis of intersections of all FuGIMA tracings with AF boundaries (defined by kernel density estimate, KDE = 50 %) revealed that many FuGIMA cells (25 of 58, 43 %) intersected with one AF: 19 with AF6, 5 with AF9 and 1 with AF7. About a quarter of FuGIMA-traced cells (14 of 58, 24 %) intersected with more than one AF in varying combinations (Figure 2F). The total number of intersections per AF changed with the applied threshold for KDE. However, as we varied KDE from 25 to 75 %, the number of cells overlapping with AFs 5, 7 and 8 remained constant ($n = 6, 1$ and 2 , respectively), suggesting that overall intersection patterns of response classes do not depend on the stringency with which these AFs are annotated (Figure S3C).

DS-RGCs project to pretectal neuropil area AF5

Monocular DS-responsive pretectal neurons may inherit their tuning from DS-RGCs that project to AF5. To test this prediction, we measured responses to moving gratings in RGC axon terminals and aligned the functional responses from multiple fish in a second standard brain, which we constructed based on the *isl2b:Gal4 x UAS:mCherry* labeling pattern (Figure S5A). The *isl2b* promoter allows targeting of the vast majority of RGCs (Pittman et al., 2008), and Dil injection confirmed that the *isl2b:Gal4* line labels most of the RGCs terminating in the ventrally located AF4, AF5 and AF6 (Figure S5E). For imaging of axon terminals of DS-RGCs in the pretectum, we expressed synaptophysin-tagged GCaMP6s (syGCaMP6s) in RGCs (*isl2b:Gal4; UAS:syGCaMP6s*). Fusion to synaptophysin targets the calcium indicator to presynaptic terminals (Dreosti et al., 2009; Dunn et al., 2016; Nikolaou et al., 2012). Recorded syGCaMP6s signals were then mapped onto the RGC standard brain (see STAR Methods), and accuracy of the mapping was confirmed by overlay of multiple brains with the RGC standard brain (Figures S5F-K).

We examined visual motion-induced activity in RGC terminals by presenting monocular moving gratings to the contralateral eye of the fish. Visual stimuli were presented from the side of the fish, and recorded brain areas included most of the tectal neuropil (AF10) and more ventral AFs in the pretectum and thalamus, including AF4, AF5 and AF6 (Figures 2B, 3A). Response profiles of AF4 and AF6 were largely consistent with previous studies, with AF4 being activated by ON and AF6 by OFF whole-field luminance changes (Temizer et al., 2015; Zhang et al., 2017) (Figures S6A-C). We then identified pixels that exhibited DS signals ('DS pixels'; see STAR Methods). Within the tectum, DS pixels localized to the posterior half of the SFGS1; Figures 3B, C and S7D, E), as described previously (Nikolaou et al., 2012). In a more ventral optical plane, DS pixels were found predominantly in AF5 (64.7 %), with fewer DS pixels in AF6 (23.9 %; $n = 6$; Figures 3D, J). This difference was further

augmented, when the relatively larger number of synaptic puncta within AF6 were considered. DS pixels represented about 30-40 % of the total pixels in AF5, whereas in AF6 the DS pixels comprised about 10% of the total pixels (Figure 3L). The responses localized to AF6 by our anatomical mask were observed in terminals close to the boundary to AF5, suggesting that the corresponding terminals might sit on branches of AF5-projecting RGCs (Figures 3D, I). In addition, a sparse subset of RGC terminals in AF6 was orientation selective (OS) (Figures S6F-J). In conclusion, the majority of the DS-RGC inputs are sent to AF5.

AF5 (and SFGS1) receive retinal DS responses regardless of RGC soma position within the retina

In a previous study (Naumann et al., 2016), motion stimuli were presented from below, which activates predominantly the dorsal part of the retina (Robles et al., 2014; Stuermer, 1988). It is conceivable that dorsally positioned DS-RGCs project to different AFs than those that were activated by motion shown from the side. To test this possibility, we repeated above imaging experiments while displaying moving gratings from below (Figures 3E-H). Similar to the presentation from the side, the majority of DS-RGC inputs were found in AF5 (70.8 %), while fewer were found in AF6 (18.4 %; $n = 7$ fish; Figure 3J). DS-RGC inputs from dorsal retina were also observed in SFGS1 (Figures 3F, G and S6D, E). This indicates that DS-RGCs project to AF5 and SFGS1 regardless of their soma positions along the dorsoventral axis of the retina.

To localize DS-RGC pixels within the larger neuropil volume surrounding the AFs, we registered an image stack from the *HuC:GCaMP5G* line to our reference brain. As expected, RGC axons occupied only a small subvolume of the pretectal neuropil labeled in *HuC:GCaMP5G* (Figure 3Ki). Registration of visual responses to whole-field motion in our standard brain revealed that DS responses in the panneuronal *HuC:GCaMP5G* neuropil extended outside of the AFs (Figure 3Kii, iii).

To establish a 3D map of DS representations in RGC terminals, we mapped DS pixels identified in multiple fish onto the standard brain. In the tectum, DS pixels occupied the posterior half of the neuropil volume when the stimulus was presented from the side (Figure 3M, Movie S3). When the stimulus was projected from below, DS pixels were preferentially identified in the ventral tectum (Figure 3N, Movie S4). This location is consistent with the topographic organization of the retinotectal projection (Robles et al., 2014; Stuermer, 1988). Notably, in the pretectum, a co-registration of DS pixels obtained from a single fish, which was stimulated both from the side and from below, shows that the identified DS pixels were co-localized in a similar volume, corresponding to AF5 (Figure 3O). In summary, our results demonstrate that RGC terminals exhibiting DS-responses in the pretectal neuropil are situated predominantly in AF5 and that this is independent of the position of the visual stimulus.

AF5- and SFGS1-projecting DS-RGCs show very similar DS tuning, consistent with collateral branching from the same axon

We hypothesized that the DS-RGC axon terminals in AF5 are collateral branches of RGCs projecting to SFGS1. If so, preferred directions of RGC axons in AF5 should be identical to those in SFGS1. When the visual stimuli were presented from the side (Figures 4A-D, H), the majority of the DS pixels were tuned to forward stimulus motion ($\sim 270^\circ$) in both the tectum (Figure 4B) and AF5 (Figure 4C), with a much smaller population of DS pixels with broadly distributed preferred directions between 30° and 180° . In the dorsal part of the tectum, we observed three populations of DS-RGCs, tuned to whole-field motion in a forward (270°), oblique-backward (around 45°) and downward (around 160°) direction, respectively, as reported previously (Lowe et al., 2013; Nikolaou et al., 2012) (Figures 4D, H). When the visual stimuli were presented from below, the majority of DS pixels in SFGS1 and AF5 preferred the forward direction ($\sim 0^\circ$) as well (Figures 4E-G). These results are in agreement with a direction-of-motion sensitive visual pathway composed of three differently tuned classes of DS-RGCs, whose axons branch in AF5 on their way to SFGS1.

DS-RGC terminals spatially overlap with dendrites of monocular DS-pretectal cells in AF5

We next tested the prediction that the neurites of monocular DS pretectal neurons coincided in space with DS-RGC terminals. In FuGIMA experiments, calcium responses in the neuropil are invisible due to nuclear localized GCaMP. Therefore, we registered two sets of functional imaging data to the FuGIMA standard brain: DS signals recorded in RGC terminals (*isl2b:Gal4, UAS:syGCaMP6s*) and DS signals from all neurons (*HuC:GCaMP5G*) (Figure 5A). In this overlay, DS-RGC pixels overlapped with dendrites from monocular DS cells, but not with those of translation-selective neurons (Figure 5G). Neurites of both monocular DS and translation-selective cells were also seen outside the RGC neuropil, caudal to AF6 (Figures 5B-D). This region was contained in the broader pretectal DS neuropil revealed by *HuC:GCaMP5G* imaging (Figures 5H, I). Tracings of control neurons (non-motion-sensitive) did not overlap with DS-RGC pixels (Figure 5E). Taken together, registration of two 3D maps of functional data to the FuGIMA dataset suggests that monocular DS neurons receive direct input from DS-RGCs in AF5 and that additional DS responses in the pretectum emanate from branches of pretectal optic flow responsive neurons.

Distinct classes of pretectal neurons from the optic flow-processing region project to premotor centers

We hypothesized that translation-selective neurons might project to premotor centers that drive the OMR. The FuGIMA method relies on relatively slow, distance-dependent diffusion of paGFP and

is therefore unsuited to label long-range projections. To investigate the connections of the DS pretectal area, we employed “virtual tract tracing” by interrogating the cellular-resolution brain atlas of Kunst et al. (2019). At the time of analysis, this dataset contained the morphologies of 1743 single cell tracings, all co-registered within a standard brain. Specifically, we focused on pretectal projection neurons (PPNs) whose cell bodies reside in immediate vicinity of FuGIMA neurons (Figure 6A).

38 PPNs were found to reside within the cloud-shaped “FuGIMA volume of interest” (FuGIMA VOI, offset between cell body center and edge of volume $\sim 10\ \mu\text{m}$; Figure S7A). Cell bodies of these neurons (Figure S7B) tend to be located laterally compared to those of the FuGIMA neurons (Figure 6B). Axons of PPNs terminate in the hindbrain reticular formation (25 “pretecto-reticular” PPNs, 18 = 72% thereof in the contralateral hemisphere), or the cerebellum (8 “pretecto-cerebellar” PPNs) in a mutually exclusive pattern. A large fraction of neurons also terminate in the hypothalamus (25 of 38), the thalamus (19 of 38), the raphe (21 of 38), the pretectum (18 of 38) and tegmentum (14 of 38; including the nucleus of the medial longitudinal fascicle, the oculomotor nucleus and the nucleus isthmi), in various combinations. AFs encompassing PPN termini are AF9 (9 of 38), AF6 (3 of 38) and AF6 (1 of 38). The cell bodies of pretecto-reticular PPNs reside in the posterior-lateral part of the FuGIMA VOI (Figure 6E). Their axons heavily branch in an area directly posterior and about $20\ \mu\text{m}$ ventral to the main branching area of FuGIMA cells, partially crossing the dorsal border of the hypothalamus (Figures 6D, E). Most of them (18 of 25) project bilaterally (Figures 6D, E). In contrast, cell bodies of the pretecto-cerebellar PPNs were mainly found in an anterior cluster lateral to AF9 (Figure 6F). Their neurites branch in the vicinity of the cell body, contacting AF6 ($n = 4$), AF8 ($n = 4$) or AF9 ($n = 13$), again in varied combinations, and terminate in two patches of the medial cerebellum (Figures 6D, F). The traced set of PPNs did not intersect with AF4, AF5 or AF7. In conclusion, two mutually exclusive groups of PPNs connect the optic-flow sensitive region to the reticular formation (often with collaterals in the hypothalamus) and to the cerebellum (often with collaterals in thalamus and pretectum).

Discussion

This study has revealed the cellular composition, as well as the afferent and efferent pathways, of the optic-flow processing center in the zebrafish pretectum. We demonstrate that signals from DS-RGCs are transmitted primarily to retinal arborization field AF5 in the pretectal neuropil. DS-RGC axon terminals spatially overlap with putative dendrites of simple, monocular DS pretectal neurons in AF5, but not with those of complex, translation-selective neurons. Complementation of the FuGIMA dataset with tracings from a single-neuron atlas has revealed projection targets of pretectal neurons, i.e., the reticular formation, the tegmentum, the hypothalamus, and the cerebellum. Based on our findings, we propose a model of processing stages in the optic-flow responsive pathway (Figure 7). Direction selectivity, transmitted by RGC axons to AF5 is inherited by simple, monocular DS neurons and is then combined across the two eyes, likely in the densely innervated neuropil dorso-posterior to AF6, to generate translation-selective tuning in complex cells. The behaviorally relevant binocular optic flow information, computed in the pretectum, is then further relayed to premotor areas in the hindbrain to ultimately drive optomotor behavior.

We demonstrate that DS-RGCs project mainly to AF5. A smaller fraction of DS responsive RGC terminals were also found in AF6. It is noteworthy that, to generate the consensus anatomical mask, AF boundaries were drawn by outlining the silhouettes of neuropil shapes in multiple fish. Functional data were not taken into consideration in these AF annotations, and it is conceivable that axon collaterals do not respect our annotated anatomical boundaries. It is plausible that the DS responses detectable in AF6 originate from branches of RGC axons that are primarily targeting AF5. This interpretation is in contrast to a previous study (Naumann et al., 2016), which implicated AF6 in pretectal DS-RGC processing. Naumann et al. identified a conglomerate of neuropil areas exhibiting DS responses as "AF6". The fish they imaged carried the HuC:GCaMP5G transgene, in which GCaMP is expressed in almost all neurons. Because GCaMP expression was therefore not limited to RGCs, this approach does not differentiate AFs or disambiguate RGC terminals from axons or dendrites that arise from other neurons. When we registered our two imaging datasets performed in HuC:GCaMP5G transgenic fish and RGC terminals into the FuGIMA dataset, the DS neuropil area detected in HuC:GCaMP5G transgenic fish overlaps with both RGC terminals and neurites of motion-responsive pretectal neurons. This result suggests that Naumann et al.'s "AF6" is likely a mix of AF5, AF6 and additional neuropil formed by pretectal neurons; it is certainly not exclusively AF6.

A previous comprehensive analysis of projection patterns of RGC axons revealed that AF5-projecting RGCs do not form collaterals in AF6, and vice versa (Robles et al., 2014). Furthermore, all AF5- and AF6-projecting RGCs in addition innervate specific layers of the tectum. AF6-projecting

RGCs innervate the deepest layer of the SFGS (SFGS6) and the stratum griseum centrale (SGC) (Robles et al., 2014), which do not show DS responses (Gabriel et al., 2012; Nikolaou et al., 2012). AF5-projecting RGCs, on the other hand, innervate the most superficial layer of the SFGS layer (SFGS1), which receives DS-RGC input (Gabriel et al., 2012; Nikolaou et al., 2012; this study). Assuming that multiple axonal branches of single DS-RGCs share the same tuning, our functional imaging result is therefore consistent with the anatomical organization of RGC projection patterns, further supporting AF5 as a center for DS motion processing.

We applied the FuGIMA technique (Förster et al., 2018) to tie tuning properties of individual neurons to their morphologies. This method is based on diffusion of the fluorescent paGFP and is therefore well suited to label local neurites, particularly dendrites, whose calibers are generally bigger than those of axons (Vishwanathan et al., 2017), but cannot be used to trace axons over long (>200 μ m) distances. We focused on monocular DS neurons, i.e., neurons that respond to movement detected by the contralateral eye, located in the anterior medial cluster of the pretectum, as reported before (Kubo et al., 2014). Ipsilateral monocular DS neurons, which were present in the much larger dataset of Kubo et al. (2014), are missing in our FuGIMA dataset (Figure S2E). We suspect that this discrepancy is rooted in the different transgenic lines used (*HuC:GCaMP5G* by Kubo et al. (2014) and *Gal4^{S1101t} x UAS:FuGIMA* in this study, respectively).

We hypothesized that at least a subset of the translation-selective pretectal cells might be projection neurons (PPNs), which convey information to the premotor centers that drive the OMR. Activity in the reticular formation and the tegmentum has been shown to be correlated with forward swimming and/or turning behavior (Chen et al., 2018; Naumann et al., 2016; Portugues et al., 2014; Vladimirov et al., 2018). Another potential recipient of optic-flow related information from the pretectum is the cerebellum. Previous work described cerebellar tuning to whole-field motion in cerebellar granule and Purkinje cells (Knogler et al., 2017; Matsui et al., 2014). Purkinje cells in the medial part of the cerebellum were active during OMR, whereas the lateral part was active during the OKR (Matsui et al., 2014). We interrogated a single-neuron atlas (Kunst et al., 2019) to search for PPNs whose cell bodies reside in the optic-flow responsive region. Most PPNs from this dataset send axons to either of two targets, the reticular formation or the cerebellum. In addition, many PPN axons form collateral branches in the hypothalamus, thalamus, raphe, pretectum, and tegmentum. A mutually exclusive innervation of cerebellum and reticular formation by pretectal efferents has also been reported for adult zebrafish (Yáñez et al., 2018). The PPNs that we describe here are not characterized functionally. However, 10 out of 38 PPNs arborize in AF6, 8, 9, which some of the FuGIMA-reconstructed neurons also innervate, suggesting that a subset, if not all, of the PPNs correspond to optic flow responsive cells that we analyzed with FuGIMA. Binocular integration

depends on interhemispheric transfer of DS information (Kubo et al., 2014; Naumann et al., 2016). Interestingly, when we scanned the single-cell atlas anterior to the FuGIMA volume, we discovered a population of commissural neurons in the pretectum that might subserve this function (unpublished observations). Commissural neurons projecting to the contralateral pretectum have been described in adult zebrafish (Yáñez et al., 2018).

In conclusion, our results identify a cell-resolved retina-pretectum-hindbrain pathway of the optic flow computation underlying the OMR. A combination of functional and anatomical approaches can offer a unique opportunity to gain new insights into neural circuits that cannot be obtained by a single approach alone. Our circuit model provides a blueprint for the identification of synaptic connectivity and circuit mechanisms underlying optic-flow processing in the vertebrate brain.

Acknowledgments

We thank Irene Arnold-Ammer for plasmid construction, Estuardo Robles for advice on the annotations of RGC arborization fields, Marco Dal Maschio for assistance with 2p microscopy, Thomas Helmbrecht and Vilim Štih for writing code enabling fast regressor based analysis of functional imaging time series, Michael Kunst for advice on image registration with ANTs and sharing of the single-neuron database prior to publication, Nawwar Mokayes for programming, Aristides B. Arrenberg and agency Prudenter Agas for illustrations of the visual stimulation setup, the entire Baier lab for constructive feedback throughout the project, the Max Planck Computing and Data Facility in Garching for processing the image registration and the staff of the MPIN fish facility for outstanding fish care. Funding was provided by the Max Planck Society (all authors) and the DFG Priority Programme “Computational Connectomics” (SPP 2041, FK).

Author contributions

HB and FK conceived the project. AK performed FuGIMA experiments, generated the *UAS:FuGIMA* and *UAS:FuGIMA-C3PA* transgenic lines and performed anatomical registrations and complementation analyses. YW performed the imaging on RGC terminal responses and analyzed the direction-selective responses in RGCs. FK generated the *UAS:syGCaMP6s* transgenic line. AK, YW, and FK annotated arborization fields. AK, YW, HB and FK wrote the manuscript.

Declaration of Interests

The authors declare no competing interests.

Figures

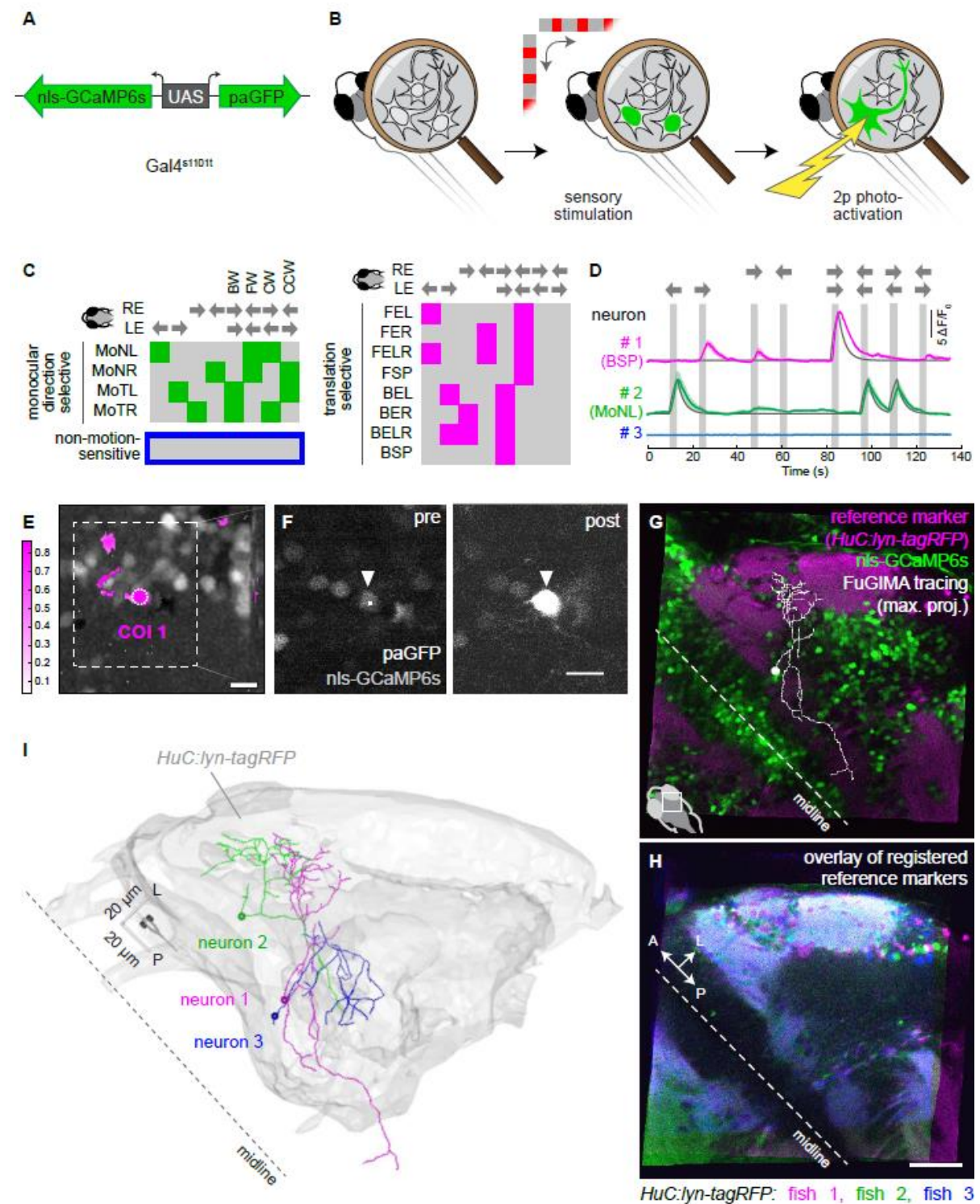


Fig. 1

Figure 1: FuGIMA enables morphological reconstructions of functionally characterized pretectal neurons. (A) The bidirectional genetic construct *UAS:FuGIMA* enables co-expression of nls-GCaMP6s and paGFP using the Gal4/UAS system. (B) FuGIMA workflow: Inactive nls-GCaMP6s and paGFP show little/no fluorescence. During stimulation with horizontally moving gratings, neuronal activity is recorded to determine a cell-of-interest (COI). PaGFP is focally photoactivated with a two-photon (2p) laser ($\lambda=750$ nm) and subsequently labels the cell of interest's morphology by diffusion. (C) Top: The presented visual stimulus consists of eight motion phases, i.e., four monocular (nasalward left, temporalward left, temporalward right, nasalward right) and four binocular (backward - BW, forward - FW, clockwise - CW, counter-clockwise - CCW) phases (see also Figure S2A). Below: Of 2^8 possible regressors, the following response types were investigated (barcode visualization): four monocular direction-selective types (green square), eight translation-selective response types (magenta square), and the non-motion-sensitive type (blue outline). Response type names are adapted from Kubo *et al.* (2014). Filled squares symbolize neuronal activity during the stimulation phase. The color code applies to other panels of this figure. Mo: monocular, N: nasalward, T: temporalward, L: to the left eye, R: to the right eye, F: forward translation, B: backward translation, E: excited by, SP: specific. (D) nls-GCaMP6s fluorescence time series of example neurons of distinct response types identified by regressor-based analysis (overlaid on the respective regressor, grey). Solid colored line: average of three repetitions, shaded area: SEM, grey bars: stimulation periods. (E) Overlay of field-of-view (mean $\Delta F/F_0$) and pixel-wise regressor based analysis (color bar: Pearson's correlation coefficient), highlighting two neurons best correlated with the regressor 1 shown in (D, top trace). The white dotted circle indicates example neuron 1 (COI1), white dashed square indicates field of view used in (F). (F) Photoactivation of neuron 1. Before photoactivation, most nuclei exhibit dim nls-GCaMP6s fluorescence. After photoactivation of the soma, neuron 1 exhibits bright paGFP fluorescence (white arrowhead: neuron 1, small white square: approximate photoactivation region) (G) Tracing of photoactivated neuron 1 (white, maximum intensity projection) superimposed on one plane of the registered experimental z-stack (green: nls-GCaMP6s/paGFP; magenta: *HuC:lyn-tagRFP*). (H) Overlay of the reference marker (*HuC:lyn-tagRFP*) derived from three experimental fish that have been registered to the standard brain. (I) 3D rendering of the standard brain surface (grey) with three registered tracings (dorsal view). The color of the three tracings corresponds to that used in (D). Scale bars: 10 μ m in (E, F), 50 μ m in (H). See also Figure S1.

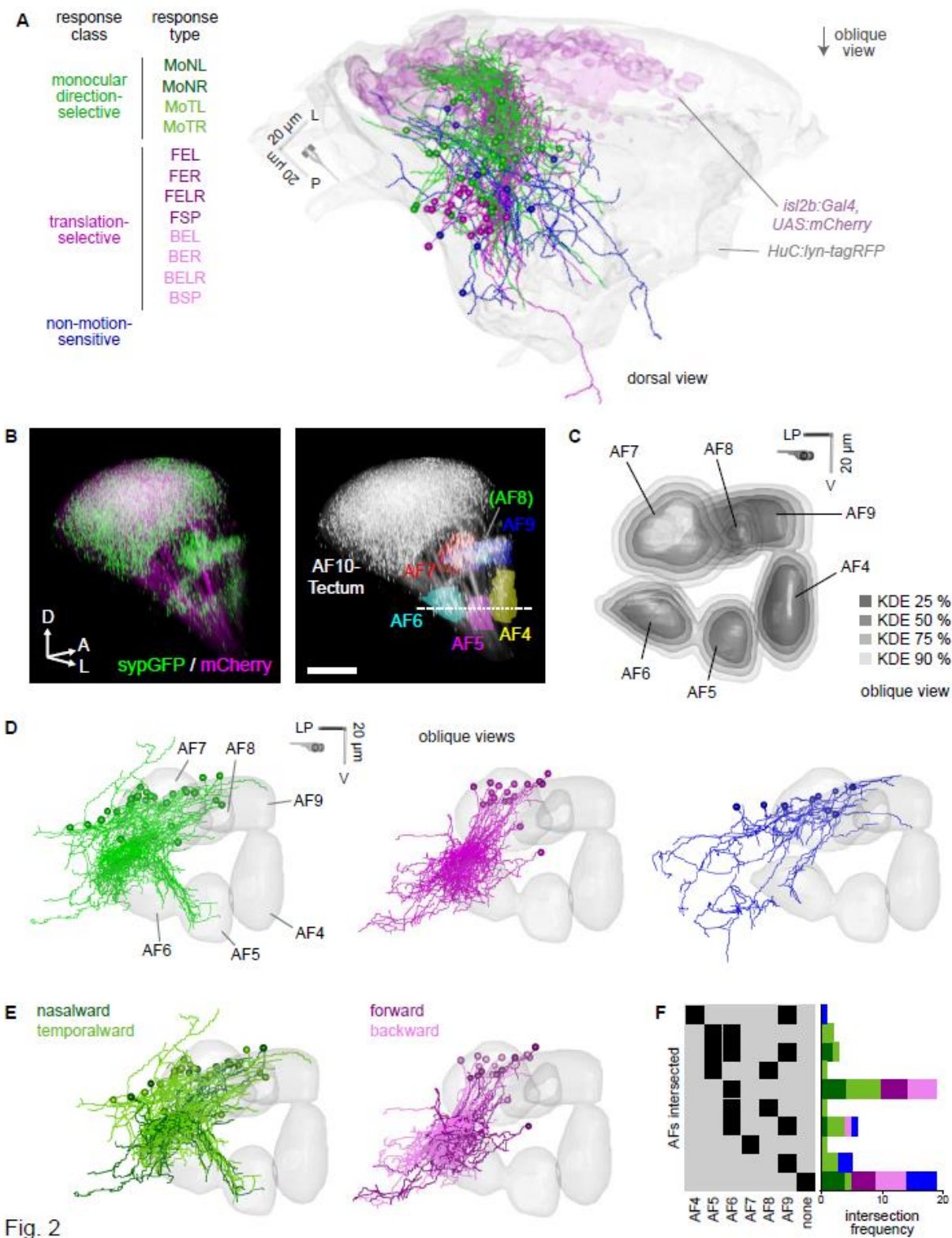


Fig. 2

Figure 2: Monocular DS and translation-selective neurons show different morphologies. (A) 3D rendering of all FuGIMA tracings (n=58 tracings) with the standard brain (*HuC:lyn-tagRFP*) and RGC terminals as labeled with *isl2b:Gal4, UAS:mCherry*. The tracings are color-coded according to the neurons' response class (dorsal view). See also Movie S1. **(B)** Anatomical representation of AFs. (Left) SypGFP signal driven by *atoh7:Gal4* driver reveals distinct AFs at 6 dpf (compound of three fish). (Right) Annotation of AFs in the same 3D volume. Dotted line corresponds to the optical planes for imaging AF4, AF5 and AF6. See also Movie S2. **(C)** Boundaries of AFs (from the RGC standard brain) after registration to the FuGIMA standard brain. 3D rendering of a thresholded kernel-density estimation (KDE) of co-registered AF masks from (B) (thresholded to 25, 50, 75, and 90 %, n = 7 bridging z-stacks, from 4 fish). See also Figure S3. **(D)** 3D rendering of FuGIMA tracings grouped by response class together with AF masks (oblique views, AFs 4 – 9, KDE=50%). **(E)** Further classification of FuGIMA neurons by direction selectivity (left: light green, monocular temporalward; dark green, monocular nasalward. Right: light magenta, backward; dark magenta: forward) **(F)** Analysis of morphological types of all FuGIMA neurons. Intersections of individual tracings with AFs 4-9 reveals widespread intersections between FuGIMA tracings and the AFs (black squares symbolize the intersection with the indicated AF). Right: intersection frequency according to response class. Scale bar: 50 μ m in (B). See also Figures S2-4.

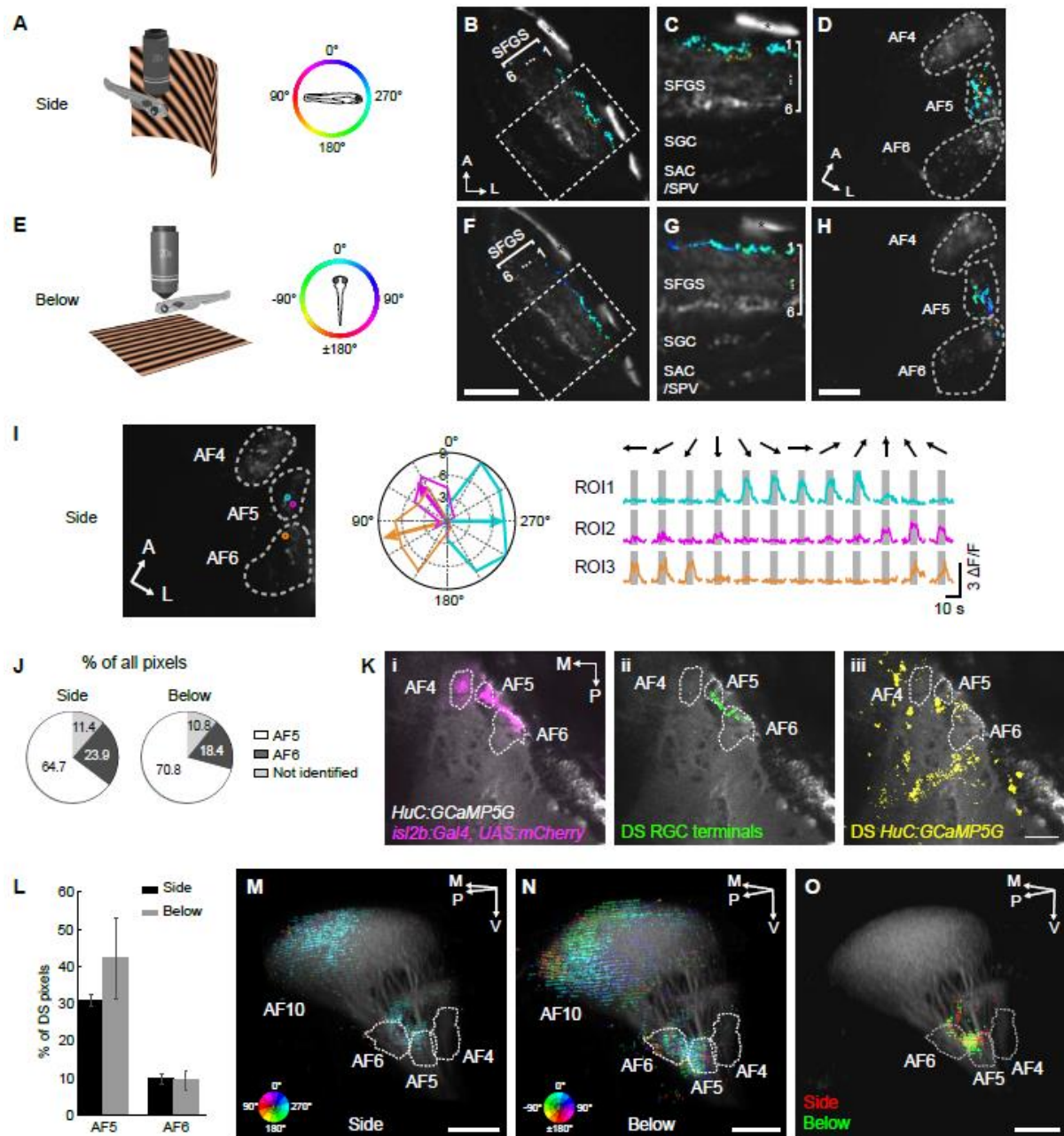


Fig. 3

Figure 3: Direction-selective RGCs largely terminate in arborization fields AF5 and tectum (AF10). (A) Schematic of the experimental setup for visual stimulation with moving gratings presented from the side. Color indicates direction of motion. (B-D) DS pixels in AF10 (B, C) and AF4, AF5 and AF6 (D). (E) Schematic of the experimental setup for visual stimulation with moving gratings presented below. (F-H) DS pixels in AF10 (F, G) and AF4, 5 and 6 (H). In (B-D) and (F-H), DS pixels are plotted on top of the mean image of syGCaMP6s (grey). (I) Representative responses of DS-RGC terminals in AF5 and AF6. Visual stimuli were presented from the side. ROIs correspond to synaptic puncta marked in the left image. Polar plot (middle) is derived from the $\Delta F/F$ traces shown on the right. (J) Distribution of DS pixels identified in ventral AFs. The pie charts show the percentage of DS pixels residing in AF5, AF6 and a region neither AF5 nor 6 ("not identified"), summed from 6 and 7 fish for side and below stimulus presentation, respectively. (K) Overlay of a registered *HuC:GCaMP5G* image (grey) with RGC axons (i, *isl2b:Gal4, UAS:mCherry*), DS-RGC terminals (ii, identified from below projection, sum of 6 fish), and DS neuropil of *HuC:GCaMP5G* fish (iii, identified from below projection, sum of 5 fish) in an optical plane that contains AF4, AF5 and AF6. DS-RGCs and DS neuropil represent all DS populations tuned to any direction of motion. (L) Percentage of DS pixels relative to the entire pixel counts in AF5 and 6. Average pixel counts in each AF were quantified using anatomical stacks of *isl2b:Gal4, UAS:sypGFP* fish (see STAR Methods for details). N = 6 fish (side) and 7 fish (below) for each AF. Error bars represent SEM. (M, N) 3D representations of DS-RGC terminals. For side-presented 3D map (M), both AF10 and AF4, AF5 and AF6 volumes are pooled from 6 imaged volumes. For below-presented 3D map (N), both AF10 and AF4, AF5 & AF6 volumes are pooled from 7 imaged volumes. Color wheels represent the preferred directions of DS pixels. The intensity of DS pixels corresponds to the probability of a particular pixel to be DS across all imaged fish (the maximum intensity corresponds to the frequency of 0.67 and 0.57 for M and N, respectively). See also Movies S3 and S4. (O) Comparison of DS-RGC terminals responsive to side vs. below presentations. Composite 3D map of a single fish that underwent both side and below presentations. Note that DS-RGC terminals identified by side (red) and below (green) presentations co-localize in AF5. A, anterior; P, posterior; L, lateral; M, medial; V, ventral; SFGS, stratum fibrosum et griseum superficiale; SGC, stratum griseum centrale; SAC, stratum album centrale; SPV, stratum periventriculare; *, skin auto-fluorescence. Scale bars: 20 μm (F), and 10 μm (H), 30 μm (K) and 50 μm in (M-O). See also Figures S5, 6.

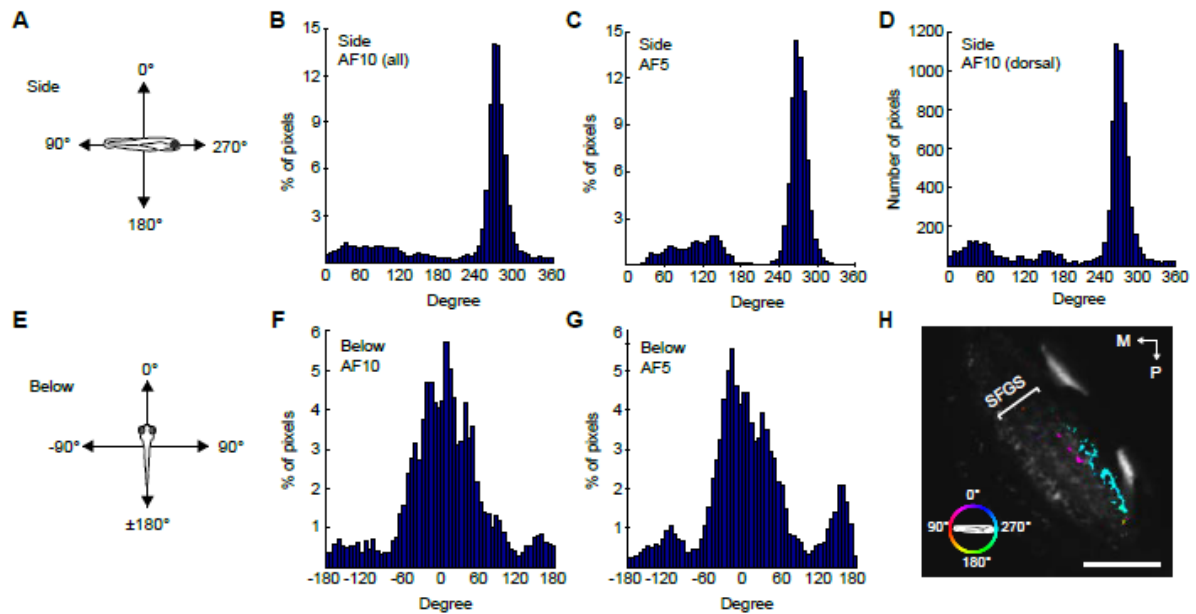


Figure 4: Distribution of preferred directions of DS-RGCs reveals shared inputs in AF5 and tectum. (A) Direction space of motion stimulus presented from the side. (B,C) Distributions of preferred directions of DS-RGC terminals in AF10 (B) ($n = 6$ fish) and AF5 (C) ($n = 6$ fish). Motion was presented from the side. (D) Distribution of preferred direction of DS-RGC terminals in the dorsal AF10. In contrast to (B) where the entire AF10 was sampled, only 3 planes (separated by $4\ \mu\text{m}$) in AF10 were selected in this histogram, as was reported previously (Nikolaou et al., 2012). (E) Direction space of motion stimulus presented from below. (F,G) Distributions of preferred directions of DS-RGC terminals in AF10 (F) ($n = 7$ fish) and AF5 (G) ($n = 7$ fish). Motion was presented from below. (H) DS response map of a single representative optical plane in the dorsal AF10 analyzed in (D). P, posterior; M, medial. Scale bar: $30\ \mu\text{m}$ in (H).

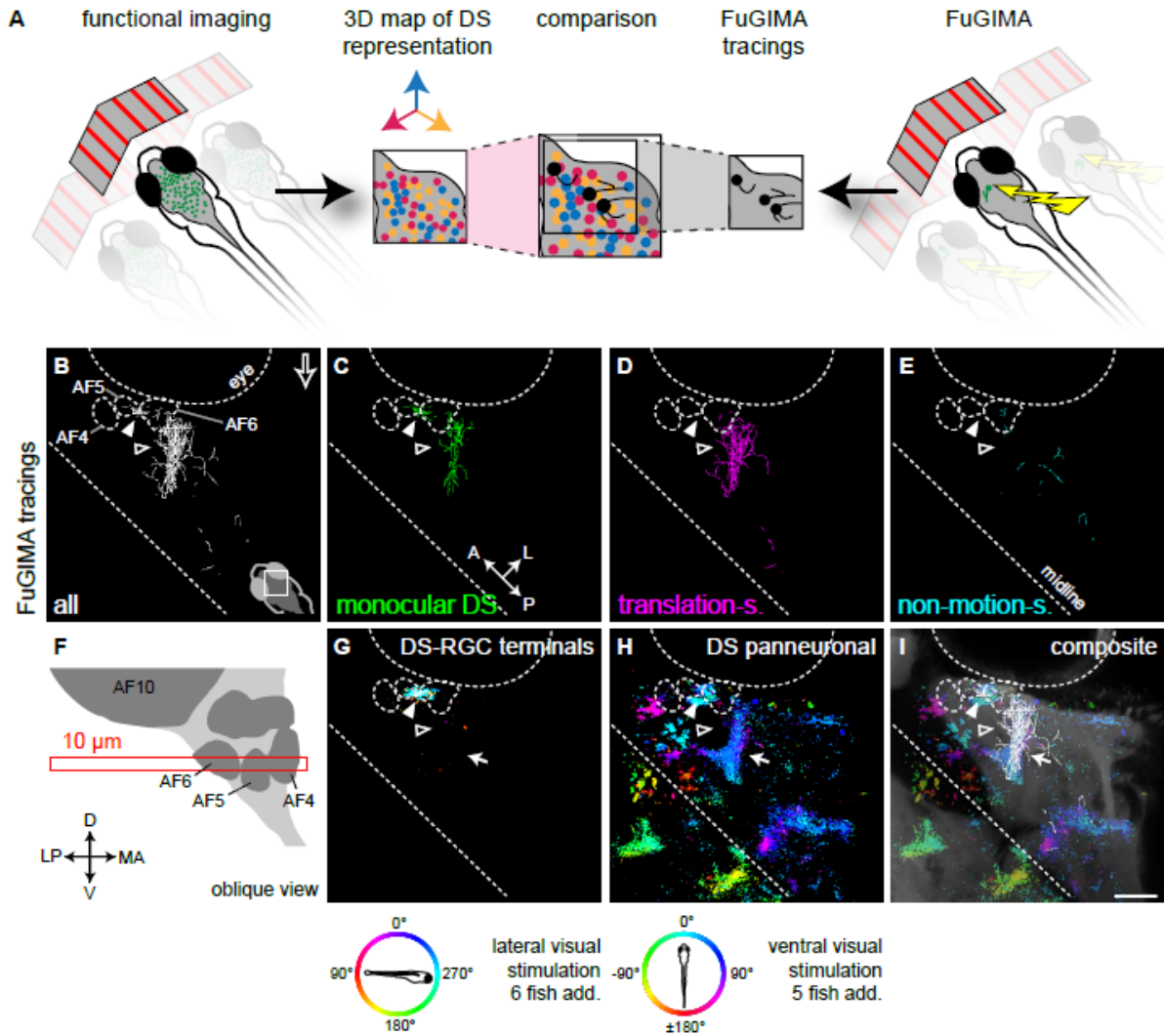


Figure 5: Co-registration of FuGIMA with two functional imaging datasets shows overlap of DS-RGC input with monocular DS, but not with translation-selective neurons. (A) Schematic illustrating acquisition and integration of the functional maps and the FuGIMA dataset. **(B-I)** A slice of the FuGIMA volume at the level of the AFs 4 – 6 with FuGIMA tracings and co-registered functional maps of DS-RGC terminals and DS neurons (right hemisphere, maximum intensity projection over $z = 10 \mu\text{m}$, see schematic in (F); of 58 FuGIMA tracings, 42 of the following classes extend into the slice: 19 monocular DS, 17 translation-selective, 6 not motion-sensitive). **(B-E)** FuGIMA tracings (open white arrowhead: FuGIMA tracing bundle, filled white arrowhead: small tracing patch at the border of AFs 5 and 6, open arrow: direction of oblique view): **(B)** all (white), **(C)** monocular DS (green), **(D)** translation-selective (magenta), **(E)** Non-motion-sensitive (blue). **(F)** Schematic of z-stack slicing (oblique view onto optic tract (light grey) and AFs (dark grey)) **(G)** registered 3D map of DS-RGC terminals (*isl2b:Gal4, UAS:syGCaMP6s*, see color wheel below for key of moving gratings presented from side, composite of 6 fish). **(H)** Registered 3D map of DS-panneuronal (*HuC:GCaMP5G*, white arrow: broad band of DS pixels, see color wheel below for key of moving gratings presented from below, composite of 5 fish), **(I)** Composite of DS-panneuronal with all FuGIMA tracings and standard brain reference marker (*HuC:lyn-tagRFP* in grey). For (G)-(I), imaging artifact DS pixels located of the eye cup were removed with a mask. Scale bar: 50 μm in (I).

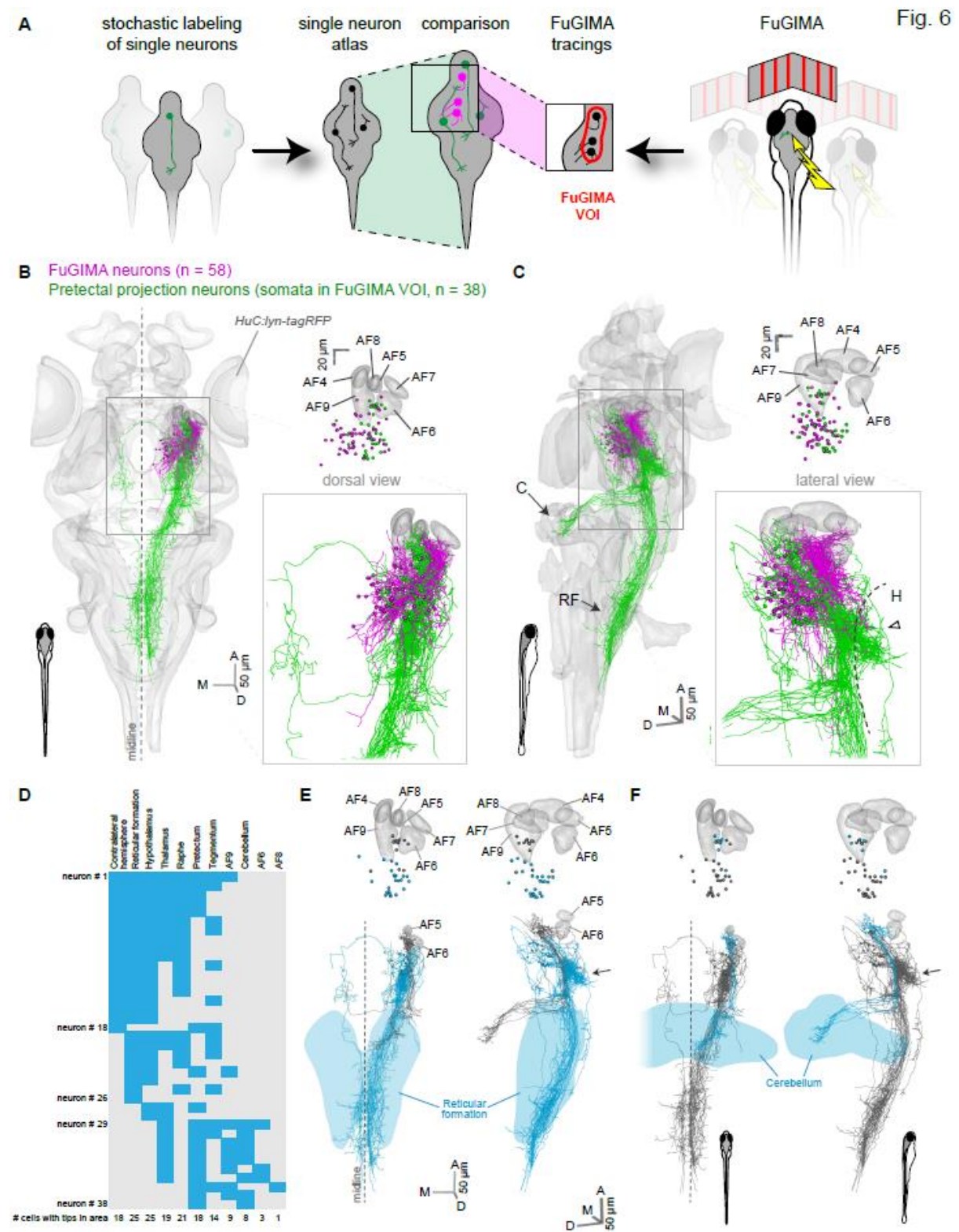


Figure 6: Pretectal projection neurons target the cerebellum and ventral hindbrain. (A) Schematic illustrating the strategy to combine the single-neuron atlas of Kunst et al. (2019) and the FuGIMA dataset. **(B, C)** 3D representation of the standard brain (*HuC:lyn-tagRFP*) together with all FuGIMA neurons (magenta, $n = 58$) as well as pretectal projection neurons (PPNs, green, $n = 38$), chosen based on their soma location within the FuGIMA “volume-of-interest” (FuGIMA VOI, Figure S7). **(B)** Left: dorsal view, top right: dorsal view of cell bodies with AFs 4-9, bottom right: detail of tracings. **(C)** as (B), but lateral view (C: cerebellum, RF: reticular formation, H: hypothalamus, dashed line: dorsal border of hypothalamus, open arrowhead: dense branching of PPNs). **(D)** Intersection analysis of PPNs with annotated brain areas, i.e., contralateral hemisphere, reticular formation, hypothalamus, thalamus, raphe, pretectum, tegmentum, AF9, cerebellum, AF6, and AF8. Each row represents one neuron, blue filled rectangles symbolize intersection with the annotated brain area. **(E)** 3D rendering of intersection of PPNs with the reticular formation (blue: intersecting tracings ($n = 25$ of 38 PPNs), grey: not intersecting PPNs, light blue: reticular formation, top: somata and AFs 4 - 9, bottom: tracings and AFs 5 - 6, left: dorsal view, right: lateral view, arrow: dense branching area in dorsal hypothalamus). **(F)** As (E), but intersection of PPNs with the cerebellum (blue: intersecting tracings ($n = 8$ of 38 PPNs), light blue: cerebellum). See also Figure S7 and Movie S5.

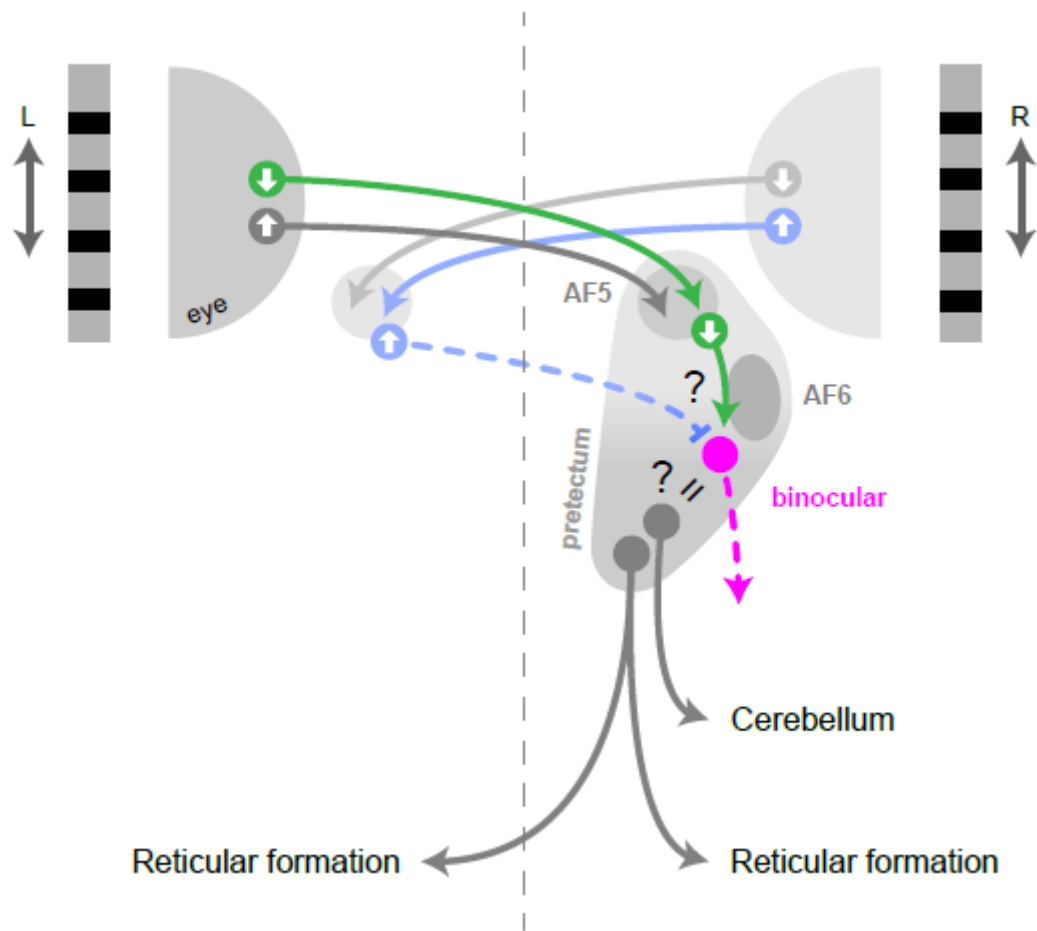
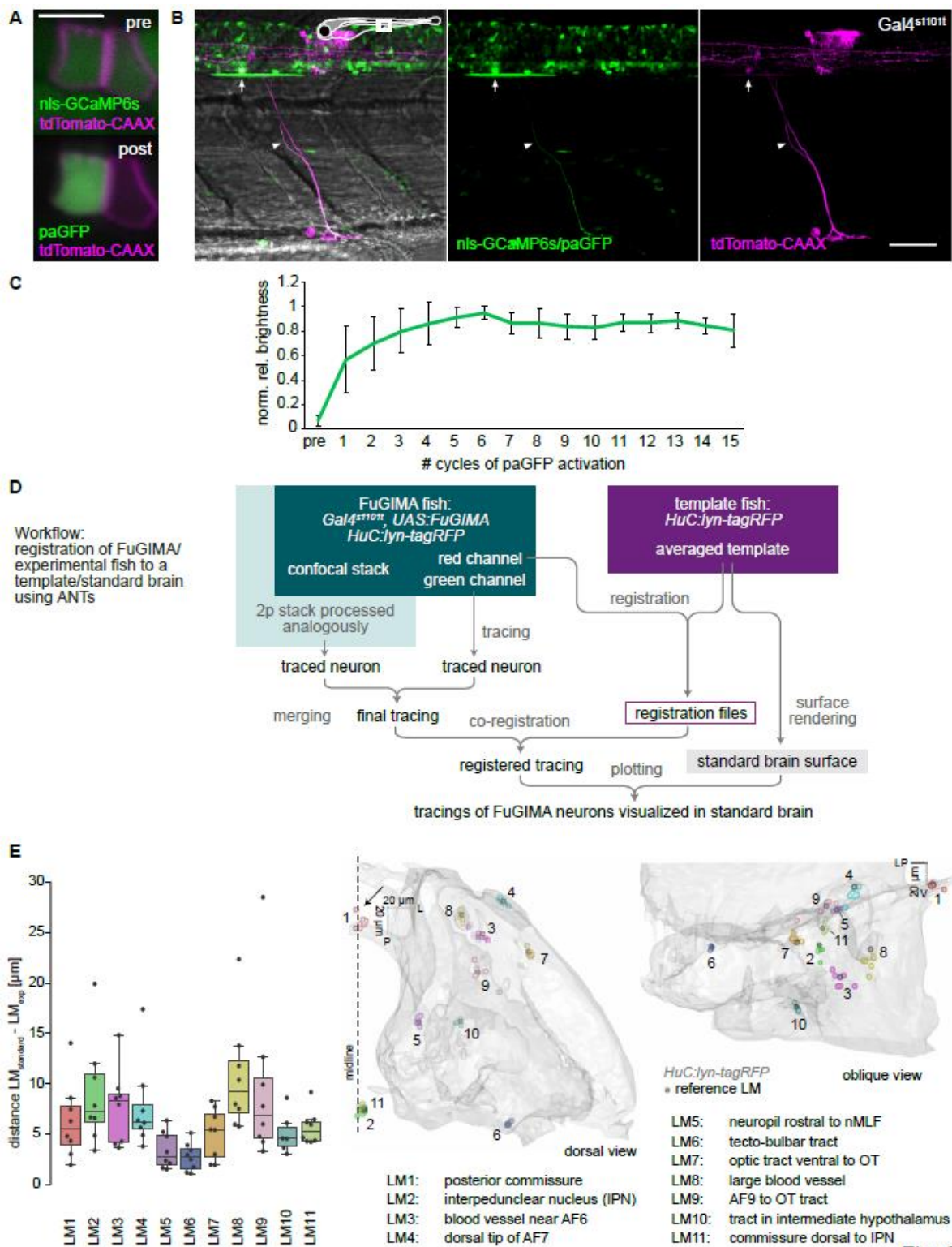


Figure 7: Model for the optic-flow processing pathway. The majority of pretectal DS-RGCs terminate in AF5, where they likely synapse onto simple monocular DS neurons. Monocular DS neurons project to a neuropil region within the pretectum, close to the dorsal edge of AF6, where they overlap with translation-selective neurons. Binocularity can be established via inhibition by predicted commissural monocular DS neurons. Information about translational optic flow is transmitted by mutually exclusive populations of pretectal projection neurons to premotor centers either in the cerebellum or in the reticular formation, together evoking directed optomotor responses.

Supplemental information



Supplementary Figure S1 (related to Figure 1): Characterization of paGFP activation in single cells, registration procedure of tracings and alignment precision of landmarks. (A) Application of the FuGIMA photoactivation protocol in a single spinal cord neuron co-expressing *UAS:FuGIMA* and *UAS:tdTomato-CAAX* (driver: *Gal4^{1101t}*). Photoactivation in a single spinal cord neuron, pre- and post-photoactivation with a single activation cycle (brightness/contrast adapted separately). (B) Lateral views of the tail with the photoactivated neuron extending from the spinal cord after full photoactivation protocol of 15 cycles. (Inset: rectangle on fish schematic indicates the field of view. Green: nls-GCaMP6s/paGFP, magenta: tdTomato-CAAX, white arrow: soma of photoactivated neuron, arrowhead: filled neurite). (C) Time course of paGFP brightness in the soma over the course of 15 cycles of photoactivation ($n = 5$ pretectal neurons in 3 fish, mean \pm STD). (D) Workflow of image registration enabling visualization of FuGIMA neurons in the standard brain. Experimental z-stacks are split into two separately processed channels. Neurons are traced in the nls-GCaMP6s/paGFP channel and tracings of neurons imaged at both the two-photon (2p) and the confocal microscope are merged. In parallel, the reference marker channel (*HuC:lyn-tagRFP*) is registered to the standard brain (averaged *HuC:lyn-tagRFP*). The resulting registration files are applied to tracings (co-registration), enabling their visualization within the volume of the standard brain. (E) Quantification of distances between the location of landmarks in the standard brain and in the registered experimental fish. Left: combined box plot and swarm plot (middle horizontal line: median, horizontal box outlines: first and third quartile, whiskers: last points included in 1.5 * interquartile range from the respective quartile), right: 3D rendering of landmarks in the standard brain (grey surface: reference marker *HuC:lyn-tagRFP*, dark grey: landmark position in standard brain, colors: registered landmarks from experimental fish, $n = 8$ z-stacks from 6 fish for LM 1 – 9 and 11, $n = 6$ z-stacks from 4 fish for LM 10, middle: dorsal view, black arrow: viewing direction for lateral view, shown on the right, LM, landmark). Scale bar: 5 μ m in (A), 50 μ m in (B).

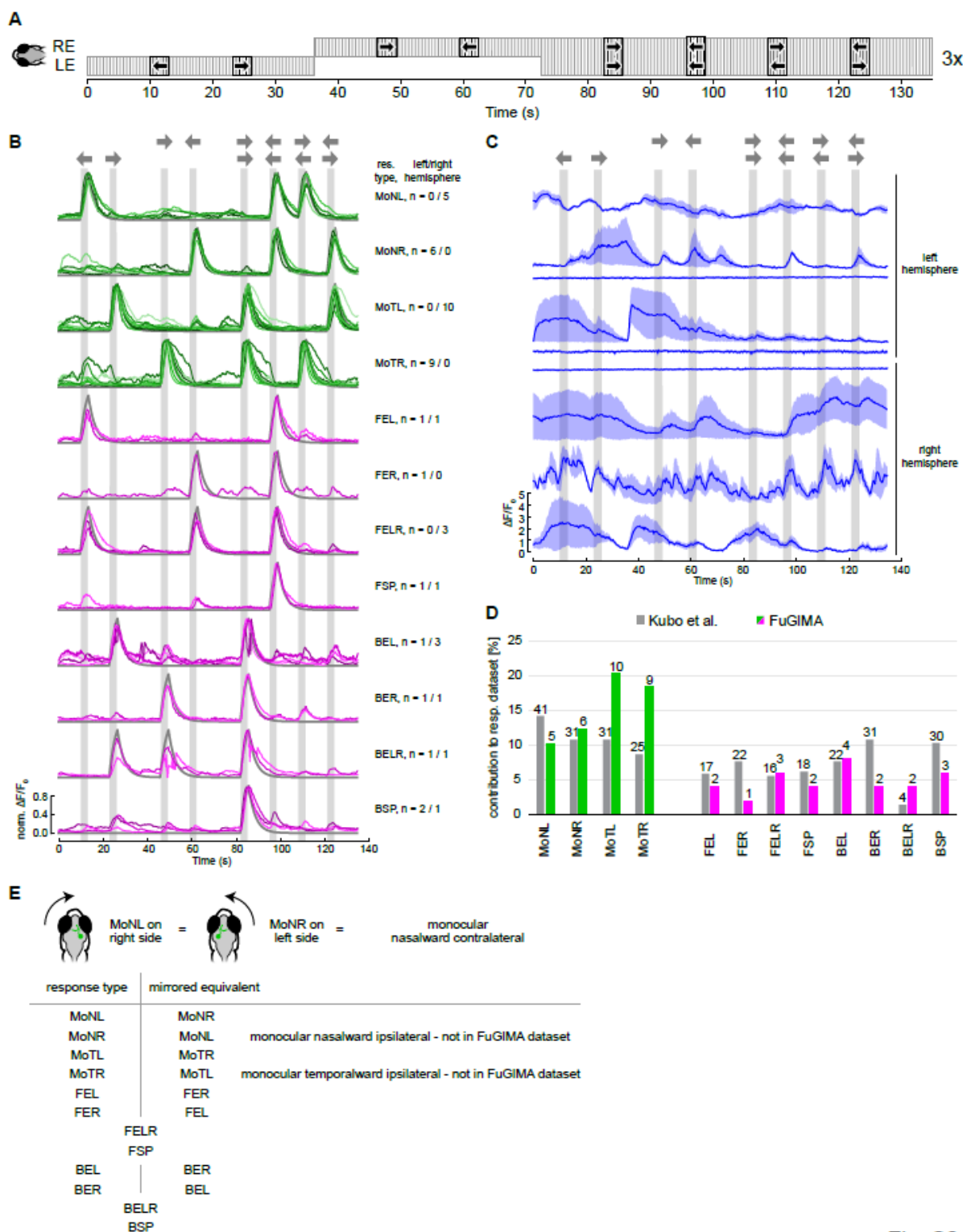
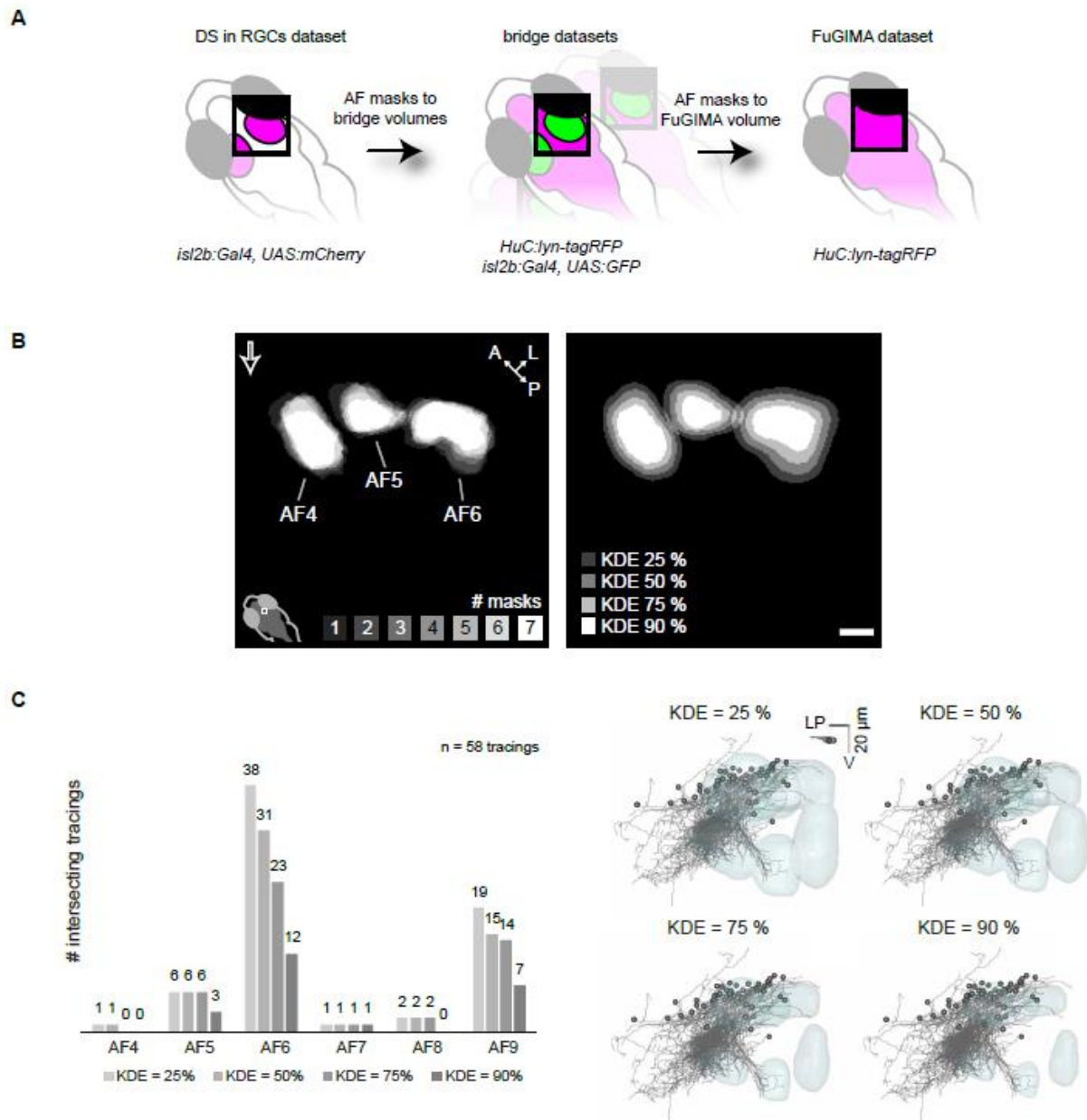


Fig. S2

Supplementary Figure S2 (related to Figures 1 and 2): Visual stimulus protocol, functional imaging time series of all FuGIMA neurons and comparison of response type sampling with Kubo *et al.* (2014). **(A)** During functional imaging, fish are presented with the following whole-field motion stimulus, consisting of eight motion phases with three repetitions (same order): Horizontally moving gratings (3 s each, black arrows) are presented in four monocular phases (left nasalward, left temporalward, right temporalward, right nasalward), followed by four binocular phases (backward, forward, clockwise and counter-clockwise) and interspersed by the presentation of stationary gratings (grey, 10 s) (RE: right eye, LE: left eye). **(B)** Normalized fluorescence traces of motion-sensitive pretectal FuGIMA neurons grouped according to their response type, numbers indicate occurrence in FuGIMA dataset and hemisphere of origin. **(C)** Fluorescence traces of non-motion-sensitive pretectal FuGIMA neurons and hemisphere of origin (blue line: average over three repetitions, light blue: SEM). **(D)** Comparison of response type frequency between Kubo *et al.* (2014) (number of cells per fish) and this work (total number of cells in the dataset). Proportions of response type are normalized to the total number of neurons across the investigated motion-sensitive response types (four monocular DS and eight translation-selective), absolute number of neurons are indicated on top of each bars. **(E)** FuGIMA neurons were imaged in both left and right hemispheres. Mirroring leads to a change in response type name as indicated.



Supplementary Figure S3 (related to Figure 2): Establishment of arborization field approximation boundaries and effect of boundary stringency on intersections with FuGIMA tracings. (A) Schematic illustrating registration of AF masks from the RGC standard volume via bridging z-stacks (derived from multiple fish) to the FuGIMA reference brain. **(B)** Generation of approximation boundaries of AFs based on a kernel-density estimation (KDE) over registered AF masks (underlying Figure 2C). Left: Overlap of registered AF masks (n = 7 bridging z-stacks, from 4 fish, open arrow: direction of oblique view), right: KDE of registered masks, thresholded to 25, 50, 75, and 90 %. **(C)** Quantification of intersections of FuGIMA tracings with AF boundaries of various stringency (KDE=25, 50, 75, and 90%). Right: 3D renderings of AF boundaries of various stringency and the full FuGIMA dataset (oblique view). Scale bar: 20 μm in (B).

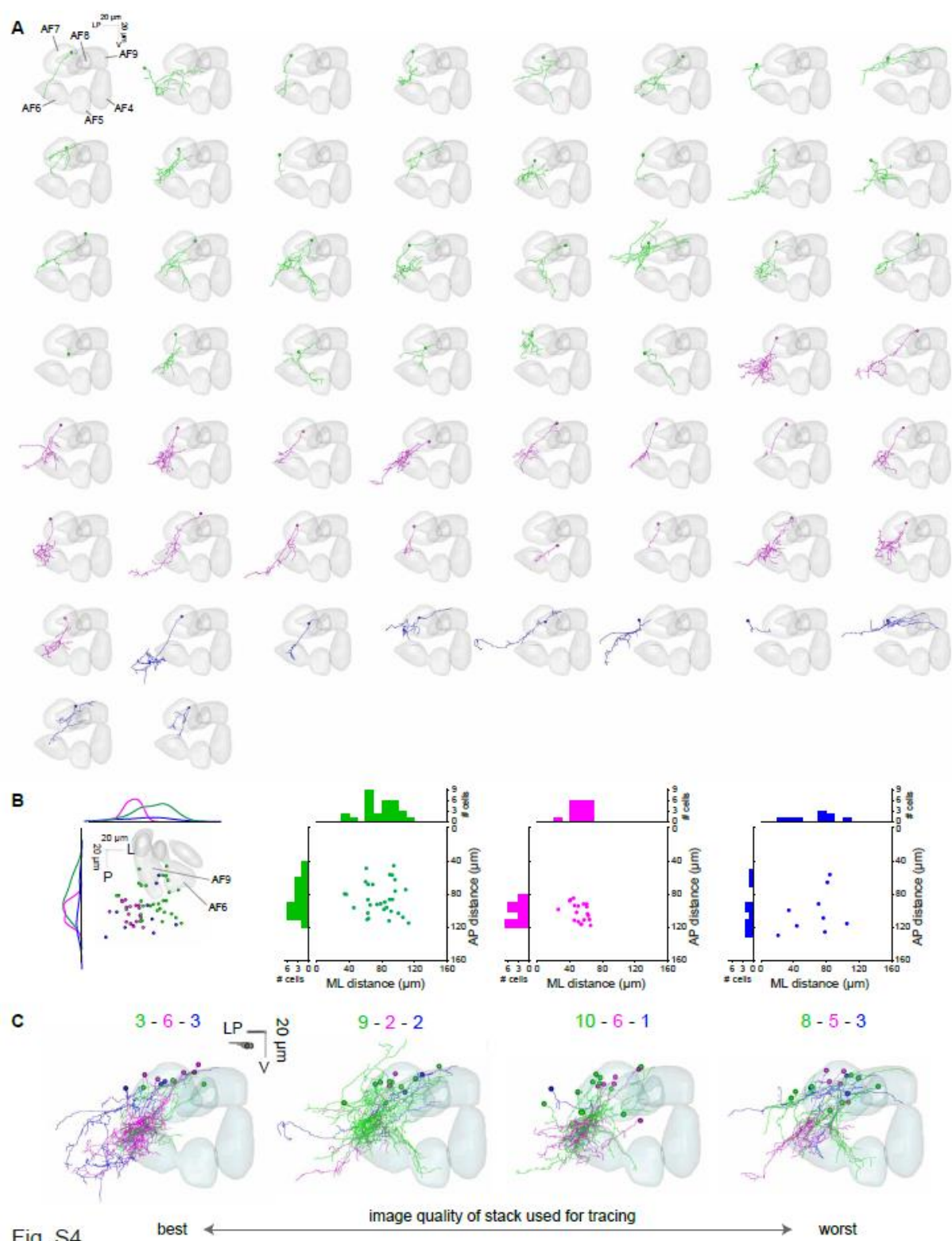
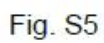
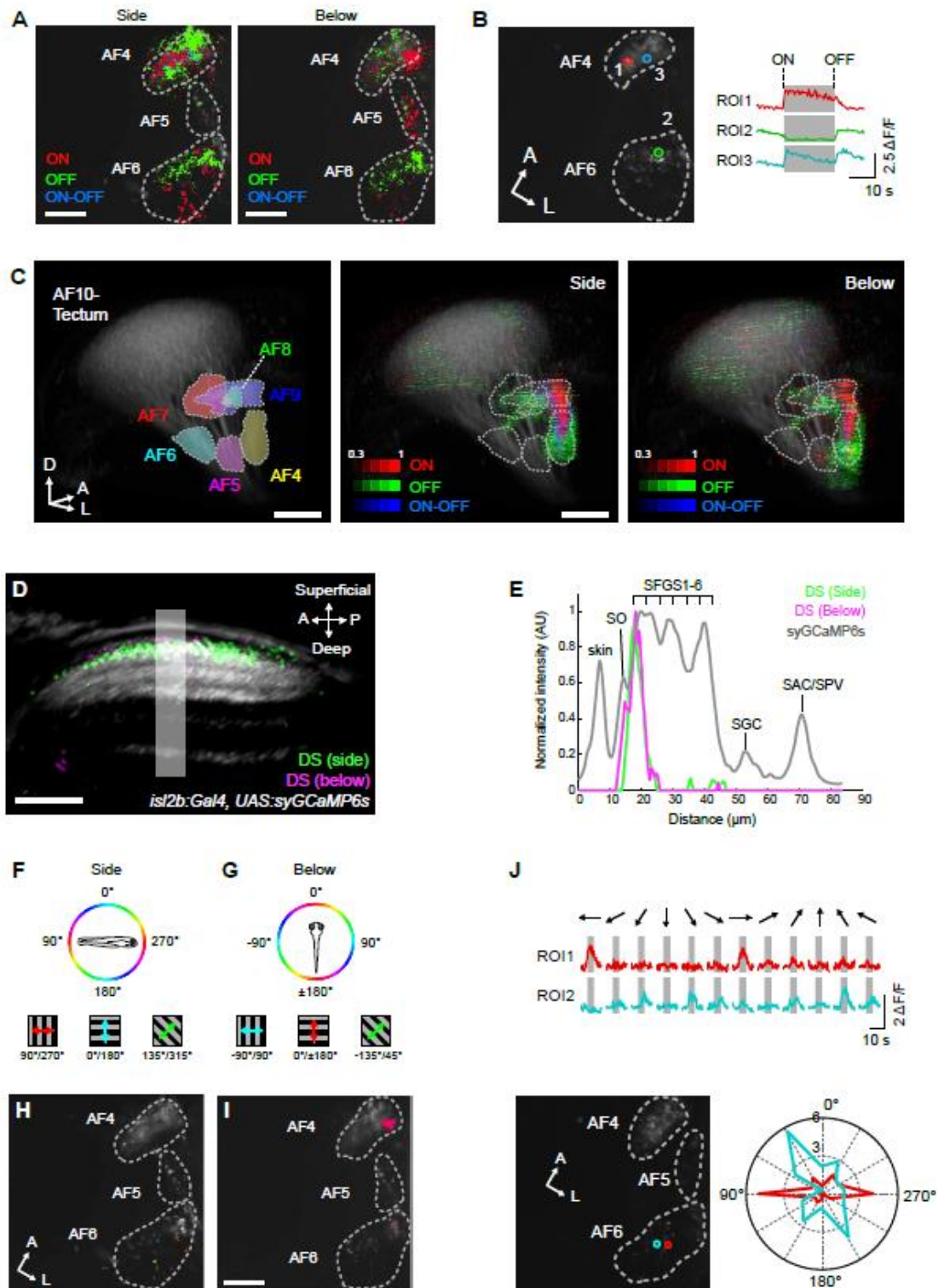


Fig. S4

Supplementary Figure S4 (related to Figure 2): Morphology of all FuGIMA neurons, soma locations regarding response class and split of dataset according to z-stack quality. (A) Individual FuGIMA neurons plotted together with AF masks (KDE=50%), tracings color-coded according to response class (green: monocular DS, magenta: translation-selective, blue: non-motion-sensitive, color-code as in Figure 1C, oblique view). **(B)** Soma location of FuGIMA neurons color-coded according to their response class. (Left) Montage of 3D rendering of FuGIMA somata with surfaces of AFs 4-9 and KDE for ML and AP distributions. (Right) Plot of soma location with histogram of ML and AP distribution (separated by response class). ML: medial-lateral, AP: anterior-posterior, distance measured from the origin as defined in Kubo et al., 2014. **(C)** Split of FuGIMA dataset into four categories according to image quality of the z-stack ("best" to "worst", manual annotation). For each category, the tracings of each class are color-coded as in (A), and the number of each class is stated on top. All four categories contain tracing of all response classes, with relatively more translation and non-motion-sensitive tracings emanating from the best quality z-stacks.



Supplementary Figure S5 (related to Figure 3): Image registration work flow to generate a 3D map of direction-selectivity, characterization of *isl2b:Gal4*, *UAS:syGCaMP6s* expression and overlay from image registration. (A) Schematic workflow for registering functional responses with anatomical structures. For clarity, only 3 preferred directions are represented here. See STAR Methods for details. **(B, C)** Subcellular localization of syGCaMP6s in the tectum/AF10 (B) and AF4, AF5 and AF6 (C) in *isl2b:Gal4*, *UAS:syGCaMP6s*, *UAS:mCherry* fish. Note that syGCaMP6s expression exhibits punctate signals in RGC terminals, in contrast to uniform mCherry signals in *en passant* RGC axon bundles. SO, stratum opticum; SFGS, stratum fibrosum et griseum superficiale; SGC, stratum griseum centrale; SAC, stratum album centrale. **(D)** Schematic illustration of AFs (modified from Burrill and Easter (1994)). Blue dotted lines indicate approximate z-planes shown in other panels of this figure. OT, optic tract. **(E)** Lipophilic dye Dil injection of the RGC axons in *isl2b:Gal4*, *UAS:Dendra-kas* fish. Note that the *isl2b:Gal4* line labels most of RGCs projecting to AF4, AF5 and AF6. **(F-K)** Overlay of 6 different transgenic fish (*isl2b:Gal4*, *UAS:syGCaMP6s*, *UAS:mCherry*) that have been registered into a reference system (RGC standard brain based on *isl2b:Gal4*, *UAS:mCherry*). Z-position indicates the distance from the dorsal most surface of AF10. Note that both syGCaMP6s **(F-H)** and mCherry **(I-K)** patterns from 6 fish occupy conserved space in the registered volume. A, anterior; P, posterior; D, dorsal; V, ventral, M, medial. Scale bars represent 30 μm .



Supplementary Figure S6 (related to Figure 3): Mapping of orientation-selectivity, direction-selectivity, and luminance responses in RGC terminals. (A) Response profile to luminance changes in AF4, 5 and 6 presented from the side or below. Pixels are color coded according to the mutually exclusive luminance response types: pixels responsive to increase in luminance (ON), decrease in luminance, and both increase and decrease in luminance (ON-OFF). **(B)** Representative luminance response in AF4 and 6. Visual stimuli were presented from the side. ROIs correspond to synaptic puncta marked in the right panel. Note that AF5 is not contained in this optical plane. In (A) and (B), functional pixels are plotted on top of the mean image of syGCaMP6s (grey). **(C)** 3D representation of luminance response in RGC terminals. (Left) 3D model of AFs (as Figure 2B). For side presented 3D map, both AF10 and AF 4, 5 and 6 volumes are pooled from 6 functionally imaged volumes. For underneath presented 3D map, both AF10 and AF 4, 5 and 6 volumes are pooled from 7 functionally imaged volumes. The intensity of pixels corresponds to the frequency of a particular pixel to be luminance responsive across all imaged fish. Note that AF4 and AF9 contain highly luminance responsive RGC terminals and AF5 is weakly ON responsive (right panel). **(D)** Localization of DS pixels in tectal sublaminae. After registration into the RGC reference brain, DS pixels identified by the side (green) and below (magenta) presentations of visual stimuli were overlaid to the average image of *isl2b:Gal4, UAS:syGCaMP6s* signals of the same registered volume. DS pixels tuned to forward motion are plotted here for both side and below stimulus presentations. The volume was sliced obliquely to reveal laminar structure along the superficial-deep axis within the tectal neuropil. **(E)** Intensity plot along region indicated by a box shown in (D). Note that DS pixels for both stimulus positions (side, below) occupy SFGS1. **(F, G)** Color scheme of orientation space for motion presented from the side (F) and below (G). **(H, I)** Orientation selectivity (OS) in AF4, AF5 and AF6. The motion was presented from the side (H) and below (I). The color code is shown in (F, G). OS pixels are plotted on top of the mean image of syGCaMP6s (grey). **(J)** Representative responses of OS-RGC terminals in AF6. Visual stimuli were presented from the side. ROIs correspond to synaptic puncta marked by the two circular ROIs in the bottom left image. Polar plot (bottom right) is derived from the $\Delta F/F$ traces shown above. A, anterior; P, posterior; D, dorsal, L, lateral. SO, stratum opticum; SFGS, stratum fibrosum et griseum superficiale; SGC, stratum griseum centrale; SAC, stratum album centrale. Scale bars: 10 μm (A, I), 30 μm (D) and 50 μm (C).

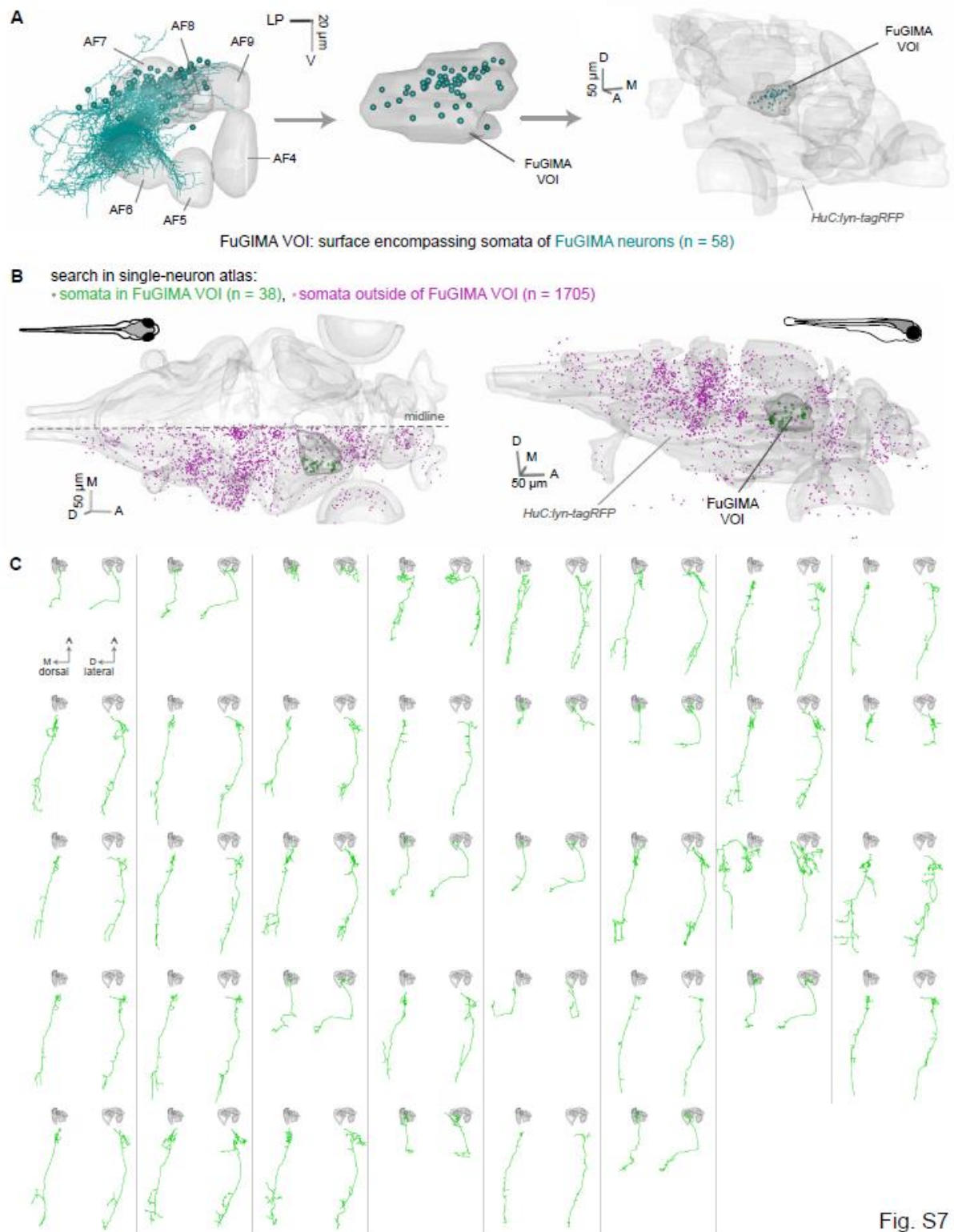


Fig. S7

Supplementary Figure S7 (related to Figure 6): Search strategy to complement FuGIMA tracings with a single-neuron atlas and results. (A) Definition of the FuGIMA “volume-of-interest” (FuGIMA VOI), the search area to find neurons complementing FuGIMA neurons (pretectal projection neuron (PPNs) in a single-neuron atlas. The surface encompasses the somata of all FuGIMA neurons ($n = 58$ neurons) and is registered to the volume of a single-neuron atlas (Kunst et al., under review). **(B)** 3D rendering of the single-neuron atlas standard brain (*HuC:lyn-tagRFP*, Kunst et al., under review) and all somata from this single-neuron atlas, color-coded according to position within (green, $n = 38$, pretectal projection neurons, PPNs) or outside of the FuGIMA VOI (magenta, $n = 1705$, out of 1743 tracings in the atlas) (left: dorsal view, right: lateral view). **(C)** Individual tracings of PPNs, plotted with AFs 4 – 9; two plots per neuron: dorsal view (left) and lateral view (right), respectively.

Movie S1: Different morphologies of monocular DS and translation-selective neurons (related to Figure 2A,D). 3D rendering of the FuGIMA dataset ($n=58$ tracings) together with the FuGIMA standard brain (light grey, *HuC:lyn-tagRFP*), RGC terminals (light magenta, *isl2b:Gal4, UAS:mCherry*) and AF annotations (dark grey). Tracings color-coded according to the neuron’s response class (green: monocular DS, magenta: translation-selective, blue: non-motion-sensitive) and were smoothed for visualization.*

Movie S2: Clustered RGC terminals and derived AF annotations (related to Figure 2B). 3D rendering of RGC axons (*atoh7:Gal4, UAS:mCherry*), RGC terminals (*atoh7:Gal4, UAS:sypGFP*) and AF annotations (yellow: AF4, magenta: AF5, cyan: AF6, red: AF7, green: AF8, blue: AF9) at 6 dpf (compound of three fish).*

Movie S3: 3D map of DS representations in RGC terminals (stimulation from the side) with AF annotations (related to Figure 3M). 3D rendering of RGC axons (*isl2b:Gal4, UAS:mCherry*) and DS-RGC terminals identified during visual stimulation to the side of the fish (DS pixels color-coded according to their preferred direction, see color-wheel) and AF annotations (grey: AFs 4 – 9). Both AF10 and AF4, AF5 and AF6 volumes are pooled from 6 imaged volumes; the intensity of DS pixels corresponds to the probability of a particular pixel to be DS across all imaged fish (maximum intensity = frequency of 0.67).*

Movie S4: 3D map of DS representations in RGC terminals (stimulation from below) with AF annotations (related to Figure 3N). As Movie S4, but DS pixels responsive to the visual stimulus presented from below the fish (both AF10 and AF4, AF5 & AF6 volumes are pooled from 7 imaged volumes; maximum intensity = frequency of 0.57).*

Movie S5: Cerebellum and ventral hindbrain targeted by pretectal projection neurons (related to Figure 6B-F). 3D rendering of all FuGIMA tracings ($n=58$, magenta) and pretectal projection neurons (PPNs, $n=38$, green, chosen based on their somata located close to FuGIMA somata; see Figure S7), plotted together with the standard brain of the single-neuron atlas (light grey: *HuC:lyn-tagRFP* (Kunst et al., 2019)) and AF annotations (dark grey: AFs 4 – 9). Later in the movie, PPNs are color-coded according to whether they intersect with the cerebellum or the reticular formation (blue: intersecting tracings, $n=8$ or $n=25$ of 38 PPNs, respectively, grey: not intersecting tracings, light blue: cerebellum or reticular formation, respectively).*

*For movies, please refer to the online version of the manuscript, once published.

STAR Methods

CONTACT FOR REAGENT AND RESOURCE SHARING

Further information and requests for resources and reagents should be directed to and will be fulfilled by the Lead Contact, Fumi Kubo (fumikubo@nig.ac.jp).

EXPERIMENTAL MODEL AND SUBJECT DETAILS

Animal care and transgenic zebrafish

Adult and larval zebrafish (*Danio rerio*) were housed and handled according to standard procedures (Westerfield, 2007). Animal experiments were performed according to regulations of the Max Planck Society and the regional government of Upper Bavaria (Regierung von Oberbayern; approved protocols: ROB-55.2Vet-2532.Vet_02-16-31 and 55.2-1-54-2532-101-2012). We used the following previously described transgenic lines: *HuC:GCaMP5G (Tg(elavl3:GCaMP5G)a4598)*; *Tg(isl2b:Gal4-VP16)zc65*; *Tg(atox7:Gal4-VP16)s1992t*; *Tg(UAS:mCherry)s1984t*; *Tg(UAS:Dendra-kras)s1998t*; *Tg(UAS:sypGFP);Et(E1b:Gal4-VP16)s1101t (= Gal4^{s1101t})*, *HuC:lyn-tagRFP (Tg(elavl3:lyn-tagRFP)mpn404)*; *Tg(elavl3:H2B-GCaMP6s)*. Transgenic fish were kept in either a TL or TLN (nacre) background and larvae lacking trunk pigmentation (outcrossed to TLN, nacre) were used in the experiment. Zebrafish larvae were raised in Danieau's solution until day 5 or 6 post-fertilization (dpf). As sex determination has not yet taken place in larvae, we used future males and females indiscriminately.

Line establishment

To generate the *UAS:syGCaMP6s* plasmid, the synaptophysin coding sequence (Meyer and Smith, 2006) was fused with GCaMP6s and inserted into a pTol2-14xUAS vector. *Tg(UAS:syGCaMP6s)mpn156* transgenic fish were generated using the standard Tol2 transposon system.

To co-express nls-GCaMP6s and either paGFP (for *UAS:FuGIMA*) or C3PA-GFP (for *UAS:FuGIMA-C3PA*), we fused nls-GCaMP6s and either paGFP (Patterson and Lippincott-Schwartz, 2002) or C3PA-GFP (Ruta et al., 2010) to the two sides of a bidirectional 14x UAS sequence (Janus-UAS; (Distel et al., 2010; Paquet et al., 2009) in a Tol2 vector harboring a transgenesis marker ("bleeding heart", *cmlc2:mCherry*). The transgenic lines *Tg(UAS:paGFP,nlsGCaMP6s)mpn161* and *Tg(UAS:C3PA-GFP,nlsGCaMP6s)mpn162* were generated in the background of *Gal4^{s1101t}* using the standard Tol2 transposon system. Most FuGIMA experiments were conducted in the F2 and F3 generations of the *UAS:FuGIMA* line, which showed considerable variegation and silencing of the transgene expression.

Of the 58 FuGIMA tracings, three were performed with *UAS:FuGIMA-C3PA*, *Gal4^{s1101t}* or *HuC:Gal4*. These neurons belong to the monocular direction-selective response type class and do not intersect with AF5.

METHOD DETAILS

RGC axons and pretectal neuropil functional imaging

Calcium imaging of RGC terminals was performed in triple transgenic zebrafish larvae expressing syGCaMP6s and mCherry in RGCs (*Tg(isl2b:Gal4-VP16)zc65*, *Tg(UAS:syGCaMP6s)mpn156*, *Tg(UAS:mCherry)s1984t*) between 5 and 6 dpf. Larvae were mounted in 2% low-melting agarose with the dorsal side up. The fish were positioned in the center of a dish with a diameter of 3 cm. Larvae were intraspinally injected with α -bungarotoxin (2 mg/mL α -bungarotoxin (Invitrogen, B1601), FastRed 10% v/v, 1x Danieau's solution). A moveable objective microscope (MOM, Sutter Instruments) was used to record GCaMP signals (920 nm, 10-20 mW after the objective) with a 20x objective (Olympus, NA 1.0). ScanImage software (Pologruto *et al.*, 2003) was used for image acquisition. We typically recorded one of two volumes per fish, each covering AF10 or AF 4, AF5 and AF6 volume. For recording of AF10, ca. 20 z-planes were imaged with the z-step size of 4 μ m. For recording of AFs 4, 5 and 6, ca. 25 z-planes were imaged with the z-step size of 3 μ m. For each z-plane, images were acquired with a spatial resolution of 256x256 pixels (pixel size of 0.33 μ m for AF10 and 0.19 μ m for AFs 4, 5 and 6) at a frame rate of 2.38 Hz. Since the average diameter of a presynaptic bouton in zebrafish RGCs is \sim 0.8 μ m (Meyer and Smith, 2006), the physical lateral dimensions of pixels are below that of a typical presynaptic bouton. Sinusoidal grating stimuli were generated by custom written scripts using PsychoPy and presented onto a screen positioned either below or on the side of the fish using a digital light processing (DLP) projector (DLP LightCrafter™ 4500), using the red channel only, which allowed simultaneous visual stimulation and detection of green fluorescence. The visual stimuli consisted of whole-field luminance change (lowest luminance \rightarrow highest luminance \rightarrow lowest luminance) followed by gratings moving in 12 equally spaced angular directions presented in a random order. For each presentation of a different direction, the gratings initially stay stationary for 10 sec, in motion for 5 sec, and back to stationary for 5 sec, and this process was repeated for all grating presentations. The total length of the visual stimulus protocol was about 5 min. For the projection from the side of the fish, spatial and temporal frequency of the gratings was 0.06 cycle/degree and 1.8 Hz, respectively. The projected image filled a visual field of approximately 120° in azimuth and \pm 35° in elevation. For the projection from below the fish, gratings were designed as described in the recent study (Naumann *et al.*, 2016). Briefly, the gratings of the spatial period of 1 cm moving at 10 mm/sec were presented onto a 12 cm x 12 cm

screen. In contrast to this recent study, the complete screen area was covered by the grating (no stimulus omission directly below the fish).

Calcium imaging of pretectal neuropil was performed in *HuC:GCaMP5G* fish between 5 and 6 dpf. A volume centered around the pretectal neuropil was imaged with the z-step size of 5 μm . For each z-plane, images were acquired with a spatial resolution of 512x512 pixels (pixel size of 0.19 μm) at a frame rate of 2.38 Hz. The visual stimulus was presented from below the fish, as described above.

Pixelwise calcium imaging analysis (RGC template)

Raw time series of two-photon recordings were first corrected for motion artifacts by a hidden Markov model (HMM)-based algorithm using the SIMA toolkit (Kaifosh *et al.*, 2014) and then processed by a uniform filter for noise removal. For each pixel in the filtered motion corrected recordings, its fluorescence time series was divided into 14 phases based on the visual stimuli. These 14 phases consisted of 1 ON phase (whole-field luminance increase), 1 OFF phase (whole-field luminance decrease), and 12 motion phases. The normalized signal intensity changes ($\Delta F/F_0$) were calculated for each phase, and they were tested for correlation with the stimulus time series convolved with a kernel with syGGCaMP6s kinetics ($\tau_{\text{decay}} = 1.2$ sec). Pixels were considered motion responsive, if 1) their Pearson correlation coefficients were above the threshold of 0.35 in no less than 2 motion phases and 2) their t-scores (the coefficient from linear regression divided by error) in at least one motion phase were above noise threshold of 1.3. For each motion responsive pixel, we generated a response profile which consisted of the integral response over motion presentation for 12 directions.

To identify DS and OS populations, we plotted the response profiles as vectors in direction and orientation space, and we calculated the vector sum. The angle of the vector sum represents the preferred direction or orientation, and the normalized length of the vector sum (L_{dir} and L_{ori} as calculated below) represents the degree of selectivity. This has been shown to be a robust method to quantify direction and orientation selectivity (Mazurek *et al.*, 2014).

$$L_{\text{dir}} = \left| \frac{\sum_k R(\theta_k) \exp(i\theta_k)}{\sum_k R(\theta_k)} \right|$$

$$L_{\text{ori}} = \left| \frac{\sum_k R(\theta_k) \exp(2i\theta_k)}{\sum_k R(\theta_k)} \right|$$

θ_k represents a direction of motion, and $R(\theta_k)$ is the integral response during the motion phase in the direction of θ_k . An empirical threshold of 0.4 was set for L_{ori} and 0.5 for L_{dir} . Pixels that surpassed

the threshold were considered DS or OS. If a pixel was classified as both DS and OS, that pixel was regarded as DS, for which we have set a more stringent threshold. This ensured that DS and OS pixels are mutually exclusive. These thresholded, binary DS and OS pixels were color coded according to their preferred direction or orientation and plotted on top of the anatomical references, which are the mean images of the motion-corrected time series. To generate histograms of preferred direction (Figure 4), we first obtained the distribution of the preferred direction of DS pixels for each individual fish. The total number of DS pixels was normalized across different fish, and then the average of the normalized distribution was plotted. To compare with the previously published result of distribution of preferred directions of DS-RGC terminals (Figure 4D), we selected 3 planes (separated by 4 μm) in the dorsal part of AF10 (approximately 30 - 45 μm from the dorsal surface of the tectum). The luminance response was determined independently of the response to motion stimuli (Figure S6). Pixels were deemed luminance responsive, if they show activity correlated with changes in light intensity (Pearson correlation coefficient > empirically derived threshold 0.45). The activity of ON pixels increases when luminance rises, while that of OFF pixels increases when luminance drops. ON-OFF pixels show an increase in activity when luminance rises and drops. For a pixel to be regarded as luminance responsive, mutually exclusive criteria were used: i.e. ON if $\text{ON} > 0.45$ and $\text{OFF} < 0.45$, and OFF if $\text{ON} < 0.45$ and $\text{OFF} > 0.45$, and ON-OFF if $\text{ON} > 0.45$ and $\text{OFF} > 0.45$.

Image registration for RGC and pretectal neuropil

After calcium imaging, we acquired anatomical z-stacks of the same fish (*isl2b:Gal4, UAS:syGCaMP6s, UAS:mCherry*). We first obtained small stacks (256x256 pixels) with the two-photon microscope, using syGCaMP6s and covering the functionally imaged volume (either AF10 or AF4, AF5 and AF6, or both in a few cases). Additionally, one overview stack with a higher resolution (1024x1024 pixels) was taken at the confocal microscope (LSM700, Carl Zeiss, Jena, Germany) with a 20x objective (W Plan-Apochromat 20x/1.0, Carl Zeiss, NA 1.0) with a z-step size of 1 μm and using both syGCaMP6s and mCherry channels.

In order to visualize the DS and OS RGC terminals imaged in multiple fish and compare them with the *HuC:GCaMP5G* expression pattern, we developed a three-step registration procedure (Figure S5A): 1) the mean image of the motion corrected time series were manually aligned (custom written Python script) onto the two-photon anatomical z-stack using the syGCaMP6s signal as reference. As such, we registered the functional information to the anatomical z-stacks. To circumvent changes of pixel values and thereby changes of DS/OS information caused by the image registration, we binned functional data according to preferred direction/orientation. Namely, we created 12 separate channels, with each channel corresponding to one of the 12 bins of preferred directions. 2) the two-

photon anatomical z-stacks were registered to the confocal stack of the same fish using syGCaMP6s as the reference channel. To facilitate gross alignment between the stacks, we pre-aligned the z-stacks according to manual landmark selection using the plugin “Name Landmarks and Register” (by Mark Longair and Greg Jefferis) in Fiji (Schindelin *et al.*, 2012; Schneider *et al.*, 2012). The stacks were then precisely registered by the image registration library ANTs (Advanced Normalization Tools) (Avants *et al.*, 2008; Avants *et al.*, 2011; Avants *et al.*, 2010) using syGCaMP6s signal as a reference for registration. The parameters for the command `antsRegistration` recently applied to zebrafish live images (Marquart *et al.*, 2017) were used, except for variation of the initial transform parameter and the application of a mask. This mask was drawn in Fiji with the plugin segmentation editor (by Johannes Schindelin, Francois Kuzstos and Benjamin Schmid) and restricted the search for corresponding pixels to the area containing RGC terminals. 3) The resulting stack was then registered to the template (RGC standard brain) which was generated from six different stacks (*isl2b:Gal4, UAS:mCherry*) using the command `antsMultivariateTemplateConstruction2` in ANTs. Using the mCherry signal as a reference channel, we applied the same settings as for the previous round of ANTs registration (but without mask). Therefore, for each step of registration, the previous template stack served as the pattern to be registered. If a pitch difference between the experimental fish and the template was greater than $\pm 5^\circ$ (as calculated from the transformation information), DS and OS bins were recalculated accordingly before applying image registration. After anatomical stacks underwent registration, functional stacks containing DS/OS information were treated as additional channels and subjected to the same transformations using the command `antsApplyTransforms` (Marquart *et al.*, 2017). As DS/OS depicting pixels were broadened due to registration, we applied a threshold of a pixel intensity value 50 to eliminate the smearing effect of the registration (custom Python script). This threshold was determined visually to display the same spatial extent of DS/OS information in the template volume as in the original two-photon frames. To visualize the *isl2b* template in the context of the *HuC:GCaMP5G* expression pattern, we registered a single *isl2b:Gal4, UAS:mCherry, HuC:GCaMP5G* fish to the template via the mCherry channel. For registering DS neuropil signals imaged in *HuC:GCaMP5G* fish ($n=6$ fish), the same image registration protocol was applied except that 1) pre-alignment of the two-photon anatomical z-stacks using manual landmark selection was skipped (during step 2 of the registration protocol) and 2) the confocal anatomical stacks of the functionally imaged fish were registered to our reference brain via the previously aligned *HuC:GCaMP5G* pattern.

Segmentation of AFs and 3D rendering

Segmentation of AFs was performed based on presynaptic puncta signals in *atoh7:Gal4, UAS:sypGFP* fish after they had been registered to the RGC standard brain using ANTs. AFs were manually

segmented using published anatomical information about AFs (Burrill and Easter, 1994; Robles et al., 2014). Note that our segmentation of AFs relied only on anatomical features, without referring to functional maps of RGC terminals. We noted some variability of SypGFP localization patterns across different individual fish, especially at the boundary between AF5 and AF6. To account for this individual fish differences, 3 fish were segmented by 3 annotators each, and average of the 9 annotations was used to generate a consensus mask for AF4, AF5 and AF6. To quantify the number of DS pixels in different AFs, we used original calcium time series before anatomical registration to avoid the smearing effect (thereby leading to changes in the absolute number of pixels of each RGC puncta) caused by the registration. To count DS pixels in the original calcium time series in each AF, we either drew masks of AFs directly on the original calcium time series (with the aid of anatomical stacks) or back-transformed our consensus AF masks (drawn on the registered image volume) to the original calcium time series using inverse transformation. To determine the proportion of DS pixels relative to the entire number of pixels in AFs, we first quantified the pixel counts in AF5 and AF6 using the synaptic puncta signals of 9 anatomical stacks obtained from *isl2b:Gal4, UAS:sypGFP* fish. Subsequently, the number of DS pixels was divided by the average pixel counts in each AF to derive the percentage of DS pixels per total number of pixels in each AF. 3D rendering of registered image stacks was performed using Imaris software. Autofluorescence of the skin and the eyes was removed by applying 3D masks and the volumes corresponding to AFs were highlighted in Imaris. Movies were prepared using Imaris and Fiji.

Lipophilic Dye labeling

6 day old *isl2b:Gal4, UAS:Dendra-kras* transgenic larvae were fixed in 4% paraformaldehyde in PBS for 1hr at 4 °C. 1% solutions of Dil in chloroform were pressure injected between the lens and the retina to visualize all axonal projections. Fluorescent images were acquired one day after the injection.

Functional imaging and analysis (FuGIMA dataset)

Larvae were mounted in agarose (LMP-agarose, 1.5 % w/v in Danieau's solution), and intraspinaly injected with alpha-bungarotoxin (2 mg/mL α -bungarotoxin (Invitrogen, B1601), FastRed 10% v/v, 1x Danieau's solution) before the experiment to abolish movements. During injection, larvae were under anesthesia with tricaine (0,02 %, MS-222, Sigma-Aldrich) and the tricaine was washed out after injection. We used a two-photon microscope (Femtonics 3DRC microscope, Femtonics, Tuzlo, Hungary) for functional imaging as well as acquisition of z-stacks. The visual stimuli were presented to the fish using a custom-built red LED arena (four flat panels covering 360° around the fish; no grating presentation in ~ 30° in front of the fish). In each experiment session, gratings moved

horizontally in eight phases (3 s each at spatial frequency of 0.033 cycles/degree and temporal frequency of 2 cycles/sec, interspersed with 10 s stationary gratings, Figure S2A). Four of the eight phases are monocular, four are binocular: 1) left nasalward, 2) left temporalward, 3) right temporalward, 4) right nasalward, 5) backward, 6) forward, 7) clockwise, 8) counterclockwise. The sequence of eight phases was repeated three times. During visual stimulation, GCaMP fluorescence was imaged at about 3 Hz using the laser tuned to 920 nm (0.5 x 0.5 $\mu\text{m}/\text{pixel}$, ca. 15 mW after the objective, imaging region of about 90 x 98 μm). Response types of recorded neurons were identified using a custom written python script (regressor based analysis, near-online analysis: approx. 2 minutes run time). First, traces of the three repetitions were averaged. Second, the averaged time series of each pixel were correlated to 256 regressors (visual stimulus time series convolved with nls-GCaMP6s kernel, $\tau = 3$ s, τ determined visually to resemble the fluorescence trace), and the best-correlated regressor was determined for each pixel (threshold of Pearson's correlation coefficient > 0.3). For each regressor-of-interest (e.g. monocular DS and translation-selective response types), we generated a map of correlated pixels overlaid on the mean $\Delta F/F_0$ image (Figure 1E), based on which cells of interest were chosen. The selected cells of interest were further manually inspected for variability in response across repetitions, baseline fluorescence (indicator of transgene expression level), and accessibility for photoactivation (separation from neighboring neurons).

To improve display of fluorescence traces, functional imaging time series were motion corrected with CalmAn (Giovannucci et al., 2018; Pnevmatikakis and Giovannucci, 2017). We extracted average brightness from ROIs centered on the cell of interest (using Fiji), and calculated $\Delta F/F_0$ with F_0 being the mean of the 10th percentile. For neurons of the monocular DS and translation selective type, we plotted the mean trace of three repetitions, grouped by response type. For non-motion-selective neurons we in addition plotted the variance over three stimulus repetitions of the trial (SEM). Regressor traces were manually overlaid with corresponding fluorescence traces.

Photoactivation of paGFP and z-stack acquisition

Photoactivation of paGFP in selected cells of interest was performed according to a detailed published protocol (Förster et al., 2018). Briefly, a ROI of about 0.8 x 0.8 μm (0.2 x 0.2 $\mu\text{m}/\text{pixel}$, 4 x 4 pixel) was placed in the center of the nucleus in 3D. Initially, paGFP was photoactivated with trial pulses of 200 ms (one and three pulses, laser wavelength 750 nm, ca. 10 - 17 mW after the objective, 1 Hz). If no neighboring cells were photoactivated, the ROI was re-centered and the first full cycle of photoactivation was delivered (40 x 200 ms, 1 Hz, Figure 1F). In cases of residual movement of the fish, tricaine was added before photoactivation. The whole protocol consisted of 15 cycles, with typically five minutes intervals between two activation cycles. However, in the dataset containing

58 neurons, 3 were photoactivated with less than 5 cycles and 11 with 5-10 cycles of photoactivation. Typically, paGFP fluorescence intensity in the photoactivated soma rapidly increased with the first photoactivation cycle, reaching the maximum after several cycles of photoactivation, suggesting that maximum level of the photoactivation is achieved after several cycles of photoactivation (Figure S1C). To control progress of diffusion, z-stacks capturing both green and red fluorescence (1020 nm, 1 μ m z-step) were typically acquired every five cycles, as well as a high resolution stack after the last activation period.

We quantified the degree of photoactivation by calculating the normalized fluorescence change after each cycle of photoactivation (mean of n=5 neurons in 3 fish). An experiment was terminated, if 1) a directly neighboring neuron was also photoactivated, 2) fluorescence in the neurite did not strongly increase after the first cycle of photoactivation, or 3) the sample drifted. Furthermore, as the pretectum is located directly ventral to the tectum, we photoactivated few neurons resembling tectal neurons' morphology (neurite targeting the tectal neuropil, perpendicular branching in the neuropil layers), which were excluded. Two-photon and confocal microscopy offer different advantages: while two-photon microscopy achieves superior resolution in deeper tissue, it typically does not allow to image close to the eye pigment epithelium (due to photomultiplier tube (PMT) saturation). As confocal microscopy does not show this restriction, we acquired a large z-stack at the confocal microscope (LSM 700, Carl Zeiss, Jena, Germany 20x/1.0 NA, water-dipping objective) in addition to the two-photon z-stack.

To exclude the possibility that tracing quality underlies differential neurite trajectories of different response types, we manually sorted z-stacks into four groups according to their image quality and compared tracings between groups. We did not find systematic differences in tracing length or overall morphology among the four groups (Figure S4C). Furthermore, all four groups contained tracings of all three response classes. Translation-selective neurons were even slightly overrepresented in the "best" image group. It is thus unlikely that we overlooked particular features, such as AF5 targeting, of translation-specific neurons.

Tracing of FuGIMA neurons and consolidation

Neurons were semi-manually traced from the confocal and two-photon z-stacks using the Fiji plugin Simple Neurite Tracer (Longair *et al.*, 2011) or the software neuTube (Feng *et al.*, 2015) (Figure 1G). Neurons were traced in both confocal and two-photon z-stacks, if available, as the two imaging modalities complement one another (see above). Finally, we merged the tracings of the same neuron after co-registration (see section Image registration below) using a custom written python code. For merging, node locations of two tracings were compared and corresponding nodes were

identified based on a maximal distance between them (defined by an empirically chosen tolerance factor). Residual nodes were then added to the merged tracing (OR operation). To assess the labeling distance of paGFP, we photoactivated a neuron co-expressing a membrane-tagged red fluorescent protein and FuGIMA. Briefly, we injected the plasmid *pTol2-UAS:tdTomato-CAAX* into embryos (*Gal4^{s1101t}, UAS:FuGIMA*) at the two to four cell stage and selected larvae with sparse expression of tdTomato. We applied the full photoactivation protocol on a spinal cord neuron co-expressing FuGIMA and tdTomato-CAAX. While tdTomato in the soma was considerably photo-bleached, it colocalized with paGFP in the neurite. Neurons highlighted with paGFP can be followed over 200 μm , as shown in a spinal cord neuron co-expressing tdTomato-CAAX (Figures S1A,B).

Image registration of FuGIMA data

The basis of comparisons across fish is their registration to a standard brain. We established the FuGIMA standard brain using the ANTs from four z-stacks of four live fish expressing *HuC:lyn-tagRFP*, *HuC:H2B-GCaMP6s* (imaged at the confocal microscope). The FuGIMA standard brain is centered on the pretectum of the right hemisphere and extends 311.2 x 311.2 x 161 μm (x/y/z direction, 0.69 x 0.69 x 1 μm voxel size). To compare tracings from different experimental fish in one volume, z-stacks were registered to the standard brain (overlay of three registered example z-stacks: Figure 1I, registration workflow: Figure S1D). As preparation, the *HuC:lyn-tagRFP* channel was corrected for depth-dependent decrease of brightness (Fiji plugin Attenuation Correction (Biot et al., 2008)). If the experimental z-stack was centered on the contralateral hemisphere, the z-stack was flipped and rotated prior to registration using Fiji. Z-stacks were registered to the standard brain using the software ANTs (Avants et al., 2008; Avants et al., 2011; Avants et al., 2010) and based on the common reference labeling pattern of *HuC:lyn-tagRFP*. We used the parameters recently determined for live samples (Marquart et al., 2017). Tracings (.swc files) were co-registered using the command `ANTsApplyTransformsToPoints` contained in the package ANTsR using R. If both confocal and two-photon-stacks were available, two-photon-stacks were registered to the confocal stack of the same fish and confocal stacks were registered to the FuGIMA standard brain. In the case of insufficient registration precision (visually determined), we either altered parameter *r* to change search initialization or applied a mask to restrict the search area. Search masks (binary .tiff files) were drawn manually or derived from previous rounds of registration. To verify the accuracy of our registration, we annotated eleven anatomical landmarks in the standard brain and individual z-stacks ($n = 8$ z-stacks from 6 fish for LM 1 – 9 and 11, $n = 6$ z-stacks from 4 fish for LM 10). After co-registration into the standard brain, we calculated the distance between the landmark of the standard brain and the individual brains using R. The deviations of the landmark positions of the registered fish from those

of the standard brain were on average $6.7 \pm 2.8 \mu\text{m}$ (STD, 11 landmarks, 4 or 6 z-stacks from 6 fish, Figure S1E).

To facilitate comparison of tracing results across datasets, we described the x,y-position of FuGIMA neuron somata relative to a previously defined coordinate system origin (as in Kubo et al., 2014). For this, we extracted soma coordinates from .swc files, subtracted the origin coordinates (intersection of planes connecting the anterior tips of the AF9 containing neuropil, the midline, and the plane just dorsal to the anterior tips of AF9), and transformed the coordinates (45° rotation between the RGC and FuGIMA standard brain volumes). Soma locations (relative to the origin) were plotted in histograms (bin size = $16 \mu\text{m}$, visually determined).

To combine visualization of neuronal tracings with landmark annotations, the latter were transformed to surfaces. For this, registered z-stacks were binarized, if necessary manually smoothed (both Fiji), and surface renderings were produced using the software Amira (Thermo Fisher Scientific/FEI, smoothing: unconstrained smoothing, extent=5). Neuronal tracings and landmark surfaces were plotted using R with the packages rgl (Adler, Murdoch, and others) and NeuroAnatomy Toolbox package (Jefferis and Manton, 2014). For the accompanying videos, FuGIMA tracings were smoothed. The video was assembled using Fiji, then converted and compressed with the software FFmpeg.

Integration of RGC and FuGIMA datasets

We had generated consensus AF masks in the RGC standard brain (see section Segmentation of AFs and 3D rendering above). To transfer these masks into the FuGIMA volume, we applied a two-step registration process (Figure S3A): 1) we registered the RGC standard brain (based on *isl2b:Gal4, UAS:mCherry*) to individual “bridge”-z-stacks of fish expressing *isl2b:Gal4, UAS:GFP, HuC:lyn-tagRFP* (n=7 z-stacks from 4 fish), 2) then we registered the “bridge”-z-stacks to the FuGIMA standard brain (based on *HuC:lyn-tagRFP*). As we observed slight differences in the localization of co-registered AF masks, we applied a kernel-density estimation (KDE) to the collection of binarized z-stacks. After normalizing the maximum pixel intensity to 100, the stack was thresholded (pixel values = 25, 50, 75, and 90) and surfaces were generated. We utilized the KDE=50% mask for further analysis of tracing intersections with AFs.

To compare FuGIMA tracings with functional information (z-stacks), we first registered the functional imaging datasets (DS in RGC terminals and all neurons) to the FuGIMA standard brain. Streaks of DS pixels were found in the region of the eye cup in the panneuronal DS stack, resulting from PMT saturation. We removed those pixels with a mask. To convert .swc files of tracings to

rastered data (z-stacks) we applied a custom-written Fiji macro script. Resulting pixelated tracings were smoothed in Fiji to improve the impression of continuous neurites for display.

Complementation with the single-neuron atlas

To compare FuGIMA neurons with a single-neuron atlas (Kunst et al., 2019), we registered the FuGIMA dataset to the standard brain of this single-neuron atlas. The single-neuron atlas standard brain is based on the synapsin pattern (antibody staining, fixed samples) and contains several registered expression patterns to enable registration of external datasets based on those patterns (e.g. fixed *HuC:lyn-tagRFP*). To register the FuGIMA standard brain (acquired live, a sub-volume of the fish brain) into the single-neuron atlas volume (fixed, whole-brain), we employed registration in three steps as follows: 1) FuGIMA volume to a sub-volume of the live *HuC:lyn-tagRFP* standard brain (at this time not yet registered to the single-neuron atlas), 2) extension to the full live standard brain volume, 3) live standard brain to fixed *HuC:lyn-tagRFP* standard brain. Co-registration of FuGIMA tracings (.swc files) and landmark annotations (.tiff stacks), followed by surface rendering of landmarks allowed to visualize both datasets together. We searched among 1743 tracings from the web-interface of the single neuron atlas for tracings complementing the FuGIMA tracings (Pretectal projection neurons, PPNs) (<https://fishatlas.neuro.mpg.de/zebrafishatlas/>, download: 25. Oct. 2018, combined results of searches in different brain regions). To define the search volume for PPNs (FuGIMA VOI), we dilated FuGIMA somata and merged patches in the binary .tiff stack (distance surface to soma approx. 10 μm (x/y) and 11 μm (z), in the FuGIMA standard volume). After co-registration of the FuGIMA VOI to the single-neuron atlas volume, we identified PPNs with somata in the FuGIMA VOI (custom written python script). For the innervation analysis, we retrieved the number of tips per PPN for all 78 brain region annotations and one additional area “contralateral hemisphere”. To focus on the most prominently targeted areas, we depicted areas with > 5 intersecting PPNs, omitting similar annotations i.e. only “cerebellum”, no additional “corpus cerebelli”, and included all annotated AFs intersecting with PPNs. For visualization, we ordered the list starting with the contralateral hemisphere, then in the order of most intersections.

QUANTIFICATION AND STATISTICAL ANALYSIS

The statistical information is provided in each of the sections above.

The analyzed number of zebrafish and brains is indicated in the main text and figure legends. Error bars correspond to SEM unless stated otherwise.

DATA AND SOFTWARE AVAILABILITY

Data and software will be made available upon request.

KEY RESOURCES TABLE

REAGENT or RESOURCE	SOURCE	IDENTIFIER
Chemicals, Peptides, and Recombinant Proteins		
Alpha-Bungarotoxin	Invitrogen	B1601
Dil (1,1'-Diocetyl-3,3,3',3'-Tetramethylindocarbocyanine Perchlorate)	Invitrogen	D3911
Tricaine	Sigma-Aldrich	MS-222
Experimental Models: Organisms/Strains		
Zebrafish <i>Tg(ato7:Gal4-VP16)s1992t, a. k. a. ath5:Gal4</i>	Del Bene et al., 2010	ZFIN ID: ZDB-FISH-150901-27082
Zebrafish <i>Tg(elavl3:lyn-tagRFP)mpn404, a. k. a. HuC:lyn-tagRFP</i>	Dal Maschio et al., 2017	ZFIN ID: ZDB-ALT-170731-38
Zebrafish <i>Tg(elavl3:GCaMP5G)a4598</i>	Ahrens et al., 2013	ZFIN ID: ZDB-FISH-150901-22335
<i>Tg(elavl3:Has.H2B-GCaMP6s)jf5</i> aka <i>HuC:H2B-GCaMP6s</i>	Freeman et al., 2014	ZFIN ID: ZDB-FISH-170711-1
Zebrafish <i>Et(E1b:Gal4-VP16)s1101t)</i>	Scott et al., 2007	ZFIN ID: ZDB-FISH-150901-5255
Zebrafish <i>Tg(isl2b:Gal4-VP16, myl7:TagRFP)zc65</i>	Fujimoto et al., 2011	ZFIN ID: ZDB-FISH-150901-13523
Zebrafish <i>Tg(UAS:mCherry)s1984t</i>	Heap et al., 2013	ZFIN ID: ZDB-FISH-150901-14417
Zebrafish <i>Tg(UAS:syn-GFP) a. k. a. UAS:sypGFP</i>	Heap et al., 2013	ZFIN ID: ZDB-FISH-150901-21811
Zebrafish <i>Tg(UAS:Dendra-kras)s1998t</i>	Arrenberg et al., 2009	ZFIN ID: ZDB-ALT-110808-3
Zebrafish <i>Tg(UAS:syGCaMP6s)mpn156</i>	This paper	NA
Zebrafish <i>Tg(UAS-Janus:nlsGCaMP6s,PA-GFP)mpn161, a.k.a. UAS:FuGIMA</i>	This paper	NA
Zebrafish <i>Tg(UAS-Janus:nlsGCaMP6s,C3PA-GFP)mpn162, a.k.a UAS:FuGIMA-C3PA</i>	This paper	NA
Software and Algorithms		
ImageJ/Fiji	Schindelin et al., 2012	https://fiji.sc/
Simple Neurite Tracer (Fiji plugin)	Longair et al., 2011	https://imagej.net/Simple_Neurite_Tracer
Attenuation Correction (Fiji plugin)	Biot et al., 2008	http://imagejdocu.tudor.lu/doku.php?id=plugin:stacks:attenuation_correction:start
Name Landmarks and Register (Fiji plugin)	Mark Longair and Greg Jefferis, 2006	https://imagej.net/Name_Landmarks_and_Register
NeuTube	Feng et al., 2015	https://www.neutracing.com/
Advanced Normalization Tools (ANTs)	Avants et al., 2008; Avants et al., 2011; Avants et al., 2010	http://stnava.github.io/ANTs/
RStudio Version 1.0.143	RStudio	https://www.rstudio.com/

Python 2.7	Python.org	https://www.python.org
Python 3	Python.org	https://www.python.org
Amira	Thermo Fisher Scientific	https://www.fei.com/software/amira-for-life-sciences/
Imaris	Bitplane	http://www.bitplane.com/
FFmpeg		https://ffmpeg.org/
CalmAn (Calcium Imaging Analysis toolbox)	Giovannucci et al., 2018; Pnevmatikakis and Giovannucci, 2017	https://github.com/flattironinstitute/CalmAn
R package nat (NeuroAnatomy Toolbox)	Jefferis and Manton, 2014	http://jefferis.github.io/nat/
R package rgl	Daniel Adler, Duncan Murdoch and others	https://CRAN.R-project.org/package=rgl
Other		
Confocal microscope LSM 700, with a 20x/1.0 NA water-dipping objective	Carl Zeiss	https://www.zeiss.com/microscopy
Movable object two-photon microscope with a 20x water-dipping objective (Olympus, NA 1.0)	Sutter Instruments/ Olympus	https://www.sutter.com/ https://www.olympus-lifescience.com/de/
Femtonics 3DRC two-photon microscope, with 16x or 20x water-dipping objective	Femtonics	http://femtonics.eu/
Tracings, brain area annotations, and standard brain	Single-neuron atlas of Kunst et al., 2019	https://fishatlas.neuro.mpg.de/zebrafishatlas/

References

- Ahrens, M.B., Orger, M.B., Robson, D.N., Li, J.M., and Keller, P.J. (2013). Whole-brain functional imaging at cellular resolution using light-sheet microscopy. *Nature methods* 10, 413-420.
- Arrenberg, A.B., Del Bene, F., and Baier, H. (2009). Optical control of zebrafish behavior with halorhodopsin. *Proc Natl Acad Sci U S A* 106, 17968-17973.
- Avants, B.B., Epstein, C.L., Grossman, M., and Gee, J.C. (2008). Symmetric diffeomorphic image registration with cross-correlation: evaluating automated labeling of elderly and neurodegenerative brain. *Med Image Anal* 12, 26-41.
- Avants, B.B., Tustison, N.J., Song, G., Cook, P.A., Klein, A., and Gee, J.C. (2011). A reproducible evaluation of ANTs similarity metric performance in brain image registration. *Neuroimage* 54, 2033-2044.
- Avants, B.B., Yushkevich, P., Pluta, J., Minkoff, D., Korczykowski, M., Detre, J., and Gee, J.C. (2010). The optimal template effect in hippocampus studies of diseased populations. *Neuroimage* 49, 2457-2466.
- Baier, H. (2000). Zebrafish on the move- towards a behavior-genetic analysis of vertebrate vision. *Current opinion in neurobiology* 10, 451-455.
- Barlow, H.B., and Hill, R.M. (1963). Selective sensitivity to direction of movement in ganglion cells of the rabbit retina. *Science* 139, 412-414.
- Biot, E., Crowell, E., Höfte, H., Maurin, Y., Vernhettes, S., and Andrey, P. (2008). A new filter for spot extraction in N-dimensional biological imaging. In *Fifth IEEE International Symposium on Biomedical Imaging (ISBI'08): From Nano to Macro*, 975-978.
- Burrill, J.D., and Easter, S.S., Jr. (1994). Development of the retinofugal projections in the embryonic and larval zebrafish (*Brachydanio rerio*). *J Comp Neurol* 346, 583-600.
- Cazin, L., Precht, W., and Lannou, J. (1980). Pathways mediating optokinetic responses of vestibular nucleus neurons in the rat. *Pflugers Arch* 384, 19-29.
- Chen, X., Mu, Y., Hu, Y., Kuan, A.T., Nikitchenko, M., Randlett, O., Sompolinsky, H., Engert, F., and Ahrens, M.B. (2018). Brainwide organization of neuronal activity and convergent sensorimotor transformations in larval zebrafish. *Neuron* 100, 876-890.e5.

Dal Maschio, M., Donovan, J.C., Helmbrecht, T.O., and Baier, H. (2017). Linking neurons to network function and behavior by two-photon holographic optogenetics and volumetric imaging. *Neuron* 94, 774-789 e775.

Del Bene, F., Wyart, C., Robles, E., Tran, A., Looger, L., Scott, E.K., Isacoff, E.Y., and Baier, H. (2010). Filtering of visual information in the tectum by an identified neural circuit. *Science* 330, 669-673.

Dhande, O.S., and Huberman, A.D. (2014). Retinal ganglion cell maps in the brain: implications for visual processing. *Current opinion in neurobiology* 24, 133-142.

Distel, M., Hocking, J.C., Volkmann, K., and Koster, R.W. (2010). The centrosome neither persistently leads migration nor determines the site of axonogenesis in migrating neurons in vivo. *J Cell Biol* 191, 875-890.

Dreosti, E., Odermatt, B., Dorostkar, M.M., and Lagnado, L. (2009). A genetically encoded reporter of synaptic activity in vivo. *Nat Methods* 6, 883-889.

Dunn, T.W., Gebhardt, C., Naumann, E.A., Riegler, C., Ahrens, M.B., Engert, F., and Del Bene, F. (2016). Neural Circuits Underlying Visually Evoked Escapes in Larval Zebrafish. *Neuron* 89, 613-628.

Feng, L., Zhao, T., and Kim, J. (2015). neuTube 1.0: A New Design for Efficient Neuron Reconstruction Software Based on the SWC Format. *eNeuro* 2.

Förster, D., Kramer, A., Baier, H., and Kubo, F. (2018). Optogenetic precision toolkit to reveal form, function and connectivity of single neurons. *Methods* 150, 42-48.

Freeman, J., Vladimirov, N., Kawashima, T., Mu, Y., Sofroniew, N.J., Bennett, D.V., Rosen, J., Yang, C.T., Looger, L.L., and Ahrens, M.B. (2014). Mapping brain activity at scale with cluster computing. *Nature methods* 11, 941-950.

Fujimoto, E., Gaynes, B., Brimley, C.J., Chien, C.B., and Bonkowsky, J.L. (2011). Gal80 intersectional regulation of cell-type specific expression in vertebrates. *Developmental dynamics: an official publication of the American Association of Anatomists* 240, 2324-2334.

Gabriel, J.P., Trivedi, C.A., Maurer, C.M., Ryu, S., and Bollmann, J.H. (2012). Layer-specific targeting of direction-selective neurons in the zebrafish optic tectum. *Neuron* 76, 1147-1160.

Gebhardt, C., Baier, H., and Del Bene, F. (2013). Direction selectivity in the visual system of the zebrafish larva. *Front Neural Circuits* 7, 111.

- Giovannucci, A., Friedrich, J., Gunn, P., Kalfon, J., Koay, S.A., Taxidis, J., Najafi, F., Gauthier, J.L., Zhou, P., Tank, D.W., *et al.* (2018). CalmAn: An open source tool for scalable Calcium Imaging data Analysis. Biorxiv.
- Heap, L.A., Goh, C.C., Kassahn, K.S., and Scott, E.K. (2013). Cerebellar output in zebrafish: an analysis of spatial patterns and topography in eurydendroid cell projections. *Front Neural Circuits* 7, 53.
- Helmbrecht, T.O., Dal Maschio, M., Donovan, J.C., Koutsouli, S., and Baier, H. (2018). Topography of a visuomotor transformation. *Neuron* 100, 1429-1445 e1424.
- Jefferis, G.S.X.E., and Manton, J.D. (2014). NeuroAnatomy Toolbox v1.5.2. ZENODO.
- Kaifosh, P., Zaremba, J.D., Danielson, N.B., and Losonczy, A. (2014). SIMA: Python software for analysis of dynamic fluorescence imaging data. *Front Neuroinform* 8, 80.
- Knogler, L.D., Markov, D.A., Dragomir, E.I., Stih, V., and Portugues, R. (2017). Sensorimotor Representations in Cerebellar Granule Cells in Larval Zebrafish Are Dense, Spatially Organized, and Non-temporally Patterned. *Current biology: CB* 27, 1288-1302.
- Kubo, F., Hablitzel, B., Dal Maschio, M., Driever, W., Baier, H., and Arrenberg, A.B. (2014). Functional architecture of an optic flow-responsive area that drives horizontal eye movements in zebrafish. *Neuron* 81, 1344-1359.
- Kunst, M., Laurell, E., Mokayes, N., Kramer, A., Kubo, F., Fernandes, A. M., Förster, D., Dal Maschio, M., Baier, H. (2019). A cellular-resolution atlas of the larval zebrafish brain. *Neuron*, this issue.
- Longair, M., and Jefferis, G.S. (2006). Name landmarks and register. Fiji plugin. https://imagej.net/Name_Landmarks_and_Register. Accessed: 19.09.2014.
- Longair, M.H., Baker, D.A., and Armstrong, J.D. (2011). Simple Neurite Tracer: open source software for reconstruction, visualization and analysis of neuronal processes. *Bioinformatics* 27, 2453-2454.
- Lowe, A.S., Nikolaou, N., Hunter, P.R., Thompson, I.D., and Meyer, M.P. (2013). A systems-based dissection of retinal inputs to the zebrafish tectum reveals different rules for different functional classes during development. *J Neurosci* 33, 13946-13956.
- Marquart, G.D., Tabor, K.M., Horstick, E.J., Brown, M., Geoca, A.K., Polys, N.F., Nogare, D.D., and Burgess, H.A. (2017). High-precision registration between zebrafish brain atlases using symmetric diffeomorphic normalization. *Gigascience* 6, 1-15.

Masseck, O.A., and Hoffmann, K.P. (2009a). Comparative neurobiology of the optokinetic reflex. *Ann N Y Acad Sci* 1164, 430-439.

Masseck, O.A., and Hoffmann, K.P. (2009b). Question of reference frames: visual direction-selective neurons in the accessory optic system of goldfish. *J Neurophysiol* 102, 2781-2789.

Matsui, H., Namikawa, K., Babaryka, A., and Koster, R.W. (2014). Functional regionalization of the teleost cerebellum analyzed in vivo. *Proc Natl Acad Sci U S A* 111, 11846-11851.

Mazurek, M., Kager, M., and Van Hooser, S.D. (2014). Robust quantification of orientation selectivity and direction selectivity. *Front Neural Circuits* 8, 92.

Meyer, M.P., and Smith, S.J. (2006). Evidence from in vivo imaging that synaptogenesis guides the growth and branching of axonal arbors by two distinct mechanisms. *J Neurosci* 26, 3604-3614.

Naumann, E.A., Fitzgerald, J.E., Dunn, T.W., Rihel, J., Sompolinsky, H., and Engert, F. (2016). From whole-brain data to functional circuit models: The zebrafish optomotor response. *Cell* 167, 947-960 e920.

Neuhauss, S.C., Biehlmaier, O., Seeliger, M.W., Das, T., Kohler, K., Harris, W.A., and Baier, H. (1999). Genetic disorders of vision revealed by a behavioral screen of 400 essential loci in zebrafish. *J Neurosci* 19, 8603-8615.

Nikolaou, N., Lowe, A.S., Walker, A.S., Abbas, F., Hunter, P.R., Thompson, I.D., and Meyer, M.P. (2012). Parametric functional maps of visual inputs to the tectum. *Neuron* 76, 317-324.

Orger, M.B., Gahtan, E., Muto, A., Page-McCaw, P., Smear, M.C., and Baier, H. (2004). Behavioral screening assays in zebrafish. *Methods in Cell Biology* 77, 53-68.

Orger, M.B., Kampff, A.R., Severi, K.E., Bollmann, J.H., and Engert, F. (2008). Control of visually guided behavior by distinct populations of spinal projection neurons. *Nature neuroscience* 11, 327-333.

Orger, M.B., Smear, M.C., Anstis, S.M., and Baier, H. (2000). Perception of Fourier and non-Fourier motion by larval zebrafish. *Nature Neuroscience* 3, 1128-1133.

Paquet, D., Bhat, R., Sydow, A., Mandelkow, E.M., Berg, S., Hellberg, S., Falting, J., Distel, M., Koster, R.W., Schmid, B., and Haass, C. (2009). A zebrafish model of tauopathy allows in vivo imaging of neuronal cell death and drug evaluation. *The Journal of Clinical Investigation* 119, 1382-1395.

- Patterson, G.H., and Lippincott-Schwartz, J. (2002). A photoactivatable GFP for selective photolabeling of proteins and cells. *Science* 297, 1873-1877.
- Pittman, A.J., Law, M.Y., and Chien, C.B. (2008). Pathfinding in a large vertebrate axon tract: isotypic interactions guide retinotectal axons at multiple choice points. *Development* 135, 2865-2871.
- Pnevmatikakis, E.A., and Giovannucci, A. (2017). NoRMCorre: An online algorithm for piecewise rigid motion correction of calcium imaging data. *Journal of neuroscience methods* 291, 83-94.
- Pologruto, T.A., Sabatini, B.L., and Svoboda, K. (2003). ScanImage: flexible software for operating laser scanning microscopes. *Biomed Eng Online* 2, 13.
- Portugues, R., and Engert, F. (2009). The neural basis of visual behaviors in the larval zebrafish. *Current opinion in neurobiology* 19, 644-647.
- Portugues, R., Feierstein, C.E., Engert, F., and Orger, M.B. (2014). Whole-brain activity maps reveal stereotyped, distributed networks for visuomotor behavior. *Neuron* 81, 1328-1343.
- Rinner, O., Rick, J.M., and Neuhauss, S.C. (2005). Contrast sensitivity, spatial and temporal tuning of the larval zebrafish optokinetic response. *Invest Ophthalmol Vis Sci* 46, 137-142.
- Robles, E., Laurell, E., and Baier, H. (2014). The retinal projectome reveals brain-area-specific visual representations generated by ganglion cell diversity. *Current biology: CB* 24, 2085-2096.
- Ruta, V., Datta, S.R., Vasconcelos, M.L., Freeland, J., Looger, L.L., and Axel, R. (2010). A dimorphic pheromone circuit in *Drosophila* from sensory input to descending output. *Nature* 468, 686-690.
- Sabbah, S., Gemmer, J.A., Bhatia-Lin, A., Manoff, G., Castro, G., Siegel, J.K., Jeffery, N., and Berson, D.M. (2017). A retinal code for motion along the gravitational and body axes. *Nature* 546, 492-497.
- Schiff, D., Cohen, B., and Raphan, T. (1988). Nystagmus induced by stimulation of the nucleus of the optic tract in the monkey. *Experimental brain research* 70, 1-14.
- Schindelin, J., Arganda-Carreras, I., Frise, E., Kaynig, V., Longair, M., Pietzsch, T., Preibisch, S., Rueden, C., Saalfeld, S., Schmid, B., et al. (2012). Fiji: an open-source platform for biological-image analysis. *Nature methods* 9, 676-682.
- Schneider, C.A., Rasband, W.S., and Eliceiri, K.W. (2012). NIH Image to ImageJ: 25 years of image analysis. *Nat Methods* 9, 671-675.

Scott, E.K., Mason, L., Arrenberg, A.B., Ziv, L., Gosse, N.J., Xiao, T., Chi, N.C., Asakawa, K., Kawakami, K., and Baier, H. (2007). Targeting neural circuitry in zebrafish using GAL4 enhancer trapping. *Nature methods* 4, 323-326.

Semmelhack, J.L., Donovan, J.C., Thiele, T.R., Kuehn, E., Laurell, E., and Baier, H. (2014). A dedicated visual pathway for prey detection in larval zebrafish. *eLife* 3.

Stuermer, C.A. (1988). Retinotopic organization of the developing retinotectal projection in the zebrafish embryo. *J Neurosci* 8, 4513-4530.

Temizer, I., Donovan, J.C., Baier, H., and Semmelhack, J.L. (2015). A Visual Pathway for Looming-Evoked Escape in Larval Zebrafish. *Current biology: CB* 25, 1823-1834.

Vishwanathan, A., Daie, K., Ramirez, A.D., Lichtman, J.W., Aksay, E.R.F., and Seung, H.S. (2017). Electron Microscopic Reconstruction of Functionally Identified Cells in a Neural Integrator. *Current biology: CB* 27, 2137-2147 e2133.

Vladimirov, N., Wang, C., Hockendorf, B., Pujala, A., Tanimoto, M., Mu, Y., Yang, C.T., Wittenbach, J.D., Freeman, J., Preibisch, S., *et al.* (2018). Brain-wide circuit interrogation at the cellular level guided by online analysis of neuronal function. *Nature methods* 15, 1117-1125.

Wang, K., Hinz, J., Haikala, V., Reiff, D.F., and Arrenberg, A.B. (2019). Selective processing of all rotational and translational optic flow directions in the zebrafish pretectum and tectum. *BMC Biol* 17, 29.

Westerfield, M. (2007). *The zebrafish book. A guide for the laboratory use of zebrafish (Danio rerio)*, 5th edn (Univ. of Oregon Press, Eugene).

Wylie, D.R., Bischof, W.F., and Frost, B.J. (1998). Common reference frame for neural coding of translational and rotational optic flow. *Nature* 392, 278-282.

Yáñez, J., Suarez, T., Quelle, A., Folgueira, M., and Anadon, R. (2018). Neural connections of the pretectum in zebrafish (*Danio rerio*). *J Comp Neurol* 526, 1017-1040.

Zhang, B.B., Yao, Y.Y., Zhang, H.F., Kawakami, K., and Du, J.L. (2017). Left Habenula Mediates Light-Preference Behavior in Zebrafish via an Asymmetrical Visual Pathway. *Neuron* 93, 914-928 e914.

3 Discussion

With the work presented in the three manuscripts of this cumulative thesis, my colleagues and I developed a new optogenetic technique to analyze single neurons in terms of function and morphology and applied it to neural circuits in the larval zebrafish. We investigated early stages of processing in the optic-flow responsive circuit in the pretectum. In the following, I first want to highlight some broader implications of the findings from the manuscripts. Second, I will extend the discussion from the respective manuscripts, commenting on the neuronal organization of the larval zebrafish pretectum. Third, I will discuss potential technical improvements for FuGIMA as well as other features of the experiments.

3.1 Broader implications of the described findings

While specific technical or biological findings were discussed in the respective manuscripts, a few additional general implications can be pointed out. Although others had described these before, I want to point out how this work enhances our understanding of motion processing and neuronal circuits in general.

The notion of cell types oftentimes includes the feature of soma position, e.g. as belonging to a brain nucleus. However, dendritic morphology is potentially more determining, as it curtails possible inputs to a neuron. Specifically, somata of both monocular DS and translation-selective pretectal neurons are located in the AMC of the pretectum, albeit differing in their function (**manuscript 3**). By tracing individual neuronal morphologies of these neuron types, we found that monocular DS, but not translation-selective neurons, can receive direct DS inputs from RGC axons. This result, therefore, highlights the importance of dendritic morphology for the description of a cell type.

Different neuronal circuits can process information from one visual channel differently. This is shown by the example of DS information, which is represented in AF5 (**manuscript 3**) and SFGS1 of the optic tectum. Specifically, while DS information reaches those two areas via the same RGCs, the pretectum extracts information about optic flow and the optic tectum extracts information for prey and predator detection, thereby exemplifying the divergence of visual channels.

While the comprehensive technique “whole-brain imaging” is becoming increasingly popular to investigate neuronal relationships throughout the larval zebrafish brain, the combination of methods offers additional benefits. This is exemplified here, as the findings presented in **manuscripts 2 and 3** could only result from a combination of techniques. Specifically, the investigation of the whole-field motion processing pathway (**manuscript 3**) utilizes anatomical

data, both derived from expression patterns and individual neuronal tracings, and functional data, in the form of a 3D map of DS representations. Moreover, also on the level of individual cells, analyses of different neuronal properties, e.g. function or morphology, are necessary for more detailed characterizations. We achieved this using FuGIMA. The finding that monocular DS and translation-selective pretectal neurons differ in their potential inputs via AF5 would not have been accessible by investigating a single neuronal property alone, thus supporting the power of methods combinations.

Taken together, the work presented in this thesis not only investigates the whole-field motion processing pathway centered on the pretectum of larval zebrafish but also contains broader implications for the investigation of neuronal circuits and motion processing.

3.2 Pretectal organization

While the pretectal/AOS architecture is well described in mammals and increasingly so in adult zebrafish, knowledge about corresponding structures in larval zebrafish is scarce. In the following, I will discuss both published results from other laboratories and data from this thesis in an attempt to describe more comprehensively the pretectal organization in larval zebrafish.

3.2.1 Specific pretectal areas described in larval zebrafish

While the pretectal projections to the cerebellum and ventral hindbrain, as identified in **manuscript 3**, were consistent with the literature, the question remains, to which pretectal nucleus the recorded FuGIMA neurons and those of the single-neuron atlas correspond.

More than 20 years ago, a seminal study characterized the retinofugal projections in embryonic and larval zebrafish and tried to correlate the larval AFs to the adult pretectal nuclei (Burrill and Easter, 1994). The authors noted that somata of neurons projecting into the AFs cluster near the respective neuropil in adult zebrafish, but are more distantly located in larvae (except for AF10). Therefore, pretectal nuclei cannot be distinguished based on cytoarchitectonic features in larvae. Furthermore, it is unclear if post-synaptic neurons remain the same between larvae and adults (Burrill and Easter, 1994). For most AFs, the authors noted several possible corresponding adult nuclei, which in turn influenced annotations of other AFs. As an example, AF5 could correspond to one of three thalamic nuclei, while AF6 could correspond to either the nAOD (dorsal accessory optic nucleus) or a thalamic nucleus (Burrill and Easter, 1994). According to Yáñez, et al. (2018), the nAOD may in turn correspond to Pi, based on its projections to the cerebellum.

In the work presented in **manuscript 3**, we systematically outlined AFs 4 – 9, however omitted the more ventrally located AFs 1 – 3. Specifically, several pretectal FuGIMA-labeled neurons project to AFs 5 and 6. Therefore, it is likely that these nuclei are pretectal instead of thalamic. Furthermore, few individual neurons of the FuGIMA dataset or the PPNs extend into AFs 4, 7, 8, and 9, thereby also suggesting those to be pretectal areas.

Based on recent work, however, we know more about two anterior-lateral pretectal areas. Two recent papers elucidate the pretectal neuronal circuits underlying prey-capture in larval zebrafish and make an effort to relate the corresponding pretectal nuclei to those described in previously published studies. Semmelhack, et al. (2014) identified AF7 as the relay center for the prey-capture specific visual channel. The authors found two morphological types of neurons extending neurites into AF7, with their somata at the same dorso-ventral level as AF7. Based on its relative location, the authors identified AF7 as the equivalent to PSp (parvocellular superficial pretectal nucleus, see section 1.4.1, page 6)(Semmelhack, et al., 2014). However, Yáñez, et al. (2018) suggested that, based on connectivity, the AF7 innervating neurons of Semmelhack, et al. (2014) correspond to APN instead. Muto, et al. (2017) identified a cluster of prey-responsive neurons in the enhancer trap line gSAzGFFM119B. This line labels a small population of neurons directly ventral to AF7 and directly dorsal to AF5, thereafter referred to as 119B-pretectal cells. Based on the connectivity of these neurons, which project to the inferior lobe of the hypothalamus and the precerebellar area, the authors speculated this population would correspond to PSm (magnocellular superficial pretectal nucleus)(Muto, et al., 2017). Consistent with the literature, the authors did not find RGC arborization around the somata of 119B-pretectal cells.

The two studies mentioned above, skillfully investigated two prey-capture selective nuclei and related their findings to previous literature. Based on their functional responses and anatomical locations, these areas seem to be independent from the motion processing pathway that I described in this thesis. However, as information on other pretectal nuclei is scarce, more information is necessary to describe the organization of the pretectum in larval zebrafish.

3.2.2 Characterization by responses to visual stimuli

Traditionally, anatomical descriptions based on clusters of somata and fiber tracts inform segmentation of a brain into functional entities. However, nuclear organization of the pretectum is ambiguous in larval zebrafish (see introduction). Therefore, maps derived from other parameters are necessary to describe this area further. One approach that can be used to define brain areas is to map the functional responses to stimuli of these regions.

For example, Kubo, et al. (2014) found several functional clusters in the pretectum when presenting optic-flow stimuli to larval zebrafish. This finding is the foundation of research presented in **manuscript 3**. Specifically, Kubo, et al. (2014) identified different types of motion-sensitive neurons in a large region encompassing the pretectal area (APT) and identified three functional clusters, termed anterior medial cluster (AMC), anterior lateral cluster (ALC), and anterior ventral cluster (AVC), in the APT. While the relatively large AMC contains neurons of various monocular and binocular response types, the smaller clusters ALC and AVC contain almost exclusively monocular DS neurons (**Figure 9A, B**, page 155). Specifically, ALC appears to be bordering the funnel-shaped area of the optic tract (**Figure 9C**, page 155). Moreover, a small, backward motion-tuned cluster is located anterior to AF9, presumably in close proximity to the posterior commissure and the fasciculus retroflexus (**Figure 9D**, page 155). Similarly, studies using whole-brain imaging find responses to whole-field motion in a large pretectal area, presumably AMC (Naumann, et al., 2016, Portugues, et al., 2014, Vladimirov, et al., 2018).

Taken together, the pretectum of larval zebrafish can be segmented on the basis of functional information. Specifically, Kubo, et al. (2014) showed that the APT contains three clusters of motion-sensitive neurons.

3.2.3 Characterization by circuit manipulation

Neuronal function can also be investigated via changes in functional responses induced by targeted cellular manipulation. A recent study on brain-wide OMR circuits in larval zebrafish initially identified neuronal clusters correlated with optic flow driven swimming behavior (OMR). Following a guided ablation of one of these clusters, visual stimulation and neural imaging were repeated to investigate circuit changes following ablation (Vladimirov, et al., 2018). Pretectal ablations of neurons tuned to swimming (likely in AMC) lead to a decrease of neuronal activity in several regions in the mid- and hindbrain. Interestingly, ablation of neurons in the inferior olive (IO) resulted in, aside from a decrease in activity in several areas, an increase in one potential pretectal cluster (**Figure 10**, page 156). While quantifications did not find this effect significant, the existence of two neighboring nuclei with opposing neuronal activity changes after IO ablation is intriguing. Furthermore, it suggests that AMC could be subdivided further. As the image volumes from Vladimirov, et al. (2018) are not yet registered to the standard brain of **manuscript 2**, direct comparisons are difficult, especially regarding the question of whether these clusters belong to the pretectum. If they were part of the pretectum, our view of the pretectal organization should incorporate these two clusters. Furthermore, this finding would point at a connection between the IO and the pretectum with

opposing signs, potentially establishing a feedback loop in the reported pretectum to IO connection (see 1.4.4, page 11).

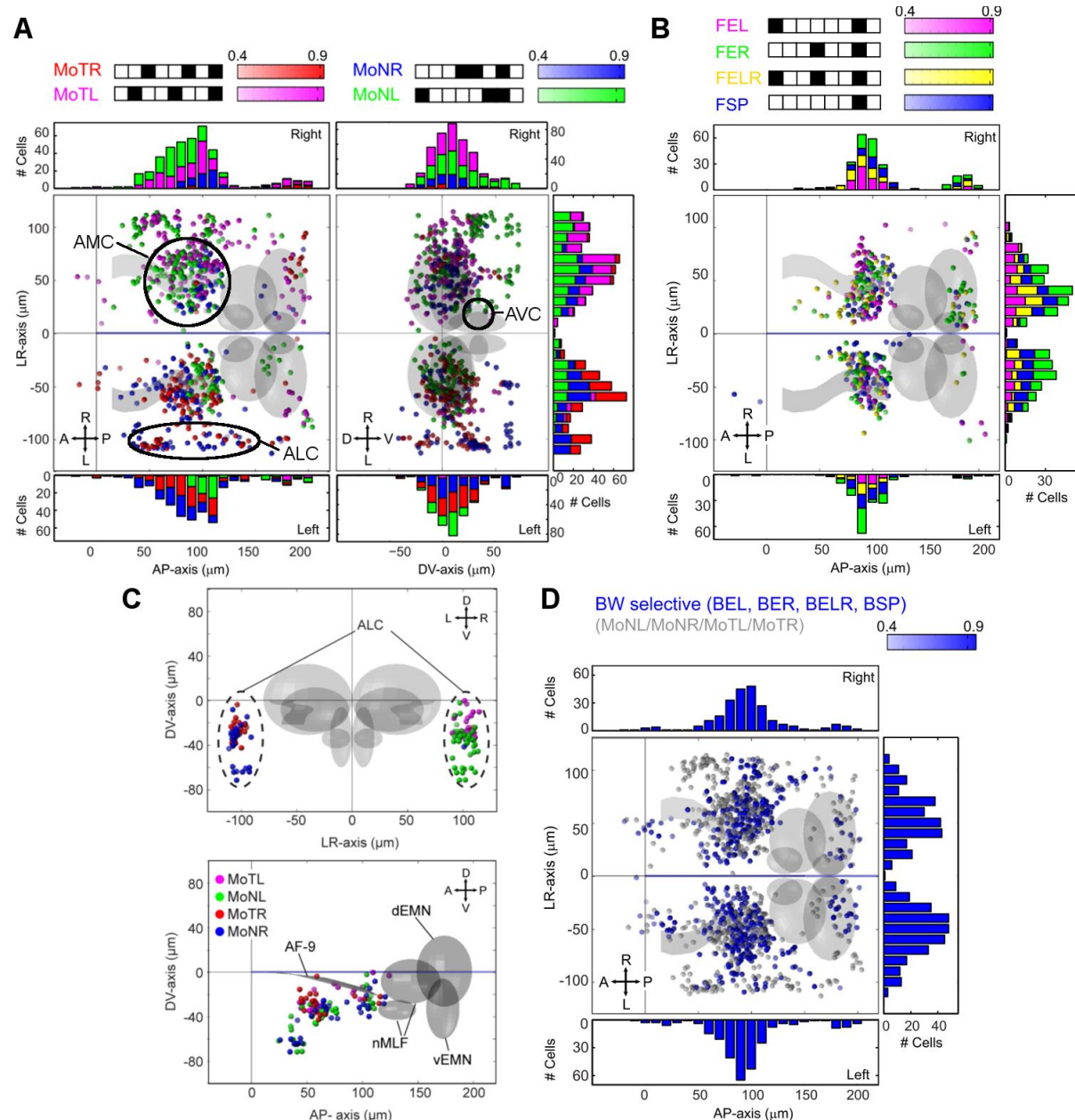


Figure 9: Localization of motion-sensitive neurons in the pretectum. **A:** Dorsal and frontal views of all simple monocular DS neurons in the field of view containing the pretectum, but also nuclei at the midbrain-hindbrain boundary, color-coded according to response type. Black ovals: pretectal functional clusters AMC, ALC and AVC (anterior medial cluster, anterior lateral cluster, and anterior ventral cluster, respectively). **B:** Dorsal view of forward-selective neurons, located in the AMC. **C:** Frontal and lateral views of neurons in the ALC. **D:** Dorsal view of backward motion-selective neurons. Grey ovals: nucleus of the medial longitudinal fasciculus, trochlear and oculomotor nuclei; grey wave: AF9. The origin of the coordinate system is placed at the intersection of the midline plane, and a line between the dorsal-anterior tips of the diencephalic neuropil (image modified from Kubo, et al. (2014)(with permission).

Taken together, circuit manipulation can aid in the segmentation of the brain by revealing functionally affected areas. Based on responses resulting from circuit manipulation, Vladimirov, et al. (2018) identified a potential subdivision of the pretectum. However, future image registration will need to confirm the pretectal location of the functionally identified clusters.

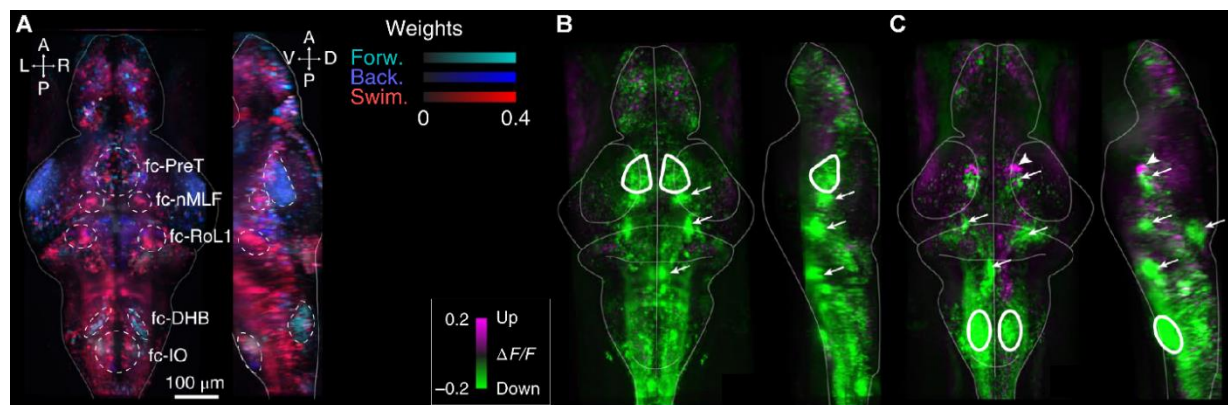


Figure 10: Brain-wide activity changes after ablation of functionally defined clusters. A: Functional map of voxels tuned to forward (cyan) or backward (blue) translational optic flow or swimming movements (red). Dotted lines highlight five functional clusters. **B:** Effect of 2p-targeted ablation in the pretectum (area circled with solid white line) on whole-brain activity (green: decreased neuronal activity; magenta: increased neuronal activity; white arrows point to clusters with strong effects after ablation). **C:** as in B, but here with ablation of the inferior olive. Image modified from Vladimirov, et al. (2018)(with permission).

3.2.4 Characterization by transgenic expression patterns

Another cellular level method for describing neurons within functional clusters is analysis of gene expression. In many cases, information about the specific expression of genes, e.g. transcription factors, is useful to differentiate a neuronal cluster from its surroundings. Furthermore, expression of e.g. neurotransmitter processing enzymes or receptors allows for more specific inferences about a neuron's role in the circuit.

With z-stacks of many transgenic lines now registered to standard brains of different atlases, such as the single-neuron atlas (**manuscript 2**), *in-silico* comparisons between expression patterns became very convenient and sufficiently precise. Although I had applied FuGIMA to the pretectum as labeled in the panneuronal line Gal4s1101t (**manuscript 3**), the question remained whether a transgenic line labeling specifically the area where FuGIMA-labelled neurons were located (FuGIMA-VOI) did exist. Furthermore, comparison of expression patterns in the pretectum could further uncover components of pretectal organization. To these ends, I compared the FuGIMA-VOI with the ~ 300 expression patterns available through the website described in **manuscript 2** (accessed: 14th of March 2019). Registered transgenic lines included those of several laboratories, as well as of different

transgenes (based on Gal4, Cre, or direct promoter fusions). While several lines showed non-specific or sparse expression in the area, I searched for more restricted expression patterns and labeled neurons clustered within or in the surroundings of the FuGIMA-VOI. Overall, I found ten interesting lines and three landmark structures as references (**Figure 11**, page 158). Dorsally, roughly at the level of AF7 and AF9, the lines Gal4s1181t, Gal4s1026t, and mpn321 overlap with the FuGIMA-VOI. The Cre lines y483Et and y523Et label AF7 and the surrounding neuropil. The line Gal4s1053t labels a medial cluster dorsal to the nMLF. Further ventrally, roughly at the level of AF5 and AF6, the line nkSAGFF(LF)234ATg (234A) labels an anterior-medial cluster ventral to the posterior commissure and the fasciculus retroflexus, *chat:Gal4* labels a medial cluster, and the lines gSAzGFFM119B and SAIzGFFD1112B (1112) label a lateral cluster close to the optic tract.

Taken together, a comprehensive analysis of expression patterns identified neuronal clusters in close proximity of the FuGIMA-VOI. Unfortunately, the described *in-silico* co-localization analysis did not reveal transgenic lines specifically expressing in the FuGIMA-VOI. As the expression pattern database of the single-neuron atlas does not contain all transgenic lines currently available within the global zebrafish neuroscience community, many lines remain to be screened. Alternatively, one might want to establish new transgenic lines with pretectal expression, as based on literature (see 3.4.2, page 163). In general, inclusion of transgenic lines generated by different laboratories proved very helpful as a resource when planning experiments and for segmentation of brain areas (see 3.2.4, page 156; (Gupta, et al., 2018)).

3.2.5 Correspondences between larval and adult zebrafish pretectum

Based on current literature and comparing the described functional, anatomical and gene expression annotations, I speculate on the correspondence between pretectal nuclei in adult zebrafish and pretectal areas in larval zebrafish in the following.

As stated in Muto, et al. (2017), pretectal 119B cells, which are also labeled in the line 1112, could correspond to PSm. AF7 and the surrounding neurons, as suggested by Semmelhack, et al. (2014) could correspond to PSp, as it receives retinal afferents and projects to the ventral hindbrain. As the Cre lines y483 and y523 express in that area, labeled neurons could mediate orienting behaviors towards prey. The PPn is located below the posterior commissure, lateral to the ventricle and wrapping around the fasciculus retroflexus (Yáñez, et al., 2018). Therefore the neurons labeled in the line 234A or the pretectal *chat:Gal4* cluster might correspond to PPn. Pretectal neurons of the single-neuron atlas that are located within the FuGIMA-VOI (pretectal projection neurons, PPNs) extended mainly either to the cerebellum or the ventral hindbrain and were spatially separated (**manuscript 3**). In adult zebrafish, three nuclei project to the cerebellum: Pi, PCe, and PCo.

Therefore, the anterior, cerebellum-projecting PPN group might correspond to either of these three nuclei. The APN, a large pretectal nucleus does not receive retinal afferents, but projects to the ventral hindbrain. Therefore, the APN might correspond to the second group of PPNs, included in the posterior part of the *Gal4s1026t* expression pattern (**manuscript 3**). Nevertheless, as some *FuGIMA-VOI* neurons extend their neurites into AFs 5 and 6, these areas could also be included in an enlarged PSp.

These described clusters in larval zebrafish could correspond to pretectal nuclei of adult zebrafish. To test these hypotheses, it would be informative to study the identity of neurons labeled in an expression pattern longitudinally, from larva to adult.

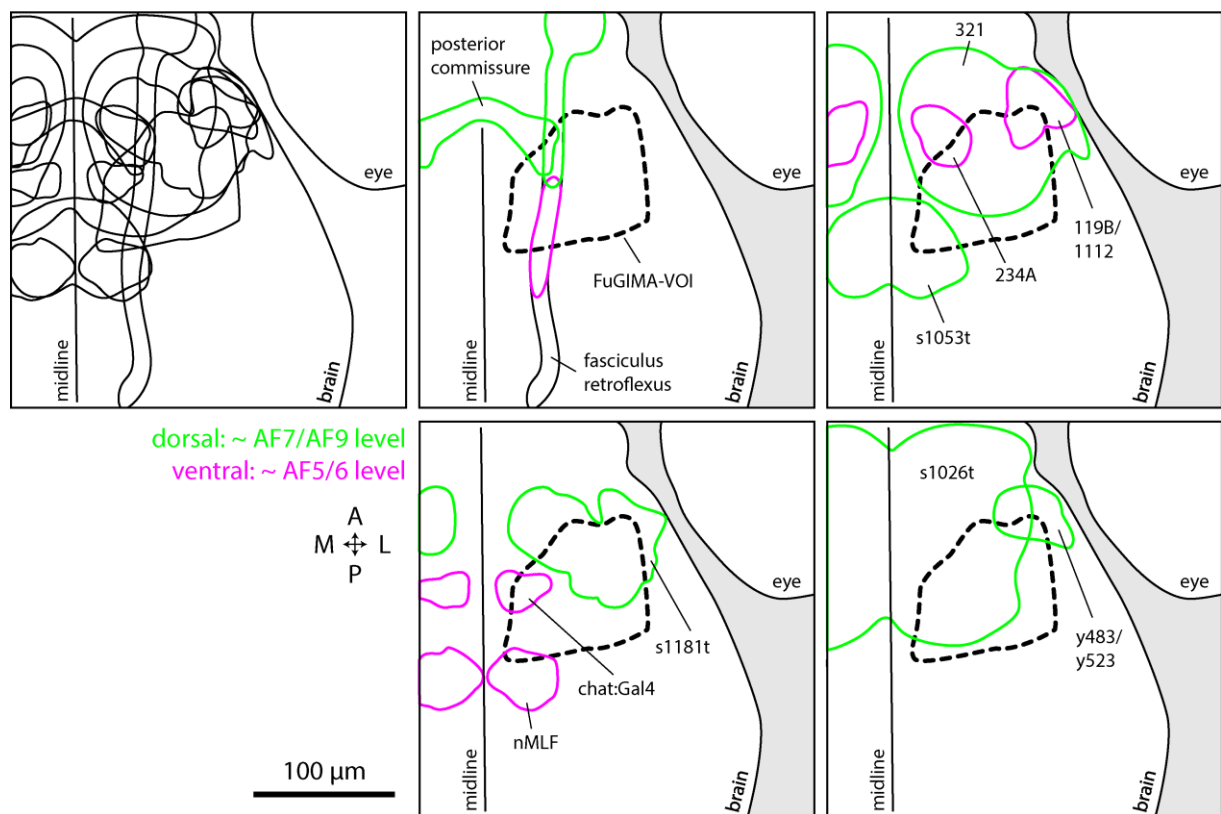


Figure 11: Neuronal clusters overlapping with/in close proximity to the *FuGIMA-VOI*. Outlines of neuronal clusters identified in transgenic lines (chosen for clustered expression in the investigated region), as downloaded from the single-neuron atlas. While clusters are depicted as maximum intensity projections, green outlines symbolize a dorsal localization (roughly AF7/AF9) and magenta outlines a more ventral position (roughly AF5/AF6). 234A, 119B/1112: enhancer/gene trap lines *nkSAGFF(LF)234A*, *nkGSAIzGFFM119BGt* and *SAIzGFFD1112B* of the Kawakami lab (Muto, et al., 2017); *y483Et/y523Et*: Enhancer trap Cre lines of the Burgess lab (Tabor, et al., 2019); *s1053t*, *s1181t*, *s1026t*: enhancer trap lines of the Baier lab (Scott and Baier, 2009); *chat:Gal4*: BAC-transgenic line of the Baier lab (Förster, et al., 2017); 321: *mpn321Gt*, gene trap line of the Baier lab; nMLF: nucleus of the medial longitudinal fasciculus, as labeled with backfills.

3.3 Potential improvements of FuGIMA

With FuGIMA, my co-authors and I were able to investigate relationships between function and morphology of neurons in an unprecedented way and we envision that FuGIMA will continue to prove helpful in further studies. Nevertheless, as with any technique, advantages, disadvantages and potential improvements become evident, therefore I will highlight a few of the potential improvements in the following sections in addition to technical considerations addressed in **manuscript 1**.

3.3.1 Increasing the signal-to-noise ratio of paGFP

Fluorescently labeling small cellular structures with FPs is limited by the brightness and concentration of FP molecules contained in the investigated volume, e.g. the volume scanned by the microscope. In the case of paGFP, not all molecules are typically photoactivated; therefore, the effective concentration of bright paGFP molecules is even lower. One solution to the bottleneck of a low signal-to-noise ratio in FuGIMA is therefore the improvement of paGFP labeling.

Several techniques exist to improve the detection of weak FP expression in fixed specimens, most notably immunohistochemistry. While no antibodies for activated paGFP currently exist (see section 1.5.7.2, page 18), other methods such as tissue-clearing might be an option to increase detectability. To date, chemical treatments conferring the superior optical features of tissue-clearing methods often decrease detection of FPs, e.g. by quenching of fluorescence due to removal of the aqueous environment surrounding the protein (Richardson and Lichtman, 2015). One approach to decreasing vulnerability of GFP for tissue clearing and related methods could come via improved GFP variants. Recently, a monomeric ultra-stable GFP (muGFP) with improved hydrophobic/hydrophilic interactions was developed and successfully subjected to the tissue-clearing method CLARITY (Chung, et al., 2013, Scott, et al., 2018). The two underlying amino acid changes could be incorporated into the paGFP sequence, thus potentially rendering paGFP more stable. Thereby, one could trace FuGIMA neurons more accurately over longer distances due to a reduced background signal in cleared samples.

Another option to improve the signal-to-noise ratio is to increase the number of expressed paGFP molecules per cell. In the current version, the genes encoding nls-GCaMP6s and paGFP are fused to either side of a bidirectional UAS (Janus-UAS; (Distel, et al., 2010, Paquet, et al., 2009)), intended to lead to comparable and linked expression levels (**Figure 8**, page 20). As the expression levels of nls-GCaMP6s proved more than sufficient for functional imaging in our hands, the ratio could be shifted to favor paGFP expression. In that case, the FuGIMA plasmid should be reengineered to contain e.g.

two bicistronic open reading frames on either side of the Janus-UAS, in total with one nls-GCaMP6s and three paGFP genes. Furthermore, the expression level of paGFP molecules could be increased by improvements in codon usage, addition of introns, 3' untranslated regions, and releasing factor recognition sequences, which are not yet routinely used in the zebrafish community (Horstick, et al., 2015). Nevertheless, it remains to be seen whether such a construct can indeed increase the expression level of paGFP. However, cellular processes, e.g. protein degradation and gene silencing, can interfere with very high expression levels of transgenes, therefore the plasmid sequence should be empirically optimized.

These suggested molecular improvements directly address current limitations of the paGFP signal-to-noise ratio. However, their implementation requires the generation of a novel transgenic line, which in itself introduces great variability in transgene expression. To address this gap, methods to insert a transgene at a genetic locus known to support strong and little variegated expression, e.g. with CRISPR/Cas9, are currently being developed. Thus, the generation of a better FuGIMA line will be possible with improved transgene targeting and molecular improvements of paGFP.

3.3.2 Automated targeting of cells

Photoactivation of paGFP in the soma of functionally characterized neurons required constant interaction of the experimenter for the duration of the photoactivation protocol (**manuscript 1**). Specifically, I re-identified and manually outlined the region-of-interest for photoactivation (paROI) (**manuscript 1** and **manuscript 3**). Moreover, the paROI needed refocusing to accommodate for sample drift during the photoactivation protocol. As the protocol lasted over an hour, its repetitive nature can increase the likelihood of errors. With FuGIMA, accidentally hitting a neighboring neuron typically required abortion of the trial, as unambiguous labeling of neighboring neurons hampered correct tracing. Therefore, I suggest decreasing photoactivation errors by automatizing the targeting/refocusing steps.

A recent study developed automated targeting of single neurons with a 2p microscope. There, the authors used a custom-written Fiji plugin to select individual cells for automatic laser ablation (Vladimirov, et al., 2018). If the sample is sufficiently stable (drift approx. $< 2 \mu\text{m}$ for the duration of the protocol), such automated targeting could decrease the error rate and allow more rapid switching between neurons, therefore enabling a higher throughput (currently up to 2 neurons per fish; **manuscript 3**).

Automatic re-focusing to compensate for sample drift would be technically more challenging. Here, the experimenter would define a sample plane, then the microscope would automatically acquire a

z-stack, calculate the best fitting plane compared to the defined sample plane and re-focus to that position. While technologically possible and probably in use in other applications, such an automatic re-focusing system does not yet exist in typical microscopes in the field.

Taken together, automatic targeting of neurons for photoactivation and re-focusing of the sample could decrease the error rate and increase the throughput per sample, thereby facilitating the application of FuGIMA.

3.3.3 Automated tracing

One step in the FuGIMA protocol with immense impact on the results is the tracing of neurons from image z-stacks. Specifically, the signal-to-noise ratio in our dataset (**manuscript 3**) was too low to employ automatic modes of tracing in the applications Imaris (Bitplane, Zürich, Switzerland) or Single Neurite Tracer (Longair, et al., 2011). Instead, we opted to trace neurons manually/semi-manually, which took about one to two hours per neuron. Furthermore, we tested merging tracings (traced by multiple annotators). However, this did not improve confidence in the tracings (unpublished results). From these experiences, I suggest the consideration of automatic tracing for future uses of FuGIMA. This could become feasible in the near future, as several improved filament tracing algorithms were developed recently: even though most are developed for analysis of electron microscopy volumes (EM; which faces the same problem to a more existential extent; see section 4.1, page 164), some are applicable to light microscopy data (reviewed in Acciai, et al. (2016)). Specifically, algorithms including supervised learning could prove useful, as z-stacks for a given biological question might look alike, thus alleviating transferability issues. In contrast, cross-species application might not be feasible, e.g. algorithms tailored to mouse neuronal morphologies, as the complexity of larval zebrafish neurons is often lower. Therefore, with upcoming improvements in the field of automatic filament tracing, I expect that neurons will become traceable in an automated fashion with an acceptable error rate even from high noise images, thus highly facilitating FuGIMA.

3.4 Further technical considerations

3.4.1 Perspective on identified pretectal projection neurons

While some pretectal projections exist in other adult animals and adult zebrafish, our complementation analysis identified only two pretectal projection pathways that emanated from the region where FuGIMA neurons localized (**manuscript 3**). This discrepancy might be rooted in the 1) incomplete neuronal connectivity of developing larvae, 2) incomplete representation of

neuron types in the single-neuron atlas, or 3) incomplete description of the pretectum with the FuGIMA-VOI.

The first argument, that the discrepancy between reported and observed pretectal connectivity is explained by the developmentally immature state of the experimental animals, seems less compelling to me. Zebrafish undergo rapid development mostly in the embryonic (up to 72 hpf) and larval stages. As zebrafish larvae of 5-6 dpf perform already OKR and increasingly stable OMR, the underlying neural circuits are sufficiently mature to drive these behaviors. Furthermore, developing neurons, which are not yet integrated into these circuits, should not be picked up with FuGIMA, since they should not exhibit stimulus-locked activity. BGUG, the method underlying neuronal tracings of the single-neuron atlas, can, in principle, label mature and immature neurons. However, empirically, the majority of PPNs contained long projections with arborizations, thus supporting their mature state. Therefore, both the FuGIMA dataset and PPNs do likely not contain immature neurons, whereby the discrepancy in pretectal connectivity is less likely caused by the different developmental stages of the animals.

The second argument, that this discrepancy is explained by an incomplete representation of neuron types in the single-neuron atlas due to technical reasons, appears more plausible. While the brain of a larval zebrafish at 7 dpf contains about 78000 neurons (Hill, et al., 2003), the single neuron atlas currently contains about 2 % thereof (2.23%, 1743 tracings of 6 dpf larvae at the time of retrieval from the atlas). Thus, it is likely, that less numerous cell types are not yet contained in the single-neuron atlas. We envision that further datasets will be added to the atlas, both with datasets acquired in-house, as well as from the zebrafish neuroscience community. Therefore, a future repetition of the analysis will likely show an enriched connectivity pattern, more closely resembling pretectal connectivity in adult zebrafish.

The third argument, that the observed discrepancy is explained by the spatially incomplete description of the pretectum by the FuGIMA-VOI seems most compelling. The FuGIMA-VOI was not meant to describe the entire pretectum, but rather search for PPNs in the single-neuron atlas. Specifically, the FuGIMA-VOI comprises of monocular DS, translation-selective and non-motion-sensitive neurons in the AMC. The AMC might display a different connectivity compared to the other pretectal regions. Indeed, when searching for somata in an enlarged volume dorso-anteriorly to the FuGIMA-VOI, I find more neurons projecting to the cerebellum and ventral hindbrain, but in addition also to the contralateral pretectum via the postoptic commissure and to the ipsilateral optic tectum (data not presented). This strengthens the hypothesis, that different pretectal areas have differing connectivity, as shown in adult zebrafish.

Overall, we found prominent pretectal projection patterns with our approach, thus displaying the utility of cross-dataset comparisons and the power of the single-neuron atlas as an unprecedented resource for circuit level analysis. The discrepancy of reported pretectal projections between adult and larval zebrafish as described above is thus likely due to sampling of the single-neuron atlas and an underrepresentation of the pretectum by the FuGIMA-VOI. A future extension of the single-neuron database will address the issue of neuronal coverage and will complete our understanding of projections from pretectal subpopulations.

3.4.2 New transgenic lines to investigate pretectal processing

While we were able to analyze pretectal neurons functionally and morphologically with FuGIMA, manipulation of pretectal subpopulations would be informative to further elucidate local processing. However, no transgenic zebrafish lines specifically labeling DS-RGCs or the pretectum, neither in its entirety, nor in a subpopulation-specific way, are currently available (see 3.2.4, page 156). Therefore, a step towards refined investigation is the generation of novel transgenic lines with specific expression patterns, based on e.g. candidate genes described in the literature on RGCs/pretectum/AOS in rodents. Future RNA-seq datasets of the zebrafish pretectum, such as recently acquired for mouse pretectum (Guo and Li, 2019), will identify differentially expressed genes, thereby contributing to the candidate gene list. As gene expression signatures underlying many transgenic lines are often present in multiple tissues, it is advantageous to confine expression to neurons e.g. with the application of a neuron-restrictive silencing element (NRSE) derived motif (Bergeron, et al., 2012). Furthermore, intersectional gene expression strategies such as the combination of the Gal4/UAS and QF2/QUAS-systems can additionally sharpen expression patterns (Subedi, et al., 2014). However, a recent effort of the Baier laboratory to establish more transgenic lines based on regulatory elements of candidate genes using BAC transgenesis was only successful for a subset of queried markers (Förster, et al., 2017). Emerging genome editing techniques, such as those based on CRISPR/Cas9, will likely allow the generation of better transgenic lines and therefore facilitate zebrafish neuroscience research.

4 Outlook

4.1 Functional imaging combined with electron microscopy (EM)

The gold standard to infer anatomy and connectivity of neurons is electron microscopy (EM). Recent advances in the field, i.e. rapid acquisition of 3D volumes with serial block-face scanning EM and large-scale circuit reconstruction, allow one to investigate increasingly large samples, enabling the analysis of connectivity of a particular neuronal network (Denk and Horstmann, 2004, Saalfeld, et al., 2009). Two bottlenecks, namely storage of and access to very large datasets (in the tens of terabyte range and more) and tracing of neurons (manual vs. automatic), are being cleared with progress in information technology (reviewed in Kornfeld and Denk (2018)). While EM enthusiasts might claim that elucidating the connectome will be synonymous with understanding a computer chip, this is certainly not yet the case. This is because EM data offers “snapshots” of anatomical connectivity but does not directly reveal functional properties of the underlying neuronal network. Instead, by integrating information about function and morphology by combining techniques, we increase our understanding of neuronal processing, as showcased for the DS circuit in the retina (Briggman, et al., 2011). Recently developed computational methods to merge datasets acquired at the light and electron microscopes facilitate the accomplishment of this aim (Drawitsch, et al., 2018). While light microscopy is ubiquitous, only decreasing costs will make volumetric EM accessible beyond laboratories currently spearheading its technological development. However, at least two limitations inherent to the technique prevent its widespread application: Firstly, sample preparation, image acquisition, and neuronal reconstruction are currently very time consuming (each on the order of weeks to months, depending on sample size), typically limiting the number of analyzable samples to one or two. Secondly, volumetric EM is not compatible with live imaging due to toxic heavy-metal based staining solutions necessary as contrast agents. Therefore, questions regarding e.g. functional response types cannot be addressed with EM-based reconstructions alone.

In vivo and medium-to-high throughput methods based on fluorescence microscopy, such as FuGIMA, are superior in that respect. Moreover, FuGIMA could be applied in comparisons between wild-type animals and mutants, which typically require several experimental animals. Due to the opposing strength-weakness profiles, combined EM/functional imaging and FuGIMA might also complement each other.

Along the same line, the results obtained with FuGIMA (**manuscript 3**) will need to benchmark themselves against an EM-based reconstruction with a similar neuronal population. This project currently conducted by colleagues at the MPIN aims at reconstructing functionally characterized

motion-sensitive neurons in the pretectum of one larval zebrafish. The direct comparison between the two projects will thus highlight the advantages and disadvantages of either technique. Ideally, combined EM/functional imaging and FuGIMA should complement each other.

4.2 What is next? Function-guided inducible gene expression (FuGIGEx)

As described in this thesis, FuGIMA is a powerful, all-optical method to combine functional and morphological analysis of single neurons. Following the discussion regarding limitations of FuGIMA, I want to conclude with thoughts about a dream technique that could become its successor.

While labeling of thin neurites with paGFP is not trivial, constitutively fluorescent FPs are routinely used to singly label neurons e.g. with BGUG (Scott, et al., 2007)(**manuscript 2**). Therefore, a system that combines strong labeling with the possibility to switch it on, e.g. light-induced gene expression of FPs, would be advantageous. Such a system should be inducible with short illuminations (in the range of a few minutes or less), independent of cofactors which are not endogenously available in the organism, have a “switch”-like behavior (two states rather than a graded response) and, very importantly, a “tight” off state (activation only in the presence of illumination). Over the last years, several research groups engineered proteins-of-interest (POI) with light-inducible activity. The main principle of action depends on light-dependent dimerization of protein domains derived from plant photoreceptors, fused to two parts of the split POI. Upon illumination, the dimerizer domains pull the POI parts together, thereby reconstituting POI activity. Light-dependent gene expression was achieved directly with split transcription factors including Gal4 (light-inducible transcription) or indirectly with split Cre (light-inducible recombination)(Beyer, et al., 2015, Kawano, et al., 2016, Kennedy, et al., 2010, Müller, et al., 2013, Pathak, et al., 2017, Reade, et al., 2017). Depending on the used photosensitive domains, activation parameters, e.g. induction times and illumination wavelength, differ. As most of these techniques were developed for mammalian cell culture, I expect that they will not be transferable to larval zebrafish without some modifications improving induction tightness to account for light scattering. After adaption and improvements, such a technique could be used in conjunction with functional imaging, thereby establishing Function-guided Inducible Gene Expression (FuGIGEx), the successor of FuGIMA, as outlined in **Figure 12** (page 166). In FuGIGEx, functional characterization is followed by light-inducible gene expression. Researchers could use this technique not only to analyze the morphology of neurons via expression of structural markers, but also to exchange the effector to e.g. pharmaco-genetically ablate functionally-characterized neurons (Curado, et al., 2007, Mathias, et al., 2014) or manipulate their activity with optogenetics. I am looking forward to seeing this dream technique extend the zebrafish toolbox in the future.

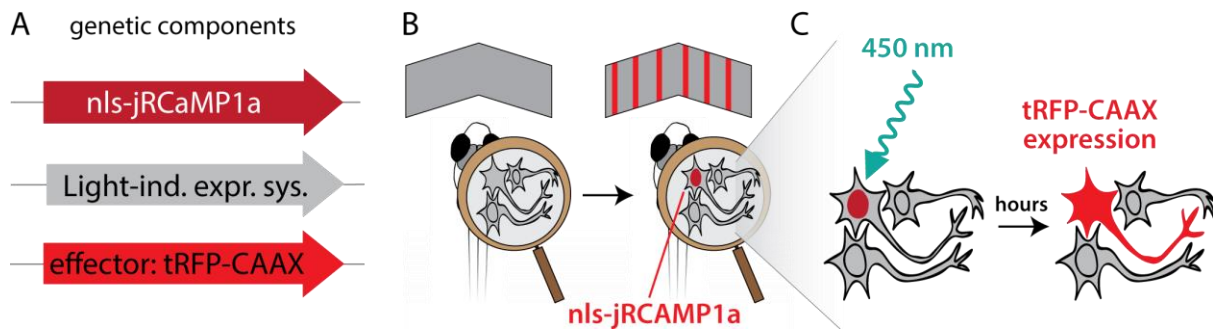


Figure 12: A better FuGIMA? Function-guided inducible gene expression (FuGIGEx). To overcome potential limitations of FuGIMA caused by suboptimal labeling with paGFP, inducible gene expression in a functionally characterized neuron would be advantageous. **A:** FuGIGEx is based on three components, a nuclear localized Ca^{2+} indicator (e.g. the red GECI nls-jRCaMP1a (Dana, et al., 2016)), the light-inducible gene expression system, and finally the effector (e.g. a membrane localized red FP such as tRFP-CAAX for morphological analysis). Please note that wavelengths for functional/anatomical imaging and induction of the gene expression system must be compatible. **B:** As with FuGIMA, neurons are functionally characterized with functional imaging based on nuclear-localized genetically encoded activity indicators. **C:** Furthermore, illumination with focused light (2p mode) induces gene expression and over time labels the neuron.

References

The Nobel Prize in Chemistry 2008. Nobel Media AB (<https://www.nobelprize.org/prizes/chemistry/2008/summary/>, accessed: 8 Jan 2019).

Abbas, F., Triplett, M.A., Goodhill, G.J. and Meyer, M.P. (2017). A three-layer network model of direction selective circuits in the optic tectum. *Front Neural Circuits* 11. 88.

Acciai, L., Soda, P. and Iannello, G. (2016). Automated Neuron Tracing Methods: An Updated Account. *Neuroinformatics* 14. 353-367.

Ahrens, M.B., Li, J.M., Orger, M.B., Robson, D.N., Schier, A.F., Engert, F. and Portugues, R. (2012). Brain-wide neuronal dynamics during motor adaptation in zebrafish. *Nature* 485. 471-477.

Anadón, R. (2017). Enlightening the pretectum. *J Comp Neurol* 525. 711-714.

Antinucci, P. and Hindges, R. (2016). A crystal-clear zebrafish for in vivo imaging. *Sci Rep* 6. 29490.

Arunachalam, M., Raja, M., Vijayakumar, C., Malaïammal, P. and Mayden, R.L. (2013). Natural history of zebrafish (*Danio rerio*) in India. *Zebrafish* 10. 1-14.

Asakawa, K., Suster, M.L., Mizusawa, K., Nagayoshi, S., Kotani, T., Urasaki, A., Kishimoto, Y., Hibi, M. and Kawakami, K. (2008). Genetic dissection of neural circuits by Tol2 transposon-mediated Gal4 gene and enhancer trapping in zebrafish. *Proc Natl Acad Sci U S A* 105. 1255-1260.

Avants and Johnson (2014). Advanced Normalization Tools (ANTS) documentation. (<http://stnava.github.io/ANTSDoc/>, accessed: 2 Aug 2016).

Avants, B.B., Epstein, C.L., Grossman, M. and Gee, J.C. (2008). Symmetric diffeomorphic image registration with cross-correlation: evaluating automated labeling of elderly and neurodegenerative brain. *Med Image Anal* 12. 26-41.

Avants, B.B., Tustison, N.J., Song, G., Cook, P.A., Klein, A. and Gee, J.C. (2011). A reproducible evaluation of ANTs similarity metric performance in brain image registration. *Neuroimage* 54. 2033-2044.

Avants, B.B., Yushkevich, P., Pluta, J., Minkoff, D., Korczykowski, M., Detre, J. and Gee, J.C. (2010). The optimal template effect in hippocampus studies of diseased populations. *Neuroimage* 49. 2457-2466.

- Baden, T., Berens, P., Franke, K., Román Rosón, M., Bethge, M. and Euler, T. (2016). The functional diversity of retinal ganglion cells in the mouse. *Nature* 529. 345-350.
- Bae, Y.K., Kani, S., Shimizu, T., Tanabe, K., Nojima, H., Kimura, Y., Higashijima, S. and Hibi, M. (2009). Anatomy of zebrafish cerebellum and screen for mutations affecting its development. *Dev Biol* 330. 406-426.
- Barker, A.J. and Baier, H. (2015). Sensorimotor decision making in the zebrafish tectum. *Curr Biol* 25. 2804-2814.
- Barker, A.J., Helmbrecht, T.O., Grob, A.A. and Baier, H. (2017). Detection of whole-field luminance changes by superficial interneurons in the zebrafish tectum. *Biorxiv*, doi: 10.1101/178970.
- Barlow, H.B. and Hill, R.M. (1963). Selective sensitivity to direction of movement in ganglion cells of the rabbit retina. *Science* 139. 412-414.
- Bergeron, S.A., Hannan, M.C., Codore, H., Fero, K., Li, G.H., Moak, Z., Yokogawa, T. and Burgess, H.A. (2012). Brain selective transgene expression in zebrafish using an NRSE derived motif. *Front Neural Circuits* 6. 110.
- Beyer, H.M., Juillot, S., Herbst, K., Samodelov, S.L., Müller, K., Schamel, W.W., Römer, W., Schäfer, E., Nagy, F., Strähle, U., *et al.* (2015). Red Light-Regulated Reversible Nuclear Localization of Proteins in Mammalian Cells and Zebrafish. *ACS Synth Biol* 4. 951-958.
- Bianco, I.H., Ma, L.H., Schoppik, D., Robson, D.N., Orger, M.B., Beck, J.C., Li, J.M., Schier, A.F., Engert, F. and Baker, R. (2012). The tangential nucleus controls a gravito-inertial vestibulo-ocular reflex. *Curr Biol* 22. 1285-1295.
- Blab, G.A., Lommerse, P.H.M., Cognet, L., Harms, G.S. and Schmidt, T. (2001). Two-photon excitation action cross-sections of the autofluorescent proteins. *Chemical Physics Letters* 350. 71-77.
- Borst, A. and Euler, T. (2011). Seeing things in motion: models, circuits, and mechanisms. *Neuron* 71. 974-994.
- Briggman, K.L., Helmstaedter, M. and Denk, W. (2011). Wiring specificity in the direction-selectivity circuit of the retina. *Nature* 471. 183-188.

Brockerhoff, S.E., Hurley, J.B., Janssen-Bienhold, U., Neuhauss, S.C., Driever, W. and Dowling, J.E. (1995). A behavioral screen for isolating zebrafish mutants with visual system defects. *Proc Natl Acad Sci U S A* 92. 10545-10549.

Burrill, J.D. and Easter, S.S., Jr. (1994). Development of the retinofugal projections in the embryonic and larval zebrafish (*Brachydanio rerio*). *J Comp Neurol* 346. 583-600.

Cazin, L., Precht, W. and Lannou, J. (1980). Pathways mediating optokinetic responses of vestibular nucleus neurons in the rat. *Pflugers Arch* 384. 19-29.

Chen, T.W., Wardill, T.J., Sun, Y., Pulver, S.R., Renninger, S.L., Baohan, A., Schreiter, E.R., Kerr, R.A., Orger, M.B., Jayaraman, V., *et al.* (2013). Ultrasensitive fluorescent proteins for imaging neuronal activity. *Nature* 499. 295-300.

Chung, K., Wallace, J., Kim, S.Y., Kalyanasundaram, S., Andalman, A.S., Davidson, T.J., Mirzabekov, J.J., Zalocusky, K.A., Mattis, J., Denisin, A.K., *et al.* (2013). Structural and molecular interrogation of intact biological systems. *Nature* 497. 332-337.

Curado, S., Anderson, R.M., Jungblut, B., Mumm, J., Schroeter, E. and Stainier, D.Y. (2007). Conditional targeted cell ablation in zebrafish: a new tool for regeneration studies. *Dev Dyn* 236. 1025-1035.

Dana, H., Mohar, B., Sun, Y., Narayan, S., Gordus, A., Hasseman, J.P., Tsegaye, G., Holt, G.T., Hu, A., Walpita, D., *et al.* (2016). Sensitive red protein calcium indicators for imaging neural activity. *Elife* 5.

Datta, S.R. and Patterson, G.H. (2012). Optical highlighter molecules in neurobiology. *Curr Opin Neurobiol* 22. 111-120.

Datta, S.R., Vasconcelos, M.L., Ruta, V., Luo, S., Wong, A., Demir, E., Flores, J., Balonze, K., Dickson, B.J. and Axel, R. (2008). The *Drosophila* pheromone cVA activates a sexually dimorphic neural circuit. *Nature* 452. 473-477.

Davison, J.M., Akitake, C.M., Goll, M.G., Rhee, J.M., Gosse, N., Baier, H., Halpern, M.E., Leach, S.D. and Parsons, M.J. (2007). Transactivation from Gal4-VP16 transgenic insertions for tissue-specific cell labeling and ablation in zebrafish. *Dev Biol* 304. 811-824.

Day, R.N. and Davidson, M.W. *Aequorea victoria* Fluorescent Proteins (<http://zeiss-campus.magnet.fsu.edu/articles/probes/jellyfishfps.html>, accessed: 7 Jan 2019).

Del Bene, F., Wyart, C., Robles, E., Tran, A., Looger, L., Scott, E.K., Isacoff, E.Y. and Baier, H. (2010). Filtering of visual information in the tectum by an identified neural circuit. *Science* 330. 669-673.

Denk, W. and Horstmann, H. (2004). Serial block-face scanning electron microscopy to reconstruct three-dimensional tissue nanostructure. *PLoS Biol* 2. e329.

Denk, W., Strickler, J.H. and Webb, W.W. (1990). Two-photon laser scanning fluorescence microscopy. *Science* 248. 73-76.

Dhande, O.S. and Huberman, A.D. (2014). Retinal ganglion cell maps in the brain: implications for visual processing. *Curr Opin Neurobiol* 24. 133-142.

Dhande, O.S., Stafford, B.K., Lim, J.A. and Huberman, A.D. (2015). Contributions of Retinal Ganglion Cells to Subcortical Visual Processing and Behaviors. *Annu Rev Vis Sci* 1. 291-328.

Distel, M., Hocking, J.C., Volkmann, K. and Köster, R.W. (2010). The centrosome neither persistently leads migration nor determines the site of axonogenesis in migrating neurons in vivo. *J Cell Biol* 191. 875-890.

Drawitsch, F., Karimi, A., Boergens, K.M. and Helmstaedter, M. (2018). FluoEM, virtual labeling of axons in three-dimensional electron microscopy data for long-range connectomics. *Elife* 7.

Dunn, T.W. (2015). Brain-Wide Neural Dynamics Underlying Looming-Evoked Escapes and Spontaneous Exploration (Doctoral dissertation, Harvard University, Graduate School of Arts & Sciences).

Easter, S.S., Jr. and Nicola, G.N. (1996). The development of vision in the zebrafish (*Danio rerio*). *Dev Biol* 180. 646-663.

Easter, S.S., Schmidt, J.T. and Leber, S.M. (1978). The paths and destinations of the induced ipsilateral retinal projection in goldfish. *J Embryol Exp Morphol* 45. 145-159.

Engeszer, R.E., Patterson, L.B., Rao, A.A. and Parichy, D.M. (2007). Zebrafish in the wild: a review of natural history and new notes from the field. *Zebrafish* 4. 21-40.

Fetcho, J.R. (2012). Neuroscience: Crystal-clear brains. *Nature* 485. 453-455.

Finger, T.E. and Karten, H.J. (1978). The accessory optic system in teleosts. *Brain Res* 153. 144-149.

- Förster, D., Arnold-Ammer, I., Laurell, E., Barker, A.J., Fernandes, A.M., Finger-Baier, K., Filosa, A., Helmbrecht, T.O., Kölsch, Y., Kühn, E., *et al.* (2017). Genetic targeting and anatomical registration of neuronal populations in the zebrafish brain with a new set of BAC transgenic tools. *Sci Rep* 7. 5230.
- Förster, D., Kramer, A., Baier, H. and Kubo, F. (2018). Optogenetic precision toolkit to reveal form, function and connectivity of single neurons. *Methods* 150. 42-48.
- Frank, D.D., Jouandet, G.C., Kearney, P.J., Macpherson, L.J. and Gallio, M. (2015). Temperature representation in the *Drosophila* brain. *Nature* 519. 358-361.
- Friedrich, R.W., Jacobson, G.A. and Zhu, P. (2010). Circuit neuroscience in zebrafish. *Curr Biol* 20. R371-381.
- Gabriel, J.P., Trivedi, C.A., Maurer, C.M., Ryu, S. and Bollmann, J.H. (2012). Layer-specific targeting of direction-selective neurons in the zebrafish optic tectum. *Neuron* 76. 1147-1160.
- Gahtan, E., Tanger, P. and Baier, H. (2005). Visual prey capture in larval zebrafish is controlled by identified reticulospinal neurons downstream of the tectum. *Journal of Neuroscience* 25. 9294-9303.
- Gibson (1954). The visual perception of object motion and subjective movement. *Psychology Review* 61. 304-314.
- Giolli, R.A., Blanks, R. and Lui, F. (2005). The accessory optic system- basic organization with an update on connectivity, neurochemistry, and function. *Progress in Brain Research* 151. 407-440.
- Grama, A. and Engert, F. (2012). Direction selectivity in the larval zebrafish tectum is mediated by asymmetric inhibition. *Front Neural Circuits* 6. 59.
- Guo, Q. and Li, J.Y.H. (2019). Defining developmental diversification of diencephalon neurons through single cell gene expression profiling. *Development* 146.
- Gupta, T., Marquart, G.D., Horstick, E.J., Tabor, K.M., Pajevic, S. and Burgess, H.A. (2018). Morphometric analysis and neuroanatomical mapping of the zebrafish brain. *Methods* 150. 49-62.
- Henderson, J.N., Gepshtein, R., Heenan, J.R., Kallio, K., Huppert, D. and Remington, S.J. (2009). Structure and mechanism of the photoactivatable green fluorescent protein. *J Am Chem Soc* 131. 4176-4177.
- Hill, A., Howard, C.V., Strähle, U. and Cossins, A. (2003). Neurodevelopmental defects in zebrafish (*Danio rerio*) at environmentally relevant dioxin (TCDD) concentrations. *Toxicol Sci* 76. 392-399.

Horseman, B.G., Macauley, M.W. and Barnes, W.J. (2011). Neuronal processing of translational optic flow in the visual system of the shore crab *Carcinus maenas*. *J Exp Biol* 214. 1586-1598.

Horstick, E.J., Jordan, D.C., Bergeron, S.A., Tabor, K.M., Serpe, M., Feldman, B. and Burgess, H.A. (2015). Increased functional protein expression using nucleotide sequence features enriched in highly expressed genes in zebrafish. *Nucleic Acids Res* 43. e48.

Huang, Y.Y. and Neuhauss, S.C. (2008). The optokinetic response in zebrafish and its applications. *Front Biosci* 13. 1899-1916.

Ibbotson, M.R., Marotte, L.R. and Mark, R.F. (2002). Investigations into the source of binocular input to the nucleus of the optic tract in an Australian marsupial, the wallaby *Macropus eugenii*. *Exp Brain Res* 147. 80-88.

Kalueff, A.V., Stewart, A.M. and Gerlai, R. (2014). Zebrafish as an emerging model for studying complex brain disorders. *Trends Pharmacol Sci* 35. 63-75.

Kawakami, K., Asakawa, K., Muto, A. and Wada, H. (2016). Tol2-mediated transgenesis, gene trapping, enhancer trapping, and Gal4-UAS system. *Methods Cell Biol* 135. 19-37.

Kawakami, K., Shima, A. and Kawakami, N. (2000). Identification of a functional transposase of the Tol2 element, an Ac-like element from the Japanese medaka fish, and its transposition in the zebrafish germ lineage. *Proc Natl Acad Sci U S A* 97. 11403-11408.

Kawano, F., Okazaki, R., Yazawa, M. and Sato, M. (2016). A photoactivatable Cre-loxP recombination system for optogenetic genome engineering. *Nat Chem Biol* 12. 1059-1064.

Kennedy, M.J., Hughes, R.M., Peteya, L.A., Schwartz, J.W., Ehlers, M.D. and Tucker, C.L. (2010). Rapid blue-light-mediated induction of protein interactions in living cells. *Nat Methods* 7. 973-975.

Kimmel, C.B., Ballard, W.W., Kimmel, S.R., Ullmann, B. and Schilling, T.F. (1995). Stages of embryonic development of the zebrafish. *Dev Dyn* 203. 253-310.

Klar, M. and Hoffmann, K.P. (2002). Visual direction-selective neurons in the pretectum of the rainbow trout. *Brain Res Bull* 57. 431-433.

Klein, A., Andersson, J., Ardekani, B.A., Ashburner, J., Avants, B., Chiang, M.C., Christensen, G.E., Collins, D.L., Gee, J., Hellier, P., *et al.* (2009). Evaluation of 14 nonlinear deformation algorithms applied to human brain MRI registration. *Neuroimage* 46. 786-802.

- Knogler, L.D., Kist, A.M. and Portugues, R. (2019). Motor context dominates output from purkinje cell functional regions during reflexive visuomotor behaviours. *Elife* 8.
- Kornfeld, J. and Denk, W. (2018). Progress and remaining challenges in high-throughput volume electron microscopy. *Curr Opin Neurobiol* 50. 261-267.
- Kubo, F., Hablitzel, B., Dal Maschio, M., Driever, W., Baier, H. and Arrenberg, A.B. (2014). Functional architecture of an optic flow-responsive area that drives horizontal eye movements in zebrafish. *Neuron* 81. 1344-1359.
- Lauter, G., Soll, I. and Hauptmann, G. (2013). Molecular characterization of prosomeric and intraprosomeric subdivisions of the embryonic zebrafish diencephalon. *J Comp Neurol* 521. 1093-1118.
- Lenn, N.J. (1972). An electron microscopic study of accessory optic endings in the rat medial terminal nucleus. *Brain Res* 43. 622-628.
- Lister, J.A., Robertson, C.P., Lepage, T., Johnson, S.L. and Raible, D.W. (1999). Nacre encodes a zebrafish microphthalmia-related protein that regulates neural-crest-derived pigment cell fate. *Development* 126. 3757-3767.
- Longair, M.H., Baker, D.A. and Armstrong, J.D. (2011). Simple Neurite Tracer: open source software for reconstruction, visualization and analysis of neuronal processes. *Bioinformatics* 27. 2453-2454.
- Marquart, G.D., Tabor, K.M., Brown, M., Strykowski, J.L., Varshney, G.K., LaFave, M.C., Mueller, T., Burgess, S.M., Higashijima, S. and Burgess, H.A. (2015). A 3D searchable database of transgenic zebrafish Gal4 and Cre lines for functional neuroanatomy studies. *Front Neural Circuits* 9. 78.
- Marquart, G.D., Tabor, K.M., Horstick, E.J., Brown, M., Geoca, A.K., Polys, N.F., Nogare, D.D. and Burgess, H.A. (2017). High-precision registration between zebrafish brain atlases using symmetric diffeomorphic normalization. *Gigascience* 6. 1-15.
- Martersteck, E.M., Hirokawa, K.E., Evarts, M., Bernard, A., Duan, X., Li, Y., Ng, L., Oh, S.W., Ouellette, B., Royall, J.J., *et al.* (2017). Diverse central projection patterns of petinal ganglion cells. *Cell Rep* 18. 2058-2072.
- Masseck, O.A. and Hoffmann, K.P. (2009a). Comparative neurobiology of the optokinetic reflex. *Ann N Y Acad Sci* 1164. 430-439.

Masseck, O.A. and Hoffmann, K.P. (2009b). Question of reference frames: visual direction-selective neurons in the accessory optic system of goldfish. *J Neurophysiol* 102. 2781-2789.

Mathias, J.R., Zhang, Z.Y., Saxena, M.T. and Mumm, J.S. (2014). Enhanced Cell-Specific Ablation in Zebrafish Using a Triple Mutant of Escherichia Coli Nitroreductase. *Zebrafish* 11. 85-97.

Matsui, H., Namikawa, K., Babaryka, A. and Köster, R.W. (2014). Functional regionalization of the teleost cerebellum analyzed in vivo. *Proc Natl Acad Sci U S A* 111. 11846-11851.

Mckenna, O.C. and Wallman, J. (1981). Identification of Avian Brain-Regions Responsive to Retinal Slip Using 2-Deoxyglucose. *Brain Research* 210. 455-460.

Meyers, J.R. (2018). Zebrafish: Development of a Vertebrate Model Organism. *Current Protocols Essential Laboratory Techniques* 16. e19.

Miesenböck, G. (2009). The Optogenetic Catechism. *Science* 326. 395-399.

Mohr, M.A., Argast, P. and Pantazis, P. (2016). Labeling cellular structures in vivo using confined primed conversion of photoconvertible fluorescent proteins. *Nat Protoc* 11. 2419-2431.

Morin, L.P. and Studholme, K.M. (2014). Retinofugal projections in the mouse. *J Comp Neurol* 522. 3733-3753.

Müller, K., Engesser, R., Schulz, S., Steinberg, T., Tomakidi, P., Weber, C.C., Ulm, R., Timmer, J., Zurbriggen, M.D. and Weber, W. (2013). Multi-chromatic control of mammalian gene expression and signaling. *Nucleic Acids Res* 41. e124.

Muto, A., Lal, P., Ailani, D., Abe, G., Itoh, M. and Kawakami, K. (2017). Activation of the hypothalamic feeding centre upon visual prey detection. *Nat Commun* 8. 15029.

Nakai, J., Ohkura, M. and Imoto, K. (2001). A high signal-to-noise Ca²⁺ probe composed of a single green fluorescent protein. *Nat Biotechnol* 19. 137-141.

Naumann, E.A., Fitzgerald, J.E., Dunn, T.W., Rihel, J., Sompolinsky, H. and Engert, F. (2016). From whole-brain data to functional circuit models: The zebrafish optomotor response. *Cell* 167. 947-960 e920.

Neuhauss, S.C., Biehlmaier, O., Seeliger, M.W., Das, T., Kohler, K., Harris, W.A. and Baier, H. (1999). Genetic disorders of vision revealed by a behavioral screen of 400 essential loci in zebrafish. *J Neurosci* 19. 8603-8615.

- Nikolaou, N., Lowe, A.S., Walker, A.S., Abbas, F., Hunter, P.R., Thompson, I.D. and Meyer, M.P. (2012). Parametric functional maps of visual inputs to the tectum. *Neuron* 76. 317-324.
- Orger, M.B., Gahtan, E., Muto, A., Page-McCaw, P., Smear, M.C. and Baier, H. (2004). Behavioral screening assays in zebrafish. *Methods Cell Biol* 77. 53-68.
- Orger, M.B., Kampff, A.R., Severi, K.E., Bollmann, J.H. and Engert, F. (2008). Control of visually guided behavior by distinct populations of spinal projection neurons. *Nat Neurosci* 11. 327-333.
- Orger, M.B., Smear, M.C., Anstis, S.M. and Baier, H. (2000). Perception of Fourier and non-Fourier motion by larval zebrafish. *Nat Neurosci* 3. 1128-1133.
- Paquet, D., Bhat, R., Sydow, A., Mandelkow, E.M., Berg, S., Hellberg, S., Falting, J., Distel, M., Köster, R.W., Schmid, B. and Haass, C. (2009). A zebrafish model of tauopathy allows in vivo imaging of neuronal cell death and drug evaluation. *J Clin Invest* 119. 1382-1395.
- Pathak, G.P., Spiltoir, J.I., Hoglund, C., Polstein, L.R., Heine-Koskinen, S., Gersbach, C.A., Rossi, J. and Tucker, C.L. (2017). Bidirectional approaches for optogenetic regulation of gene expression in mammalian cells using Arabidopsis cryptochrome 2. *Nucleic Acids Res* 45. e167.
- Patterson, G.H. and Lippincott-Schwartz, J. (2002). A photoactivatable GFP for selective photolabeling of proteins and cells. *Science* 297. 1873-1877.
- Pereira, A., Volchan, E., Vargas, C.D., Penetra, L. and Rocha-Miranda, C.E. (2000). Cortical and subcortical influences on the nucleus of the optic tract of the opossum. *Neuroscience* 95. 953-963.
- Perez Koldenkova, V. and Nagai, T. (2013). Genetically encoded Ca(2+) indicators: properties and evaluation. *Biochim Biophys Acta* 1833. 1787-1797.
- Piston, D.W., Campbell, R.E., Day, R.N. and Davidson, M.W. Optical Highlighter Fluorescent Proteins (<http://zeiss-campus.magnet.fsu.edu/articles/probes/highlighterfps.html>, accessed: 7 Jan 2019).
- Portugues, R. and Engert, F. (2009). The neural basis of visual behaviors in the larval zebrafish. *Curr Opin Neurobiol* 19. 644-647.
- Portugues, R., Feierstein, C.E., Engert, F. and Orger, M.B. (2014). Whole-brain activity maps reveal stereotyped, distributed networks for visuomotor behavior. *Neuron* 81. 1328-1343.
- Preuss, S.J., Trivedi, C.A., vom Berg-Maurer, C.M., Ryu, S. and Bollmann, J.H. (2014). Classification of object size in retinotectal microcircuits. *Curr Biol* 24. 2376-2385.

Randlett, O., Wee, C.L., Naumann, E.A., Nnaemeka, O., Schoppik, D., Fitzgerald, J.E., Portugues, R., Lacoste, A.M., Riegler, C., Engert, F. and Schier, A.F. (2015). Whole-brain activity mapping onto a zebrafish brain atlas. *Nat Methods* 12. 1039-1046.

Reade, A., Motta-Mena, L.B., Gardner, K.H., Stainier, D.Y., Weiner, O.D. and Woo, S. (2017). TAE: a zebrafish-optimized optogenetic gene expression system with fine spatial and temporal control. *Development* 144. 345-355.

Renninger, S.L. and Orger, M.B. (2013). Two-photon imaging of neural population activity in zebrafish. *Methods* 62. 255-267.

Richardson, D.S. and Lichtman, J.W. (2015). Clarifying Tissue Clearing. *Cell* 162. 246-257.

Rinner, O., Rick, J.M. and Neuhauss, S.C. (2005). Contrast sensitivity, spatial and temporal tuning of the larval zebrafish optokinetic response. *Invest Ophthalmol Vis Sci* 46. 137-142.

Robles, E., Laurell, E. and Baier, H. (2014). The retinal projectome reveals brain-area-specific visual representations generated by ganglion cell diversity. *Curr Biol* 24. 2085-2096.

Roeser, T. and Baier, H. (2003). Visuomotor behaviors in larval zebrafish after GFP-guided laser ablation of the optic tectum. *J Neurosci* 23. 3726-3734.

Ronneberger, O., Liu, K., Rath, M., Ruebeta, D., Mueller, T., Skibbe, H., Drayer, B., Schmidt, T., Filippi, A., Nitschke, R., *et al.* (2012). ViBE-Z: a framework for 3D virtual colocalization analysis in zebrafish larval brains. *Nat Methods* 9. 735-742.

Rubenstein, J.L., Martinez, S., Shimamura, K. and Puelles, L. (1994). The embryonic vertebrate forebrain: the prosomeric model. *Science* 266. 578-580.

Ruta, V., Datta, S.R., Vasconcelos, M.L., Freeland, J., Looger, L.L. and Axel, R. (2010). A dimorphic pheromone circuit in *Drosophila* from sensory input to descending output. *Nature* 468. 686-690.

Saalfeld, S., Cardona, A., Hartenstein, V. and Tomancak, P. (2009). CATMAID: collaborative annotation toolkit for massive amounts of image data. *Bioinformatics* 25. 1984-1986.

Sabbah, S., Gemmer, J.A., Bhatia-Lin, A., Manoff, G., Castro, G., Siegel, J.K., Jeffery, N. and Berson, D.M. (2017). A retinal code for motion along the gravitational and body axes. *Nature* 546. 492-497.

Scheer, N. and Campos-Ortega, J.A. (1999). Use of the Gal4-UAS technique for targeted gene expression in the zebrafish. *Mech Dev* 80. 153-158.

Schiff, D., Cohen, B. and Raphan, T. (1988). Nystagmus induced by stimulation of the nucleus of the optic tract in the monkey. *Exp Brain Res* 70. 1-14.

Schiller, P.H. (2010). Parallel information processing channels created in the retina. *Proc Natl Acad Sci U S A* 107. 17087-17094.

Schmidt, M., Schiff, D. and Bentivoglio, M. (1995). Independent efferent populations in the nucleus of the optic tract: an anatomical and physiological study in rat and cat. *J Comp Neurol* 360. 271-285.

Schuster, K. and Ghysen, A. (2013). Labeling defined cells or subsets of cells in zebrafish by Kaede photoconversion. *Cold Spring Harb Protoc* 2013. 1073-1075.

Scott, D.J., Gunn, N.J., Yong, K.J., Wimmer, V.C., Veldhuis, N.A., Challis, L.M., Haidar, M., Petrou, S., Bathgate, R.A.D. and Griffin, M.D.W. (2018). A novel ultra-stable, monomeric green fluorescent protein for direct volumetric imaging of whole organs using CLARITY. *Sci Rep* 8. 667.

Scott, E.K. and Baier, H. (2009). The cellular architecture of the larval zebrafish tectum, as revealed by Gal4 enhancer trap lines. *Front Neural Circuits* 3. 13.

Scott, E.K., Mason, L., Arrenberg, A.B., Ziv, L., Gosse, N.J., Xiao, T., Chi, N.C., Asakawa, K., Kawakami, K. and Baier, H. (2007). Targeting neural circuitry in zebrafish using Gal4 enhancer trapping. *Nat Methods* 4. 323-326.

Semmelhack, J.L., Donovan, J.C., Thiele, T.R., Kuehn, E., Laurell, E. and Baier, H. (2014). A dedicated visual pathway for prey detection in larval zebrafish. *Elife* 3.

Shcherbakova, D.M., Sengupta, P., Lippincott-Schwartz, J. and Verkhusha, V.V. (2014). Photocontrollable fluorescent proteins for superresolution imaging. *Annu Rev Biophys* 43. 303-329.

Spence, R., Gerlach, G., Lawrence, C. and Smith, C. (2008). The behaviour and ecology of the zebrafish, *Danio rerio*. *Biol Rev Camb Philos Soc* 83. 13-34.

Stahl, F.W. (1995). George Streisinger - Biographical Memoir (Washington D.C.: National Academies Press).

Subedi, A., Macurak, M., Gee, S.T., Monge, E., Goll, M.G., Potter, C.J., Parsons, M.J. and Halpern, M.E. (2014). Adoption of the Q transcriptional regulatory system for zebrafish transgenesis. *Methods* 66. 433-440.

Svoboda, K. and Yasuda, R. (2006). Principles of two-photon excitation microscopy and its applications to neuroscience. *Neuron* 50. 823-839.

Tabor, K.M., Marquart, G.D., Hurt, C., Smith, T.S., Geoca, A.K., Bhandiwad, A.A., Subedi, A., Sinclair, J.L., Rose, H.M., Polys, N.F. and Burgess, H.A. (2019). Brain-wide cellular resolution imaging of Cre transgenic zebrafish lines for functional circuit-mapping. *Elife* 8.

Temizer, I., Donovan, J.C., Baier, H. and Semmelhack, J.L. (2015). A visual pathway for looming-evoked escape in larval zebrafish. *Curr Biol* 25. 1823-1834.

Vladimirov, N., Wang, C., Hockendorf, B., Pujala, A., Tanimoto, M., Mu, Y., Yang, C.T., Wittenbach, J.D., Freeman, J., Preibisch, S., *et al.* (2018). Brain-wide circuit interrogation at the cellular level guided by online analysis of neuronal function. *Nat Methods* 15. 1117-1125.

Volchan, E., Rocha-Miranda, C.E., Picanco-Diniz, C.W., Zinsmeister, B., Bernardes, R.F. and Franca, J.G. (1989). Visual response properties of pretectal units in the nucleus of the optic tract of the opossum. *Exp Brain Res* 78. 380-386.

Wang, K., Hinz, J., Haikala, V., Reiff, D.F. and Arrenberg, A.B. (2019). Selective processing of all rotational and translational optic flow directions in the zebrafish pretectum and tectum. *BMC Biol* 17. 29.

Wullimann, M.F., Rupp, B. and Reichert, H. (1996). *Neuroanatomy of the zebrafish brain: a topological atlas* (Basel, Boston, Berlin: Birkhäuser).

Yáñez, J., Suárez, T., Quelle, A., Folgueira, M. and Anadón, R. (2018). Neural connections of the pretectum in zebrafish (*Danio rerio*). *J Comp Neurol* 526. 1017-1040.

Yin, C., Li, X. and Du, J. (2019). Optic tectal superficial interneurons detect motion in larval zebrafish. *Protein Cell* 10. 238-248.

Zhang, B.B., Yao, Y.Y., Zhang, H.F., Kawakami, K. and Du, J.L. (2017). Left habenula mediates light-preference behavior in zebrafish via an asymmetrical visual pathway. *Neuron* 93. 914-928 e914.

Zimmermann, M.J.Y., Nevala, N.E., Yoshimatsu, T., Osorio, D., Nilsson, D.E., Berens, P. and Baden, T. (2018). Zebrafish differentially process color across visual space to match natural scenes. *Curr Biol* 28. 2018-2032 e2015.

Eidesstattliche Erklärung (Affidavit)

Ich versichere hiermit an Eides statt, dass die vorliegende Dissertation von mir selbständig und ohne unerlaubte Hilfe angefertigt wurde.

Erklärung

Hiermit erkläre ich, dass

- die Dissertation nicht ganz oder in wesentlichen Teilen einer anderen Prüfungskommission vorgelegt worden ist und
- ich mich nicht anderweitig einer Doktorprüfung ohne Erfolg unterzogen habe.

München, den 10. Mai 2019

Anna Kramer